

Discovery of Co-existing Non-collinear Spin Textures in D_{2d} Heusler Compounds

Dissertation

Zur Erlangung des Doktorgrades der Naturwissenschaften
(Dr. rer. nat)

Der

Naturwissenschaftlichen Fakultät II
Chemie, Physik und Mathematik

der Martin-Luther-Universität
Halle-Wittenberg

Vorgelegt von

Herrn **Jagannath Jena**
geb. am 30.04.1991 in Bhubaneswar, Indien

Gutachter:

Prof. Dr. Stuart S. P. Parkin

Prof. Dr. Christian Back

Prof. Dr. Istvan Kézsmárki

Tag der öffentlichen Verteidigung: 20.05.2021

*Dedicated to my sister, Kati, for
her unconditional love*

Content

Abbreviations	viii
Abstract	x
1. Introduction	1
2. Magnetic skyrmions	5
2.1 Non-collinear magnetism	5
2.2 Magnetic skyrmions	6
2.3 Magnetic antiskyrmions	9
2.4 Topological definition of skyrmions	11
2.5 Energy terms for stabilizing skyrmions	13
2.5.1 Exchange interaction	13
2.5.2 Zeeman interaction and anisotropies	14
2.5.3 Dzyaloshinskii-Moriya interaction	15
2.5.4 Dipole-dipole interactions	18
2.6 Towards application of skyrmions	18
2.7 Stabilization of different spin textures in single material system	20
2.8 Summary	21

3. Experimental methods	23
3.1 Magnetization measurements	23
3.2 Scanning electron microscopy and electron backscatter diffraction	24
3.3 Focused ion beam	27
3.4 Transmission electron microscopy	30
3.5 Electron diffraction	31
3.6 Lorentz transmission electron microscopy	33
3.7 High-resolution and scanning transmission electron microscopy	35
3.8 Summary	37
4. Elliptical Bloch skyrmions and antiskyrmions in a D_{2d} inverse Heusler compound	39
4.1 Introduction	39
4.2 Methods	40
4.2.1 Experimental details	40
4.2.2 Micromagnetic simulations	41
4.3 Results and discussion	42
4.3.1 Round and square antiskyrmions	42
4.3.2 Elliptical Bloch skyrmions	46
4.3.3 Enhanced stability of elliptical Bloch skyrmions	48
4.3.4 Elliptical Bloch skyrmions chiral twins	50
4.3.5 Switching between round and square antiskyrmions	53
4.3.6 Simultaneous existence of elliptical skyrmions and antiskyrmion	55
4.3.7 Magnetic phase diagram	57
4.4 Summary	59
5. Evolution and competition between chiral spin textures in D_{2d} nano-stripes	61
5.1 Introduction	61
5.2 Methods	63
5.2.1 Experimental details	63
5.2.2 Micromagnetic simulations	63
5.3 Results and discussion	64

5.3.1 Nano-stripes along different crystallographic directions	64
5.3.2 Helices and antiskyrmions in [010] oriented nano-stripe	66
5.3.3 Difference between helices and other domains in D_{2d} system	72
5.3.4 Antiskyrmion chains in differently oriented nano-stripes	74
5.3.5 Co-existence of skyrmions and antiskyrmions at room temperature	81
5.4 Summary	83
6. Stability, collapse dynamics and fractional form of antiskyrmions and elliptical Bloch skyrmions	85
6.1 Introduction	85
6.2 Experimental details	86
6.3 Results and discussion	86
6.3.1 Metastability of square antiskyrmions	86
6.3.2 Collapse dynamics of antiskyrmions and elliptical skyrmions	89
6.3.3 Fractional elliptical Bloch skyrmions and antiskyrmions	92
6.3.4 In-plane field dependent metastability of spin textures	95
6.3.5 Evaluation of spin textures from the helical state	98
6.3.6 Stability of elliptical skyrmions against heating	100
6.4 Summary	102
7. Observation of antiskyrmions and Bloch skyrmions in a low moment ferrimagnetic Heusler compound	103
7.1 Introduction	103
7.2 Experimental methods	104
7.2.1 Bulk polycrystalline synthesis	104
7.2.2 Powder XRD, EDXS, and EBSD	104
7.2.3 Magnetization measurements	107
7.2.4 Microscopic characterizations	109
7.3 Results and discussion	111
7.3.1 Magnetic antiskyrmions in $Mn_2Rh_{0.95}Ir_{0.05}Sn$	111
7.3.2 Field driven formation of antiskyrmions	112
7.3.3 Helical periods of $Mn_2Rh_{0.95}Ir_{0.05}Sn$ and $Mn_{1.4}Pt_{0.9}Pd_{0.1}Sn$	115
7.3.4 Bloch skyrmions in $Mn_2Rh_{0.95}Ir_{0.05}Sn$	116

7.3.5 Field driven formation of Bloch skyrmions	117
7.3.6 Stability of Bloch skyrmions against heating	122
7.4 Summary	124
8. Conclusion and outlook	125
8.1 Conclusion	125
8.2 Future perspectives	128
Appendix	131
References	143
Author contributions	157
Acknowledgements	159
Curriculum vitae	161
List of publications	163
Eidesstattliche Erklärung	165

Abbreviations

BLS	Brillouin light scattering
CCD	charge-coupled device
DC	direct current
DMI	Dzyaloshinskii-Moriya interaction
DPC	differential phase contrast
EBS	electron back scattering diffraction
EDXS	energy-dispersive X-ray spectroscopy
FC	field cooled
FEG	field emission gun
FIB	focused ion beam
GIS	gas injection system
HAADF	high angle annular dark-field
HT	high tension
LAED	low angle electron diffraction
LTEM	Lorentz transmission electron microscope
MFM	magnetic force microscope
NV	nitrogen-vacancy
PXRD	powder X-ray diffraction
SAED	selected area electron diffraction
SEM	scanning electron microscope
SOC	spin-orbit coupling
SP-STM	spin polarized scanning tunneling microscope
SQUID	superconducting quantum interference device
STEM	scanning transmission electron microscopy
STXM	scanning transmission X-ray microscopy
TEM	transmission electron microscopy
VSM	vibrating-sample magnetometer
XMCD	X-ray magnetic circular dichroism
ZFC	zero-field cooled

Abstract

Non-collinear spin textures are of great interest both fundamentally and technologically. One of the most interesting such textures is a skyrmion, which is a vortex-like localized topological spin texture that possesses numerous interesting features. Its exotic properties include robustness against impurities and external perturbations, high mobility, long lifetimes and a low threshold current for movement. These make magnetic skyrmions fundamentally interesting and attractive for technological applications such as high-density memory devices, especially in a racetrack storage device and for neuromorphic computing. Over the last decade, extensive studies have been carried out concerning two types of isotropic topological spin textures: Bloch skyrmions and Néel skyrmions that have chiral boundaries with helicoid and cycloid propagating walls, respectively. They have been observed in the bulk system with B20 compounds and those with C_{3v} crystal symmetry, respectively. Recently, a different kind of anisotropic spin texture termed an ‘*antiskyrmion*’ (composed of alternating chiral boundaries of helicoids and cycloids) has been observed in a ferromagnetic inverse tetragonal Heusler compound $Mn_{1.4}Pt_{0.9}Pd_{0.1}Sn$ with D_{2d} symmetry. In this thesis, an unanticipated discovery of a novel spin texture namely an ‘*elliptical Bloch Skyrmion*’ having a *topological charge* -1 has been found in the same D_{2d} system whose crystalline symmetry supports *antiskyrmions* with *topological charge* $+1$. The *simultaneous existence* of these distinct nano-objects with opposite topological charges depends on the temperature and field history. These spin textures are also found in $Mn_2Rh_{0.95}Ir_{0.05}Sn$, a *low saturation magnetization ferrimagnetic* inverse tetragonal Heusler compound, thereby opening a path toward fully zero moment spin textures. In addition to its fundamental importance, the findings presented in this thesis permit an *advanced version of the magnetic racetrack* data storage device that could be more feasible than conventional racetracks. Instead of utilizing the presence or absence of skyrmions as binary bits, a sequence of skyrmions can be read as ‘1’ bits and antiskyrmions as ‘0’ bits that is more robust against thermal drift, and the necessity of maintaining defined distances among the data bits is not needed.

I

Introduction

Chirality is a general characteristic of many diverse objects such as solid and liquid crystals, molecules, and light, and gives rise to rich phenomena. In magnetism, chirality is exhibited by spin textures in materials that lack inversion symmetry and is a consequence, for example, of an asymmetric exchange interaction, a relativistic phenomenon called the Dzyaloshinskii-Moriya exchange interaction (DMI)^{1,2}. One of the most interesting spin textures that was recently discovered is the skyrmion which is chiral and has been observed in several distinct families of acentric magnetic compounds^{3,4}. Their small size, intrinsic stability that derives from their topologically protected properties, as well as the low current densities required for their motion have great potential for the ever-growing demand of energy efficient data-storage devices⁵. Such devices may overcome the forecast breakdown of Moore's law⁶ exponential growth of storage and operation speed. In the proposed non-volatile storage device, magnetic racetrack memory, the presence and absence of nano size skyrmions can be used to encode '1' and '0' bits⁷. Based on the work presented in this thesis, the concept of a skyrmion based racetrack operation can be extended. For example, spin textures with opposite topological charges, a sequence of skyrmions and antiskyrmions (Fig. 1), can be used as the digital bits. This concept could be more reliable against thermal drift and thus superior to a racetrack based on a single type of a topological spin texture. Such a device may overcome the need to maintain a well-defined distance between successive magnetic bits in a racetrack⁸. Here, in this thesis, the discovery of several non-collinear spin textures having distinct topological charges in a single D_{2d} Heusler compound is presented.

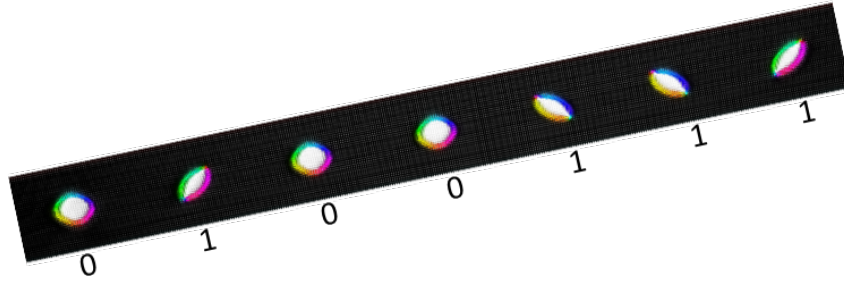


Figure 1 | *Skyrmion-antiskyrmion racetrack.* Co-existence of skyrmions (elliptically shaped) and antiskyrmions in a racetrack geometry. Skyrmions are encoded as ‘1’ bits and antiskyrmions as ‘0’ bits.

The main focus of this study is the investigation of magnetic textures in D_{2d} Heusler compounds and the main goals of the thesis are as follows:

- (I) Discovering new spin textures in D_{2d} Heusler compounds and studying their detailed properties to enrich the field of topology in magnetism.
- (II) Optimizing the nano-track geometry and generating isolated and single chains of topologically protected non-trivial nano-objects that will establish new hallmarks for technological applications.
- (III) Studying the stability of spin textures with magnetic fields and temperatures using various protocols and finding a way to observe the striking behavior of spin textures near the specimen edges.
- (IV) Exploring new compound with different compositions having distinct magnetic properties in the D_{2d} family that can host different spin textures.

The next few paragraphs give chapter-wise outlines considering the above-mentioned goals.

In Chapter 2, the basics of non-collinearity in magnetism are introduced with a particular focus on Bloch skyrmions, Néel skyrmions and antiskyrmions. The energy terms require to stabilize those topological spin textures are presented. The intrinsic stability of various spin textures and their implication as potential candidates in future technology are also mentioned in this chapter.

The experimental tools which are employed in this thesis are mentioned in chapter 3. The step-wise preparation of thin specimen from the bulk crystal is presented in detail. The working principle of various techniques are elaborated to investigate structural and magnetic properties of bulk samples and thin specimens.

Chapter 4 is devoted to the surprising discovery of a topologically charged object namely an elliptical Bloch skyrmion (topological charge -1) in the D_{2d} compound $Mn_{1.4}Pt_{0.9}Pd_{0.1}Sn$ whose symmetry should provide support only for one topological object, namely an antiskyrmion (topological charge +1). The interactions responsible for the formation of two distinct oppositely topologically charged objects and their properties are discussed in detail. In addition, other than round shaped antiskyrmions, their deformation to square-shaped objects is discussed. The formation of the crystal $Mn_{1.4}Pt_{0.9}Pd_{0.1}Sn$ is only possible when the compound has significant numbers of Mn vacancies. The reason for this is not properly understood.

Differently oriented nano-tracks are investigated to study the anisotropic behavior of antiskyrmions in chapter 5. Sparse state and a single chain of antiskyrmions, elliptical Bloch skyrmions, and their simultaneous existence are observed at room temperature. Furthermore, the nucleation of nano-objects depending on the starting configurations is demonstrated in different reliable ways.

The various possible metastable states of spin textures are examined depending upon the field and temperature. The role of the in-plane magnetic field is shown extensively by obtaining the different initial states through the temporary application of in-plane components of fields. In addition, the stability of fractional antiskyrmions and fractional elliptical skyrmions, which bear fractional charge numbers, near the edge of the extended specimen are described in chapter 6.

In chapter 7, antiskyrmions and Bloch skyrmions are also observed in a second D_{2d} compound of $Mn_2Rh_{0.95}Ir_{0.05}Sn$ that is without any significant Mn vacancies unlike $Mn_{1.4}Pt_{0.9}Pd_{0.1}Sn$. The stability of spin textures is inspected over a wide range of temperature and field. This compound is a ferrimagnet which has a magnetic moment less than half of the ferromagnetic compound $Mn_{1.4}Pt_{0.9}Pd_{0.1}Sn$.

Chapter 8 summarizes the results of the thesis, and gives an outlook on the future research projects.

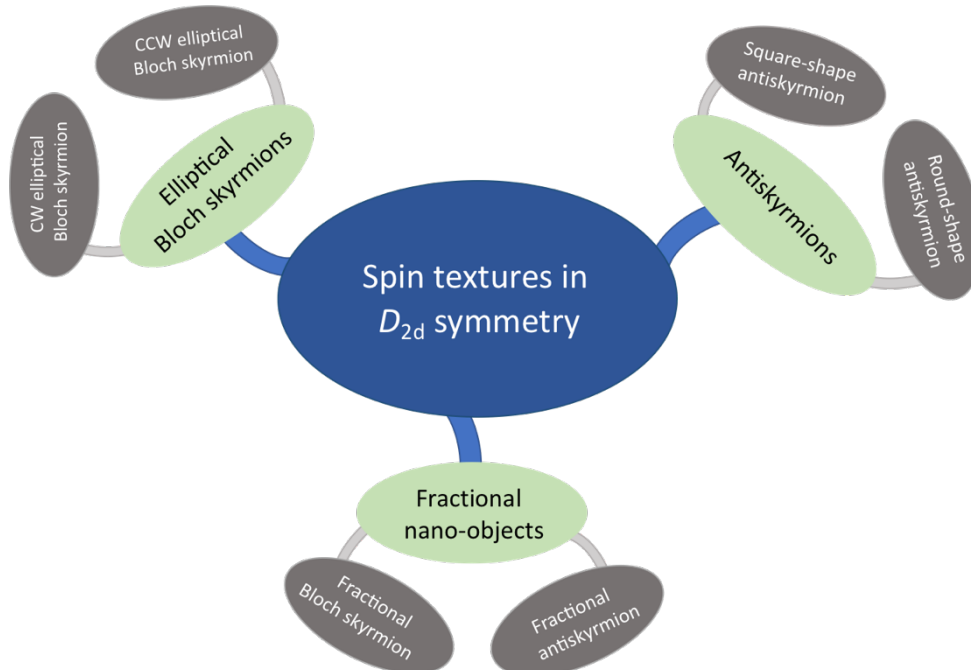


Figure 2 | *Spin textures in D_{2d} symmetry*. Schematic diagram of different spin textures which are presented in this thesis for systems with D_{2d} symmetry. CW and CCW correspond to clock-wise and counter clock-wise chiralities for elliptical Bloch skyrmions.

2

Magnetic skyrmions

2.1 Non-collinear magnetism

The most common demonstration of magnetism is collinear magnetism, such as ferromagnetism, ferrimagnetism and antiferromagnetism, where magnetic moments are aligned either parallel or antiparallel to each other bearing a common magnetization axis. The first non-collinear magnetic structure was discovered experimentally about 50 years ago^{9, 10}. In contrast to the collinear magnetism, the magnetization axis for all atoms in non-collinear magnets is not the same but changes direction spatially. The complex non-collinear magnetic structures exist in various magnetic systems. They occur in matters with competing exchange interaction among different neighbors such as helimagnet of lanthanides, fcc-Fe, bcc-Eu, or in LaMn_2Ge_2 ¹¹⁻¹³. Several magnetically disordered systems, such as, spin glasses or triangular lattice that interact antiferromagnetically with their neighbors, have non-collinear structures. Other example includes domain walls where competing monocrystalline anisotropy and exchange play an essential role for the formation of non-collinear structures. Of all these non-collinear structures, chiral magnet is particularly interesting as it warrants a special impact due to the presence of the antisymmetric exchange interaction known as Dzyaloshinskii-Moriya interaction (DMI)^{1, 2}. The distinct features in the chiral magnets are their fixed sense rotation of magnetization tied to the crystal lattice's chirality. Here the competition between the exchange interaction, which favors the parallel alignment of the spins, and DMI interaction, which favors the perpendicular spin arrangement, results in uniform canting of the spins that differs from the complex stripe pattern arising from the exchange and dipole interactions. On applying the

magnetic field along the crystallographic direction, the ground state helical structure in the chiral magnet transforms to the non-trivial topological object of fixed chirality, which is coined as magnetic skyrmion. These chiral structures, unlike conventional bubble, give rise to an interesting physical phenomenon called topological Hall effect, which is generated due to the emergent magnetic field^{14, 15}. Moreover, skyrmions can be moved in an ultralow current density¹⁶, whose magnitude is few orders smaller than that of bubbles or domain walls motion^{5, 17}.

2.2 Magnetic skyrmions

The term ‘skyrmion’ was coined by British Physicist Tony Skyrme to describe the interaction of fundamental particles such as pions using the nonlinear field model¹⁸. Nearly 30 years later, the pioneering theoretical observation of magnetic skyrmions in acentric magnets was predicted for the first time in condensed matter Physics by Bogdanov *et al.*³ in 1989. It proposed the potential stability of non-singular, localized and topologically stable spin configuration on including the chiral terms in the classical energy equation. Their existence as a periodic array of skyrmion lattice was found in several crystallographic symmetry classes¹⁹. The skyrmions are found in non-centrosymmetric chiral crystals because of the antisymmetric exchange interaction called DMI, resulting from breaking the inversion symmetry and spin-orbit coupling (SOC). Experimentally, skyrmion was confirmed by Mühlbauer *et al.*²⁰ in 2009, nearly two decades after the theoretical report. They were found in a cubic MnSi crystal via small-angle neutron scattering. In this crystal, the ground state is a helical phase and the skyrmion state (indicated as ‘A’ phase in Fig. 1a) is found over a narrow region of field and temperature near the transition temperature. When the magnetic field is applied perpendicular to the single crystal surface, six bright spots are produced in the neutron scattering which indicates the existence of skyrmion lattice (Fig. 1b and 1c). The first real space imaging of skyrmions was successfully achieved using an in-situ Lorentz TEM on a Fe_{0.5}Co_{0.5}Si single crystal thin lamella (or specimen)²¹. After that, several B20 compounds such as Cu₂OSeO₃²², FeGe²³, β -Co-Zn-Mn²⁴ alloys were found to host skyrmion. The enhanced skyrmion stability against the magnetic fields and temperatures, far below the transition temperature region, was found in thin lamellae (< 100 nm) as reported^{23, 25, 26}. The DMI which stabilizes the spin textures in these B20 compounds is known as bulk DMI and the skyrmions are called as Bloch skyrmions, as magnetic moments rotate in a tangential plane like Bloch wall propagation.

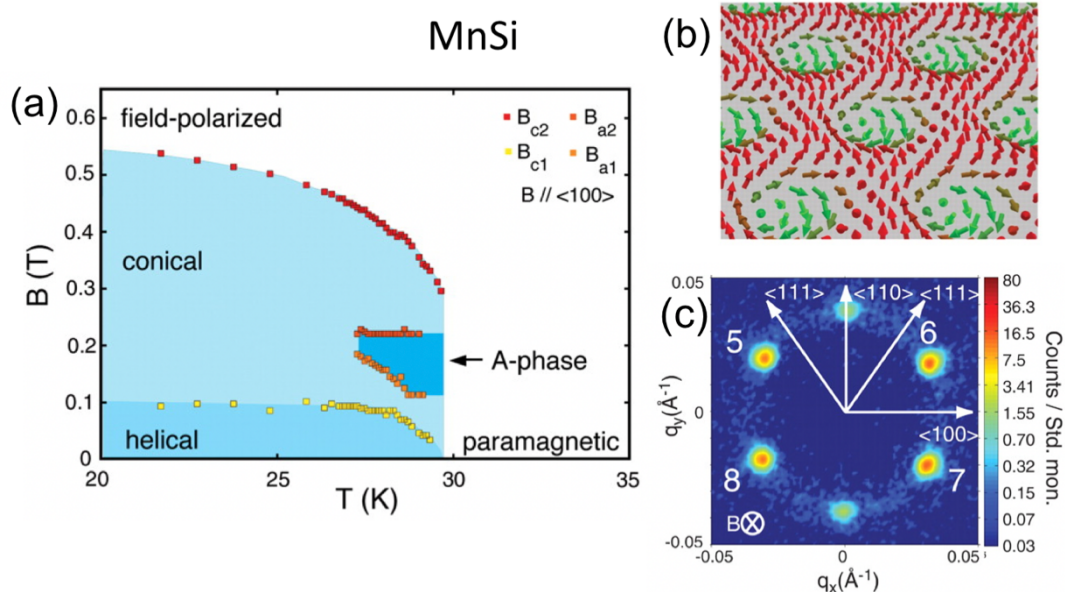


Figure 1 | First observation of magnetic skyrmion in MnSi. (a) Temperature vs Magnetic field phase diagram for bulk MnSi. (b) Schematic of triangular spin structure. (c) The six intensity maxima in the momentum space neutron scattering experiment corresponds to the triangular lattice state. From (S. Mühlbauer *et al.* Skyrmion Lattice in a Chiral Magnet. *Science* 323, 915 (2009), Ref. [20]). Reprinted with permission from AAAS.

The second type of skyrmion is known as Néel skyrmion that arises when the inversion symmetry is broken at the interface of a heavy metal and magnetic material²⁷. The DMI associated with the Néel skyrmion is known as interfacial DMI. This type of spin texture was first identified at the interface of Fe monolayer and Ir(111), where the heavy metal Ir induces DMI²⁸. Later, it has also been observed that the effective strength of DMI is significantly enhanced by sandwiching the ferromagnet in between two different heavy metals, e.g., Ir|Co|Pt multilayers (Fig. 2a) has more DMI than only Pt|Co multilayers²⁹. The DM vector originating from the top Pt|Co layer has the same direction as the DM vector originating from bottom Ir|Co layer that guarantee the additive nature of DMI strength (Fig. 2b) and the formation of Néel skyrmions (Fig. 2c). Nevertheless, it has also been seen that combining the oxide interfaces to Pt|Co shows large interfacial DMI, e.g., Pt|Co|Al₂O₃ or MgO³⁰⁻³². Contrary to Bloch skyrmion, the magnetic moment in Néel skyrmion is rotated in a radial plane when moving from core to periphery or vice versa. Moreover, Néel skyrmion were also found in bulk non-

centrosymmetric C_{nv} crystal symmetry of GaV_4S_8 ³³, VOSe_2O_5 ³⁴, PtMnGa ³⁵ and van der Waals ferromagnet like Fe_3GeTe_2 ³⁶.

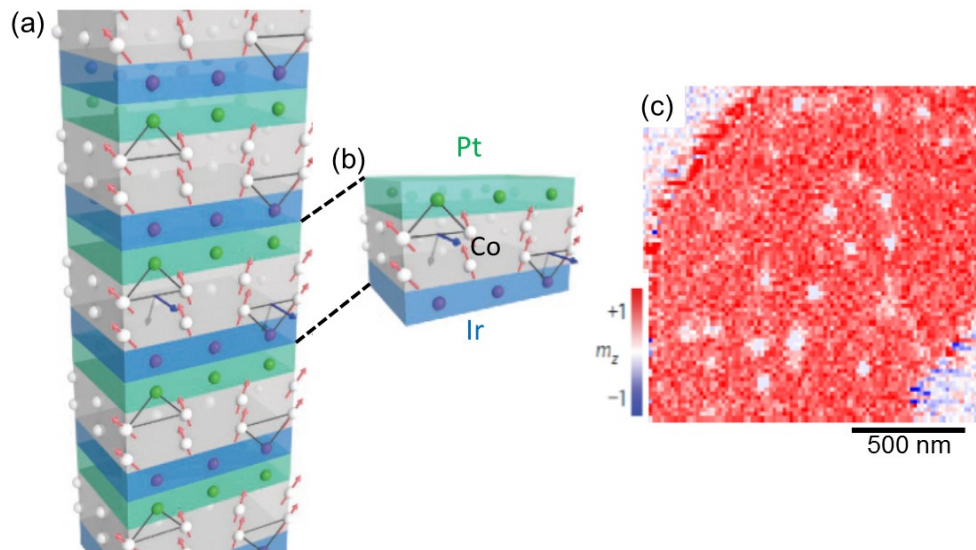


Figure 2 | Néel skyrmions in Multilayers. (a) Schematic of additive DMI properties in Pt|Co|Ir multilayers. (b) Shows the enlarged view of a small portion of the multilayer stacks. (c) Skyrmion in the $(\text{Ir}|\text{Co}|\text{Pt})_{10}$ multilayer stacks using scanning transmission X-ray microscopy (STXM) at 68 mT. Adapted by the permission from Springer Nature Terms and Conditions for RightsLink Permissions Springer Nature Customer Service Centre GmbH: Macmillan Publishers Limited, part of Springer Nature Nanotechnology, Additive interfacial chiral interaction in multilayers for stabilization of small individual skyrmions at room temperature, C. Moreau-Luchaire *et al.* 2016; Ref. [29].

Other than Bloch and Néel skyrmions, magnetic bubbles of size varying from nanometer to micrometer size were also found in centrosymmetric magnetic compounds. These bubbles are either trivial or topologically protected non-trivial spin textures, depending on the in-plane components of spin arrangement³⁷⁻⁴⁰. Recently, square skyrmion lattice induced through four-spin interactions was found in centrosymmetric tetragonal magnet GdRu_2Si_2 in the absence of inversion symmetry breaking and geometrically frustrated lattice⁴¹. Bi-skyrmion of topological charge +2 has also been reported in MnNiGa ⁴², while Loudon *et al.*⁴³ claimed the bi-skyrmion to be similar to the type II bubble in the same compound. Other than this, theoretical studies suggested the possible generation of the in-plane magnetized version of the skyrmion, called

bimeron^{44, 45}. A ring-like texture skyrmionium consists of a combined structure of two skyrmions of opposite polarity was also predicted by Bogdanov *et al.*⁴⁶ that can be stabilized by a similar DMI like skyrmion. These are also referred to as 2π skyrmions since going from the edge to the center of this object; azimuthal angle changes, for example, from 0 to 2π through π . This was realized experimentally via X-ray photoemission electron microscopy in NiFe on top of the topological insulator and using the laser pulses on alloy film of $\text{Tb}_{22}\text{Fe}_{69}\text{Co}_9$ ^{47, 48}. However, in a skyrmion hosting B20 compound FeGe, resembling skyrmionium texture was realized in confined nano-disks. Also, torus like three-dimensional soliton called magnetic hopfions were proposed theoretically, however not yet observed experimentally^{49, 50}. Besides these above mentioned spin textures, a distinctly different spin texture consisting of both Bloch and Néel spirals called ‘antiskyrmion’ was observed experimentally in D_{2d} Heusler compounds $\text{Mn}_{1.4}\text{Pt}_{0.9}\text{Pd}_{0.1}\text{Sn}$ and $\text{Mn}_{1.4}\text{PtSn}$ ⁵¹. Here, in this thesis, more focus is given towards the details of the exciting new properties of $\text{Mn}_{1.4}\text{Pt}_{0.9}\text{Pd}_{0.1}\text{Sn}$ and search for new compounds that can exhibit topological non-trivial spin textures in D_{2d} inverse tetragonal Heusler compounds.

2.3 Magnetic antiskyrmions

A different kind of topological spin texture named ‘antiskyrmion’ was found experimentally in 2017⁵¹. Theoretically, it was estimated that antiskyrmion would be found in D_{2d} and S_4 ^{3, 4}, while up to now, antiskyrmion has been found only in the D_{2d} symmetry crystal structure $\text{Mn}_{1.4}\text{Pt}_{0.9}\text{Pd}_{0.1}\text{Sn}$, an inverse tetragonal Heusler compound. The DMI that stabilizes antiskyrmion in $\text{Mn}_{1.4}\text{Pt}_{0.9}\text{Pd}_{0.1}\text{Sn}$ is anisotropic since it has no component along the long axis of the tetragonal system. The DMI vectors lie only in the basal plane orthogonally, which have same magnitude but opposite sign. This is why helices and antiskyrmions are found within the basal plane of the tetragonal compound $\text{Mn}_{1.4}\text{Pt}_{0.9}\text{Pd}_{0.1}\text{Sn}$ (Fig. 3a-b). The anisotropic DMI results in the anisotropic spin texture that composes of a chiral boundary of helicoid and cycloid propagation along $\{10\}$ (i.e. $[100]/[\bar{1}00]$ and $[010]/[0\bar{1}0]$) and $\{11\}$ (i.e. $[110]/[1\bar{1}0]$ and $[\bar{1}10]/[\bar{1}\bar{1}0]$) directions, respectively (Fig. 3c). The ground state of the system shows helical states that propagate along $[100]$ and $[010]$: favorable along the Bloch wall propagation directions. They form a triangular lattice state, as shown in Fig. 3b of Lorentz microscopy image, by applying a magnetic field perpendicular to the basal plane before providing a temporary in-plane field. The individual contrast consists of two bright lobes along $[100]$ and two gray lobes along $[010]$ crystallographic direction and there is no contrast along the $\{11\}$ direction since cycloid propagation of Néel walls do not show any LTEM contrast.

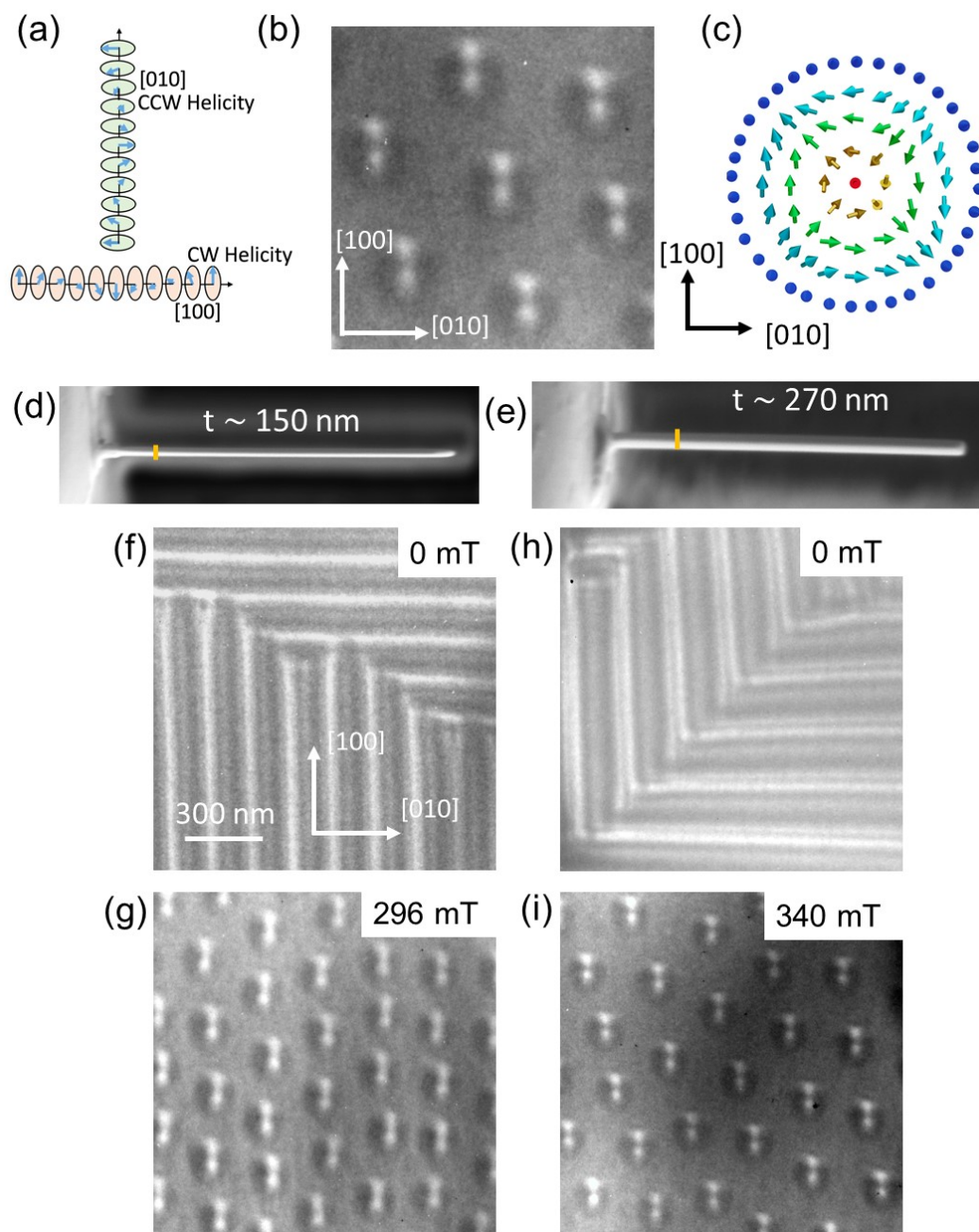


Figure 3 | *Magnetic antiskyrmion and its intrinsic stability.* (a) Shows the schematics of clockwise and counter clockwise helicities. (b) The triangular lattice of antiskyrmion. (c) The schematic of an antiskyrmion. (d), (e) Top view of scanning electron microscope (SEM) images show the thickness of the lamellae are ~ 150 nm and ~ 270 nm, respectively. (f), (g) Lorentz TEM images for the lamella shown in (d). Similarly, (h) (i) are the Lorentz TEM images for the thicker lamella of thickness ~ 270 nm.

In the case of B20 skyrmion, helix can propagate in different directions, while D_{2d} symmetry restricts their propagation along [100] and [010] directions. An important observation is found for the antiskyrmion in the D_{2d} system that they are stable up to maximum possible thickness observed in LTEM. Two lamellae of thickness ~ 150 nm (Fig. 3d), 270 nm (Fig. 3e), respectively are shown here. The thickness is obtained from the SEM overview image. The ground state of helical phase is observed where helices propagate along [100] and [010] directions (Fig. 3f and 3h). The helical periods are ~ 152 nm and 223 nm, respectively. Unlike the B20 cases, here it is shown that helical period increases with increasing thickness of the lamella^{52, 53}. After a temporary application of in-plane field components, antiskyrmions lattice are formed at higher magnetic fields. Fig. 3g and 3i show the LTEM contrast of antiskyrmions at 296 mT and 340 mT, respectively. This finding is in sharp contrast to the B20 compound formed skyrmions. For example, FeGe, the maximum stability of Bloch skyrmion is possible for the lamellae of thickness below 100 nm²³. For lamellae thicker than this, the modulated skyrmion tube breaks into the chiral bobbles⁵⁴. This distinct behavior can be understood from the associated discrete DMIs that form different spin textures in B20 and D_{2d} crystal symmetry⁴. The DMI vector along the thickness direction in the B20 compound tends to chiral modulation of magnetization after a certain critical thickness that hinders its stability against the magnetic field. On the other hand, the absence of a DMI vector along the thickness direction (in the [001] zone-axis) of the D_{2d} compound prevents the chiral magnetic modulation so that antiskyrmion stability is preserved irrespective of such higher thickness. A detailed observation about the intrinsic thickness stability of antiskyrmion on a wedge-shaped lamella was described in Saha *et al.*⁵³.

2.4 Topological definition of skyrmions

The classification of different spin textures are characterized by the skyrmion number⁵⁵

$$N_{\text{Sk}} = \frac{1}{4\pi} \iint \mathbf{m}(\mathbf{r}) \cdot \left(\frac{\partial \mathbf{m}(\mathbf{r})}{\partial x} \times \frac{\partial \mathbf{m}(\mathbf{r})}{\partial y} \right) d^3r \quad (1)$$

Here, \mathbf{m} is the normalized magnetization density. The above expressed mathematical quantity describes as the number of times spins warp around a unit sphere. Expressing the magnetization in spherical coordinates,

$$\mathbf{m}(\mathbf{r}) = [\cos \Phi(\varphi) \sin \Theta(r), \sin \Phi(\varphi) \cos \Theta(r), \cos \Theta(r)]$$

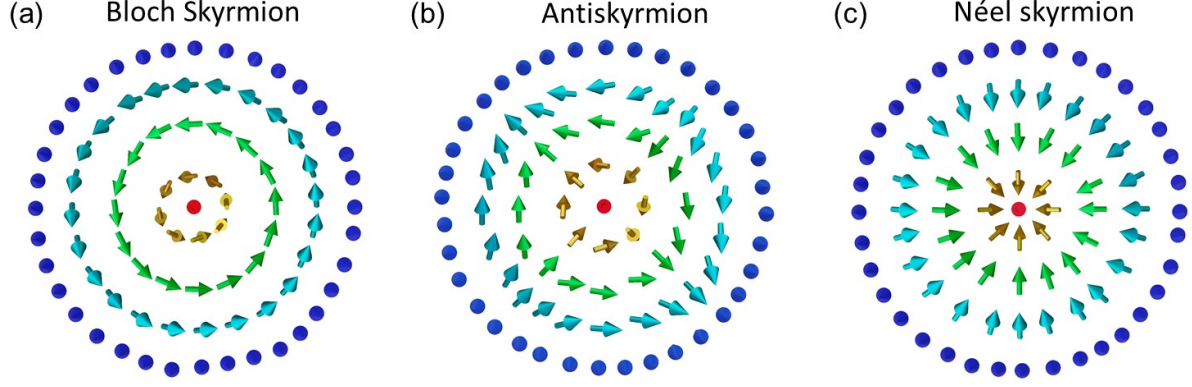


Figure 4 | Different types of skyrmion. Schematic spin textures of (a) Bloch (b) antiskyrmion and (c) Néel skyrmion.

Here, polar angle $\Phi(\varphi)$ of the magnetization depends on the polar angle φ of the position vector \mathbf{r} and $\Theta(r)$ depends on the length r of the position vector \mathbf{r} . We can rewrite the equation of topological charge from equation (1) as⁵⁶

$$N_{\text{Sk}} = \frac{1}{4\pi} \int_0^\infty dr \int_0^{2\pi} d\varphi \frac{\partial\Phi(\varphi)}{\partial\varphi} \frac{\partial\Theta(r)}{\partial r} \sin\Theta(r) = -\frac{1}{2} \cos\Theta(r) \Big|_{r=0}^\infty \cdot \frac{1}{2\pi} \Phi(\varphi) \Big|_{\varphi=0}^{2\pi}$$

$$= p \cdot m \quad (2)$$

The first term is called polarity (p) and the second term as vorticity (m). Hence, topological charge number is the product of polarity and vorticity. Polarity (p) defines the direction of the magnetization at the core of the spin texture; whether it points up ($p = +1$, for $+z$ -direction) or down ($p = -1$, for $-z$ direction). The sense of rotation of the in-plane magnetic texture is characterized by the quantity called vorticity. Hence

$$p = \pm 1, \quad m = 0, \pm 1, \pm 2, \dots$$

$$\text{So that } N_{\text{Sk}} = 0, \pm 1, \pm 2, \dots \quad (3)$$

Further, helicity is defined by the phase as

$$\Phi = m\varphi + \gamma \quad (4)$$

γ is 0 or π for Néel skyrmions and $+\frac{\pi}{2}$ or $-\frac{\pi}{2}$ for Bloch skyrmion. Since antiskyrmions are not rotationally symmetric objects like skyrmions, the helicity is no longer defined as a global offset between the polar angle of position vector and the polar angle of magnetization. Rather, it gets distinguished along different directions. For example, antiskyrmion has the profile of Néel skyrmions with helicity 0 and π along the black dashed line or has the Bloch skyrmion texture with helicity $\pm \frac{\pi}{2}$ along the purple dashed lines.

For all three types of skyrmions (Fig. 4a-c), the topological number can have +1 or -1⁵⁶. However, antiskyrmion has opposite m i.e., the in-plane magnetization rotates opposite to the position vector. Hence, antiskyrmions have opposite topological charge than that of Bloch and Néel skyrmions for a given direction of fixed core (polarity). The value of N_{Sk} is zero for the helical or ferromagnetic (field polarized) state. Since different topological numbers are assigned for the helices and skyrmions, these structures cannot be transformed into one another by continuous deformation. That is why skyrmions are regarded as topologically non-trivial objects. An energy barrier separates the skyrmions from the surrounding ferromagnetic state and this eventually leads to their longer metastability. In magnetic bubbles of centrosymmetric materials, whether N_{Sk} is zero or non-zero integer number, it depends on the internal magnetization of the spin texture. Higher order skyrmions are predicted theoretically and in this case, in-plane magnetization rotates more than once around the unit sphere such that magnitude of vorticity $|m| > 1$ ⁵⁷. The different types of skyrmions are found by the types of interactions and depend on the details of the crystal structures. The detail will be discussed in the following sections.

2.5 Energy terms for stabilizing skyrmions

In this section several important interaction energies responsible for stabilizing skyrmions in distinct symmetric group material system are discussed.

2.5.1 Exchange interaction

The Heisenberg interaction or exchange interaction is the basic interaction in magnetic materials that promotes the ordering of magnetic moment through the coupling of electron spins of neighboring atoms. The exchange interaction energy is given by

$$H_{\text{exchange}} = -\frac{1}{2} \sum_{i,j} J_{ij} (\mathbf{s}_i \cdot \mathbf{s}_j) \quad (5)$$

Where \mathbf{s}_i and \mathbf{s}_j are electron spin at i^{th} and j^{th} state, and J_{ij} is the exchange constant between them. Factor $\frac{1}{2}$ in equation (5) accounts for the double counting of each interaction. The positive value of J_{ij} aligns spins of the electron parallel to each other and hence the ground state will be ferromagnetic. For the negative value of J_{ij} , spins will be aligned antiparallel to each other that accounts for antiferromagnetic materials. Exchange is not the solo interaction present in a material that otherwise promotes single domain magnetic materials. Non-collinearity comes to play in magnetic material due to the presence of other energy terms that compete with exchange interaction.

2.5.2 Zeeman interaction and anisotropies

The Zeeman energy term is introduced to describe the interaction of magnetic moment (μ) with the externally applied magnetic field.

$$H_{\text{Zeeman}} = - \sum_i \mu \mathbf{s}_i \cdot \mathbf{B} \quad (6)$$

It is one of the important energy terms as its application makes the generation of the non-trivial topologically protected skyrmion phase over the trivial ground state helical phase. This external magnetic field is applied along certain crystallographic directions of the material systems.

The easy-axis anisotropy along the direction $\mathbf{n} = \mathbf{e}_z$ is given by

$$H_{\text{Anisotropy}} = - \frac{1}{2} \sum_i K (\mathbf{s}_i \cdot \mathbf{n})^2 \quad (7)$$

Here K is the anisotropic constant. In thin-film systems, anisotropy prefers out-of-plane direction, and skyrmions can be formed on competing with dipole-dipole interactions after the externally applied magnetic field even without DMI³⁹. The propagation directions are determined by the magnetic anisotropy⁵⁸⁻⁶⁰. For example, in the B20 system, different helimagnet propagation directions exist that correspond to the symmetry of the cubic crystal. For D_{2d} skyrmionics systems of the tetragonal Heusler compound, anisotropy plays an important role as well. It is found that the helical state is stabilized in the plane perpendicular to the easy axis [001] and the application of magnetic field (Zeeman energy) along this direction stabilizes the spin textures⁵¹. Also, one can say that the transitions between the various states largely depend on the applied magnetic field. In the D_{2d} system such as $\text{Mn}_{1.4}\text{Pt}_{0.9}\text{Pd}_{0.1}\text{Sn}$, a

unique feature has shown that the application of a temporary magnetic field helps to overcome the energy barrier between the trivial (e.g., helical phase) and non-trivial phase.

2.5.3 Dzyaloshinskii-Moriya interaction

Though there are several possible interactions responsible for the formation of non-collinear texture in magnetic material, it is skyrmion spin texture which has the fixed chirality. This fixed chirality in the skyrmionics system is induced by the antisymmetric exchange interaction called DMI^{1,2}

$$H_{\text{DMI}} = \frac{1}{2} \sum_{ij} D_{ij} \cdot (\mathbf{s}_i \times \mathbf{s}_j) \quad (8)$$

that occur due to spin-orbit coupling and lacking inversion symmetry. The magnetic skyrmion spin texture has one of the fixed chirality; $C = \mathbf{s}_i \times \mathbf{s}_j$, either ($C > 0$) right-handed or ($C < 0$) left-handed, depends on the crystal chiral symmetry. The DM interaction also induces weak magnetism on an otherwise antiferromagnetic materials, for example, Fe_2O_3 . The strength of the DMI depends on the strength of SOC and is at least one order smaller than conventional exchange interaction. The competition of DMI with parallel spin alignment due to exchange interaction results in the canting of magnetic moment at an angle < 90 degree, determined by the ratio D/J . The directional dependence of the DM vector is derived from the Moriya rules² of symmetry arguments. Considering two magnetic atoms a and b and the point c is bisecting the straight-line ab, the rules are²

- 1_ $D = 0$, when a center of inversion is located at c.
- 2_ $D \parallel$ mirror plane or $D \perp ab$, when a mirror plane perpendicular to ab passes through c.
- 3_ $D \perp$ mirror plane, when there is a mirror plane including a and b.
- 4_ $D \perp$ two-fold axis, when a two-fold rotation axis is perpendicular to ab passes through c.
- 5_ $D \parallel ab$, when there are two or more-fold rotation axis along ab.

DMI for Magnetic skyrmions

Here different DMI forms responsible for stabilizing different kind of skyrmionics textures are discussed.

Bulk DMI: This kind of DMI is observed in non-centrosymmetric bulk B20 cubic materials, e.g., MnSi, FeGe. In the continuous limit, the DMI is expressed as

$$H_{bulk} = \int \tilde{D} \left(m_y \frac{\partial m_z}{\partial x} - m_z \frac{\partial m_y}{\partial x} + m_z \frac{\partial m_x}{\partial y} - m_x \frac{\partial m_z}{\partial y} + m_x \frac{\partial m_y}{\partial z} - m_y \frac{\partial m_x}{\partial z} \right) d^3r \quad (9)$$

Here the DMI constant \tilde{D} has a dimension of energy/ (length)². The first four terms in equation (9) account for the DM vector along in-plane direction and last two terms for the bond along out-of-plane direction. The DMI of this form stabilizes Bloch skyrmion in which spins are rotated in the tangential plane.

Interfacial DMI: Unlike the previous case, here, lack of inversion symmetry is induced by the explicit formation of interfaces by two different grown layers. The DMI is formed according to the ‘Levy-Fert’ rule, where two magnetic atoms lie in a plane and a third heavy non-magnetic atom that has the same distance from each magnetic atom which obey Moriya rules 2 and 3. This form of interaction stabilizes Néel skyrmions such that the rotation of spin is in the radial plane and attributed to the cycloid propagation. The DMI vectors have equal magnitude and signs for all bonds. This DMI read as⁶¹

$$H_{interface} = \int \tilde{D} \left(m_z \frac{\partial m_x}{\partial x} - m_x \frac{\partial m_z}{\partial x} + m_z \frac{\partial m_y}{\partial y} - m_y \frac{\partial m_z}{\partial y} \right) d^3r \quad (10)$$

Anisotropic DMI: A distinctly different kind of spin texture subjected to the D_{2d} and S_4 symmetries compounds was proposed by Bogdanov *et al.*⁴ and was found experimentally in the D_{2d} Heusler system, $Mn_{1.4}Pt_{0.9}Pd_{0.1}Sn$. The spin texture in this symmetry is anisotropic owing to the anisotropic DMI. The DMI vectors have no out-of-plane direction. There are orthogonal in-plane DMI vectors which are opposite in direction and have the same magnitude. In the continuous limit, it read as

$$H_{anisotropic} = \int \tilde{D} \left(m_z \frac{\partial m_x}{\partial x} - m_x \frac{\partial m_z}{\partial x} - m_z \frac{\partial m_y}{\partial y} + m_y \frac{\partial m_z}{\partial y} \right) d^3r \quad (11)$$

The opposite sign of the DMI vectors originate due to the placement of nonmagnetic atoms above and below the magnetic atoms layers that stabilize different types of spin spirals propagating in an alternating manner. The anisotropy kind of interaction is also formed when the ultra-thin magnetic film is grown on the semiconductor or heavy metal substrate with C_{2v} symmetry⁸.

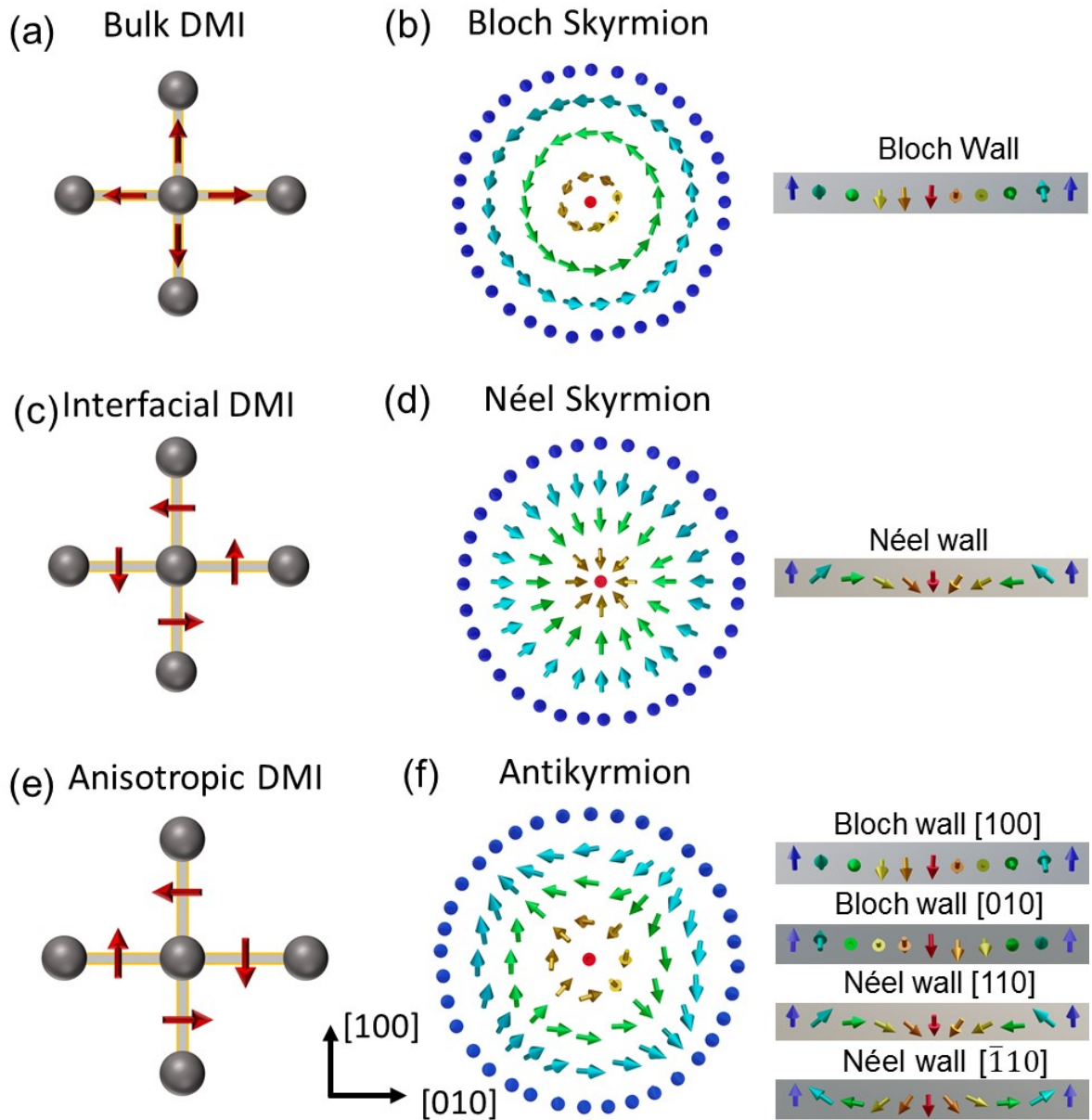


Figure 5 | Spin textures resulting from DMI interactions. Schematic representation of (a) Bulk DMI forms from acentric B20 compounds and the (b) corresponding spin texture (upper panel) and the type of spin spiral (lower panel) from which they form. Interfacial DMI (c) forms in the interface like Co/Pt and the resulting (d) spin texture and spin spiral. (e) and (f) are for the anisotropic DMI, the corresponding spin texture and the type of spin spirals along different crystallographic directions.

Other forms of DM interactions, which depend on how the inversion symmetry break, can be formed as predicted theoretically. For example, elliptical skyrmion when DM components have the same sign but have different magnitude⁶² or a different DM interaction that can produce bimeron, as reported by Göbel *et al.*⁴⁴.

2.5.4 Dipole-dipole interactions

Dipole-dipole interactions arise between all dipoles in the volume of the magnetic material. It is a long-range interaction, unlike the above discussed interactions that are limited to neighbouring moments. This interaction between the magnetic moments s_i and s_j at a distance r_{ij} is read as

$$H_{dd} = -\frac{\mu_0}{4\pi} \left(\frac{3(s_i \cdot r_{ij})(s_j \cdot r_{ij})}{r_{ij}^5} - \frac{(s_i \cdot s_j)}{r_{ij}^3} \right) \quad (12)$$

Dipole-dipole interactions mostly stabilize the bubbles of different sizes in centrosymmetric material (without DMI). In magnetic thin films, the preferential out-of-plane magnetization due to the anisotropy and the favored in-plane magnetization by dipolar interaction produces disordered helimagnetic structures. It is also observed that upon application of the external magnetic field, Bloch skyrmions with opposite helicities of $\pm\frac{\pi}{2}$ are favorable over Néel skyrmions. The degenerate opposite helicities correspond to the achiral nature of the dipole-dipole interactions^{39, 56}.

2.6 Towards application of skyrmions

After the discovery of magnetic skyrmion in cubic B20 compound MnSi, another exciting observation was found in the same system is the movement of them with electric current. It is shown that skyrmion can move with a current density of $\sim 10^6$ A/m², nearly five orders of magnitude smaller than domain wall motion¹⁶. This important finding, together with the nano-metric small size, particle-like behavior and topological properties, skyrmions are considered important for their application in high-density nonvolatile memory devices like the racetrack memory⁵ and neuromorphic computing⁶³. Other than this, as predicted, skyrmion can be utilized in transistors⁶⁴, logic gates⁶⁵, magnonic or microwave devices^{66, 67}. To utilize skyrmions in devices as an information bit, they have to manipulate individually. For example, in racetrack⁵, these quasiparticles are encoded as ‘1’ bits, and places where not present are identified as ‘0’ bits⁷. A successful demonstration of the skyrmion annihilation and nucleation is established by spin polarized scanning tunneling microscopy (SP-STM) tips⁶⁸. Besides this,

skyrmion can be generated by locally applied magnetic field^{69, 70}, electric field^{71, 72}, spin torques^{68, 73}, by heating through electron pulses⁷⁴ or laser pulses⁴⁸ or by defects^{17, 75, 76}.

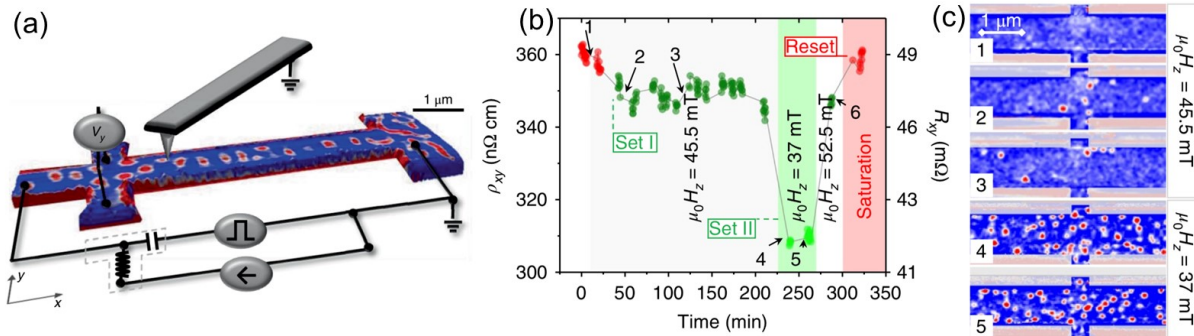


Figure 6 | Electrical detection of magnetic Skyrmion. (a) Scheme of experimental set up in a multilayer racetrack integrated with local probe magnetic force microscopy. The out-of-plane magnetization is represented by blue and red contrast. (b) Nucleation of skyrmion by current pulses at different magnetic field. This induces the variation of Hall resistivity and Hall resistance (left and right-hand scale respectively). (c) MFM phase maps, after the pulses are sent, show the variation of skyrmion density on different field strength. Adapted by the permission from Springer Nature Terms and Conditions for RightsLink Permissions Springer Nature Customer Service Centre GmbH: Macmillan Publishers Limited, part of Springer Nature Nanotechnology, Electrical detection of single magnetic skyrmions in metallic multilayers at room temperature, D. Maccariello *et al.* 2018; Ref. [77].

Also, the electrical detection and manipulation of skyrmions using magnetic force microscopy (MFM) (Fig. 6a-c) were reported^{77, 78}. The electrical detection was also examined via topological Hall effect when the spin texture in skyrmion is coupled to the conduction electron⁷⁹. However, in real space via an electric current induced motion, skyrmion shows an unwanted physical property that is highly undesirable for devices used in practical application⁸⁰. This is called the skyrmion Hall effect and it arises due to the presence of Magnus force that is originating from the finite value of the topological charge. Because of the Magnus force, skyrmion always deviates away from the current injection direction and annihilates at the boundary of the specimen. As a result, the information bit is lost in the device. This unsuitable condition can be avoided either by antiferromagnetic materials or antiferromagnetically coupled synthetic bilayer systems⁸¹. The Magnus force of skyrmions in antiferromagnets is completely canceled due to the opposite sign of the topological charge on each sublattice.

However, the detection of these antiferromagnetic skyrmions is a real problem due to the absence of a stray field. Nevertheless, in a recent study, skyrmions were observed in antiferromagnetically coupled multilayer^{82, 83}. In the synthetically coupled system, a very low current-driven motion was reported with negligible skyrmion Hall angle⁸³.

A theoretical observation on antiskyrmions reported that the angle between its propagation and current direction could be tuned. Since antiskyrmion possesses anisotropic spin arrangements, the antiskyrmion Hall angle can be varied widely as a positive and negative value. Interestingly, even it can be suppressed to zero by making the straight-line motion of antiskyrmion along a certain specific current direction⁸⁴. Moreover, the formation of skyrmion-antiskyrmion pair in a single material system can also cancel the Magnus force due to the opposite topological charge so that a perfect straight-line motion can be achieved. Additionally, producing distinct spin textures of skyrmion and antiskyrmion in a device helps to operate them as distinct bits such that one does not have to worry about the distances between the particles.

2.7 Stabilization of different spin textures in single material system

The manifestation of different kinds of topological spin textures in magnetic materials depends on the crystal structures' symmetry group. Mostly studied non-centrosymmetric B20 compounds like MnSi, FeGe, Fe_{0.5}Co_{0.5}Si, Cu₂OSeO₃, β -type Co-Zn-Mn alloys induce Bloch skyrmion. However, the observations of deformed skyrmions caused by either anisotropic strain⁸⁵, confined geometry, or the vicinity of grain boundary were reported in these compound system⁸⁶. Nevertheless, they bear the same topological charge irrespective of the LTEM contrast deformation as reported. Also, In Co₈Zn₉Mn₃ alloy, along with Bloch skyrmion, the presence of in-plane magnetic anisotropy induces the square lattice of meron and antimeron (with the topological number -1/2 and +1/2 respectively) formation in elevated magnetic fields⁸⁷. Recently, in the same family of elemental composition, domain wall skyrmions were also observed⁸⁸. A hybrid particle-like state composed of a smooth magnetization vector and a magnetic singularity called chiral bobber was predicted theoretically in several B20 compounds and was recently confirmed experimentally in FeGe^{54, 89}. Opposite helicities of degenerate Bloch skyrmions were found in hexaferrite BaFe₁₂O₁₉ for the achiral nature of the centrosymmetric compound³⁹.

A recently proposed theory suggested the possible formation of single, double and triple q (skyrmion) state in the frustrated triangular lattice system without the presence of spin-orbit or dipolar interactions. This model anticipated an energetically degenerate skyrmion and antiskyrmion near the transition temperature region⁹⁰. Further, including the dipole-dipole

interactions in a model based on the frustrated magnet, Zhang *et al.*⁹¹ reported the formation of the skyrmion, antiskyrmion and their pair annihilation. This model also demonstrated bi-skyrmion and bi-antiskyrmion formation via merging two skyrmions and two antiskyrmions as a bound state, respectively. However, recently, in the geometrically frustrated system of Gd₂PdSi₃, only Bloch type skyrmions were observed experimentally, and the formation of different spin textures in one material system has not been found yet⁹². Hoffmann *et al.*⁸ reported a theoretical study on the interfacial stabilization of antiskyrmion in multilayer stacks with C_{2v} symmetry and their existence with skyrmion. To the best of our knowledge, no material has been found that exhibits such a DMI tensor with $\det(\mathbf{D}) = 0$. Furthermore, using Brillouin light scattering, anisotropic DMI vectors of unequal strength was found on the C_{2v} symmetry of thin-film Au/Co/W(110) that favors the skyrmions in elliptical shape instead of antiskyrmion⁹³. Here, I report the experimental discovery of two different spin textures of opposite topological charges in a single material system of Mn_{1.4}Pt_{0.9}Pd_{0.1}Sn and Mn₂Rh_{0.95}Ir_{0.05}Sn, separately.

2.8 Summary

A short introductory discussion about the scope of this thesis is mentioned. A basic discussion about the various non-collinear spin textures with special attention to Bloch, Néel and antiskyrmions are discussed. The intrinsic stability of antiskyrmion resulting from the anisotropic DMI in the D_{2d} symmetry is examined using two different uniform lamellae of thickness ~ 150 nm and 275 nm. The definition of topological charge number for typical spin textures and the necessary energy terms require for their stability are mentioned.

3

Experimental methods

In this chapter, different equipment and their principles for analyzing bulk samples and thin lamellae are described. The measurements in superconducting quantum interference device (SQUID) are performed to examine the magnetic properties of bulk samples. Topography and single crystalline grains information are obtained from the scanning electron microscope (SEM) and electron backscatter diffraction (EBSD) techniques. A transmission electron microscope (TEM) is used in different operational modes to investigate structural and magnetic textures of thin specimens. Results obtained from various experiments are specified with particular attention to the D_{2d} inverse tetragonal Heusler compound $Mn_{1.4}Pt_{0.9}Pd_{0.1}Sn$.

3.1 Magnetization measurement

The magnetic properties, for example, magnetization (M) as a function of magnetic field (H) and temperature (T) of the sample, are examined in DC SQUID [MPMS3, Quantum design]. A SQUID is an ultrasensitive magnetometer normally used to measure extremely small magnetic moment (10^{-8} emu). The working principle of the device is based on superconducting loops containing Josephson junctions.

A magnetization measurement for continuously varying temperature of the $Mn_{1.4}Pt_{0.9}Pd_{0.1}Sn$ bulk sample is shown in Fig. 1a for zero-field cooled (ZFC) and field cooled (FC) modes. In the ZFC mode, the sample is cooled down in zero field from 400 K to 2 K and, then magnetization is measured in a constant magnetic field during heating from 2 K and 400 K. In the FC process, in the presence of same magnetic field, the sample is cooled down to 2 K

and, then $M(T)$ curves are measured from 2 K to 400 K. A magnetization vs. temperature curve in ZFC and FC modes is shown (Fig. 1a) for a constant magnetic field of 0.1 T. From the $M(T)$

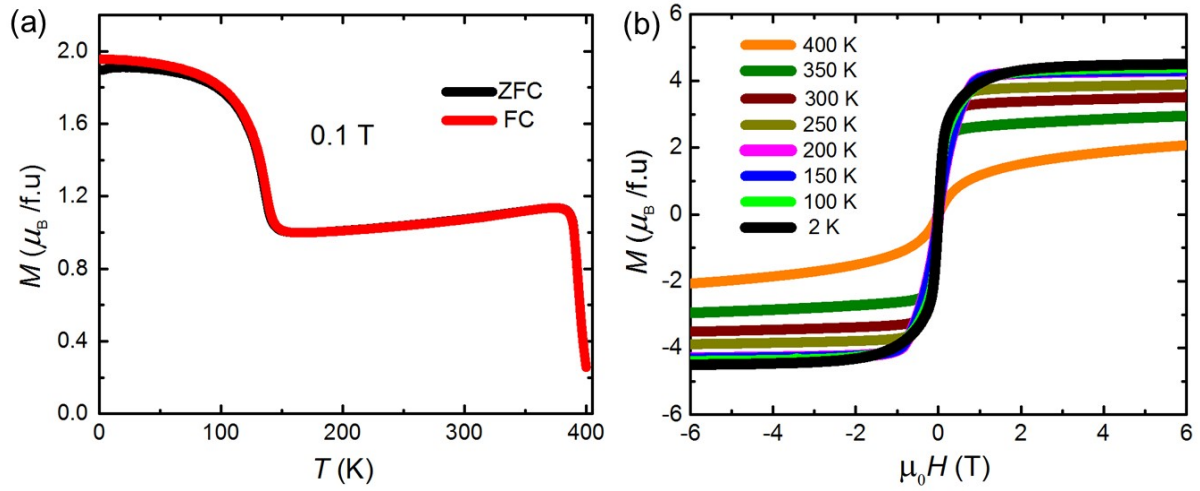


Figure 1 | Magnetization of $Mn_{1.4}Pt_{0.9}Pd_{0.1}Sn$. (a) Shows the $M(T)$ curves in zero field (black curve) and field cooled (red curve) modes. (b) $M(H)$ curves for different temperatures.

curve, it is evident that the system undergoes first magnetic transition from a high temperature paramagnetic state to a low temperature ferromagnetic state at around 390 K (T_C). A second transition occurs at a lower temperature of approximately 133 K due to the canting of the Mn moment away from the tetragonal axis. This transition temperature is commonly known as the spin reorientation transition (T_{SRT}). The plot of magnetization vs. magnetic field for different temperatures is shown in Fig.1b. The compound is a ferromagnetic soft magnet and has a saturation magnetization of $\sim 4.5 \mu_B/\text{f.u.}$ at 2 K⁵¹.

3.2 Scanning electron microscopy and electron backscatter diffraction

In a scanning electron microscope (SEM)⁹⁴, the focused electron beam scans over a surface to produce an image. The electron beam interacts with the sample, resulting in various signals that can be used to obtain surface topography and composition of the sample^{95, 96}. The penetration depth of the incident beam into the sample depends on the accelerating voltage and the density of the sample. They produce secondary electrons, backscattered electrons and X-rays after interacting with the sample. The secondary electrons eject from within a few

nanometers of the sample surface give rise to the surface topography. The X-rays and backscattered electrons originate due to the multiple scattering events inside the sample. The X-rays obtain in this interaction can be used to map the elemental distribution of the sample in an equipped energy-dispersive X-ray spectroscopy. The backscattered electrons can be used to determine the crystal structure of the sample⁹⁵.

Electron backscatter diffraction (EBSD) is a crystallographic characterization technique mostly used for polycrystalline material to provide information about the local crystal structure, its orientation, phase, strain, and the angular relationship between the crystal planes⁹⁷⁻¹⁰⁰. The identification of crystal orientation, grain, and phase helps to lift thin lamellae of particularly oriented zone-axis. Moreover, EBSD is a surface sensitive technique as the diffraction signal comes from ~5-20 nm of the sample surface. So, the surface has to be smooth and free from the thick coating, undulation due to protruding particles, contamination, oxidation layers, and damage. Therefore, no single technique is applicable for all material, and different experimental techniques have been approached to get the best surface.

The EBSD (Quantax, Bruker) is performed in a TESCAN GIA system that occupies SEM and, an EBSD detector situate approximately 90° to SEM column that has phosphorus screen, lens and CCD cameras of required resolutions. The schematic of the experimental set up is shown in Fig. 2a. The bulk sample is placed at an angle ~70° to the normal of the electron beam. The accelerating voltage of the electron from the SEM column is 20 kV. A diverging source of elastically and inelastically scattered electrons will be produced on the penetration of probe electron beam up to a few nm through the sample. Then the elastic and inelastic scattered electrons are reflected by set of crystal planes, satisfying Bragg condition $2d \sin\theta_B = n\lambda$, where d is the spacing between the planes, θ_B is the Bragg angle, n is the order of diffraction, and λ is the wavelength of incoming electrons¹⁰¹. The diffracted electrons are then channeled and produced Kikuchi bands in the phosphorus screen^{102, 103}.

Since helices and non-trivial spin structures in the D_{2d} Heusler compound are stabilized within the tetragonal basal plane, the EBSD technique is employed to detect the single crystalline orientation of [001] grains out of several possible different grains within the bulk polycrystalline sample. A SEM image of a portion of the $Mn_{1.4}Pt_{0.9}Pd_{0.1}Sn$ bulk sample is shown in Fig. 2b. The near-field backscattered image of the region is presented in Fig. 2c. The colored EBSD map of the same region is shown in Fig. 2d. The crystal orientations are identified by the inverse pole figure coloring key in which different colors represent the different crystallographic directions^{97, 104, 105} as indicated in Fig. 2e. For example, in the

tetragonal system of $Mn_{1.4}Pt_{0.9}Pd_{0.1}Sn$, red and green colors indicate the [001] and [100] orientations, respectively.

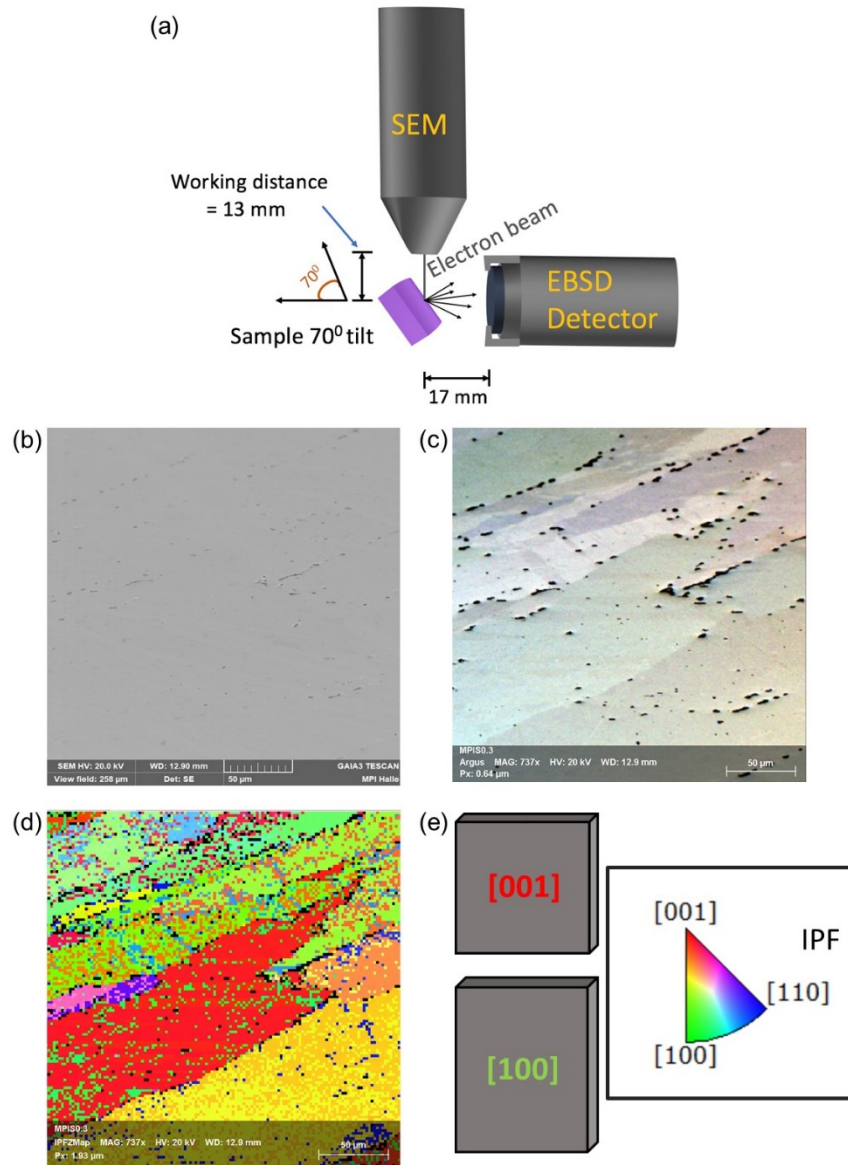


Figure 2 | Orientation map for the $Mn_{1.4}Pt_{0.9}Pd_{0.1}Sn$. (a) Schematic of EBSD set up. The distance between sample surface and the EBSD detector is ~ 17 nm. (b) Topography (SEM) image of the $Mn_{1.4}Pt_{0.9}Pd_{0.1}Sn$ sample. (c) Back scattered ARGUS image of the same region. (d) The EBSD map of the inverse pole figure (IPFZ, Z-axis normal to the sample surface) shows the different grains that are represented in different colors. (e) The IPF coloring key helps to evaluate the crystal orientation. As shown here, red color represents [001] crystal orientation from the IPFZ mapping (d).

3.3 Focused ion beam

The thin lamellae for the TEM investigation are prepared by Ga^+ ion-based focused ion beam [FEI Nanolab 600 SEM/FIB] and a scanning electron microscope (SEM). SEM system stands vertically to the stage, and Ga^+ beam-column is situated 52° to the SEM column as shown schematically in Fig. 3a. The stage can be rotated, tilted to desire angle and height with respect to SEM column (see Fig. 3b). The FIB is operated at an accelerating voltage range of 2-30 kV. The gas injection system (GIS) is used to deposit PtC_x , C, SiO_2 for the purpose of either electrical contact, or as the protection layer during lamellae preparation. Various forms of masks such as rectangular pattern, rough cross-section pattern, and cleaning cross-section pattern are used for the deposition, milling, or smooth surface cleaning during the thin lamella preparation in FIB. The Omni probe (AutoProbeTM 200) helps to transfer the thicker sample from the bulk sample to the four arms grids.

In the previous section, Fig. 2d, the red color region has a surface orientation of [001] grain perpendicular to the surface. The green color stipulates to the [100] or [010] directions. Therefore, to examine the magnetic structure on the tetragonal basal plane ([001] zone-axis) of the inverse tetragonal Heusler compounds, surface parallel lamellae are lifted out from the red color region and cross-sectional lamellae are made from the [100] grain. Here below, we will describe the preparation method for lamellae.

Surface parallel Lamellae

Step 1: We deposit approximately 200-300 nm layer of PtC_x via gas injection system (GIS) by electron beam at zero tilt of the sample stage. Further, about 1 μm thick layer of PtC_x is deposited by Ga^+ ion (at 52° tilt to the electron column) as a protection layer on it as shown in Fig. 3c. This deposition reduces significant damage during the milling procedure. **Step 2:** In this step, a rough cut is performed in a higher current in the surrounding region of the protected PtC_x layers by the rough-cross section pattern as shown in Fig. 3d. Thereafter, we polish both sides of the left-over micrometer width region to remove the damaged portion of the surface using the ion beam at a lower current (30 kV, 28 pA). **Step 3:** A flat surface is created by smooth polishing the outer sides of the micrometer width sample with a 5 kV and then a 2 kV electron energy. The polishing of the sample at both these energies is carried out on tilting angles of 56° (to clean the front side of the sample) and 48° (to clean the backside of the sample), respectively. **Step 4:** Next, in a tilted condition (52° to the electron column), we

deposit approximately 300-500 nm thick PtC_x on both sides the micrometer wide sample using electron beam. Fig. 3f shows the deposition of PtC_x on both sides of the lamella. Polishing and PtC_x deposition steps are required for damage free lifting of the sample. **Step 5:** To lift out the micrometer size sample, we cut it in an 'L' shape so that one side of it is attached to the rest bulk sample and the ion beam will cut the other two sides. We then attach a nano- manipulator, to the sample by depositing PtC_x and then cut out the remaining part attached to the bulk sample (Fig. 3g). **Step 6:** We attach our thicker sample to a four-arm grid seated perpendicularly to the electron column (Fig. 3h). The sample is attached to one of the four arms, and PtC_x is glued on the junction between the grid and the sample (Fig. 3i). **Step 7:** We cut the end portion of the nano-manipulator with the ion beam energy to separate it from the sample. (Fig. 3j). **Step 8:** After retracting the nano-manipulator, the whole FIB system is vented out and then placed the grid such that its arms face parallel to the electron column, and the sample will look like Fig. 3k. **Step 9:** After this, we tilt the sample by 52°. More PtC_x is deposited on the upper surface of the sample to protect it from the ion beam damage. **Step 10:** Then, we thin down both sides of the sample by cleaning cross-section pattern with lower currents to a few nanometers (usually 93 pA up to 800 nm thick, 48 pA up to 500nm and 28 pA up to desired thickness). **Step 11:** The final polishing is done at an energy of 5 kV and current 8 pA followed by the low energy of 2 kV and 4 pA to remove surface amorphization. These two low energy polishing are done by tilting the stage to 56° and 48°, respectively. The thickness of the lamella is measured in the zero-tilt stage condition as shown in Fig. 3l. The lamella, shown here, has two different thickness regions; the left portion is nearly 400 nm and is not transparent to the electron beam, and the right portion has a thickness of around 170 nm. The magnetic structure in the later portion of the lamella is examined in chapter (Ch.) 4. The surface width and length of the lamella can be measures at 52° tilt as shown in Fig. 3m.

Most of the lamellae studied in this thesis are lifted using the surface parallel procedures. For lifting out cross-section lamellae, we follow the same steps mentioned above except steps 3, 4, 8, and 9. The lift-out specimens from the bulk sample are directly attached to the grid situated parallel to the electron beam column. Then, steps 10 and 11 are carried out to make the required thin lamellae.

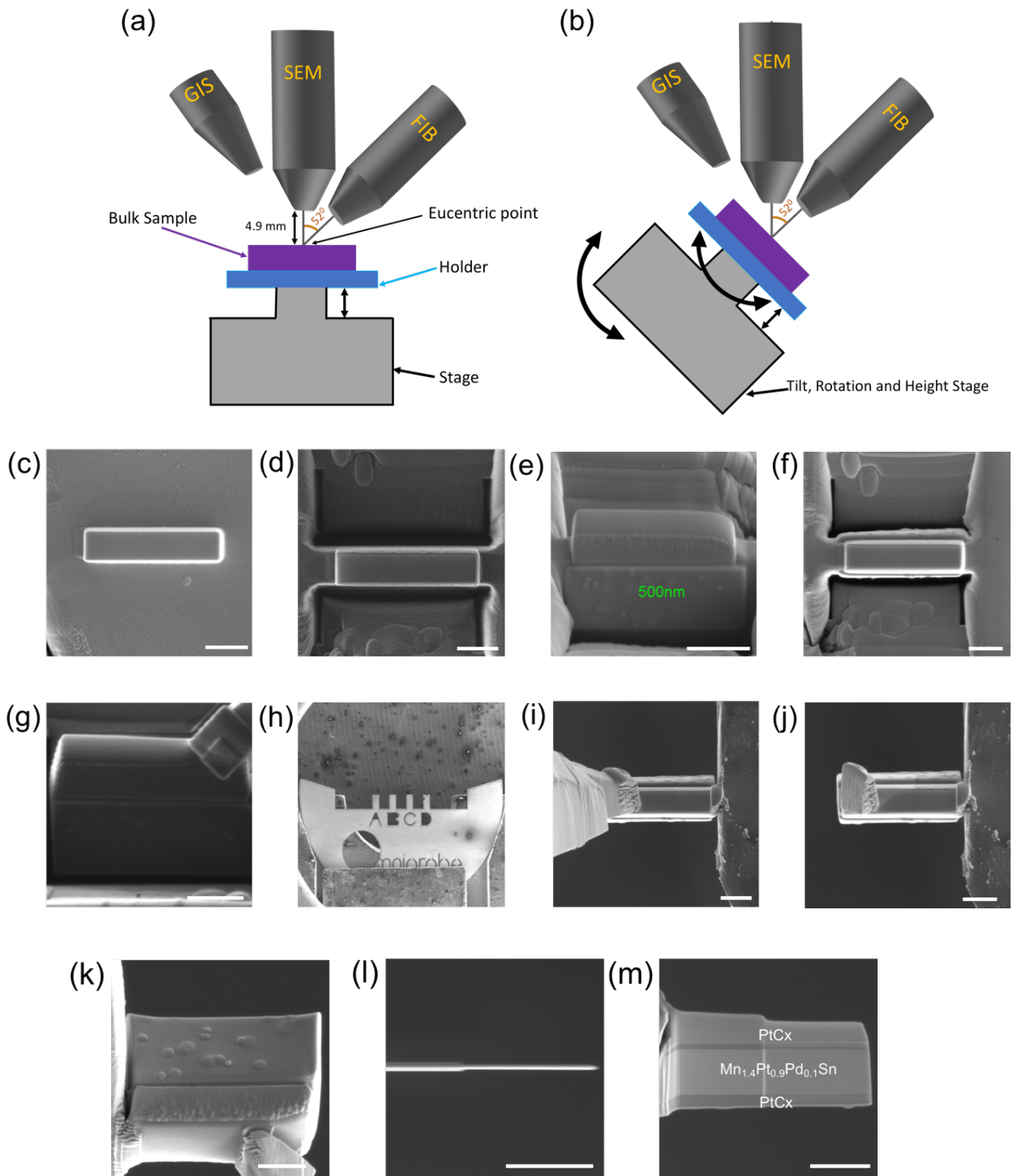


Figure 3 | Lamella preparation in a focused ion beam. (a, b) Schematic of FIB at zero and 52° tilt of stage. (c-m) show the thin lamella preparation steps of $\text{Mn}_{1.4}\text{Pt}_{0.9}\text{Pd}_{0.1}\text{Sn}$ from the initial [001] oriented grain. The 500 nm mark in (e) indicates the approximate thickness of PtC_x deposited on one side of the surface. Scale bar in each figure from (c) to (e) corresponds to 3 μm .

3.4 Transmission electron microscopy

Transmission electron microscope (TEM) is a powerful imaging technique that makes use of particles and wave nature of electrons^{102, 106}. It provides detailed insight into the electronic, compositional, structural, and magnetic properties in Material science. Specimen up to 1 μm thick can be used, depending on the atomic number of a specimen and the electron energy. However, for the atomic resolution and electron spectrometry study, specimen below 100 nm are essential.

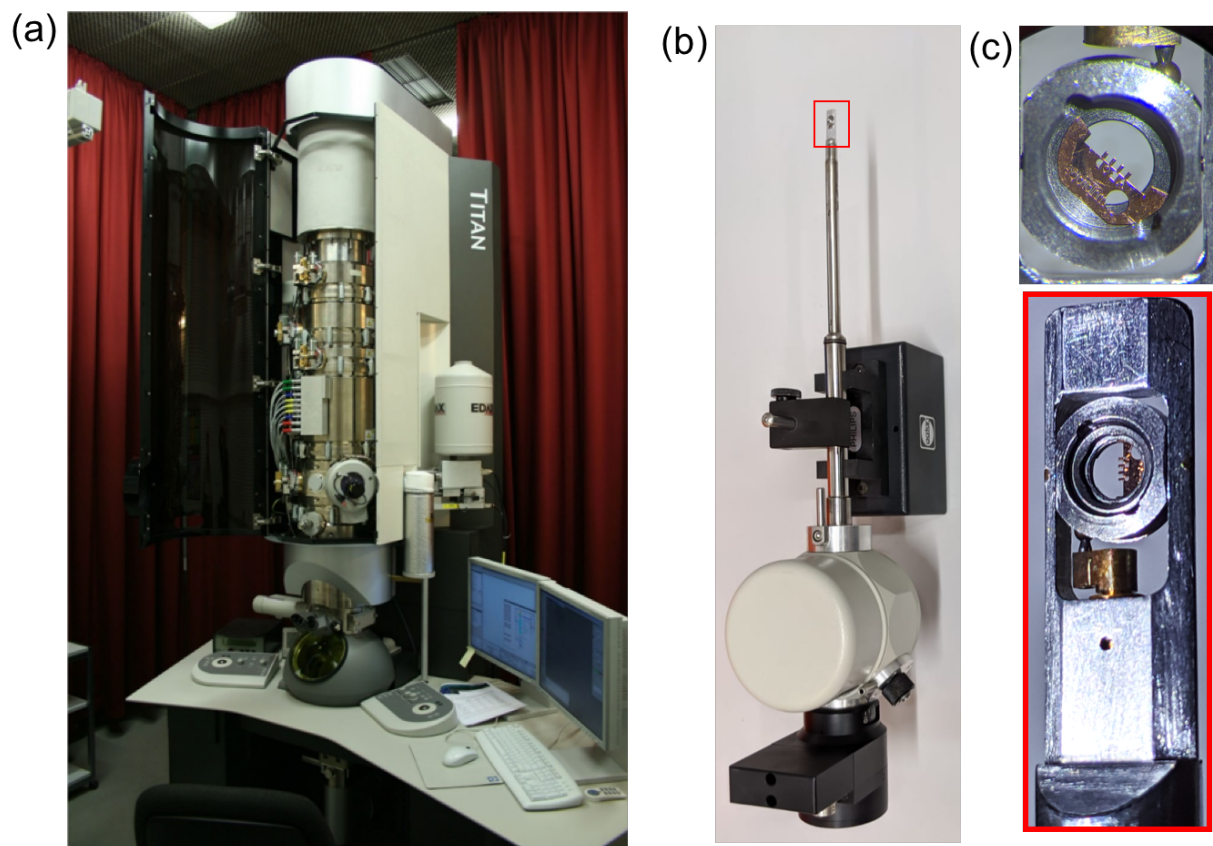


Figure 4 | Transmission electron microscope. (a) TITAN (80-300 kV, FEI) electron microscope used for the in-situ TEM studies. (b) The liquid nitrogen holder. The end portion of the holder is marked in a red rectangle and (c) the enlarged view is shown in the lower panel. The four-arms copper grid is placed in the mounting stage as shown in the upper panel. The lamella is attached to the one of the arms of the copper grid (not visible).

Two different kinds of electron sources used in TEM, namely thermionic source, which produces electrons by means of thermal excitation and while an intense electric field is applied to produce electrons in field-emission source¹⁰⁷⁻¹⁰⁹. The electrons tunnel out of the source are accelerated by the supply high tension. The condenser lens collects those electrons after passing through the highly accelerated electrode and focuses the beam on the specimen¹¹⁰. After electron passes through the thin lamella, those transmitted beams are focused by the objective lens into the charge-coupled (CCD) camera. In between the objective lenses and camera, there are additional objective apertures, intermediate lens, and projector lenses are used to enhance the contrast. The optical microscope is used to view and handle the position of the specimen or diffraction pattern through a phosphorus screen. The optical microscope window is attached to the TEM instrument's outer surface. The different mode of TEM investigation studies concern in this thesis use a field emission gun (FEG) source that has an accelerated voltage of 300 kV (FEI, 80-300 TITAN) (Fig. 4a). The magnetic field of 2.2 T is produced by an objective lens that is oriented parallel to the electron beam and perpendicular to the specimen surface placed at zero tilt. To hold the specimen inside the TEM and to provide an in-plane component of the magnetic field, a double tilt liquid nitrogen holder (tilting angle $\pm 40^\circ$) is used. It can operate from a higher temperature 365 K to the lowest possible temperature 98 K via heater controller (Gatan, model 900). Fig. 4b and 4c show the liquid nitrogen holder and the mounting stage of it.

3.5 Electron diffraction

There are two basic operations of the imaging system; projected image mode and diffraction pattern mode^{111, 112}. In the image mode, the intermediate lens is focused on the image plane of the objective while in diffraction mode, on the back focal plane of the objective lens^{102, 111} as shown in Fig. 5. Schematics of image and diffraction mode are shown in Fig. 5a and 5b. In electron diffraction, the incident electrons are treated as waves and the atoms in the nanometer-thick lamellae as a diffraction grating. After passing through the lamella, a fraction of electron scatter at particular angles, depends on the crystal structure of the sample, and rest is transmitted without deflection. This interaction results in a series of diffracted spots of different intensities along with the central zero spots resulting from the directly transmitted electrons. In selected area electron diffraction (SAED), from the whole region of the micrometer size lamella, few hundred nanometers area is selected by an aperture in the image plane, while blocking the rest

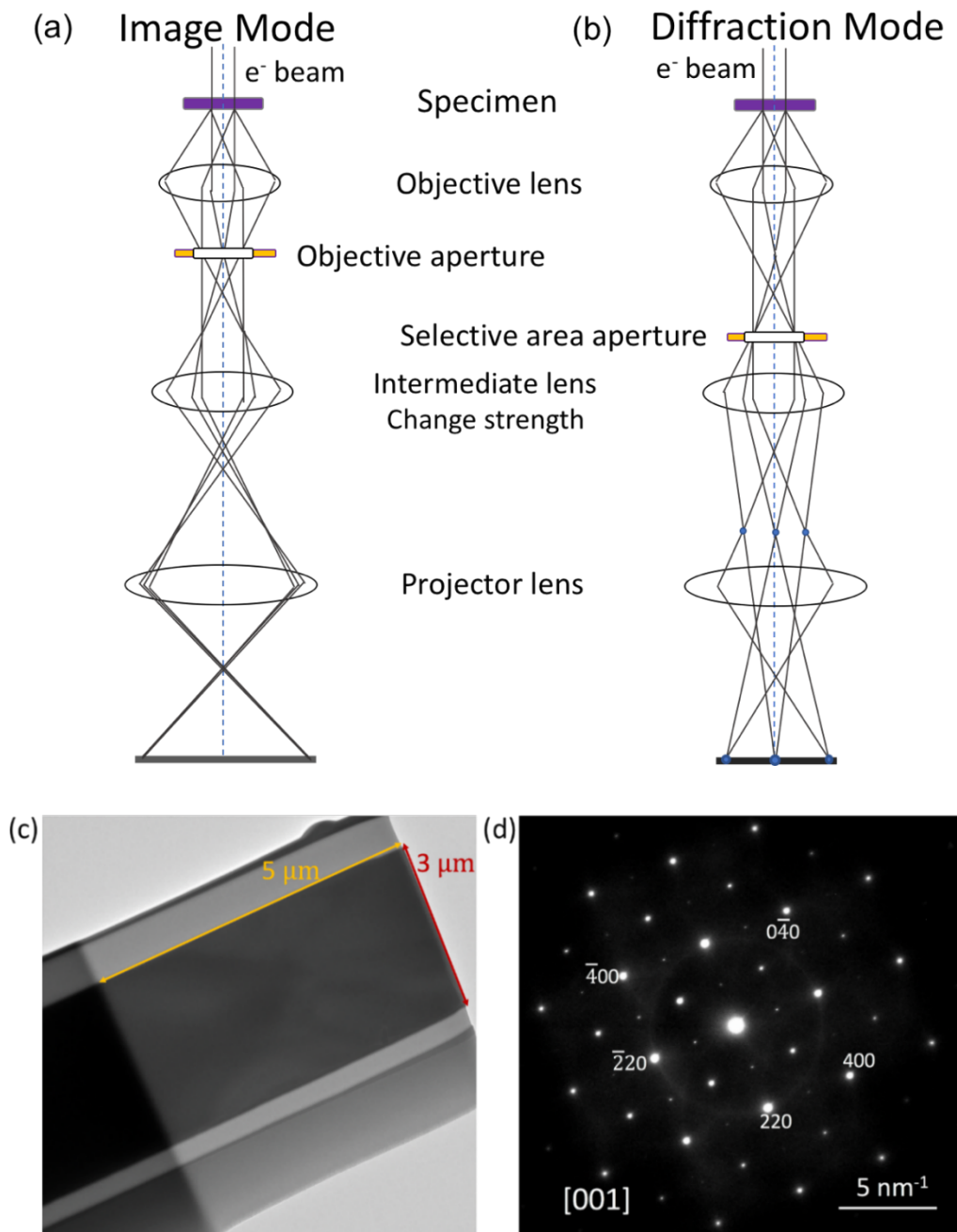


Figure 5 | Imaging and diffraction patterns. (a) and (b) show the schematic of imaging and diffraction patterns. (c) A TEM overview of the lamella (shown in Fig. 3m). The length and width of the electron transparent region of the lamella are approximately 5 μm and 3 μm, respectively. (d) The selected area diffraction (SAED) pattern of it. The red and orange arrows in the overview image are the width and length of the lamella prepared using FIB.

part^{102, 111}. This technique is often used for the single crystal analysis of the polycrystalline lamellae. Because most lamellae are distorted to some extent, diffraction spot condition changes on the slight movement of the foils. However, a fix oriented specimen area can be chosen by selected area apertures. The apertures have different sizes of holes and insert beneath the specimen below the objective lens. This SAED technique is advantageous when the investigated single-phase specimen has a different nm size orientation. We will simulate the diffraction patterns of different zone-axis in the CrystalMaker software¹¹³ using the crystal information file (CIF), which will be created based on the result of XRD measurement (see Ch. 7).

In the thesis, mostly [001] oriented zone-axis lamellae is the main focus for the apparent reason of topological spin structures stabilization within the basal plane of the tetragonal inverse Heusler compounds, Mn-Pt-Pd-Sn and Mn-Rh-Ir-Sn. A TEM image overview of single-crystalline lamella Mn_{1.4}Pt_{0.9}Pd_{0.1}Sn is shown in Fig. 5c. The selected area electron diffraction pattern of it ensures the [001] oriented zone-axis as shown in Fig. 5d.

3.6 Lorentz transmission electron microscopy

In LTEM, the magnetic induction in the specimen gives rise to the deflection of the upcoming parallel beam upon interacting with the specimen. On considering the particle nature of the electron, Lorentz force due to the presence of a magnetic field within and around the specimen is given by¹¹⁴

$$\mathbf{F} = e (\mathbf{v} \times \mathbf{B})$$

Here, e is the charge of the electron. \mathbf{v} is the velocity of the electron and \mathbf{B} is the magnetic induction averaged along the electron propagation. The component of magnetic induction parallel to the electron beam has no effect, while the deflection occurs when it is perpendicular to the beam. The deflection angle is given by

$$\beta_L = e\lambda t (\mathbf{B} \times \mathbf{n})/h$$

Here, \mathbf{n} is the unit vector parallel to the beam. The specimen thickness is denoted by t . λ is the wavelength of the electron and h is the Planck constant. The above equation shows that for the electron of constant energy, the deflection angle is proportional to the product of sample thickness and average magnetic induction. As LTEM is a transmission technique, the average magnetic induction depends on the component of magnetization perpendicular to the electron beam and the stray field above and below the specimen. The deflection due to the Lorentz force

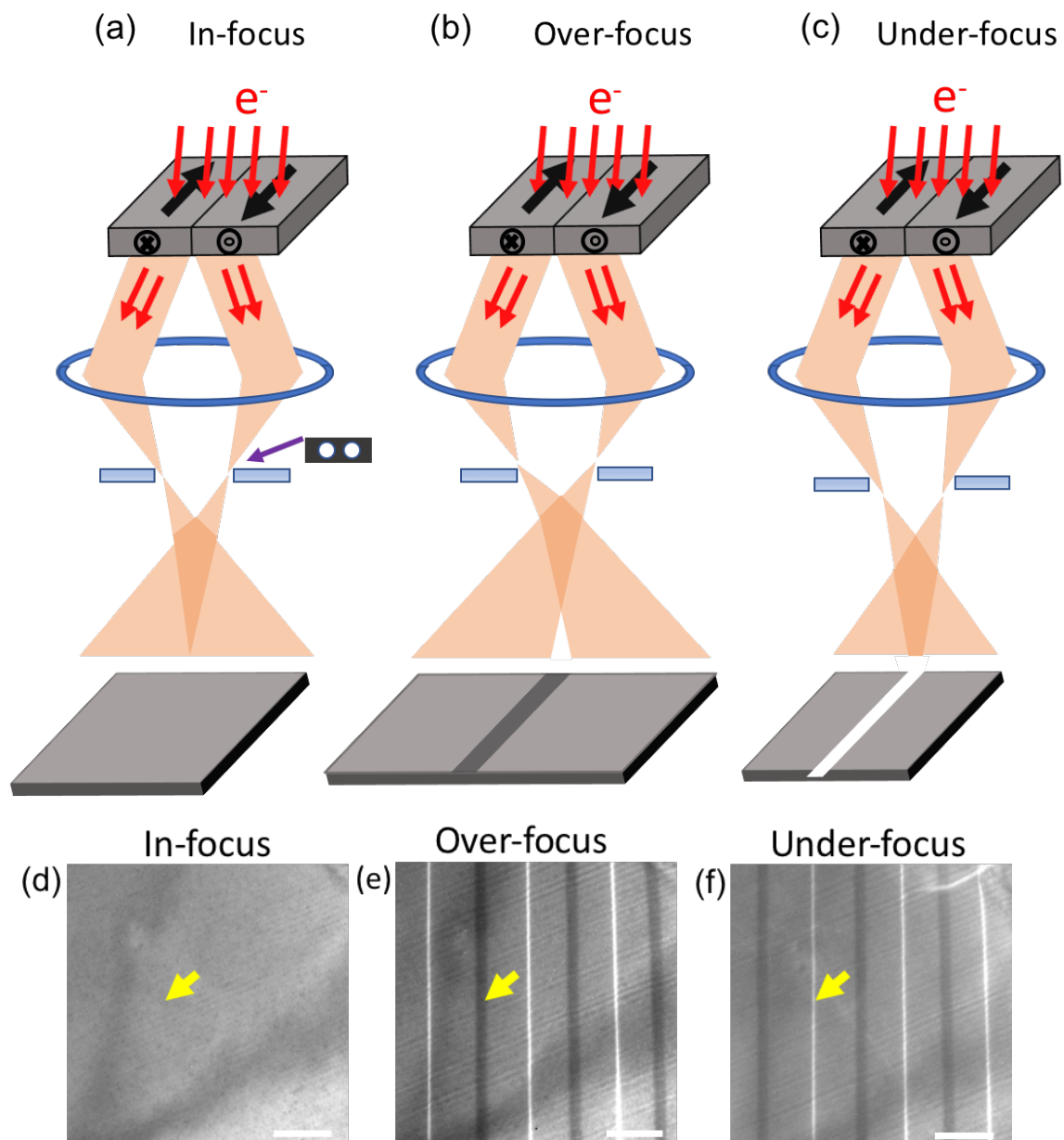


Figure 6 | Principle of Lorentz TEM. (a), (b) and (c) are schematics of Fresnel imaging Lorentz TEM mode in in-focus, over-focused and under-focused conditions for an oppositely magnetized 180° domains. In the lower panel, (d), (e) and (f) are the experimental LTEM images for 180° domains in in-focus, over-focused and under-focused conditions, respectively. The defocus value is 0.5 mm. The yellow arrows in LTEM contrasts point to the same place. The in-focus has no magnetic contrast and over and under-focused have bright and dark contrasts, respectively. The scale bars correspond to 500 nm.

(< 100 μ rad) is very much less than the Bragg scattering (typically 1-10 mrad).

Several in-situ techniques such as Foucault image mode, low angle electron diffraction (LAED), Fresnel imaging, differential phase contrast (DPC) imaging are used in the TEM for revealing magnetic structure^{102, 115, 116}. In this thesis, all the magnetic contrast images are performed under the Fresnel imaging method. It is a powerful method with nanometric spatial resolution, and the applied field is vertical to the specimen surface. The typical saturation state of the specimen is usually of much lower value than the high magnetic field contained in the objective lens (2.2 T). For this reason, the objective lens is switched off to make field free imaging of the specimen. An objective mini-lens is placed a few millimeters underneath the specimen to acquire field-free imaging. The external magnetic field is applied to the specimen through the objective lens by providing continuous current. The magnetic field can be applied up to the field polarized state of the specimen where the magnetic contrast vanishes. The LTEM contrasts are averaged over the thickness of the lamella. On the other hand, the LTEM images have no depth sensitivity, and presented magnetic contrasts are in the 2D form of a 3D lamella.

Fig. 6a-c shows the schematic of the Fresnel imaging mode of a specimen comprising of 180° domains. The electron beam experience Lorentz force on passing through the domain specimen region, and the diffraction spot splits into two as shown in Fig. 6a. The specimen formed magnetic contrast under the defocusing condition of the objective lenses. There won't be any magnetic contrast visible when the specimen is in-focus since the deflecting electrons are focused on the final image plane. The Lorentz force induced by the interaction of the beam with the magnetization forms magnetic domain walls. These domain walls are imaged as bright lines (dark lines) when magnetization on either side of the domain walls deflect the electrons towards (away from) the wall (Fig. 6b and 6c). Fig. 6d-f are the experimental Lorentz TEM for the 180° domains in $Mn_{1.4}Pt_{0.9}Pd_{0.1}Sn$ for the zone-axis other than [001]⁵¹. The orientation requires stabilizing topological spin textures in D_{2d} Heusler compounds is the basal plane of the tetragonal system.

3.7 High-resolution and scanning transmission electron microscopy

In a high-resolution transmission electron microscope (HRTEM) imaging technique, a parallel beam falls into a highly magnified nano-meter area of the specimen to see the lattice plane of the crystal. The elastically scattered electrons generated from the interaction of the parallel electron beam with the specimen are highly coherent. Therefore, interference will take place accordingly. Taking account of the phase and the amplitude information of electrons, a

lattice plane is formed. One can investigate the lattice parameter, surface structure, grain boundary, dislocation, defect, and stacking faults using the HRTEM technique^{102, 106}.

In scanning transmission electron microscope (STEM) technique, the electron beam is focused on a specimen, using condenser lenses, an objective lens, and additional scanning coils. A condenser aperture above the specimen limits the angle of illumination such that the electron beam is focused to a fine spot size of typically ~ 0.1 nm. In STEM, each atom is an independent scatterer because of the narrow probe, and hence there is no constructive or destructive interference between them. The raster illumination scanning is performed point by point to visualize the atomic position and elemental distribution of a compound or material. A high angle annular dark-field (HAADF) detector collects the scattered beam electron transmitted through the specimen. In STEM, the contrast forms as a sum of the intensities from the individual atoms of a constituting material. This is the reason HAADF is also often referred to as a Z-contrast image. Higher Z value atoms have higher contrast and vice versa^{102, 106}. The probe corrected (aberration-corrected) microscope has a longitudinal resolution of a maximum of 80 pm.

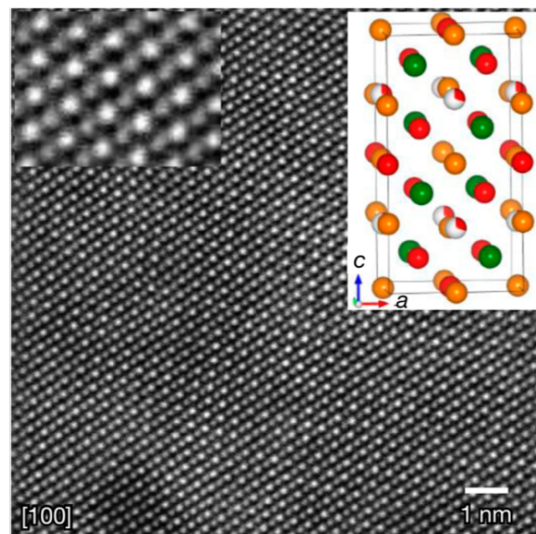


Figure 7 | STEM of $Mn_{1.4}Pt_{0.9}Pd_{0.1}Sn$. STEM image of the [100] oriented thin plate. The left inset shows the enlarged view. The right inset is the crystal structure of the Mn-Pt(Pd)-Sn system. The red, orange, green color correspond to Mn, Pt, and Sn atoms respectively. Adapted by the permission from Springer Nature Terms and Conditions for RightsLink Permissions Springer Nature Customer Service Centre GmbH: Macmillan Publishers Limited, Nature, Magnetic antiskyrmions above room temperature in tetragonal Heusler materials, A. Nayak *et al.* 2017; Ref. [51].

In order to compare the experimental STEM result, we simulate the STEM pattern using the STEM-WinHRTEM™ program¹¹⁷, based on the structure derived from the XRD measurement. In Ch. 7, we will perform such a simulation for the tetragonal inverse Heusler compound Mn₂RhSn. A STEM image of the Mn_{1.4}Pt_{0.9}Pd_{0.1}Sn [100] zone-axis oriented thin lamella is shown in Fig. 7. The alternating bright and gray atoms indicates the atomic arrangement of Mn-Pt(Pd) and Mn-Sn columns, respectively (left inset). The right inset shows the crystal structure of Mn_{1.4}Pt_{0.9}Pd_{0.1}Sn. It is a D_{2d} symmetry compound. To mention here that the D_{2d} symmetry has the following symmetry operations: E (No change), C_2 (180° rotation along the principal C_2 axis), $2C_2'$ (180° rotation along the axis perpendicular to C_2 axis and there are two such axes) and $2\sigma_d$, (there are two dihedral planes. dihedral planes- a plane which bisects the angle between two adjacent C_2' rotation axis) and $2S_4$, (90° rotation, followed by a reflection through a plane perpendicular to the rotation axis. There are two S_4 improper axes as rotation is either clockwise or anticlockwise).

3.8 Summary

Various experimental techniques used in this thesis are discussed. For measuring the magnetic properties of the bulk sample, SQUID is used. The Electron backscatter diffraction (EBSD) technique is used to determine the desired orientations from the polycrystalline sample. The step-wise thin lamella preparation methods by making use of a focused ion beam system are discussed. We have discussed the principle of Lorentz TEM mode and its application for magnetic imaging. Selected area diffraction patterns, high-resolution TEM, and STEM methods are used for the crystal structure study.

4 Elliptical Bloch skyrmions and antiskyrmions in a D_{2d} inverse Heusler compound

4.1 Introduction

Non-collinear spin textures of triangular spin lattices, spin glasses, domain walls, magnetic bubbles ranging from nanometer size to microns, and topological skyrmionic spin textures have been studied extensively for their fascinating physical properties. The topological spin textures, skyrmions and antiskyrmions, are in particular garnering lots of attention due to their distinct chiral magnetic boundaries and potential applications. Which kind of topological object a material will can stabilize depends predominantly on the DMI tensor which is determined from the underlying crystal symmetry. The most studied cubic chiral B20 structure of isotropic DMI hosts skyrmion of topological charge -1 and materials with D_{2d} symmetry host the anisotropic spin texture of antiskyrmion with topological charge +1 that arises from anisotropic DMI vectors. Due to the requirement of distinct DMI vectors for stabilizing skyrmions and antiskyrmions, the co-existence of both these topological objects had not yet been observed experimentally.

Using Lorentz transmission electron microscope (LTEM), we will observe the existence of both topological objects with opposite topological charge numbers ± 1 in the D_{2d} compound, $\text{Mn}_{1.4}\text{Pt}_{0.9}\text{Pd}_{0.1}\text{Sn}$, whose DMI otherwise supports the formation of only antiskyrmions. Individual and arrays of antiskyrmions (topological charge +1) with round and square-shapes and Bloch skyrmions of elliptical shape (topological charge -1) termed as ‘elliptical Bloch skyrmions’ can be stabilized over a wide range of temperature and field. Interestingly, these

objects can also be found at zero field without the need for performing the complicated field cooling protocols. It is shown through micromagnetic simulations that it is the presence of long-range dipole-dipole interactions in addition to the anisotropic DMI that allows for the formation of elliptical Bloch skyrmions, which only have Bloch walls. The major and minor axes of these elliptical skyrmions is tied to the crystallographic [100] and [010] directions, coinciding with the propagation direction of the spin helix. The ellipticity of the skyrmions can therefore be touted as an intrinsic property of materials with D_{2d} symmetry as the major and minor axes of the skyrmions are tied to the specific crystallographic directions in contrast to the observed distorted skyrmions in confined B20 materials. The discovery of two distinct chiral spin textures with opposite topological charges of ± 1 and their simultaneous existence in a single material makes the D_{2d} and related systems especially exceptional.

4.2 Methods

4.2.1 Experimental details

The studies here concerned the Heusler compound $\text{Mn}_{1.4}\text{Pt}_{0.9}\text{Pd}_{0.1}\text{Sn}$ that was prepared using the arc melting method in the form of single-phase poly-crystals. The Rietveld refinement of powder X-ray diffraction (PXRD) shows that the sample crystallizes with an inverse tetragonal structure in the D_{2d} symmetry group (space group $\bar{I}4_2m$, No. 121). The lattice parameters a and c are $6.3538 \pm 0.0002 \text{ \AA}$ and $12.2142 \pm 0.007 \text{ \AA}$, respectively, so that $c/a = 1.9223$. The preparation steps, structural characterization, homogeneity, single-phase properties of $\text{Mn}_{1.4}\text{Pt}_{0.9}\text{Pd}_{0.1}\text{Sn}$ were mentioned elsewhere⁵¹. The crystal orientation was mapped by *in-situ* electron backscattering diffraction (EBSD), which shows grains of typical size ~ 60 - 80 microns. Single crystalline grains oriented along [001] are chosen for the apparent reason of anisotropic DMI present in the basal plane of this tetragonal structure. In $\text{Mn}_{1.4}\text{Pt}_{0.9}\text{Pd}_{0.1}\text{Sn}$, both chiral boundaries of this associated anisotropic DMI are stabilized in the basal plane due to the presence of a heavy Pt atom breaking the inversion symmetry of a magnetic Mn layer differently along the [100] and [010] directions. From the [001] oriented grain (the red color region on EBSD mapping, see Fig. 2, Ch. 3), (3 x 5) micrometers sized lamella (Fig. 5, Ch. 3) of ~ 170 nm thickness is prepared using Ga^+ focused ion beam ([FEI Nova Nano lab 600 SEM/FIB]) technique. The SEM image at 52° tilt shows the lamella surface (Fig. 3m, Ch. 3), and for the thickness of the prepared lamella, the SEM image was taken at zero tilt condition (Fig. 3l, Ch. 3) (the stage is in zero tilt condition). The lamella attached to the copper grid is loaded inside the microscope (TITAN 80-300 kV) on a double tilt sample stage that has

controlled variable temperature range from 350 K to 100 K using a LN₂ cold stage controller (Gatan, Model 900). To image the magnetic texture, *in-situ* Lorentz TEM was used throughout the thesis. The under-focus value for the LTEM image contrast is ~1 mm. A magnetic field oriented along the TEM column and perpendicular to the surface of the lamella is applied by changing the current through the objective lens. The magnetic field values are calibrated using a Hall bar sensor. The magnetic fields mentioned for the Lorentz TEM contrasts are along the microscope column. By tilting the double tilt holder's sample stage, the specimen normal can be placed at an angle with respect to the field, so that there is a finite non-zero component of the magnetic field in the plane of the lamella.

4.2.2 Micromagnetic simulations

Micromagnetic simulations were carried out using the graphics processing unit (GPU) accelerated Mumax3 program to determine the possible different metastable states. The program was modified to include the anisotropic DMI for D_{2d} symmetry in the inverse tetragonal system. A sample dimension of 1200nm × 1200nm × 175nm was simulated with a cell size of 5nm × 5nm × 5nm. Micromagnetic simulations based on Landau-Lifshitz-Gilbert equation were performed for every discretized magnetization cell (normalized moment \mathbf{m}) according to:

$$\dot{\mathbf{m}} = -\gamma_e \mathbf{m} \times \mathbf{B}_{\text{eff}} + \alpha \mathbf{m} \times \dot{\mathbf{m}} \quad (13)$$

Here

γ_e is the gyromagnetic ratio of an electron, $\alpha = 0.3$ is the Gilbert damping constant, $\mathbf{B}_{\text{eff}} = -\frac{\delta F}{M_S \delta \mathbf{m}}$ is the effective magnetic field derived from the free energy density F , which considers the Heisenberg exchange, dipole-dipole interactions, magnetic anisotropy, external magnetic field, and the anisotropic DMI. The material parameters used are as follows: saturation magnetization $M_S = 445 \times 10^3 \text{ Am}^{-1}$ and exchange interaction $A_{\text{ex}} = 1.2 \times 10^{-10} \text{ Jm}^{-1}$. Here the form of the anisotropic DMI in tetragonal inverse Heusler compound is given by:

$$H_{\text{DMI}} = D \left(m_z \frac{\partial m_x}{\partial x} - m_x \frac{\partial m_z}{\partial x} - m_z \frac{\partial m_y}{\partial y} + m_y \frac{\partial m_z}{\partial y} \right) \quad (14)$$

and used D value is $3 \times 10^{-3} \text{ Jm}^{-2}$. The D value considered in the letter by Nayak *et al.*⁵¹ is assumed to be overestimated since the dipole-dipole interactions were neglected. A magnetic field B_z was applied along the positive Z axis and an easy-axis anisotropy along Z was considered with $K_u = 2 \times 10^{-1} \text{ MJm}^{-3}$. For calculation of the simulated LTEM images, a first-order approximation considering only a single layer (average magnetization of all layers) and a

deflection of the incoming electron beams by the Lorentz force was assumed. The incoming electrons at the position (x', y') were modeled by a Gaussian smearing function with a smearing factor $a = 60$ nm. The transmitted electron flux at (x, y) is proportional to:

$$\int \exp\{-[(x - d \cdot m_y(x', y') - x')^2 + (y + d \cdot m_x(x', y') - y')^2]/a^2\} dx' dy' \quad (15)$$

Here, $d = 2$ nm characterizes the maximum deflection of electrons by the Lorentz force.

4.3 Results and discussion

4.3.1 Round and square antiskyrmions

The in-plane magnetic field within the basal plane of the inverse tetragonal Heusler compound of $\text{Mn}_{1.4}\text{Pt}_{0.9}\text{Pd}_{0.1}\text{Sn}$ helps to overcome the energy barrier between the topologically trivial and non-trivial states and so that the antiskyrmion texture is stabilized. This is illustrated in Fig. 1 below. A schematic of the sample plane perpendicular to the electron beam is shown in Fig. 1a. Sufficiently strong out-of-plane magnetic field is applied to bring the specimen into the field polarized state at a given temperature. From there, the magnetic field is decreased gradually (Fig. 1b). We show that helical states emerge without the formation of antiskyrmions in the absence of an in-plane field component since the energy barrier between the helical phase and the antiskyrmion phase is too large. The texture exhibits helices with gradually decreasing period length as the field decreases (Fig. 1c-h). In other words, at higher fields, the ferromagnetic region between helices is larger than the lower magnetic field.

Next, a temporary in-plane component of the magnetic field is included via sample-tilting using the following protocol. The out-of-plane field is reduced to a particular value from the field polarized state. The lamella is then tilted $\sim 35^\circ$ - 40° away from the [001] zone-axis approximately along the [110] direction. It gives a temporary in-plane field on the sample surface. After that, the sample is tilted back to the initial zero tilt position (Fig. 2a, 2b). The field value is decreased in steps and each LTEM contrast is collected after temporary application of the in-plane field component followed by returning to the initial position. This procedure is continued until a periodic lattice has been formed. The field is then decreased without tilting once the closed packed lattice is formed. We did so, to not cross the barrier to the helical phase and to investigate those topologically non-trivial phases and its stability up to the lowest field value. The LTEM contrasts resulting from using this protocol at 300 K is shown in Fig. 2c to 2h. Similar contrasts were found in other regions of the lamella. At 368 mT, a few circular features emerge (Fig. 2c). The densely packaging of these objects are found (Fig. 2d)

in the field region between 336 mT and 288 mT. Those circular objects appear with two lobes of increased intensity and perpendicular to it are two spots of reduced intensity resulting from

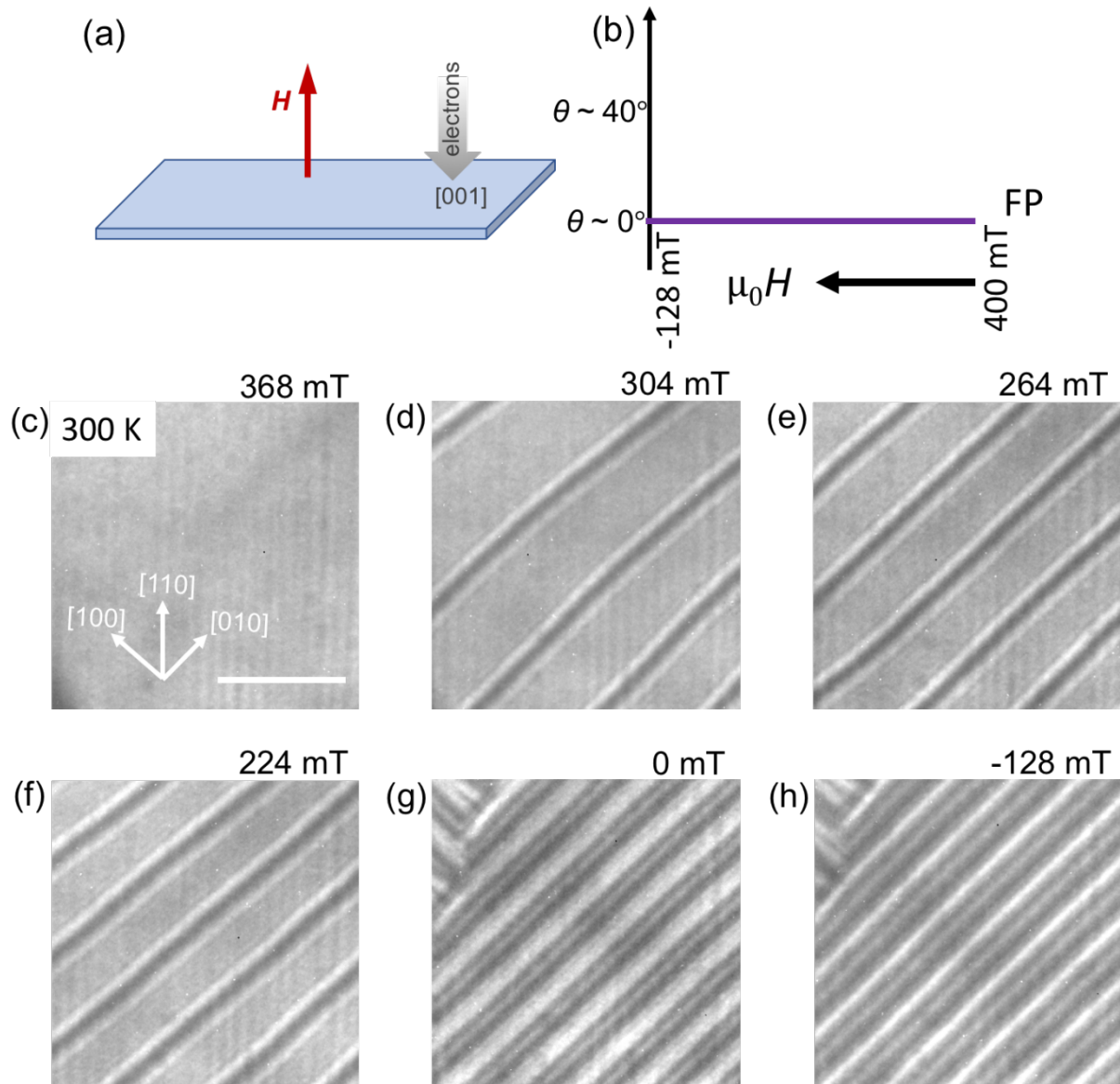


Figure 1 | Helical Phase in the absence of in-plane field components. (a) Shows the schematic of the lamella placed in the microscope. The surface of the lamella is perpendicular to the electron beam propagation. (b) Schematic of the applied magnetic field perpendicular to the lamella surface. (c-h) The LTEM contrasts show the observation of helices under the decreasing field mode from field polarized state following the protocol shown in schematics. The scale bar in (a) corresponds to 500 nm.

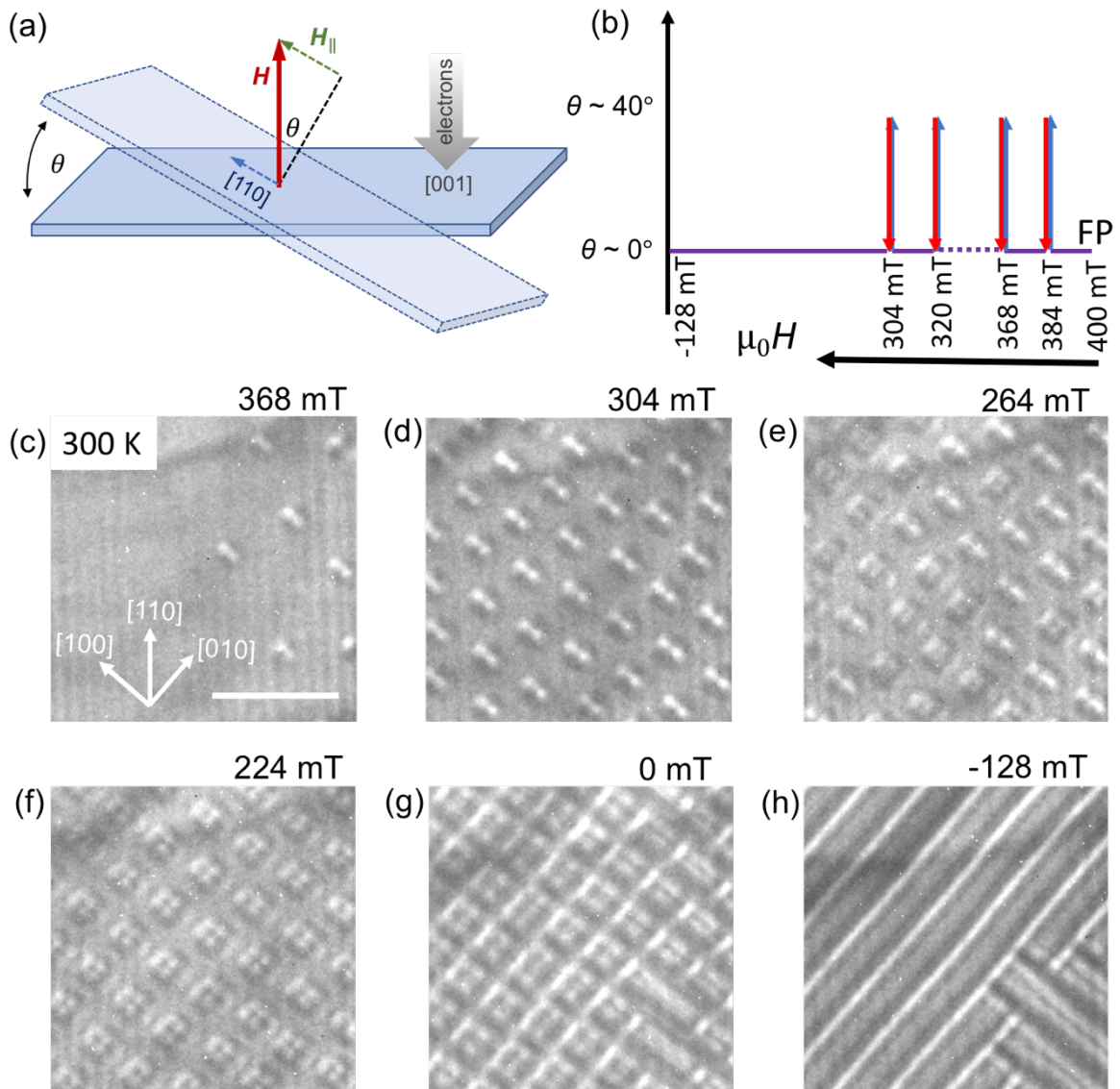


Figure 2 | Field induced stabilization of antiskyrmions in D_{2d} material. (a) Shows the schematic of the temporary tilting of the lamella. (b) Illustrates the procedure that is used for the nucleation of spin textures in the D_{2d} system. (c-h) In the bottom rows, we apply the modified protocol (see schematic a and b) where we tilt the lamella by 35° - 40° in the $[110]$ direction and come back to $[001]$ orientation (as indicated by red and blue arrows) at high fields until a dense array of antiskyrmions has formed in (d). (e) We observe two different types of features: round ones indicating conventional antiskyrmions and square ones which are topologically identical to antiskyrmions. (f) A highly periodic lattice of the square objects is stable even at vanishing field (g) and transforms into the helical phase only at a negative field of -128 mT (h). The scale bar in (c) corresponds to 500 nm.

the oppositely oriented Bloch parts along $[100]$ and $[010]$ that are consistent with the antiskyrmion texture reported earlier⁵¹. From here on, the field is applied without tilting and LTEM contrast shows a transformation of the round antiskyrmions to square-shaped objects. Intermediate transition states are observable in between the round antiskyrmions to square-shaped ones (Fig. 2e). These square shapes form a lattice starting from 224 mT (Fig. 2f), which is stable even in the absence of a field (Fig. 2g). At a negative field of -128 mT (Fig. 2h), a transition to helical phase is favored with the helix propagating along the $[100]$ and $[010]$ directions.

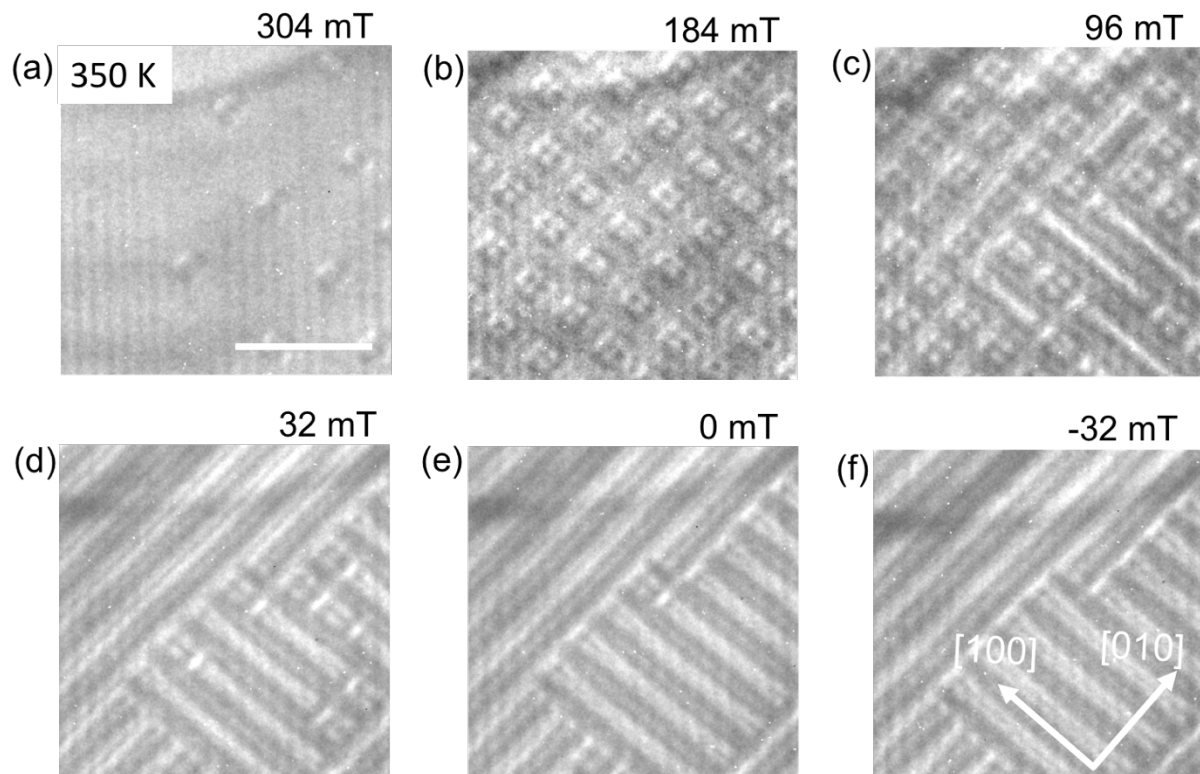


Figure 3 | Formation of square antiskyrmions. Shows the evolution of the LTEM contrast with decreasing field on applying the modified experimental protocol (applying temporal tilting along $[110]$ at high fields until a lattice of objects has formed) at the highest investigated temperature of 350 K. (a) The transition from the field polarized state, to a few isolated objects. In (b), the lattice of square antiskyrmionic features. (c-f) The transition to helical phase. The scale bar in (a) corresponds to 500 nm.

At 350 K (shown above in Fig. 3), the field dependent LTEM contrast is distinct from 300 K. Isolated features are not circular (Fig. 3a). They are square in shape. The periodic lattice of square objects appears at a reduced field of 184 mT (Fig. 3b). The number of individual objects gradually reduces, instead replaced by the helical state starting from 96 mT (Fig. 3c), and at 0 mT (Fig. 3e), only two individual square antiskyrmions remain, which transform to the helical phase at -32 mT (Fig. 3f). In Fig. 3c-f, few rectangular shape short helices are observed. More about these types of structures are discussed in Ch. 6.

4.3.2 Elliptical Bloch skyrmions

Here, the result at a lower temperature of 200 K is presented. Following the aforementioned protocol for lattice stabilization, completely distinct LTEM features are observed. Starting again from the ferromagnetic state, as the field is reduced, the sparse nano-objects observed are neither circular nor square but elliptical in shape (Fig. 4a). With decreasing magnetic field, the density of nano-objects increases (Fig. 4b). They appear as bright contrast in the center surrounded by black contrast around the periphery and appear as Bloch-like skyrmions. Skyrmions observed previously (in B20 compounds and C_{nv} symmetry) have been usually circular and not elliptical in shape, as we have observed here.

At lower fields (Fig. 4c), the hexagonal lattice appears and upon decreasing the magnetic field, individual objects increase in size so that space between them decreases (Fig. 4d-g). The nano-objects at the lower fields appear as an elliptical ring of bright contrasts with grey contrasts lying both within and outside the bright contrast (Fig. 4e-h). The objects exist in a lattice state at zero field (Fig. 4f) and remain so, even up to -32 mT (Fig. 4g). Interestingly, the nano-objects of square shape (Fig. 2) and elliptical shape found in the D_{2d} compound are stabilized in the absence of the magnetic field. The partially metastable objects and helices co-exist even for fields as large as -48 mT (Fig. 4h) in negative direction before turning to the complete helical phase at -64 mT (Fig. 4i). The black horizontal line in each LTEM image corresponds to bending contours. Periodic vertical lines in the LTEM images are non-magnetic contrasts caused by the FIB specimen preparation.

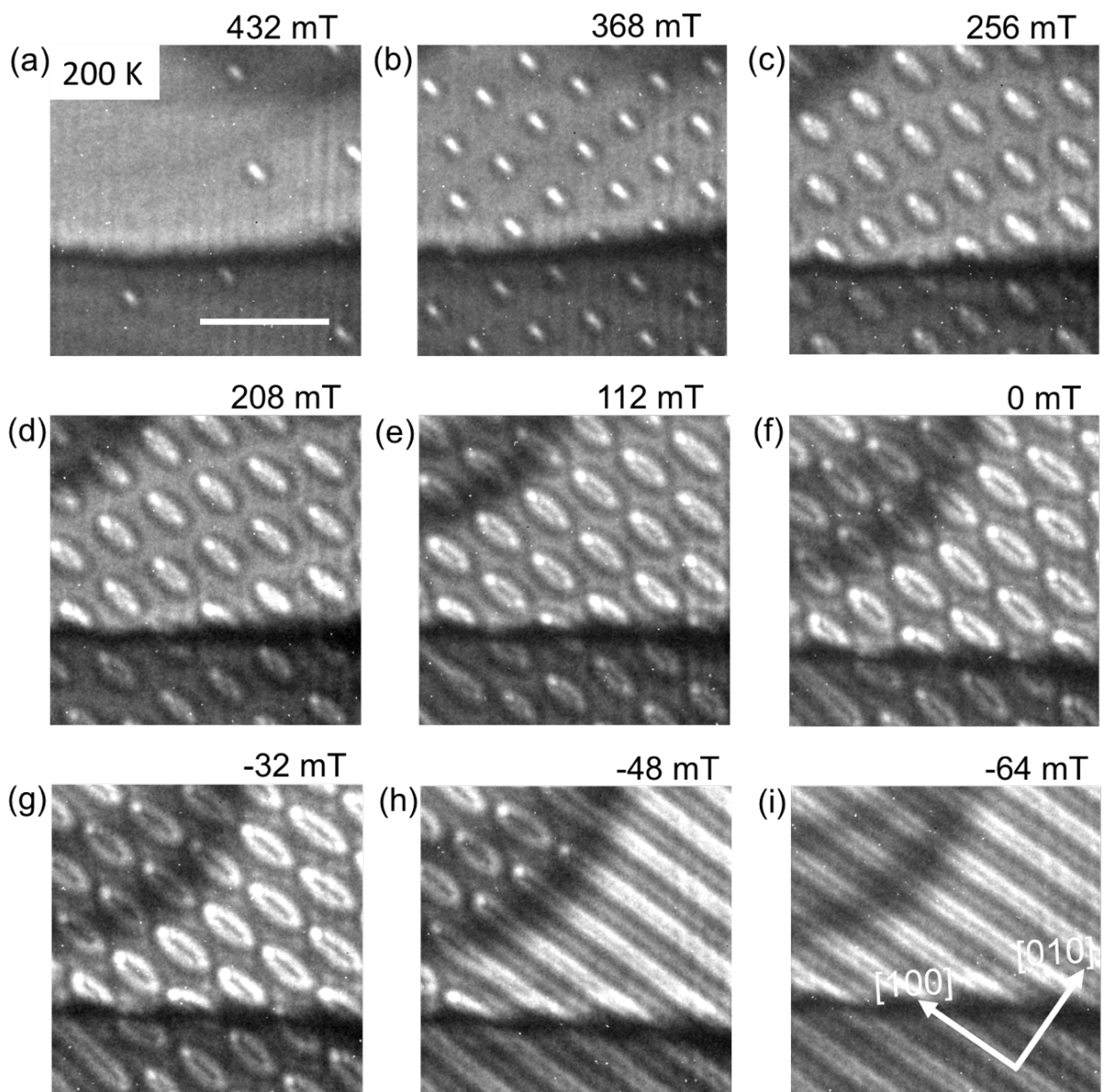


Figure 4 | Formation of elliptical skyrmions. Shows the evolution of the LTEM contrast at the temperature of 200 K with decreasing field applying the same experimental protocol i.e. applying reversible tilting along $[110]$ at high fields until a lattice of objects has formed. One observes a few isolated nano-objects at high fields (a) and then a transition to a densely packed array of skyrmions (b-g) which sustained up to -32 mT. (h, i) The helical phase found only at negative fields. The scale bar in (a) corresponds to 500 nm.

4.3.3 Enhanced stability of elliptical Bloch skyrmions

A similar result of elliptical nano-objects is found at 150 K and 200 K for this ~ 170 nm lamella (see Appendix A.1). However, at 100 K, only a few isolated elliptical objects are formed (Fig. 5a) and then the helical state has shown without forming the lattice states following the same protocol (Fig. 5b-d). On the other hand, for a thicker sample (~ 280 nm), a dense lattice state is found in a large magnetic field region even at 100 K (Fig. 6a-h), pointing towards the significance of dipole-dipole interactions in this material. It shows the enhanced stability of elliptical skyrmions both for a broader range of temperatures and thicker lamellae. We name the unanticipated elliptical shape contrast as “elliptical Bloch skyrmion” though anisotropic DMI vector in D_{2d} symmetry of the tetragonal system strictly favors the antiskyrmions over that of Bloch skyrmions.

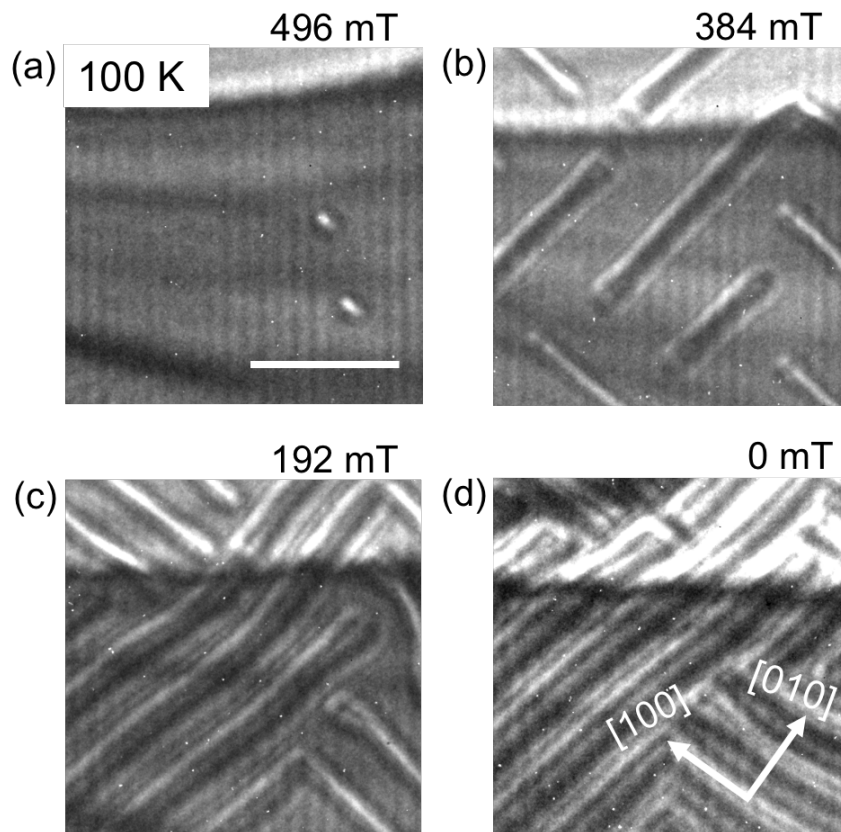


Figure 5 | Formation of Spin textures at 100 K for sample thickness of ~ 170 nm. Shows the LTEM measurements in the ~ 170 nm thick sample. The field is reduced coming from the polarized phase (on same lattice stabilization protocol) with only a few elliptical shape objects shown in (a). In (b-d) helices are formed. The scale bar in (a) corresponds to 500 nm.

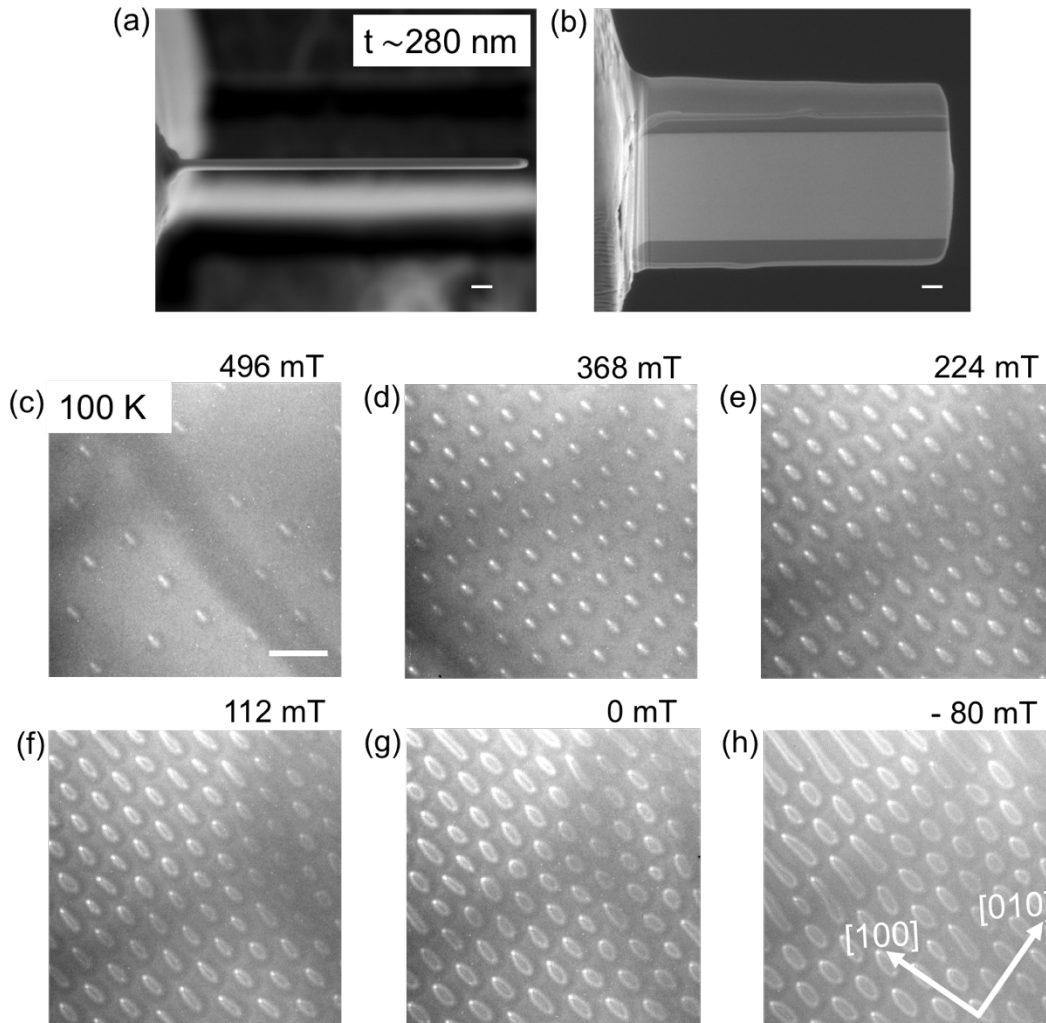


Figure 6 | Elliptical-skyrmions at 100 K for sample thicknesses of ~ 280 nm. In (a), the top view of SEM image confirms ~ 280 nm thickness whose surface overview is shown in (b). In (c-h), the Lorentz contrast of ~ 280 nm sample thickness is shown. (c) Starting again at high fields, a sparse state is found at 496 mT. (d) A dense array of elliptical skyrmions form that persists upon decreasing the field (e-f), even down to zero field (g) and below (h). The scale bars correspond to 500 nm.

The micromagnetic simulations also confirm these elliptical shapes as skyrmions constituted of Bloch walls. These skyrmions have a topological charge number opposite to that of antiskyrmions present in the same system and arise after considering dipole-dipole interactions along with DMI interactions consistent with D_{2d} symmetry. This is discussed in the section below.

4.3.4 Elliptical Bloch skyrmion chiral twin

The simulated metastable configuration depends on the initial magnetic state. After relaxing the initial configuration of topologically different circular textures, relaxed metastable configurations labeled as ‘simulation’ in Fig. 7a-d are obtained. This means that every initial circular configuration will not result in the stabilization of a metastable configuration. On choosing the initial state as circular antiskyrmion, whose Bloch part chirality differs locally as clockwise parts are favored along $[010]$ and $[0\bar{1}0]$ and anti-clockwise parts along $[100]$ and $[\bar{1}00]$, the relaxed state is a metastable configuration as shown in Fig. 7c. The green and pink arrows correspond to the clockwise chiral Bloch part and the blue and yellow correspond to the anti-clockwise Bloch part. Attributing to the same anisotropic DMI, when the initial state is set to be a particular circular Bloch skyrmion with a given chirality (here clockwise), we observe that it converges to an object with an elliptical shape (Fig. 7a), as we find experimentally (Fig. 7e). Similar to the protocol dependence of the experiments, the meta-stability of the textures in the simulations also depend on the configuration of the initial magnetic texture. In the simulation, interestingly, we find that the orientation of the major axis of the ellipse is determined by the chirality (whether clockwise or anti-clockwise) of the initial magnetic texture. The major axis is always oriented along one of the in-plane crystallographic directions: $[100]$ or $[010]$. When the initial object has clockwise chirality, the relaxed state is an elliptical object whose major axis is along $[100]$ and the minor axis along $[010]$. The highlighted Bloch parts marked in green and pink colors are favored by the anisotropic DMI and are consequently enlarged (Fig. 7a). Similarly, an anti-clockwise chiral object induces a metastable elliptical shape with the major axis is along $[010]$ and the minor axis along $[100]$ direction. In this case, blue and yellow colors mark the enlarged Bloch parts (Fig. 7i-k). The elliptical shape remains upon decreasing the field, but their overall size increases such that the ellipticity, which is the ratio between the major and minor axis length, is enhanced (Fig. 7f). This effect is also observed in LTEM simulations when using different magnetic field strengths (Fig. 7a and 5b).

Long-range dipole-dipole interactions produce those Bloch like elliptical objects since costly volume charges $\text{div}(\mathbf{m})$ are absent in Bloch walls¹¹⁸. We have indeed observed experimentally that the elliptical-skyrmions are oriented along two crystal directions only and indeed favored micromagnetic simulations shown in Fig. 7i-k. Moreover, the LTEM contrast shows that the elliptical-Bloch skyrmions in $\text{Mn}_{1.4}\text{Pt}_{0.9}\text{Pd}_{0.1}\text{Sn}$ have specific and opposite chiralities for these two crystal directions. Thus, these elliptical-skyrmions can be said to be appear as “chiral twins”.

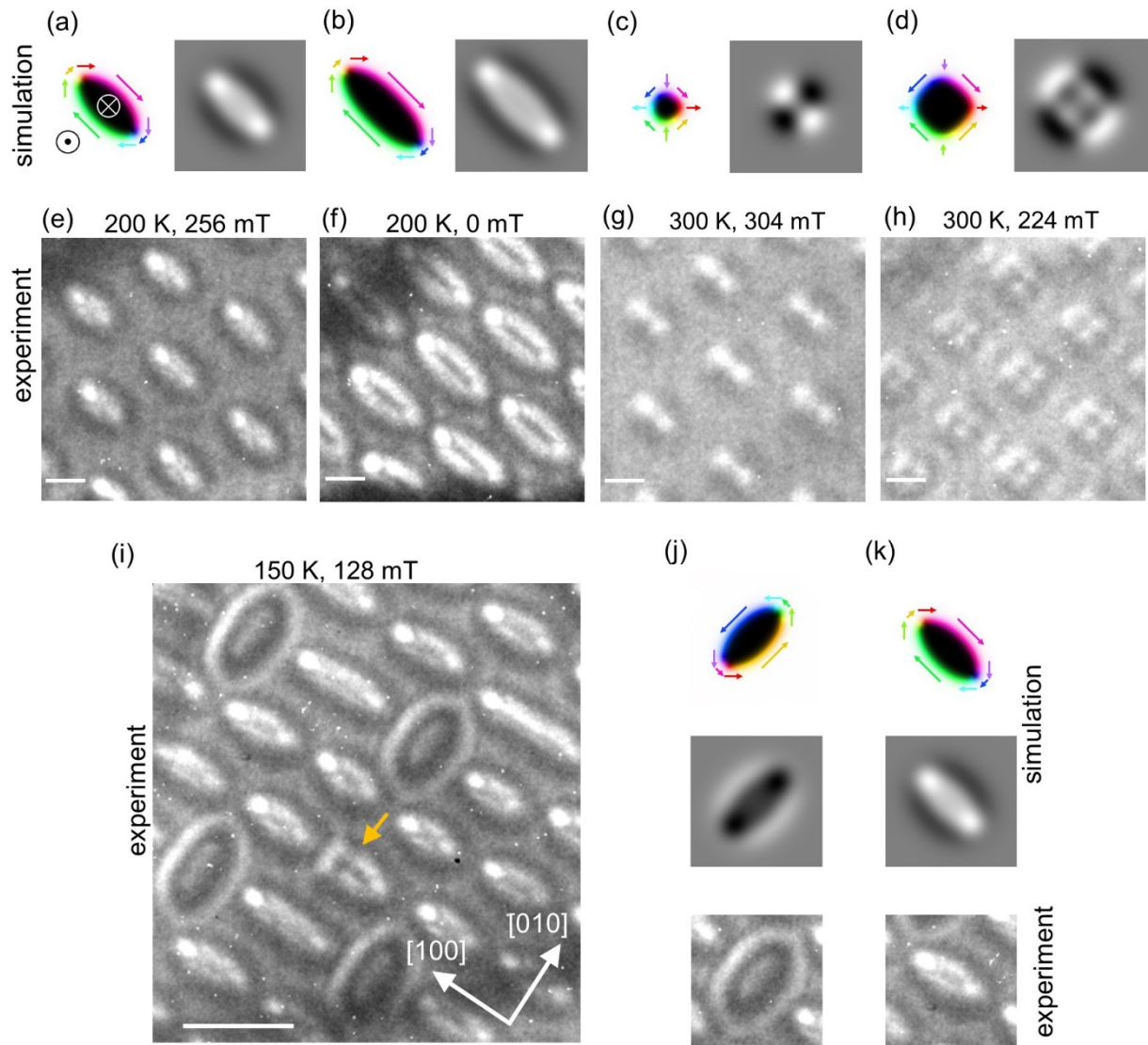


Figure 7 | Micromagnetic simulations of elliptical Bloch skyrmions and antiskyrmions. In (a)-(d) different magnetic textures are stabilized starting from a skyrmion or an antiskyrmion. The resulting textures are elongated skyrmions in (a) and (b), a round antiskyrmion in (c), and a square shaped antiskyrmion in (d). For (a) and (b) we started from a Bloch skyrmion configuration and in (c) and (d) from an antiskyrmion. The out-of-plane magnetic fields in the simulations are: 180 mT (a), 170 mT (b), 210 mT (c), and 180 mT (d). The calculated LTEM images (right panels) are in good agreement with the experimentally observed patterns (e-h). The magnified images in e-h are taken from Figs. 4(c), 4(f), 2(d), and 2(f), respectively. The scale bars for the LTEM images in (e-h) correspond to 100 nm. In (i-k) the co-existence of elliptical-skyrmions with opposite chiralities is shown at 150K and 128 mT. Micromagnetic simulations of the two objects (j), (k) confirm this interpretation. Furthermore, a topologically trivial object is highlighted by the orange arrow. The scale bar in (i) corresponds to 300 nm.

This makes elliptical skyrmions fundamentally different from DMI stabilized skyrmions in B20 materials. In B20 chiral crystals, only one chirality is favored, which is determined by the chirality of the material^{1, 2, 21, 23} and there is no experimental or theoretical evidence for elliptical skyrmions in such materials. The micromagnetic simulations in which an isotropic DMI show circularly shaped skyrmions, even after taking into account dipole-dipole interactions^{73, 119}. Though there have been reports of deformed or distorted skyrmions in several B20 materials^{85, 86, 120-122}, the deformations in these cases are irregular. They form either as a result of anisotropic q-vectors¹²⁰ or confinement in nanostructured materials, from nano-sized grains or laterally patterned confined nanostructures. More importantly, these deformations are not tied to the underlying crystal structure and hence, are not an intrinsic property as we observe here.

The dipole-dipole interactions are relevant since the saturation magnetization and the sample thickness are of considerable importance in this system. We can relate the temperature dependence to the decreased net magnetization at higher temperatures, which reduces the strength of dipole-dipole interactions and stabilizes antiskyrmions. Further, the role of the magnetization on the stability of elliptical-skyrmions is investigated on a thicker sample (fig. 6c-h). While in the previously investigated lamella (thickness ~ 170 nm), only a very few individual elliptical Bloch skyrmions could be observed at 100 K (Fig. 5a-d), in the thicker lamella of ~ 280 nm thickness, we could stabilize a well-ordered and dense elliptical skyrmion lattice (Fig. 6c-h).

The dipole-dipole interactions strength increases on increasing M_s . This results in the formation of elliptical skyrmions at low temperatures and antiskyrmions at room temperature and above. The observed antiskyrmion comes in two different forms: round and square-shaped. Considering the M_s value for the same thickness of lamella, the long-range dipole-dipole interactions become apparent in the micromagnetic simulations. As shown in Fig. 7c and 7d, the initial antiskyrmion shape remains at higher fields and at lower magnetic fields, a square deformation takes place. The dipole-dipole interactions induce the enlargement of the favorable Bloch parts along the family of in-plane $\{10\}$ directions marked in pink, blue, green and yellow arrows. On the contrary, the Néel parts are unfavorable so that spatial shrinking results in the overall size of the individual antiskyrmion appear as a square. The calculated LTEM signal agrees well with the experimental observation. The square deformation is not noticeable anymore at higher fields since both Bloch and Néel parts become almost energetically equivalent and the domain wall width is now comparable to the size of the magnetic object¹²³.

4.3.5 Switching between round and square antiskyrmions

Both round and square-shaped objects have the same topological charge of different forms, a clear noticeable transformation between them, as is observed in Fig. 8. Round antiskyrmions transform to square shape when the magnetic field is decreasing as shown in Fig. 8a and 8b. However, when the field is increased again from 112 mT, the state remains square-shaped at a higher field (Fig. 8c). The transformation to round antiskyrmions from square antiskyrmions is only possible when a temporary in-plane component field is provided by tilting the specimen and returning it back to the initial position (Fig. 8d). This indicates a small energy barrier between round and square-shaped antiskyrmion lattice in our experiments. In the micromagnetic simulation of an isolated object which is an ideal case, this barrier is absent. Thus, it can be anticipated that the interaction between neighboring objects has an influence on the metastability of magnetic objects in lamellae of D_{2d} Heusler materials.

In the case of elliptical Bloch skyrmions, there is no such contrast deformation from the higher to lower value of the magnetic field except the ellipticity due to elongation of the Bloch part attributed to the anisotropic DMI. Moreover, theoretical prediction on the dipole-dipole interactions promote degenerate conditions due to the achiral nature. In our experiment, Bloch skyrmions elongated along [100] (see Fig. 4) at temperatures between 150 K and 250 K are observed. On repeating the tilted magnetic field experiment along different in-plane directions and tilting back, the same result is reproduced as shown in Fig.9. Here the out-of-plane field is kept constant at 272 mT and the in-plane field components are realized by tilting the lamella. It is found that the elliptical shape is stable up to $\pm 3^\circ$ away from the zone-axis. After that, further tilting away, trivial bubble states of different LTEM contrasts at different tilting angles are captured in tilted condition (Fig. 9a-d). In all those cases, each individual texture deforms to a triangular shape, but after returning to the initial perpendicular direction, the configuration turns back to the initial elliptical skyrmion phase, as in Fig. 9e. Therefore, in the first case, the chirality of the skyrmions is fixed by the underlying lattice itself. This indicates that the elongation direction is not influenced by the direction of the temporary in-plane field or the temperature in our case. Furthermore, in a different part of the lamella, we even observe what appears to be a topologically trivial bubble-like object that is the combination of a skyrmion and an antiskyrmion as highlighted using the yellow arrow mark (Fig. 7i) at the perpendicular direction.

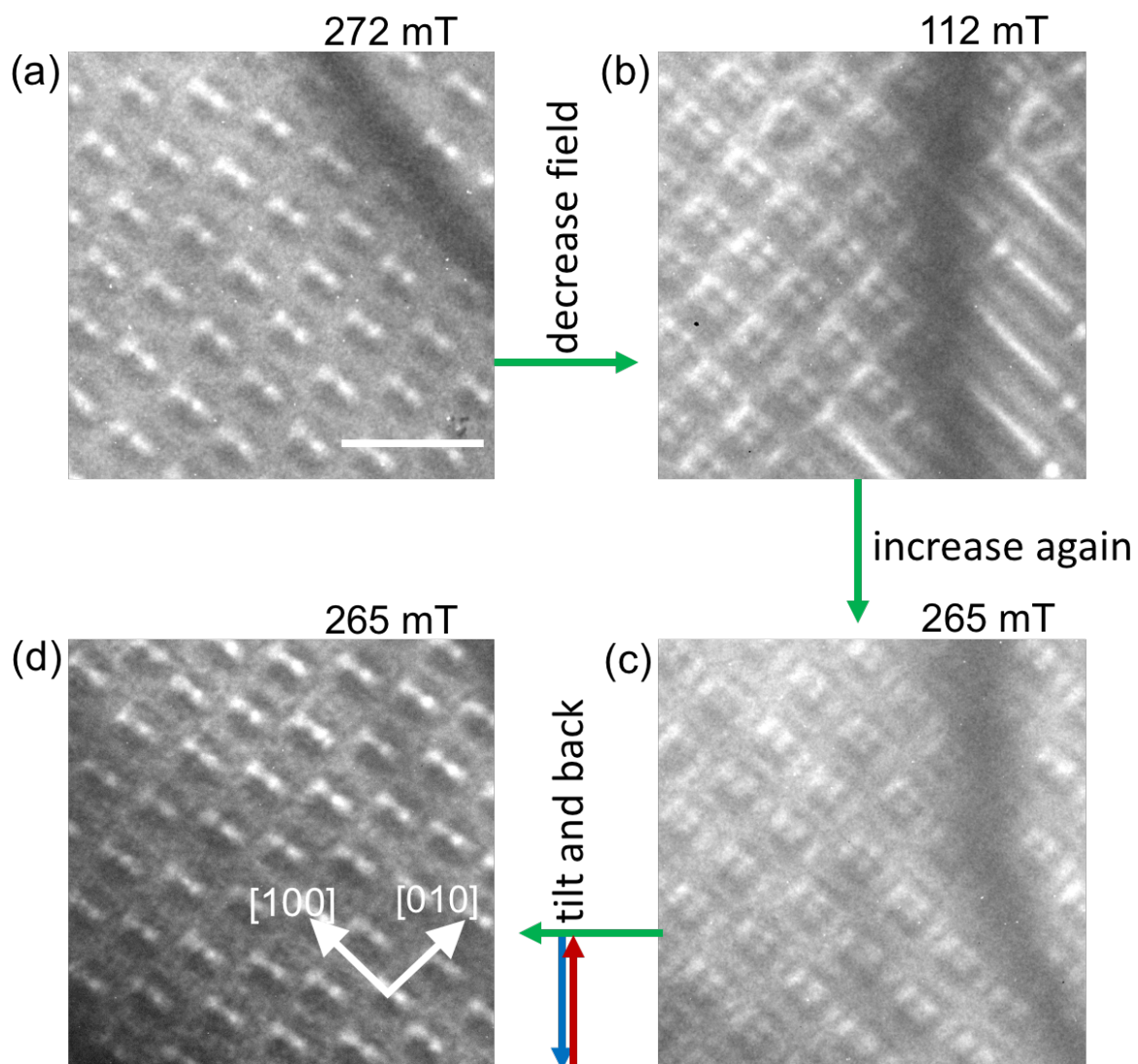


Figure 8 | Round and square shaped antiskyrmions switching. In (a), a lattice of round antiskyrmions is stabilized along the [001] zone-axis after temporarily applying an in-plane component of the field by tilting the specimen. Afterwards, the magnetic field is decreased without in-plane component of field and the texture transforms to a square-shaped antiskyrmion lattice shown in (b). From there the field is increased again but the texture remains a lattice of square-shaped antiskyrmions as shown in (c). At the same out-of-plane magnetic, a transformation from square to round skyrmion shown after temporarily providing an in-plane field (indicated by blue and red arrow), shown in (d). The scale bar in (a) corresponds to 400 nm.

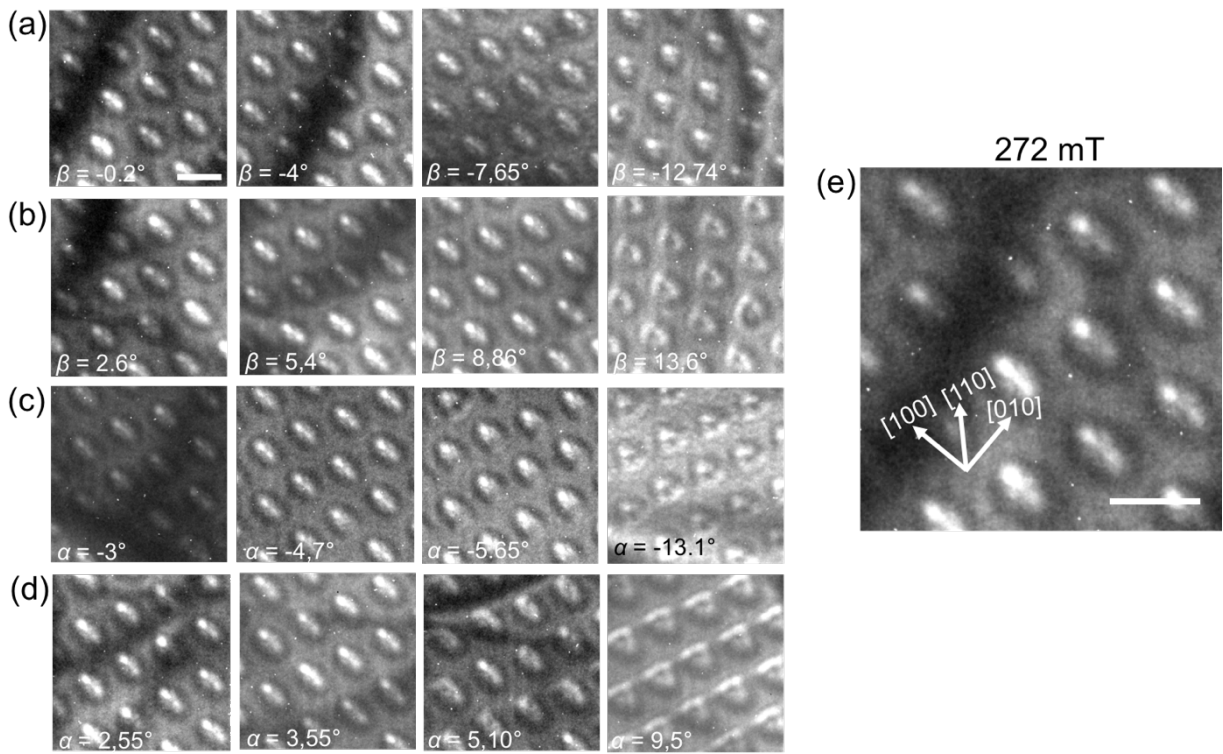


Figure 9 | Effect of tilting (*in-plane component of field*) on elliptical skyrmions. The LTEM images are acquired at 150 K and fixed out-of-plane magnetic field 272 mT. In, (a), (b), (c) and (d) we start from the skyrmion lattice state and tilt the lamella along α and β that correspond to the four different $\{11\}$ directions. Each time we start from the elliptical skyrmion lattice state, tilt the lamella, recorded LTEM contrast at different tilting angles and return back to initial position. On returning back to initial position, each time we get back the same elliptical skyrmion lattice state like (e). The scale bars correspond to 100 nm.

4.3.6 Simultaneous existence of elliptical skyrmions and antiskyrmions

The intermediate temperature region between the observed antiskyrmion and elliptical skyrmion is also examined to find out their critical behavior using this protocol. As discussed above, antiskyrmions are observed near room temperature and elliptical skyrmions at 250 K and below. The experiment is carried out at 268 K to see the possible co-existence of both nano-objects. The simultaneous existence of skyrmions in an elliptical form and antiskyrmion in a round and square shapes (depending on higher or lower field) is observed. The observation indicates that both nano-objects have comparable energy at this temperature

with a presumably decreased energy barrier. The round antiskyrmions at elevated magnetic field strengths (336 mT, Fig. 10a) and square antiskyrmions at low fields (48 mT, Fig. 10b) are observed as in agreement with the room temperature measurement and for both those field strengths, elliptical-skyrmions are also present, whose size increases when the field is decreased.

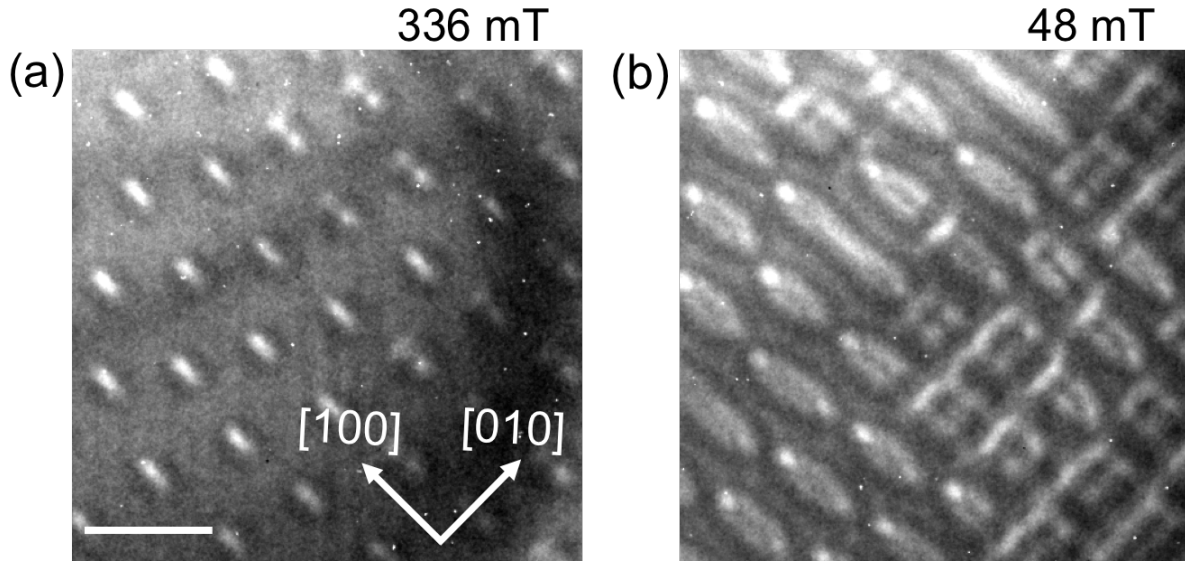


Figure 10 | Co-existence of antiskyrmions and elliptical-skyrmions. Near a transition temperature of 268 K, both topologically protected distinct nano-objects are found simultaneously. We observed round antiskyrmions at elevated magnetic field strengths (336 mT, (a)) and square antiskyrmions at low fields (48 mT, (b)). At both field strengths elliptical-skyrmions are present, whose size increases when the field is decreased. The scale bar corresponds to 300 nm.

Recently, different individual spin textures of circular Bloch skyrmions and trivial chiral bobbles (topological charge zero) near the boundary edge in the B20 compound of FeGe have also been observed⁵⁴. However, their simultaneous stability is possible only after overcoming a certain thickness larger than the equilibrium spin spiral period ($L_D = 4\frac{\pi A}{D}$, A is exchange stiffness and D is DMI constant for B20 compounds) and realized only at low temperatures. Interestingly in the D_{2d} case, the spin spiral period not only depends on the exchange stiffness and DMI constant, but dipole-dipole interactions also play an important role. As a result, the spin spiral period increases with the increasing thickness (see Ch.2, Fig. 3). In this D_{2d} symmetry compound, $Mn_{1.4}Pt_{0.9}Pd_{0.1}Sn$, the observation of both non-trivial objects is not

restricted to the thickness of the lamellae (as given here for ~ 170 nm and 280 nm) and found throughout the whole extended thickness regime. Interestingly, at room temperature, depending on the in-plane field history (see Ch. 5), we have also shown the simultaneous observation of antiskyrmions and elliptical skyrmions. Our result may help in overcoming the problem of drifting due to thermally fluctuation, the high-cost fabrication of artificial pinning centers (to move skyrmion along the track) for single type of skyrmion hosting compounds and may also lead to the straight-line movement of the nano-objects spin texture in D_{2d} compound due to the opposite Magnus force arising from opposite topological charges. The necessity of maintaining the defined distance can resolve on encoding the skyrmions and antiskyrmions as data bit carriers. Hence, this experimental realization of both topological nano-objects may lead to further development in racetrack memory or magnetic solid-state devices.

4.3.7 Magnetic phase diagram

The trivial helix phase is a dominating state in the absence of an in-plane magnetic field component. Upon application of a temporary in-plane field components, the nontrivial phases emerge in sparse or lattice form depending on the field-temperature history. This makes D_{2d} systems fundamentally unique. It is to be noted that, though theoretical studies report various possible topological spin textures^{90, 91} in frustrated systems without DMI, no experimental evidence has been observed yet.

The metastability of antiskyrmions in both round and square shape, elliptically deformed Bloch skyrmions and two different chiralities for them arise from the anisotropic DMI reported here. The anisotropic DMI favors the antiskyrmions stabilization, while the dipole-dipole interactions prefer Bloch-type elliptical skyrmions. A temperature vs. magnetic field contour plot of the phase diagram is constructed from the observed magnetic textures that are formed here is five categories: helical phase, round and square antiskyrmions, elliptical Bloch skyrmion, and field polarized state as indicated by the symbols shown in the Fig. 11. A mixed phase is shown by the corresponding symbol with an appropriately colored edge. The density of skyrmionic and antiskyrmionic nano-objects is shown as a contour plot in the background. The phase diagram in Fig. 11 corresponds to a ~ 170 nm thick lamella with a temporary tilted-field protocol for the lattice stabilization as follows: at a given temperature, the magnetic field is decreased, starting from the field-polarized state in steps of a few mT. The specimen is then tilted $\sim 40^\circ$ away from the perpendicular zone-axis direction followed by tilting back to the initial position, and the LTEM image is taken. Once a dense array of nano-objects is observed, the magnetic field is subsequently decreased without any need for in-plane field

components via tilting. In the present protocol, elliptical skyrmion stabilized at low temperatures (250 K and below) and round and square-shaped antiskyrmions near and above room temperatures. The co-existence of antiskyrmion and elliptical skyrmion is observed at a critical temperature of ~ 268 K. It is to be noted that the existence of elliptical Bloch skyrmion and antiskyrmion is an unanticipated experimental finding in the skyrmion field.

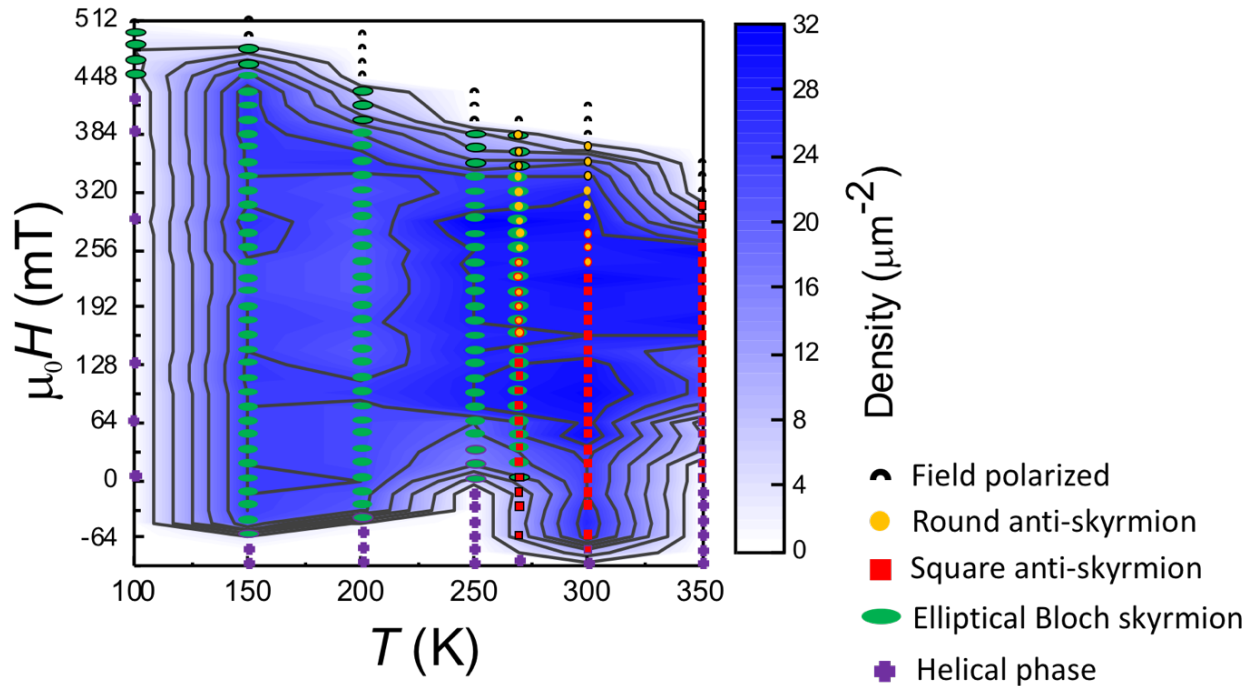


Figure 11 | Magnetic phase diagram. The magnetic phase diagram for ~ 170 nm thick specimen. The phase diagram comprises of elliptical Bloch skyrmions (250 K and below), antiskyrmions (near and above 300 K) and their simultaneous existence (268 K) of a D_{2d} inverse tetragonal Heusler compound $\text{Mn}_{1.4}\text{Pt}_{0.9}\text{Pd}_{0.1}\text{Sn}$.

4.4 Summary

In conclusion, for the first time, the co-existence of elliptical Bloch skyrmions and antiskyrmions in a single material system is found. The antiskyrmions are found in two varieties, square and round form, which can be switched reversibly. The three types of spin textures can be found as individual objects in the form of an isolated state. The lattices of elliptical-skyrmions and square-shaped antiskyrmions are observed over a wide range of

temperatures, even in zero magnetic field. It is shown that the elliptical-skyrmions are stabilized by long-range dipole-dipole interactions, which via an interplay with the anisotropic DMI in this D_{2d} system, leads to their elongation along the [100] or [010] directions, namely the propagation direction of the ground state helical phase. Besides this, elliptical Bloch skyrmions with opposite chiralities are observed whose long axis is oriented along two specific in-plane crystal directions: [010] and [100]. This makes elliptical skyrmions distinctly different from the cylindrically symmetric DMI-stabilized Bloch skyrmions in B20 materials. For the latter case, dipole-dipole interactions reinforce the DMI to favor circular skyrmions, without leading to the possibility of creation of distinct topologies, as observed here in a D_{2d} material. The novel finding of magnetic non-collinear chiral spin textures with opposite topological charges of ± 1 and their simultaneous existence in $\text{Mn}_{1.4}\text{Pt}_{0.9}\text{Pd}_{0.1}\text{Sn}$ shows that D_{2d} materials can have more excellent functionalities as compared to, for example, B20 materials. One can anticipate that their magnetization dynamics may also show greater complexity with the eventual possibility of switching between different topological textures. Additionally, the simultaneous formation of both skyrmion and antiskyrmion at a particular temperature can be used as different data bits in memory and logic devices.

5 Evolution and competition between chiral spin textures in nano-stripes

5.1 Introduction

The observation of non-collinear magnetic nano-objects has brought a revolution in the material science towards fundamental and technological applications such as magnetic racetrack data storage. These magnetic nano-objects can be written, read, moved, and deleted on an array of quasi one-dimensional nano-stripes^{5, 7}. As the carriers of information, the use of topologically protected nano-objects like skyrmions²⁰ or antiskyrmions^{51, 124} is highly anticipated^{7, 73, 125-127} in racetrack and neuromorphic devices. However, due to their topological charge, skyrmion may become pinned or annihilate on experiencing a deflection along a transverse direction^{80, 128, 129} towards the edge of the racetrack. This is called skyrmion Hall effect. It happens because of the rotational symmetry of the skyrmion and is present irrespective of the current orientation^{130, 131} due to the intrinsic Dzyaloshinskii-Moriya interaction (DMI)^{1, 2, 132} which arises from a broken inversion symmetry. Contrary, it is not the case in materials that have a D_{2d} symmetry and magnetic point group $\bar{4}2m$. For example, in the $Mn_{1.4}Pt_{0.9}Pd_{0.1}Sn$ compound, Pt atoms located above and below the Mn layers differently along the [100], and [010] direction gives rise to anisotropic DMI. Thus, the ground state helices spin textures in these materials always orient exactly along two high symmetry directions; [100] and [010]. On providing magnetic fields, antiskyrmions are formed that are only rotational invariant after a 180° rotation^{4, 132}. It implies that the anisotropic spin texture of antiskyrmions should behave

differently under applied currents along different crystallographic directions. This observation is also reported using a micromagnetic simulation study carried out by Huang *et al.*⁸⁴. Interestingly, the Hall effect (antiskyrmion Hall effect) can even be eliminated for this special nano-object along a specific direction of current application (depending on the magnetization profile). The complete abolition of transverse deflection of antiskyrmion motion to the applied current makes it interesting for potential applications in memory devices. Consequently, it is necessary to fabricate nano-tracks along different crystallographic directions and to investigate the properties of differently oriented antiskyrmions formation.

In Ch. 4, it was shown that dipole-dipole interactions play an important role in this D_{2d} inverse Heusler compound and stabilizes elongated Bloch skyrmion, a distinct topological spin texture than antiskyrmion. This extra energy term adds another advantage to this system with an anisotropic DMI because it allows for a simultaneous presence of elliptically elongated skyrmions and antiskyrmions^{133, 134}. Since both nano-objects are metastable, instead of considering the presence and absence of single kind nano-object in conventional skyrmion cases, here ‘0’ and ‘1’ bits could be encoded by referring a sequence of skyrmions and antiskyrmions⁸ which are anticipated to be read out distinctly in a racetrack and logic gate. This new possible concept of magnetic memory device should be less susceptible to diffusion and interactions between the topological objects that would be significant in conventional racetracks^{8, 54, 135}.

Single-crystalline [001] zone-axis oriented nano-stripes of different width were prepared from $Mn_{1.4}Pt_{0.9}Pd_{0.1}Sn$ along different crystallographic directions from a bulk single crystalline grain of polycrystalline sample. These nano-stripes were lifted out from the tetragonal basal plane along different crystallographic directions: [010] and different degrees of angles to [010]. The room-temperature stability and formation of single- and double-chains of magnetic nano-objects are studied in multiple geometries having widths ranging from ~ 0.35 to $0.5 \mu m$.

Investigation of antiskyrmion nucleation in different reliable ways and differently oriented helices along the edge of the nano-stripes are discussed. An increased ease of the formation of nano-objects is found due to the confinement. It also allows for the creation of antiskyrmions without the need of ‘temporal’ in-plane magnetic fields via tilting that were needed in the case of extended lamellae as discussed in the previous chapter^{51, 124, 133}. Interestingly, a single chain of these objects is located in the middle of the nano-stripes even when the stripe width is much more than the size of antiskyrmions. Furthermore, the co-existence of antiskyrmions and elliptically elongated skyrmions of opposite chiralities under

certain conditions are observed, which will be very promising for improving the reliability of magnetic racetrack devices. This work provides the details of the nucleation of isolated, single chain, and double chain formation of topological spin textures and taking a step further in the realization of advanced version magnetic logic gates and racetrack memory devices.

5.2 Methods

5.2.1 Experimental details

The nano-stripes lamellae were prepared from a single-crystalline grain of the polycrystalline bulk sample $\text{Mn}_{1.4}\text{Pt}_{0.9}\text{Pd}_{0.1}\text{Sn}$ using a dual beam system containing a focused ion beam (FIB, Ga^+ ion source) and a scanning electron microscope (SEM). Fig. 1a shows the nanowire thinned down sample (mark in green rectangle) whose outer sides are covered totally by PtC_x using GIS. It is to be noted that embedded PtC_x on both sides of a nano-stripe also helps to reduce Fresnel fringing effects near the boundaries of the lamella significantly which eventually allows for a better LTEM contrast^{75, 122, 136}. In this chapter, lamellae named as NS 1, NS 2, NS 3, NS 4, NS 5 are used. The [001] zone-axis of the nano-stripes are confirmed by selected area electron diffraction (SAED). The defocus value used in the LTEM measurement is $\sim 1.1 - 1.2$ nm.

5.2.2 Micromagnetic simulations

The interpretations of the experimental results are supported by the simulations using Mumax3. In micromagnetic simulations, the value of M_s has been taken from the experiments while all other parameters have been chosen such that the output of simulations is similar to that of experiments. The determination of these parameters is not as straight-forward as in skyrmion hosts system, like in B20 materials, because dipole-dipole interactions play a much more important role in the present material class. The following parameters are taken: the saturation magnetization $M_s = 445 \times \text{Am}^{-1}$, the exchange interaction $A_{\text{ex}} = 0.5 \times 10^{-10} \text{Jm}^{-1}$, the DMI constant $D = 0.003 \text{Jm}^{-2}$, and the anisotropy constant $K_u = 135 \text{KJm}^{-3}$. The value of exchange interaction and anisotropy constants are reduced as compared to the parameters in Ch.4 to fit better with the experimental results. Compared to the initial publication⁵¹, exchange and DMI are now both decreased which essentially means that the significance of the dipole-dipole interactions is increased. Moreover, the simulations also show nano-objects of similar dimensions as in experiments. The periodic boundary conditions are applied along the track in all simulations. The simulated thickness is 150 nm, the length is 4200 nm, and the width is

either 400 nm or 600 nm. In most cases, only half of the simulated length is shown in the figures expect for Fig. 6, where a finer grid of $2.5 \text{ nm} \times 2.5 \text{ nm} \times 10 \text{ nm}$ was used to reproduce the experimental result, the magnetization density for the micromagnetic result was discretized in $10 \text{ nm} \times 10 \text{ nm} \times 10 \text{ nm}$ cells. The direction of the moment within each cell is represented by color code. The following color code has been used throughout the micromagnetic simulation: $-Z$ ($+Z$) direction is shown in white (black) and hue colors represent in-plane moments.

5.3 Result and discussion

5.3.1 Nano-stripes along different crystallographic directions

Our motivation is to investigate skyrmionics spin textures, whose long axes ($[100]/[010]$) are oriented along different angles with respect to the boundary of nano-stripes. Fig. 1b shows an example of surface parallel lifting method, where two nano-stripes have been lifted out of the $[001]$ grain (red color area of the EBSD map) bulk sample. Fig. 1c and 1g are SEM overviews of two nano-stripes that are differently oriented. TEM images of the same stripes are shown in Fig. 1d and 1h. Due to the affirmative anisotropic DMI, the ground-state helices are always oriented along the family of $\{10\}$ (i.e. $[100]$ and $[010]$) directions. Since the helices propagation always tie with the crystallographic directions, the orientation of the helix axes to the nano-stripe depends on the stripe orientation. For this reason, in a $[100]$ or $[010]$ oriented nano-stripe (NS 1), the orientation of the helix axis with respect to the stripe direction, ϕ , can be 0° or 90° or both simultaneously (Fig. 1e) whereas, in a $[110]$ or $[\bar{1}10]$ oriented nano-stripes (NS 2), $\phi = \pm 45^\circ$ as shown in Fig. 1i.

As discussed before, the magnetic texture profile of antiskyrmion along the $[100]$ or $[010]$ directions correspond to a right-handed and left-handed Bloch walls (indicated by the orange lines in Fig. 1k). The Bloch parts give rise to bright and dark spots (corresponds to opposite helicity) in LTEM contrast of an antiskyrmion along the $[100]$ and $[010]$ directions. The white lobes in Fig. 1f is $\sim 45^\circ$ with respect to the antiskyrmions' centers in Fig. 1j, which indicates that these are rotated while comparing both nano-stripes. In the following sections, antiskyrmions in confined nano-stripes will be analyzed in more detail. Similar to the experiment, the qualitative result of micromagnetic simulations in Fig. 1l and 1m shows chain of antiskyrmions in two different nano-stripes whose Bloch parts are indeed always along the family of $\{10\}$ directions.

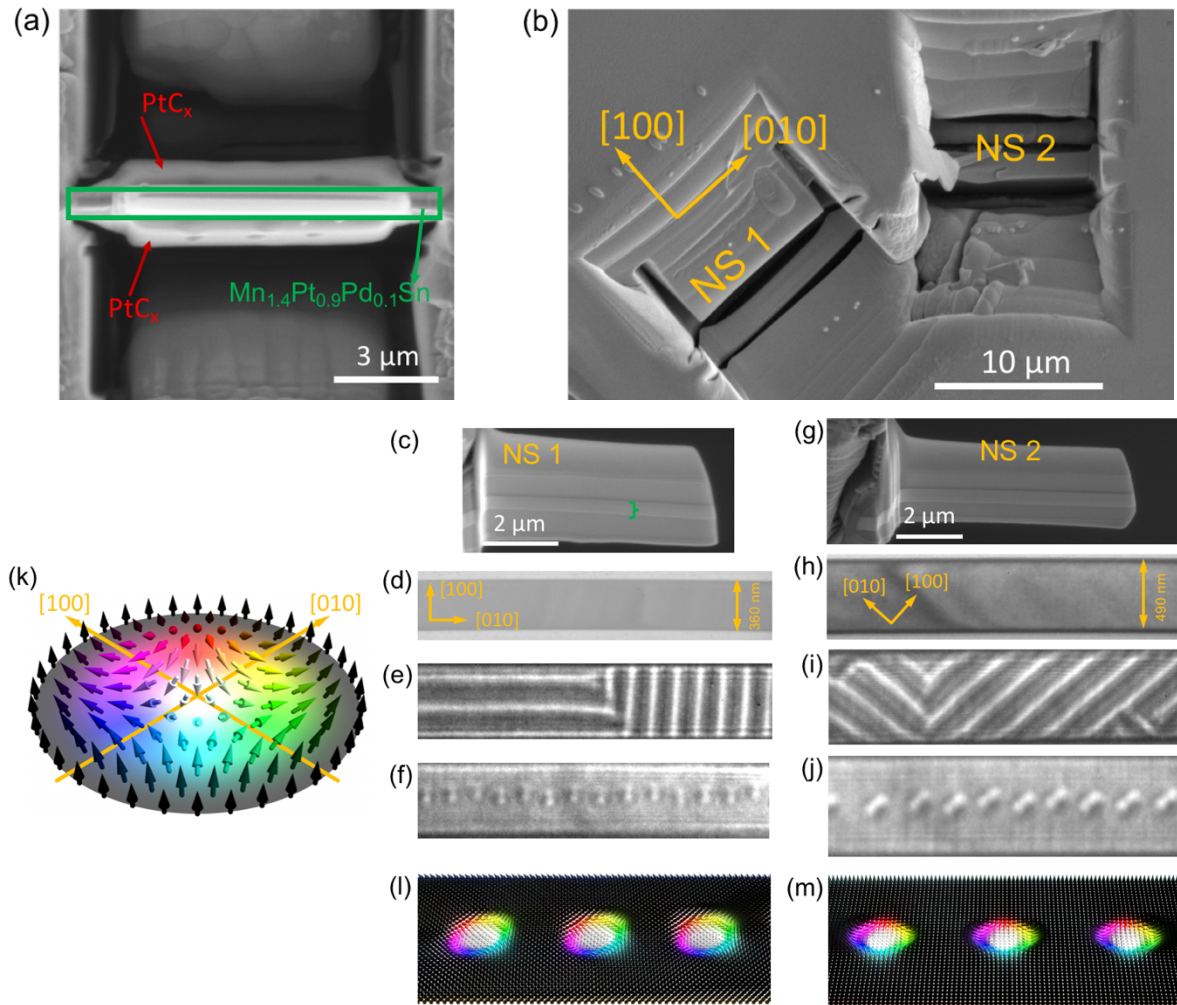


Figure 1 | Fabrication and Spin textures in oriented nano-strips. (a) SEM image of the thinned down region of $\text{Mn}_{1.4}\text{Pt}_{0.9}\text{Pd}_{0.1}\text{Sn}$ (marked by green rectangle) and the PtC_x deposited around the surrounding region. (b) SEM image of the host compound after lifted out (by FIB) the $[010]$ and $[\bar{1}10]$ oriented stripes (NS 1 and NS 2). (c-f) and (g-j) are SEM, bright field TEM, LTEM images for the portions of $[010]$ and $[\bar{1}10]$ oriented cut nano-strips, respectively that were fabricated from (b). The width and crystallographic axes of the nano-strips are indicated in the bright field TEM images. (e), (i) Lorentz TEM images of the magnetic texture at zero field in the two nano-strips that show the formation of helices whose Q-vectors are oriented along the $[100]$ and $[010]$ directions, in both cases. (k) The schematic representation of a magnetic antiskyrmion, where the color encodes the orientation of the magnetic moments. (f), (j) LTEM images of antiskyrmion chains measured in magnetic fields of 187 and 273 mT, respectively. The field is oriented perpendicular to the plane of the nano-strips. (l), (m) Micromagnetic simulations of the spin textures in nano-strips with orientations corresponding to those in (f) and (j), respectively. The color code represents the direction of the moment within each cell used in the simulation.

5.3.2 Helices and antiskyrmions in [010] oriented nano-stripes

The detailed analysis of the magnetic texture with a nano-stripe (NS 1) that was cut along the [010] direction is presented below. This stripe has a thickness of 120 nm and a 360 nm width.

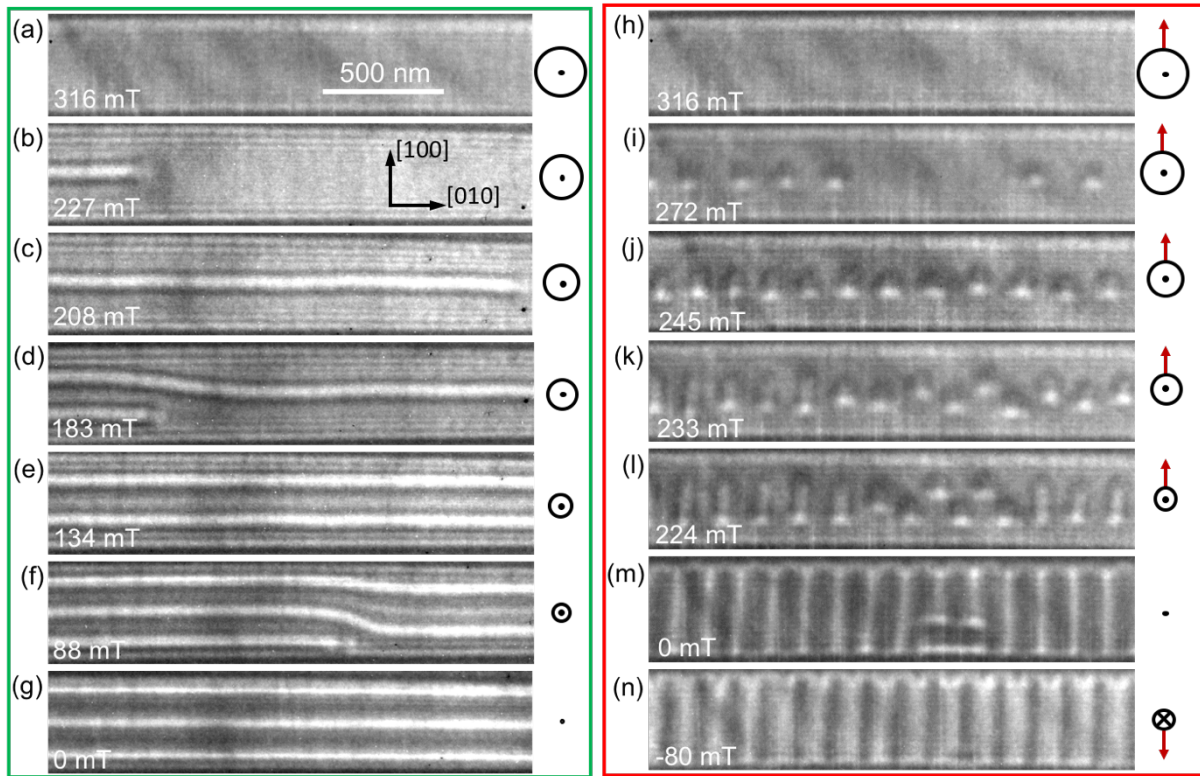


Figure 2 | Helix formation upon decreasing the magnetic field. (a) In the left side column, the magnetic field is decreased starting from polarized phase at 316 mT. (b-c) Generation of single, (d-e) second and (f-g) third helix segments. In the right column, the magnetic field is decreased under constant tilting of the specimen by $\sim 21^\circ$ and the LTEM contrasts are recorded in that tilting condition. (h) The starting configuration is again the field polarized phase at 316 mT. (i) 272 mT: non-collinear spin textures as sparse form is already found here. (j) More of those nano-objects have formed at 245 mT and the chain is rather periodic. (k) 233 mT: they start to elongate along the [100] direction (perpendicular to the nano-track direction). (l) A mixed state has formed at 224 mT. (m) At zero field, the magnetic texture is not perfectly ordered. (n) At small negative fields, a periodic helical state is formed. Using this tilted field procedure, the helical segments are oriented along the [100] direction rather than [010].

We start from the polarized state (no magnetic contrast) configuration as shown in Fig. 2a. Decreasing the perpendicularly applied magnetic field leads to the nucleation of a helices with a propagation wave vector (Q-vector) perpendicular to the nano-stripe direction without forming any non-trivial state. In the absence of external magnetic field, the helix in a D_{2d} material $Mn_{1.4}Pt_{0.9}Pd_{0.1}Sn$ changes harmonically along the Q-vector. On applying magnetic field, the helical period changes and even higher fields it gets distorted. As a result of which, there are collinear ferromagnetic regions between individual segments of the helix that are reported in Ch. 4¹³³. In the current nano-stripes, the helix segments cannot be displaced from each other due to the confined geometry. It requires a different annihilation and creation mechanism which can be described as follows. Starting from the polarized phase (316 mT) at 227 mT, Fig. 2b, a first helix segment emerges that permeates the whole visible region upon further decreasing the field to 208 mT (Fig. 2c). Across this segment, the magnetization changes by 360° , such as parallel to the field direction at the edges and opposite at the center. The helix formation process is repeated with a second helix segment shown at 183 mT in Fig. 2d and at 134 mT (Fig. 2e), the whole region is filled with two helices. Later, a third helix segment is generated as shown in Fig. 2f, and three helices are formed in the absence of magnetic field (Fig. 2g). Similar to the extended lamellae, the ratio of the area filled with helix segments over the ferromagnetic area is correlated to the applied magnetic field¹³³. However, due to the confinement in the given small width region of nano-stripe, individual helix segments are created or annihilated upon changing the field.

In an extended thin lamella, the propagation vector of the helices along the [010] and [100] directions are energetically equivalent. In a confined geometry like this, the former state is less preferable as a ground state. Since the edge of the non-collinear helix segments cost energy, a larger number of short helix segments has a higher energy than a small number of long helix segments. However, this behavior changes when the perpendicular field is decreased upon tilting the specimen as shown in Fig. 2h-2n. Similar to the earlier studies, providing in-plane magnetic field components favor the generation of nano-objects over helices as the energy barrier between these phases is decreased. At a perpendicular field of 245 mT along the microscope column (when the specimen is tilted by 21° as shown in Fig. 2j) a periodic chain of trivial bubble kind nano-objects have formed⁵¹. At the same tilt angle, the number of these nano structures increases further with decreasing field. A partially zig-zag pattern of the nano-objects due to limited space in the nano-stripe is found (Fig. 2k). However, in this measurement a dense zig-zag chain did not arise. Rather, these distorted shape nano-objects start to elongate

towards the edge on further decreased field (Fig. 2k and 2l). Due to the limited space along the nano-stripe and the application of in-plane component of field, the elongation prefers to be along the perpendicular direction [100] (see Fig. 2l). Slightly below zero field (-80 mT), all the leftover distorted and elongated nano-structures have turned into a short helix segments of Q-vector along [010] and a harmonic periodic state has formed as shown Fig. 2n. This shows that in nano-stripes the helix segments can orient using in-plane field component and magnetic textures in the D_{2d} compound is strongly dependent on the field history.

Fig. 3 shows the three different starting configurations (Fig. 3a, 3h and 3o) of magnetic textures and their behavior upon increasing the magnetic field. In Fig. 3a, the helical Q-vector is along the [100] direction of the nano-stripe similar to Fig. 2g. While increasing the field from the starting configuration, the longer helix segments shrink and disappear one after another (Fig. 3b-f), roughly the reversal behavior of the decreasing field of Fig. 2a-g. The starting configuration in Fig. 3h consists of helical Q-vector along the [010] direction. The shorter helix segments are perpendicular to the nano-stripe boundary and upon increasing field they shrink (Fig. 3h-i) until a periodic chain of nano-objects is formed at 187 mT (Fig. 3j). Since, those LTEM contrast are imaged along the perpendicular zone-axis without tilting, those are antiskyrmion chain, unlike the distorted antiskyrmion. These antiskyrmion exist up to the 200 mT. The nano-objects vanish one after another on further increasing the magnetic field (Fig. 3l). The ferromagnetic state is achieved at 225 mT (Fig. 3m). Note that in particular image of Fig. 3l, it is difficult to tell the exact texture of these individual objects due to their small size. Importantly, it is notable that this time antiskyrmions form anyway in the absence an in-plane field component.

The nucleation of antiskyrmions in the absence of in-plane fields was not found in extended lamellae so far, thus, pointing towards an increased ease of antiskyrmions in the confined geometries of D_{2d} system. The antiskyrmions formation on shrinking the helix segments with increasing magnetic field is directly related to the confinement and there is a one-to-one correspondence for the case of vertically oriented shorter helix segments (Fig. 3h-3k). It is plausible that horizontally oriented longer helix segments also shrink to single antiskyrmions. However, on increasing the field, the near boundary helices regions are trying to push the interior of the stripe and transforming sector of the track to two and then one helix before forming any antiskyrmions. Nevertheless, in a perfect stripe, only three longer helix segments fill the whole region, the resulting antiskyrmion number is vanishingly small in this arrangement and no antiskyrmions are found in this visible region as shown in Fig. 3a-f.

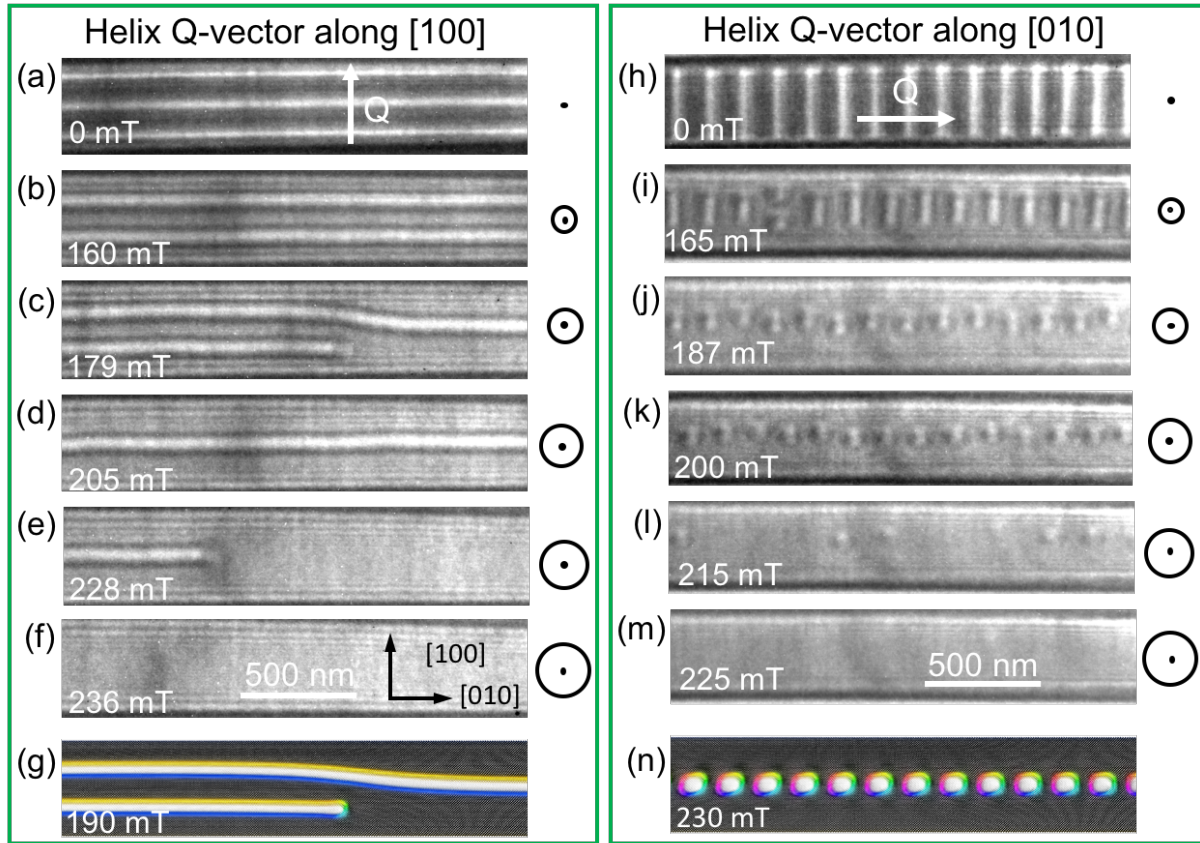


Figure 3 | Antiskyrmion formation upon increasing the magnetic field. (a) The starting configuration is a helical phase with helix segments along [010]. (b-f) upon increasing the magnetic field, the three individual segments shrink and disappear one after another as indicated. In (h), the helix segments are initially oriented along the narrow width of the nano-stripe ([100] direction). (i) They shrink and formed truncated helices. (j-k) The truncated helices transform to antiskyrmion at 187 mT and sustain up to 200 mT. (l) Further higher field at 215 mT, the antiskyrmions annihilate. (m) 225 mT: the ferromagnetic phase is restored. (g), (n) The micromagnetic simulations result is showing the exemplarily metastability of horizontal helix segments and a chain of antiskyrmions respectively.

Now, we repeat our experiment from the mixed helical configuration of both shorter and longer helix segments at 0 mT. It will be particularly interesting since it might reveal more about the interaction among helix segments and antiskyrmions. The starting configuration consists of Q-vector along both directions: [100] and [010] as shown in Fig. 4a. The nano-track is filled with vertical (shorter) segments on the right side, one horizontal (longer) helix segment

that extended throughout the nano-stripe and two horizontal segments on the left side. Upon increasing the magnetic field to 158 mT as shown in Fig. 4b, the vertical helix segments begin to shrink and the bottom horizontal helix moves away from the boundary edge while one of the upper horizontal segments disappears. When the field is further increased to 236 mT (Fig. 4c),

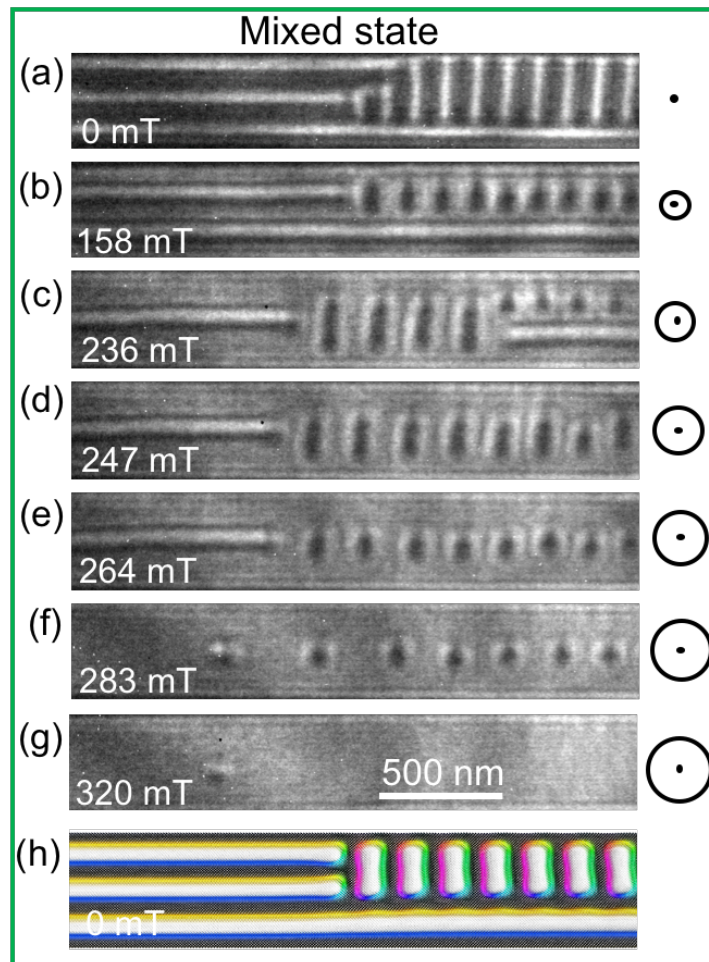


Figure 4 | Antiskyrmion formation from a mixed helical state. (a) The initial configuration is a mixed helical state with Q-vectors propagate along [100] and [010]. (b) 158 mT: the helix segments in both directions shrink. (c) The interaction of them leads to segments of different sizes along [100] at 236 mT. (d) 247 mT: the smaller vertical segments expand upon the disappearance of the helix segment at the bottom right edge. (e) 264 mT: the vertical truncated helices transform to antiskyrmion and the longer horizontal segment at 283 mT (f). (g) A single antiskyrmion is left at 320 mT. (h) The micromagnetic simulations is showing a mixture of horizontal and vertical helix segments respectively.

the long horizontal helix segment shrinks and is visible only on the right side of the stripe region and the other horizontal helix on the left moves toward the middle of the track. Consequently, the vertically oriented segments in the middle can elongate again, and the remaining vertical helix segments in the right side shrink. In Fig. 4d at 247 mT, the right horizontal helix disappears so that remaining vertical helix segments on that side get elongated. Also, the vertical helices are displaced towards the left on shrinking horizontal helices. At 264 mT, the vertical segments form antiskyrmions and the left side horizontal segment is still present (Fig. 4e). In Fig. 4f, one horizontal segment shrinks and forms antiskyrmions at 283 mT. The antiskyrmion formed from the horizontal segment appear up to 320 mT (Fig. 4g) before reaching near the transition to the ferromagnetic phase. The LTEM contrast of antiskyrmion in Fig. 4f is different than in Fig. 3j since they are imaged in under and over-focused, respectively. It is noticeable in Fig. 3h to 3k and from 4a to 4g that the magnetic field value required for antiskyrmion formation is different. It may be due to different initial helix segments configuration (see Fig. 3h and 4a) in the same confined geometry. Reminiscent of the initial helix orientation, a small deformation is still present for the antiskyrmions in this LTEM image (see image at 283 mT, Fig. 4f). The left side antiskyrmion has a notably different contrast, indicating elongation along the racetrack, while the others formed from the vertical segments are slightly elongated along the perpendicular direction. Moreover, this kind of special shrinking and expansion mechanism (of vertical helices) is not noticed in the nano-stripes of skyrmion host compounds, before.

Similar to the experimental observations, the micromagnetic simulation in Fig. 3g shows the stability of two longer helices: one helix extended in the whole region and another bottom helix starts in the middle of the shown frame. The right part of longer helix segment is located in the middle of the track but is shifted to the top in the left half where the second helix segment is present as shown in Fig. 3c. In Fig. 3n, a chain of antiskyrmions is presented from a micromagnetic configuration similar to Fig. 3h that reproduced the experimental findings as Fig. 3j. The metastability of a mixed helical phase is shown in Fig. 4h. These simulations were each initialized with a different analytically constructed magnetization density that was relaxed for at least 1 ns. What is important to observe here is that the upper and lower edges of the helix segments in Fig. 4h look exactly the same as the upper and lower half of the antiskyrmions in Fig. 3n having same in-plane configuration of red-orange-yellow-green color code, meaning that both objects are topologically equivalent (the middle part of the helix segment in Fig. 4h is

topologically trivial). It implies that the short helices at zero-field are still topologically non-trivial and in higher magnetic field they transformed to antiskyrmion via the truncated helices. Therefore, the helix edges always exhibit the profile of half an antiskyrmion, owing to the anisotropic DMI. So, both edge parts of a helix segment have a topological charge of $\frac{1}{2}$ each. Hence, short helix segments or a low field truncated individual helix segment can be considered an “elongated antiskyrmion”.

5.3.3 Difference between Helices and other domains in D_{2d} system

In the previous section, we have shown the formation of antiskyrmions from helical arrangements in a [001] zone-axis. Furthermore, if the field is decreased in an uncontrolled manner, e.g. by turning off/on instantly or ramping the field from ferromagnetic state, the resulting zero-field configuration consists of several form of helix arrangement oriented along the [100] or [010] directions. Those kinds of configuration are also shown on a different stripe (NS 3) whose left portion has [001] zone-axis oriented and right part is [100] zone-axis oriented. The zone axes are confirmed from selected area diffraction pattern measurement as shown in Fig. 5a and 5b. Upon turning off/on instantly, several configurations of helical vector propagation are formed on [001] zone-axis region, whereas the large size domains on [100] zone-axis are always oriented along the vertical direction with respect to edge (Fig. 5c-g). It is noted here that; right side domains are not helices as DMI in D_{2d} system enforces helices only within the tetragonal basal plane ([001] zone-axis). However, the domain on [100] zone-axis results are consistence with the domain structures found in a confined geometry of Ni wires¹³⁷ and other magnetic systems¹³⁸⁻¹⁴⁰. The initial configurations in Fig. 4a and Fig. 5a are few among the several configurations, where a special kind of shrinking and expansion of vertical helices is observed upon increase out-of-plane magnetic fields. That means from Fig. 5a, similar behavior, as in Fig. 4a to 4g, will be observed. However, in [100] zone-axis, the width of the domains shrinks and disappears in higher fields. Those types of magnetic domain contrasts are visible in the D_{2d} system other than [001] oriented zone-axis (see Appendix B.1), and the domain are always oriented along a fixed direction (unlike helices propagation directions of {10}) even in extended lamellae. It provides experimental proof that helices and hence topological spin textures are stabilized only in the basal plane of the $Mn_{1.4}Pt_{0.9}Pd_{0.1}Sn$ system. It is one of the distinct features in the D_{2d} system compared to B20-type compounds²⁵.

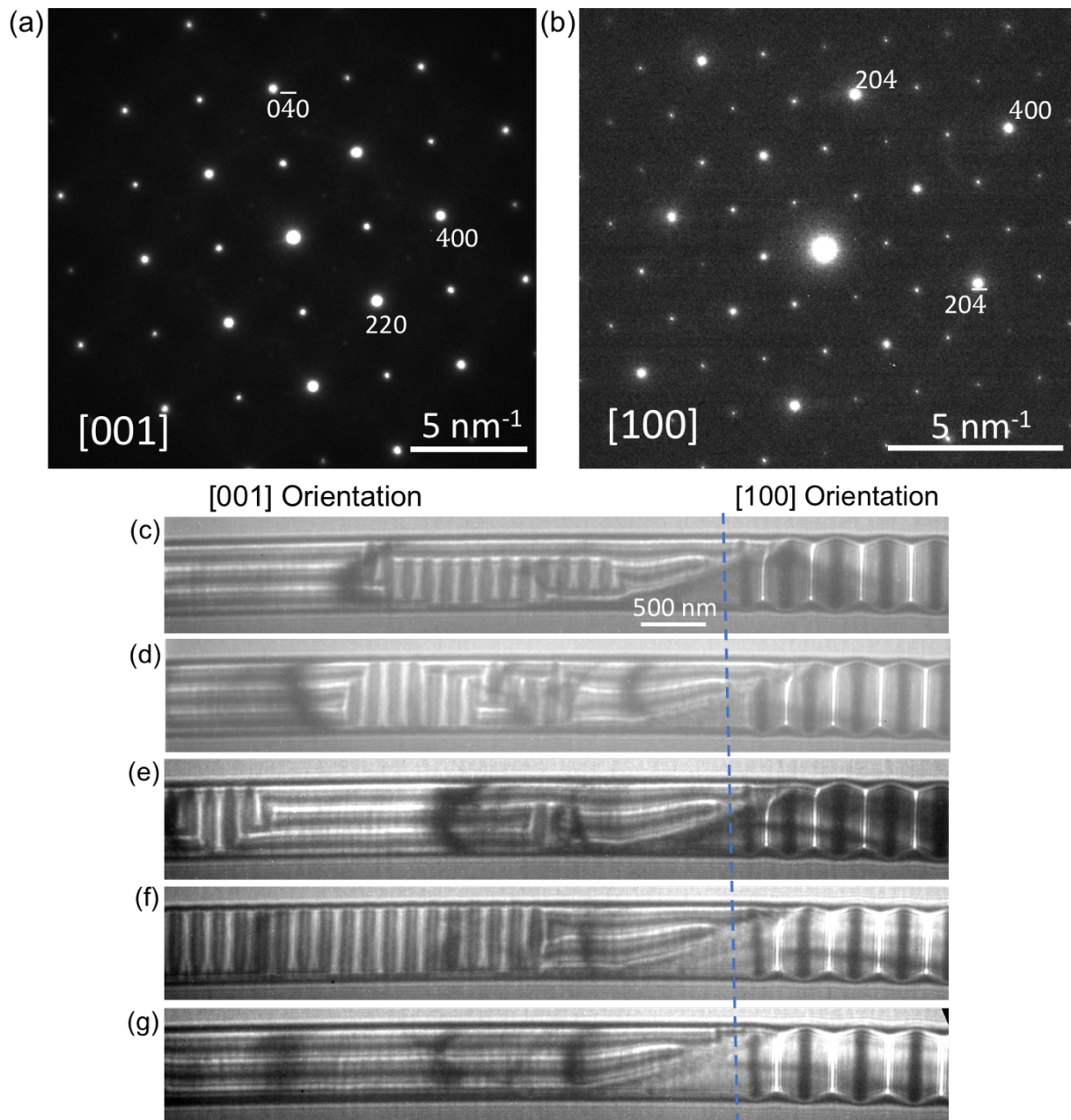


Figure 5 | Helices and magnetic domains at zero field. (a), (b) SAED patterns conform the two different orientations of [001] (left side) and [100] (right side) zone axes in a single nano-stripe. (c-g) From left to the mark line (blue color), several possible configurations of helices in a nano-stripe. The domains structure is found in the other side of this stripe. The helices in [001] zone-axis have Q-vector either parallel or perpendicular to the boundary of the stripe like shown in Fig. 3.

5.3.4 Antiskyrmion chains in differently oriented nano-stripes

In this section, the increasing (Fig. 6 and 7) and decreasing (Fig. 8) field behavior of magnetic texture with and without the application of temporary in-plane component of field are discussed on a nano-stripe (NS 4) that is oriented by $\phi \approx -28^\circ$ with respect to [100] crystallographic axis.

Here, the ground state is again a helical phase, whose helix Q-vectors are rotated by $\phi \approx -28^\circ$ compared to the helices in the stripe (NS 1) discussed above. This observation can be contrasted with B20 compounds or high anisotropy domain, where the confinement of a nano-stripe causes a strong anisotropy to the helix orientation so that they are always formed parallel or perpendicular to the boundary^{75, 136}. Here, for the nano-stripe shown in Fig. 6, 7 and 8, the helices propagation directions are not aligned parallel or perpendicular to the boundary in the D_{2d} system, instead they are tied to the crystallographic long symmetry direction. Out of two helix type, one exhibits shorter segments than the other when these pervade the whole width of the nano-stripe. Similar to the case explained for NS 1, the helical phase with the shorter (longer) segments has the higher (lower) energy as the density of the ends of the helices are decreased (increased). Therefore, the starting configuration (in Fig. 6a) consists of [100] direction helix segments that are rotated by ϕ to the nano-stripe direction. At 136 mT, the lengths of the helix segments shrink (see Fig. 6b) and antiskyrmion started to form at 187 mT (Fig. 6c). Only one segment is present at 201 mT (Fig. 6d) and at 216 mT (Fig. 6e), all the segments formed as nano-object of antiskyrmions. The bright and dark spots in the LTEM images of antiskyrmions in NS 4 are rotated by $\phi - 90^\circ$ compared to the antiskyrmions in NS 1 (Fig. 3) in agreement with the anisotropic properties of antiskyrmion. The antiskyrmions get annihilated at higher fields and only a single nano-object is left at 253 mT (Fig. 6f). The whole lamella becomes field polarized at slightly higher field value on disappearing this object.

The formation of two helical orientations domain becomes inevitable in the aforementioned confined geometry when ϕ is closer to 45° . Therefore, the behavior of the magnetic texture is examined when the starting configuration composed of a mixed helical phase with Q-vectors approximately along the [100] and [010] axes (Fig. 5u). The helix segments here do not form at an exact angle of 90° (but $\pm 4^\circ$), slightly different from helices in extended samples, probably affected by the edge interaction. Furthermore, the helix segments have relatively longer length along the [100] direction than along the [010] direction (Fig. 6g). Both types of helices shrink when the field is increased. The shortest helix in between the junction region of the helices along [100] and [010] forms a round antiskyrmion first at 176 mT

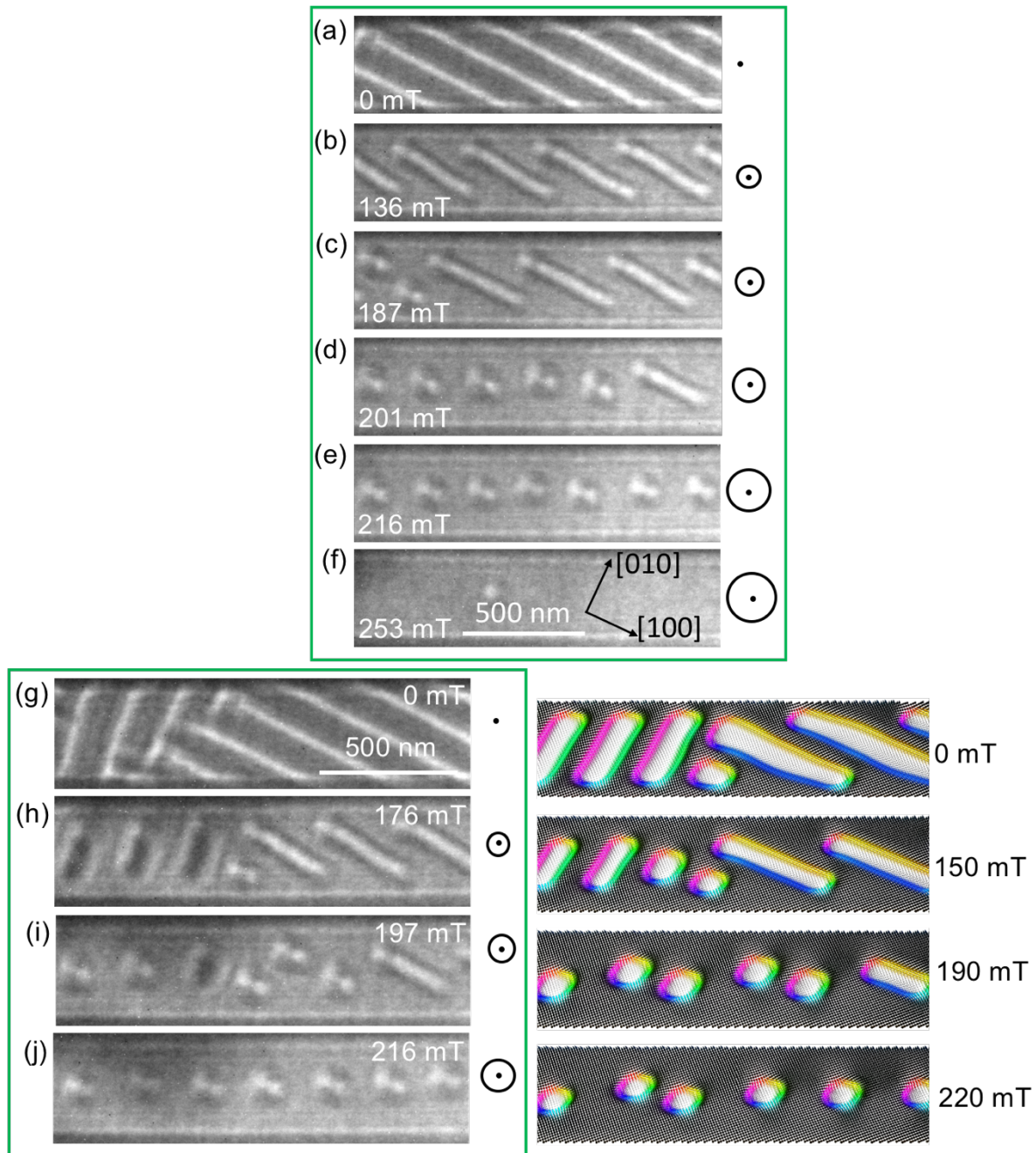


Figure 6 | *Single chain of antiskyrmions.* In the left column, the starting configuration (a) are helix segments that are elongated along the [100] direction, which is oriented at an angle $\varphi \approx -28^\circ$ with respect to the racetrack direction. (b-e) The helix segments shrink, until antiskyrmions are formed at 216 mT. (f) 253 mT: the antiskyrmions annihilate, until the field polarized state is restored. (g-j) The generation of single antiskyrmion chain starting from a mixed helical phase is shown. The nano-stripe is not tilted temporarily for the in-plane component in this case. On the right side, micromagnetic simulation results are shown.

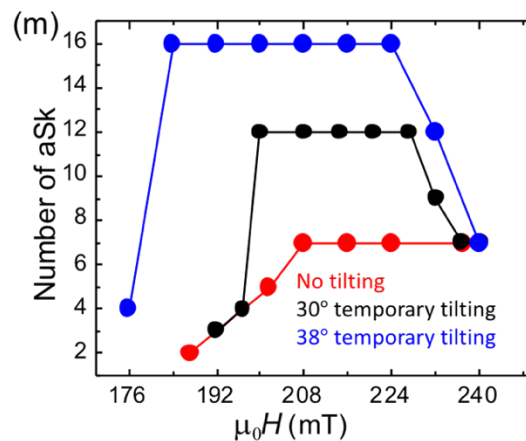
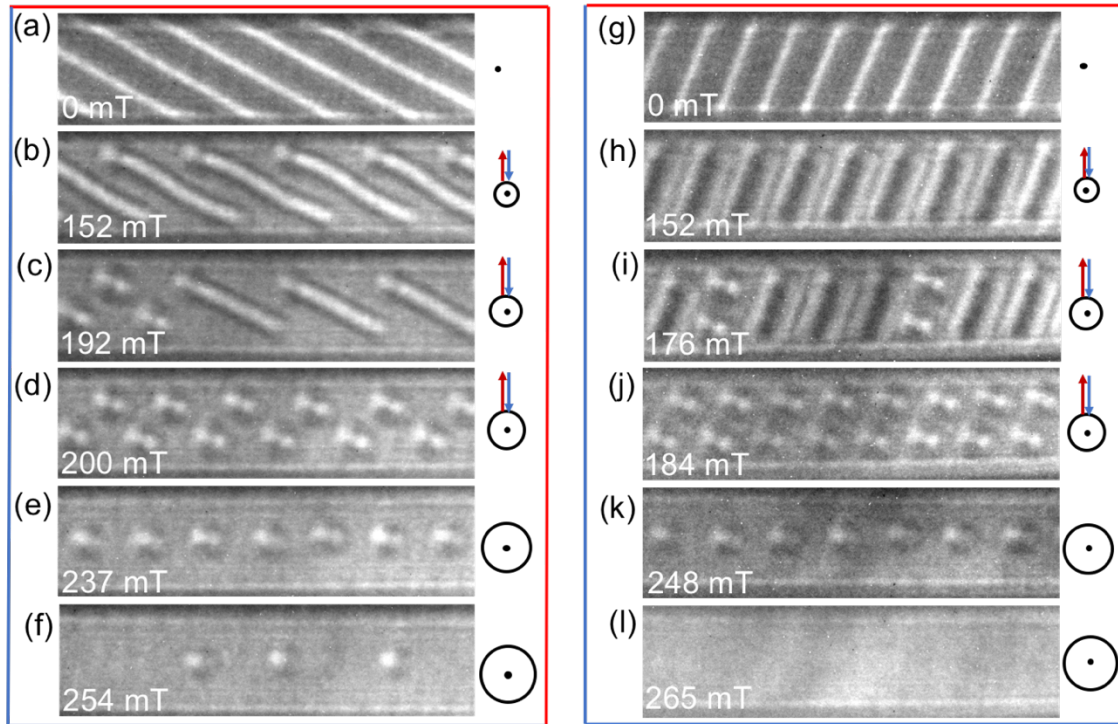


Figure 7 | Effect of temporary tilting in increasing field mode. In the column from (a) to (f), the procedure is changed. This time, the lamella is reversibly tilted by $\sim 30^\circ$ to provide a temporal in-plane field component before LTEM image is taken at zero tilt. When the region will be filled with antiskyrmions, we do not provide in-plane field component after that. (a-d) Formation of double rows of antiskyrmions via temporary in-plane field component. (e-f) The number of antiskyrmions reduces so that a single chain and sparse state nano-objects are found at 237 mT and 254 mT, respectively. In (g-l), the same temporary tilting procedure is applied, but this time it is $\sim 38^\circ$. (m) The numbers of antiskyrmions for the three scenarios are compared for different field strengths. Red curve is without in-plane field (from Fig. 6a-f). Black (Fig. 7a-f) and blue (Fig. 7g-l) curves are with the application of temporary in-plane field. The aSk corresponds to antiskyrmion.

(Fig. 6h). At 197 mT (Fig. 6i), only one truncated helix is left in the right side and a chain of antiskyrmions is formed in Fig. 6j at 216 mT. A qualitative behavior is reproduced in the micromagnetic simulations with starting configuration similar to the experimental mixed helical phase.

The formation of single antiskyrmions chain in the absence of in-plane magnetic field component is very interesting and favorable for a spintronic application in the racetrack device. Moreover, we investigate the effect of temporal in-plane fields on tilting the specimen by $\sim 30^\circ$ (away from the zone-axis) after a step-wise increase in the field. Then back to initial zero tilt position to record the LTEM contrast images. This temporal tilting procedure is continued up to the formation of dense antiskyrmion state like Fig. 7d. The tilting and come back to the initial zero tilt position is indicated by red and blue arrows on the right side of LTEM contrasts. Fig. 6a-6f and Fig. 7a-7f compare a sequence of LTEM contrasts for the same nano-stripe with and without temporary tilting procedures as the magnetic field is increased from zero magnetic field. A similar behavior is seen at first (see Fig. 6b and 7b), but in the field range where antiskyrmions form, a zig-zag double chain of antiskyrmions is observed at 200 mT (see Fig. 7d) for the case of temporal tilting, instead of a single row. The importance of in-plane magnetic fields for the antiskyrmion formation becomes apparent as shown in the recent studies in extended thin lamellae^{51, 133}. It is evident here that the application of in-plane field component via tilting breaks the energy barrier so that nucleation of dense state of antiskyrmion forms. Here, this lattice appears in its minimal shape i.e. a zig-zag chain of antiskyrmions. In this case single chain antiskyrmion formed at a higher field of 237 mT. Hence, for one mechanism, when the field is increased without tilting (Fig. 6a-f or Fig. 6g-j), the helix segments easily transform to antiskyrmions and no “new” antiskyrmions are observed, while for the temporary tilting mechanism (Fig. 7a-f), the truncated helices produce a greater density of antiskyrmions by overcoming the topologically induced energy barrier.

We also investigate the dependence of the antiskyrmion nucleation on the different tilting angles. It is found that for the tilting angle smaller than $\sim 25^\circ$, double rows of antiskyrmions are not observed. So that the truncated helices transform to a single-chain antiskyrmions. In-plane field component increases with increasing the tilt angle. For the temporary tilting angle of $\sim 30^\circ$, the energy barrier overcome so that two chain of antiskyrmions are found. Moreover, for the tilting angle $\sim 38^\circ$ (Fig. 7g-l), the double row of antiskyrmion nucleates at lower total magnetic field (176 mT, Fig. 7j). A likely explanation is as follows: The lower critical field is determined by the energy barrier that needs to be overcome so that

the tilting leads to a formation of two antiskyrmions from one elongated antiskyrmion (or truncated helix segment). If the tilting angle is larger, it is observed that a very low absolute field is required to overcome the energy barrier. On the other hand, for smaller tilting angles (smaller than $\sim 25^\circ$), we have found that no double row of antiskyrmions forms at all. The energy barrier between the truncated helices and the double chain of antiskyrmions can not overcome in these cases. Notably, the density of the antiskyrmion is higher for $\sim 38^\circ$ than $\sim 30^\circ$ for the same region of space. The upper limit is not determined by the in-plane field component. It is caused by the fact that at high magnetic fields, antiskyrmions annihilate one after another so that the texture transforms to the ferromagnet state. This process cannot be hindered by larger in-plane fields. The results of zero tilt, and the two different temporal tilt angles ($\sim 38^\circ$, and $\sim 30^\circ$) are summarized in Fig. 7m. Fig. 7m shows quantitatively, how the number of antiskyrmions increases on a temporary application of in-plane field component (black curve $\sim 30^\circ$, blue curve $\sim 38^\circ$) and no in-plane field component (red curve). The antiskyrmion formation of two separate mechanism underlines our interpretation. One caused by the topological equivalence of truncated helix segments and single row of antiskyrmion. The other one is important in both nano-stripes and in the extended lamellae and is caused by the in-plane field. One of the important features in the D_{2d} compound is that the spacing between the antiskyrmions (and hence the density) can be controlled, depending on the amount of the in-plane field strengths and the lattice spacing is independent of the helical period. This striking phenomenon is mostly absent in B20 compounds, and the lattice spacing depends on the helical period^{21, 23}.

So, the problematic helices (like Fig. 3a in NS 1) that propagate parallel to the racetrack are not present when the nano-stripe helices are oriented along a different direction with respect to the edge, which is a further advantage of these geometries for future spintronic devices. Furthermore, it is important to mention that, even though the antiskyrmions formation is strongly affected by the confined geometry, they form always in the middle of the nano-stripe, unlike edge-mediated skyrmions observed in the B20 compound like FeGe^{75, 136}. Secondly, for the nano-stripe in the B20 case, a single chain is formed only when the width of the transverse constriction stripe is nearly equivalent to skyrmion size and for the larger width, zig-zag or lattice state is found. On the other hand, a single chain spin texture in D_{2d} can induce even when the width of the stripe is much wider than individual nano-object size. On repeating these experiments for a wider nano-stripe of 490 nm width (Fig. 1j), it is found again that the single chain antiskyrmions always present in the middle of the nano-stripe.

Upon decreasing the field from the field polarized phase (Fig. 8a), a distinct behavior is found. Here also, without temporal in-plane field component, antiskyrmions form near 216 mT (Fig. 8b). Notably, it was not the case for the investigated nano-stripe NS 1, which was oriented along the high-symmetric [010] direction. Instead of forming one single longer helix segment in the middle that elongates along the track like Fig. 2a, in the nano-stripe NS 4, many antiskyrmions are formed. This is because the individual helix segment in NS 4 cannot elongate much owing to the considerable angle ϕ between the high-symmetry directions and the nano-track orientation. However, the number of antiskyrmion at 216 mT is less here than the increasing mode of magnetic field experiment (see Fig. 6e); presumably, the transitional boundary of the ferromagnetic to antiskyrmion phase or vice versa is not fixed. Further decreasing the magnetic field, the antiskyrmions elongate along the [100] direction, out of two possible helix propagation directions (Fig. 8c-g). The elongation to short helices from antiskyrmion happens easily in Fig. 8c due to the much available free space among the individual antiskyrmion. A more detailed experimental study on the elongation of nano-objects in the extended lamella will be shown in Ch. 6.

With a temporal in-plane magnetic field is provided from ferromagnetic state, a completely different behavior is found especially in the lower field value. First, only a few antiskyrmions (Fig. 8h) at a field of 215 mT and at a decreased field of 211 mT, a greater number of antiskyrmions in a single chain are present in Fig. 8i. At a field of 192 mT (Fig. 8j), two rows of antiskyrmions in zig-zag forms are present and further decreasing the field to 168 mT, a dense state of a zig-zag double chains form in Fig. 8k. From here downward, the in-plane is not provided and the out-of-plane field is decreased. Then, it is seen that antiskyrmions in this double chain are elongated (Fig. 8l-m). Again, these elongations along the [100] direction are due to the limited space and minimum energy cost. At 0 mT, the helical state is restored as usual (Fig. 8n). In Fig. 8o and 8q, the metastability of single and double antiskyrmion chains and their respective elongation (Fig. 8p and 8r) in lower field values are verified in the micromagnetic simulations. Again, similar to the experiment, the elongated antiskyrmions are along the [100] direction in both cases (Fig. 8p, 8r). Another nano-stripe of width 490 nm and 200 nm thickness (NS 2) with $\phi \approx 45^\circ$ is investigated. The similar behavior of a single chain, double chains and elongated antiskyrmions are found depending on the field history (see Appendix B.2). So, overall, we have investigated the formation of an isolated, a single chain, double chains, truncated and elongated antiskyrmions for three different lamellae whose ϕ values are 0° or 90° , 28° , and 45° .

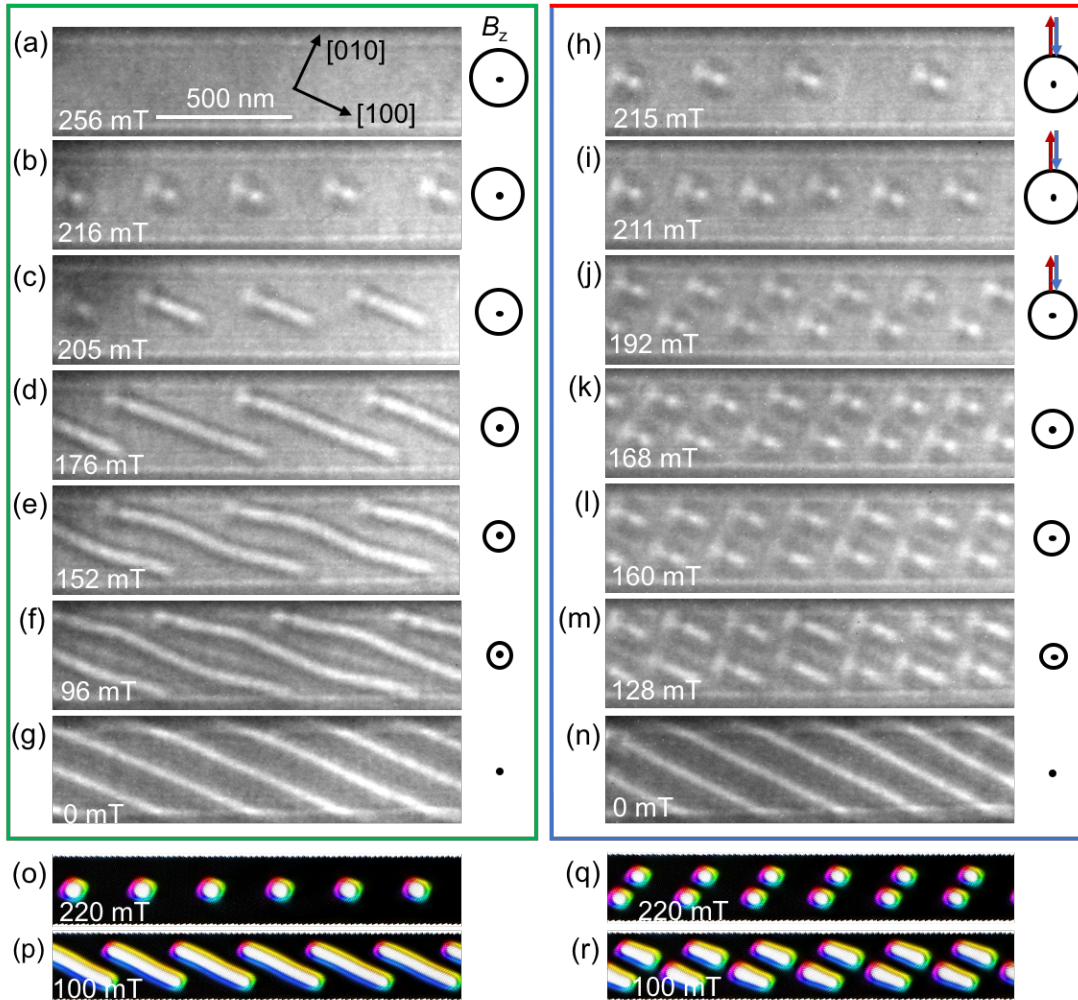


Figure 8 | Evolution of single and double antiskyrmion chains upon decreasing field mode.

In the left column, (a) the starting configuration is a polarized phase. (b) The out-of-plane field is simply decreased leading to the generation of single chain antiskyrmions. (c-g) The antiskyrmions elongate until a ground state helical phase is restored at 0 mT. In the right column, the starting configuration is again a polarized phase. (h) This time the field is reduced under reversible tilting of the nanostripe by 30° to provide a temporal in-plane component of magnetic field. This allows again for the stabilization of antiskyrmions. (i-j) On repeating the procedure of providing temporal in-plane field, a single and double chain of antiskyrmions form. (k-m) When the out-of-plane field is decreased from here, these double chains of antiskyrmions elongate. (n) The helical phase is restored at zero field. (o, p) The elongation process of an antiskyrmion chain is also shown in micromagnetic simulations at different external fields of 220 mT and 100 mT. (q, r) When more antiskyrmions are placed in the sample, a double chain of antiskyrmions is stabilized that elongates similar to the experimental result of (k-m).

5.3.5 Co-existence of elliptical skyrmions and antiskyrmions at room temperature

In Ch. 4, the simultaneous observation of Bloch skyrmions and antiskyrmions was shown in the extended thin film at ~ 268 K. The elliptically Bloch skyrmions are stabilized by dipole-dipole interactions that allow for both clockwise and counter clockwise chiralities and the DMI associated with the compound leads to their elongation along the Bloch walls propagation directions.

Fig. 9 shows room temperature LTEM images of the magnetic texture (at zone-axis of [001]) in a $\phi \approx 45^\circ$ nano-stripe (NS 5) for various temporal tilting angles. The elliptical Bloch skyrmions elongated along the [100] direction appear with a bright center and a dark ring outside and with a bright ring outside and a dark center when elongated along the [010] crystallographic direction. The starting configuration shown in Fig. 9a is a chain of antiskyrmions that has been formed using temporary tilting (along [100]) as discussed above. Here a few (four) elliptical skyrmions are already found (Fig. 9a). In Fig. 9b, the temporal tilting angle used was very small (only 1.3°). After that, all the antiskyrmions have transformed into elliptical Bloch skyrmions. The reason is the small temporal in-plane fields that stabilize the formation of elliptical skyrmions. A larger temporal tilting angle for the in-plane field component was then applied. Moreover, here again both antiskyrmions and skyrmions (i.e. 12 antiskyrmions vs. 11 skyrmions) as shown Fig. 9c are found. The experiment was carried out with multiple temporal tilting angles. The temporary tilting experiment is continued up to tilting angle of $\sim 27^\circ$, where the texture mainly consists of antiskyrmions (Fig. 9e). The LTEM contrasts is shown here at zero tilt after different degrees of tilting angles. Repeating these LTEM experiments at [001] zone-axis that generate on coming from tilting angles of $\sim 27^\circ$ and 1.3° several times, gave the identical results: mostly a single chain of mostly antiskyrmions vs. a single chain of skyrmions. The antiskyrmions have two bright and two dark spots and the white part is not elliptical but ‘dented’ in the middle. Whereas, for the skyrmions the ‘denting’ and the gray line are both missing. Still, for some objects the LTEM resolution is not sufficient to tell if it is an antiskyrmion or a skyrmion (not marked solid triangle), but a comparison with the initial configuration (Fig. 9a) shows clearly that the magnetic contrast has changed. Similar to the experiment, elliptical skyrmions and antiskyrmions are stabilized in the micromagnetic simulation. Fig. 9g shows such simulation for the simultaneous observation of antiskyrmions and oppositely elongated elliptical skyrmions at 220 mT. In Fig. 9h, the simulated LTEM contrast (derived from the same method used in Ch.4) of the spin texture in Fig. 9g is shown.

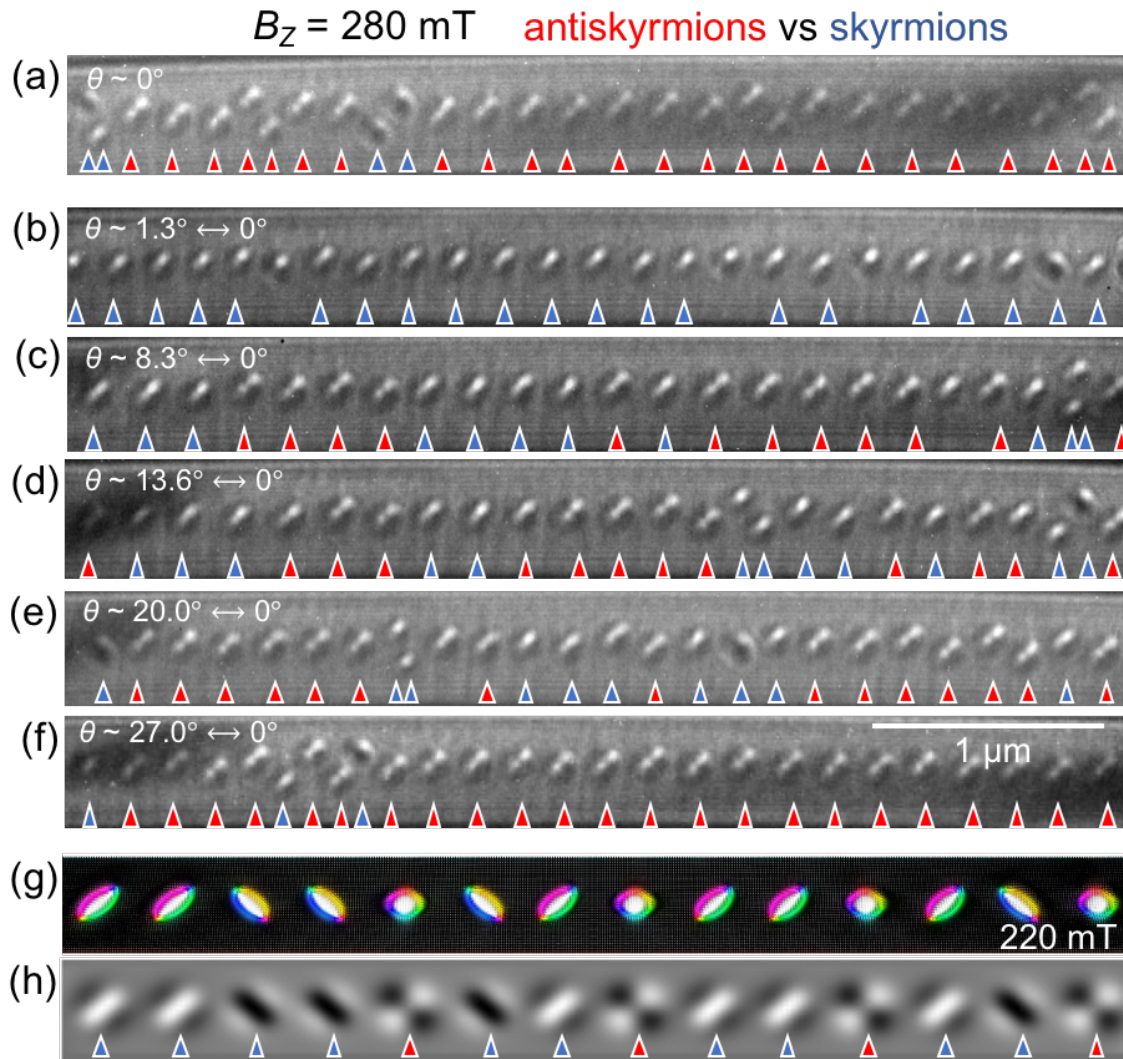


Figure 9 | *Antiskyrmions versus elliptical skyrmions in a nano-stripe along the $[\bar{1}10]$ direction.* In (a) the initial configuration at zero tilt is shown at 280 mT after tilting the stage for the in-plane component of field along $[100]$. It consists mainly of antiskyrmions (indicated by red triangles) and only showing 4 elliptical skyrmions which are elongated along the $[010]$ direction and one elliptical skyrmion that is elongated along the $[100]$ direction (both indicated by blue triangles). In (b), the stripe was reversibly tilted to get a small in-plane field along the $[100]$ direction. The result is mainly elliptical skyrmions. From (c-f), the same procedure is repeated but with larger tilting angles: the number of antiskyrmions increases with tilt angles. For a few nano-objects it is difficult to determine whether it is a skyrmion or an antiskyrmions. We did not add a marker in those cases. (g) The simultaneous formation of elliptical Bloch skyrmions and antiskyrmions in a single chain is shown in micromagnetic simulation. (h) The simulated Lorentz TEM contrast of the spin textures shown in Fig. (g).

As we can see, the dented part is only shown for the antiskyrmion and is missing for the elliptical skyrmions. Since both antiskyrmions and one type of elliptical skyrmion (of bright contrast) look similar, which explaining why it is sometimes difficult to distinguish the experimental LTEM images of antiskyrmions and bright contrast of elliptical skyrmion.

Our first ever findings of opposite topological charges in a single nano-stripe, co-existence of them and their competing density variation depending on the in-plane field may lead to concept of realizing the magnetic logic gates^{8, 54} in which elliptical skyrmion and antiskyrmion read out distinctly as different bits of ‘0’ and ‘1’ insist of general logic gates notion for reading the absence and presence of skyrmion as 0 and 1 bits in skyrmion host material. Hence, spin textures in D_{2d} host compound can be an ideal platform for advanced version concept in logic gates and racetrack memory devices in future.

5.4 Summary

In conclusion, two major findings are demonstrated here. Firstly, a single chain of antiskyrmions is formed along the middle of nano-stripes formed from a D_{2d} material even when the stripe is much wider than the individual antiskyrmions. The single chain antiskyrmions formation without the presence of in-plane field components is highly relevant for memory device application. Isolated antiskyrmion, a single chain antiskyrmions, a dense zig-zag chain antiskyrmions, elongated and truncated shape LTEM contrasts whose topological charge same to that of antiskyrmion are found in those constraint geometries depending on the field and protocol history. Secondly, antiskyrmions can co-exist with elliptical Bloch skyrmions at room temperature. Moreover, these findings take place at room temperature and do not require multilayers buildups structure. The finding of simultaneous occurrence of two distinct nano-objects makes them a highly attractive feature of D_{2d} systems that conceptually suggests the possibility of robust magnetic memory or computing devices which could encode elliptical skyrmions as ‘1’ bits and antiskyrmions as ‘0’ bits.

6 Stability, collapse dynamics and fractional form of antiskyrmions and elliptical Bloch skyrmions

6.1 Introduction

Experimentally, antiskyrmions have been found in a non-centrosymmetric inverse tetragonal Heusler compound $\text{Mn}_{1.4}\text{Pt}_{0.9}\text{Pd}_{0.1}\text{Sn}$. It has an opposite topological charge number $N_{\text{Sk}} = \frac{1}{4\pi} \iint m(\mathbf{r}) \cdot \left(\frac{\partial m(\mathbf{r})}{\partial x} \times \frac{\partial m(\mathbf{r})}{\partial y} \right) d^3\mathbf{r} = +1$ compare to the Bloch skyrmion ($N_{\text{Sk}} = -1$) due to the opposite winding of the in-plane component of the spin¹³². In Chs. 4 and 5, we have presented that for the same Heusler compound, a different spin-texture is formed solely out of Bloch walls, and having an opposite topological charge ($N_{\text{Sk}} = -1$). We named it as elliptical Bloch skyrmion. In this chapter, we will present novel observations in $\text{Mn}_{1.4}\text{Pt}_{0.9}\text{Pd}_{0.1}\text{Sn}$, a fragment of elliptical skyrmion and antiskyrmion formed near the edge of the specimen. We have named them as ‘fractional skyrmion or fractional antiskyrmion’; owing to the fractional value of N_{Sk} . They are mostly formed in low field regions or even in the negatively biased fields after the lattice state stabilization. Moreover, a collapse dynamic in the lamellae’s interior region is observed where individual antiskyrmion or elliptical skyrmion join with each other to form elongated short helical objects. Further, a detail experimental set up is optimized and will be discussed in this chapter in order to understand the role of in-plane field components to stabilize spin textures on using various protocols.

6.2 Experimental details

The orientation selection and the preparation procedure of lamellae were explained in the experimental method. Before depositing PtC_x by GIS to produce an interface with the $\text{Mn}_{1.4}\text{Pt}_{0.9}\text{Pd}_{0.1}\text{Sn}$, the vital step 3 (of Ch. 3) was followed, where smooth polishing at low energy of 5 kV (and 8 pA current) and then 2 kV (and 4 pA current) were performed. The polishing ensures a smooth interface between the magnetic material $\text{Mn}_{1.4}\text{Pt}_{0.9}\text{Pd}_{0.1}\text{Sn}$ and PtC_x (non-magnetic amorphous). The same low energies polishing was performed in the last step (step 10 of Ch. 3) of the lamella preparation method to get the smooth surface. By applying the current in the objective lens of the TEM, the magnetic field value can be adjusted from zero to +2.2 T in a positive direction (+Z-direction) and -0.28 T in opposite to that (-Z-direction). Note that the magnetic field is oriented along the microscope column and hence is parallel to the electron beam propagation direction along the Z-axis. Therefore, at zero tilt position, the applied field is always perpendicular to the specimen, unless we tilt the specimen to get the in-plane field components. The calibration of the magnetic field values is done with a Hall bar sensor.

6.3 Results and discussion

6.3.1 Metastability of square antiskyrmions

The antiskyrmions (of round and square shape) have been found at room temperature and beyond, as described in the Ch. 4. Here, we attempt to stabilize the square antiskyrmion throughout the temperature range using a field cooled protocol, i.e., cooling the specimen of a square antiskyrmion lattice state from 350 K down to various low temperatures.

A square antiskyrmion lattice is formed at 350 K and 200 mT using the lattice stabilization tilting procedure (Fig. 1a). The specimen is cooled down to 200 K under a constant magnetic field. In the same region, the LTEM contrast presented in Fig. 1c shows a short helix (rectangular shape) in the antiskyrmion lattice. Further decreasing the magnetic field to -16 mT (Fig. 1d), metastable square antiskyrmions are still existed. Thereafter, we record the LTEM images on an interval of 16 mT out-of-the plane field. The lattice remains square, and the short helix is transformed to square shape around 256 mT (Fig. 1e). Isolated state of square skyrmion formed in higher magnetic fields (Fig. 1f). However, in this extended lamella, short helices of different lengths are found, having one of the edges terminate by the boundary. Interestingly, these helices transform to square antiskyrmions in higher magnetic field values (Appendix C.1). A schematic diagram of the field-cooled stabilization of antiskyrmion at 200 K is shown in Fig.

1b. The procedure mentioned above was repeated for 100 K and 250 K. Notably, by following the field cooled procedure, we observed the presence of lattice states, though we do not find any lattice state at 100 K in zero field cooled procedure in the lamella (for the ~ 170 nm thickness lamella). Interestingly, an in-plane field component is not required in this field cooling process. Moreover, in the ~ 280 nm thick lamella, we found lattices state (elliptical skyrmion) without field cooling experiment, as mentioned in Ch. 4, which points toward the importance of thickness dependent dipole-dipole interactions. Additionally, in that thicker lamella, we also observed the antiskyrmion in the lower temperatures using the same field cooled procedure. These metastable antiskyrmions are robust and stable at any given field and temperature as long as these conditions are maintained, which is up to a maximum of 2 hours.

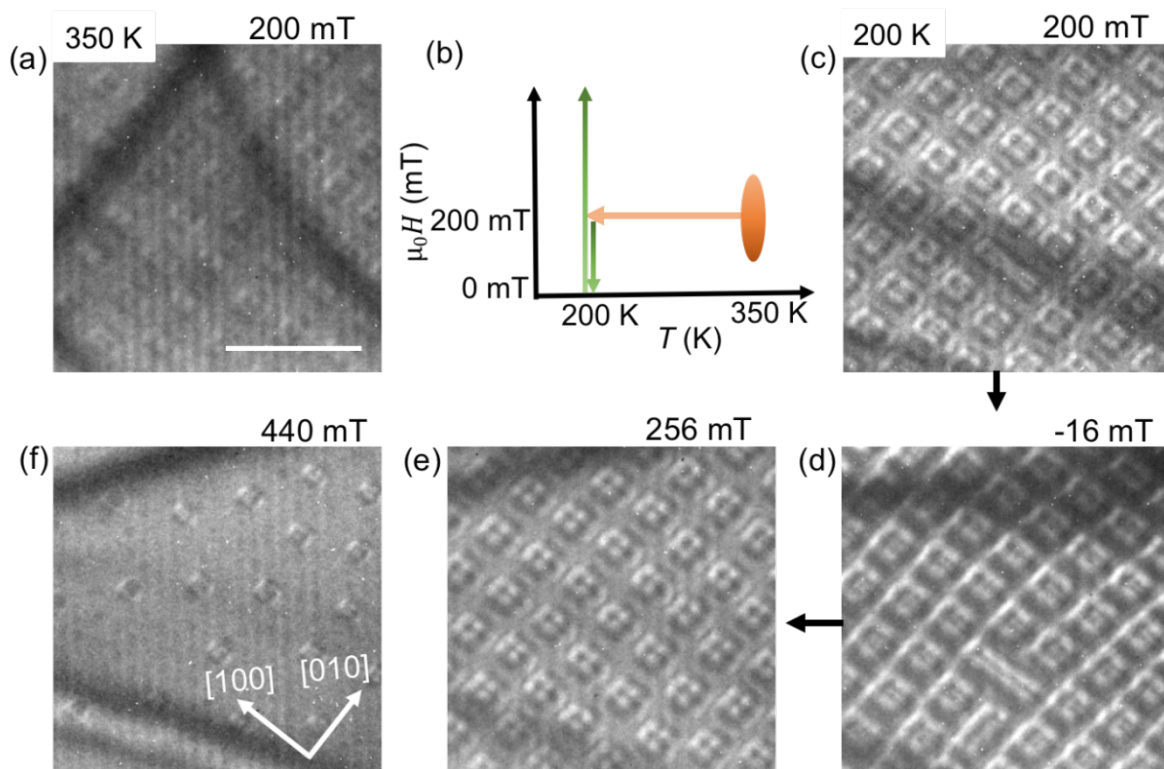


Figure 1 | Metastability of square antiskyrmions for low temperatures. (a) Magnetic antiskyrmions lattice at 350 K. (b) Schematic diagram for the field cooling procedure. (c) LTEM contrast at 200 K, after thermal stability. (d) Reduced the magnetic field to -16 mT. (e, f) LTEM contrasts at 256 mT and 440 mT on increasing the magnetic field from -16 mT. The scale bar in (a) corresponds to 500 nm.

It is observed that the square antiskyrmions can be stabilized at zero field and for an elevated magnetic field. Reversible switching between square to round antiskyrmion occurs at room temperature via a temporary in-plane field component¹³³. As we want to study the formation of square antiskyrmion throughout the field range, for that matter, we increase the out-of-plane field from the zero-field state of square antiskyrmions on keeping the lamella at zero tilt position.

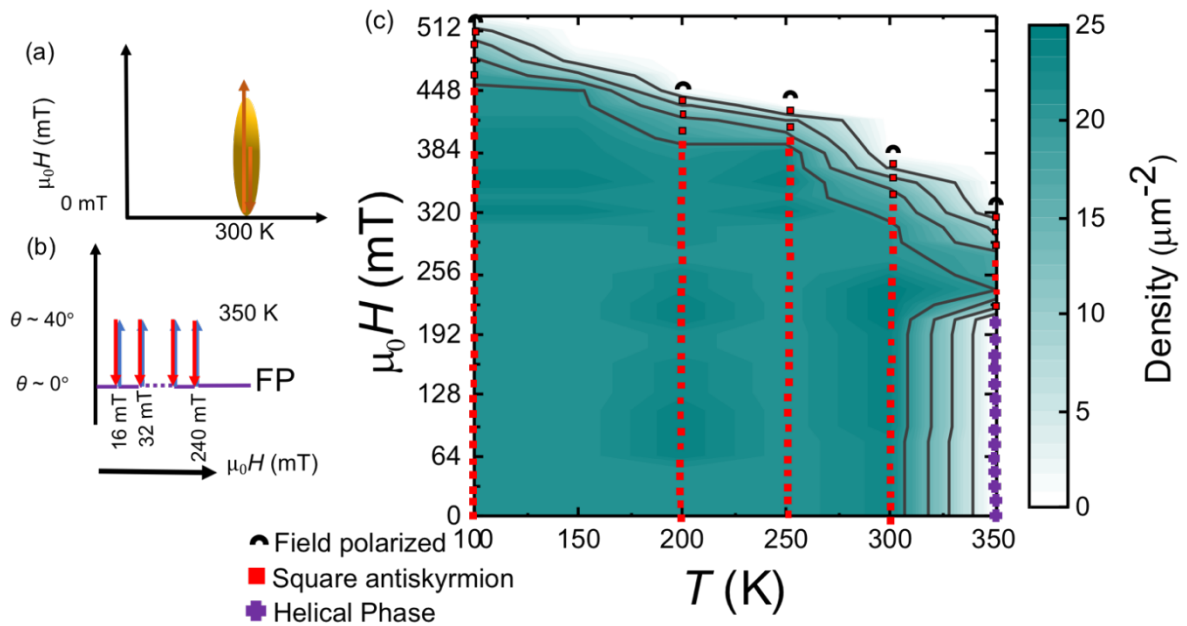


Figure 2 | Stabilization of square antiskyrmions at different temperatures. A similar field cooling protocol as shown in Fig. 1 is used for 100 K, 250 K, and square antiskyrmions are also found. (a), (b) Schematic diagrams of square antiskyrmions at 300 K and 350 K. At room temperature, after lattice stabilization, the out-of-plane magnetic field is reduced to 0 mT. The square antiskyrmion lattices are found here at 0 mT. From there, out-of-plane field increases up to saturated state through the lattice state, sparse state and then to polarized state. At 350 K, the lattice stabilization protocol of the temporal application of the in-plane field is used in increasing mode of the magnetic field. (c) Magnetic phase diagram which shows square antiskyrmions throughout the temperatures and field in increasing mode of the magnetic field.

The experiment schematically shown in Fig. 2a is performed in order to obtain the data of square antiskyrmions in the increasing field mode. At 350 K, using the temporary tilting lattice stabilization process in increasing field mode, we found only square antiskyrmions (Fig. 1b). The LTEM contrasts are presented in Fig. 9a-d (see below). The formation of square antiskyrmions using different fields, temperatures and protocol histories are summarized in Fig. 1c as a contour plot diagram.

6.3.2 Collapse dynamics of antiskyrmions and elliptical skyrmions

The square antiskyrmion at room temperature was found to be stabilized up to zero field as described in the previous chapter. It is observed that short helices of various lengths could be formed by decreasing the field in a negative direction. In the decreasing mode of field, the short helices are formed after joining two or three antiskyrmions from the lattice state. Fig. 3a

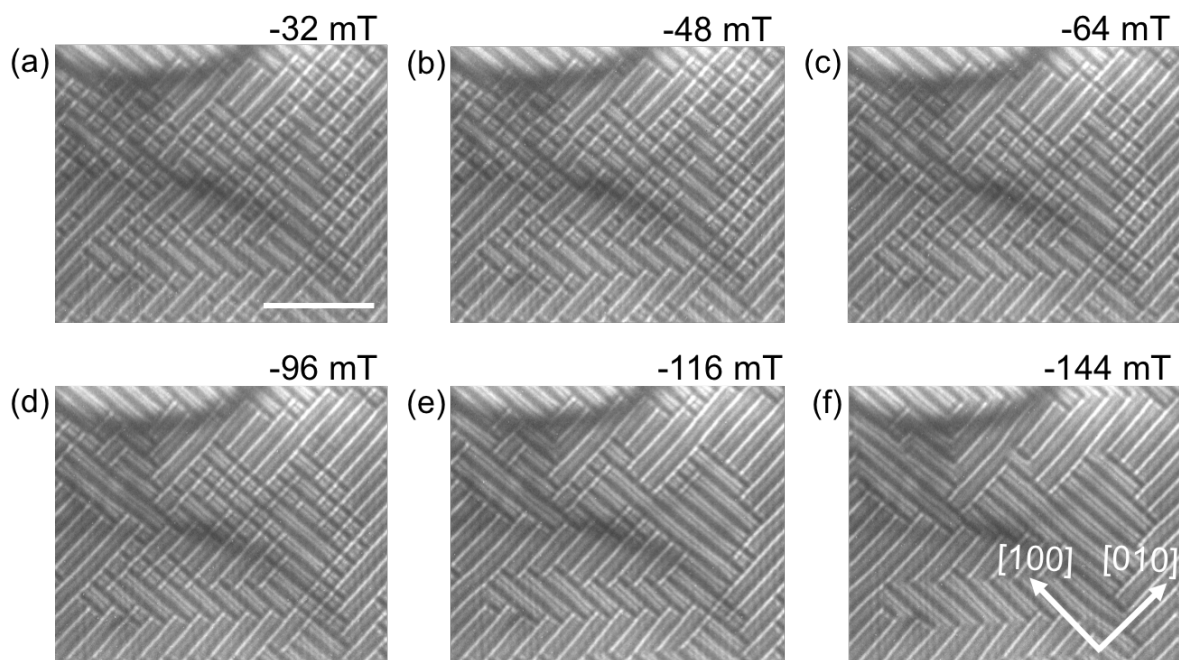


Figure 3 | Collapse dynamics of antiskyrmions. (a-f) Decrease the field from the antiskyrmions lattice and the collapsing of them produces few short helices. (b-e) By joining short rectangular helices with the other square antiskyrmions (in negative field directions), more short helices are formed. In (f), no square antiskyrmions are found. The short helices are either elongated along $[100]$ and $[010]$ directions. The scale bar in (a) corresponds to $1 \mu\text{m}$.

shows such a state where square antiskyrmions and few short helices are found. For further negative magnetic fields, more number of square antiskyrmions join with each other to form short helices. The rest square antiskyrmions join with previously occurred short helices so that more extended helices are found (Fig. 3b-d). At -116 mT (Fig. 3e), only very few square antiskyrmions are there in the junctions between the short helices of different lengths. In Fig. 3f, no antiskyrmions of square-shaped nano-objects are found.

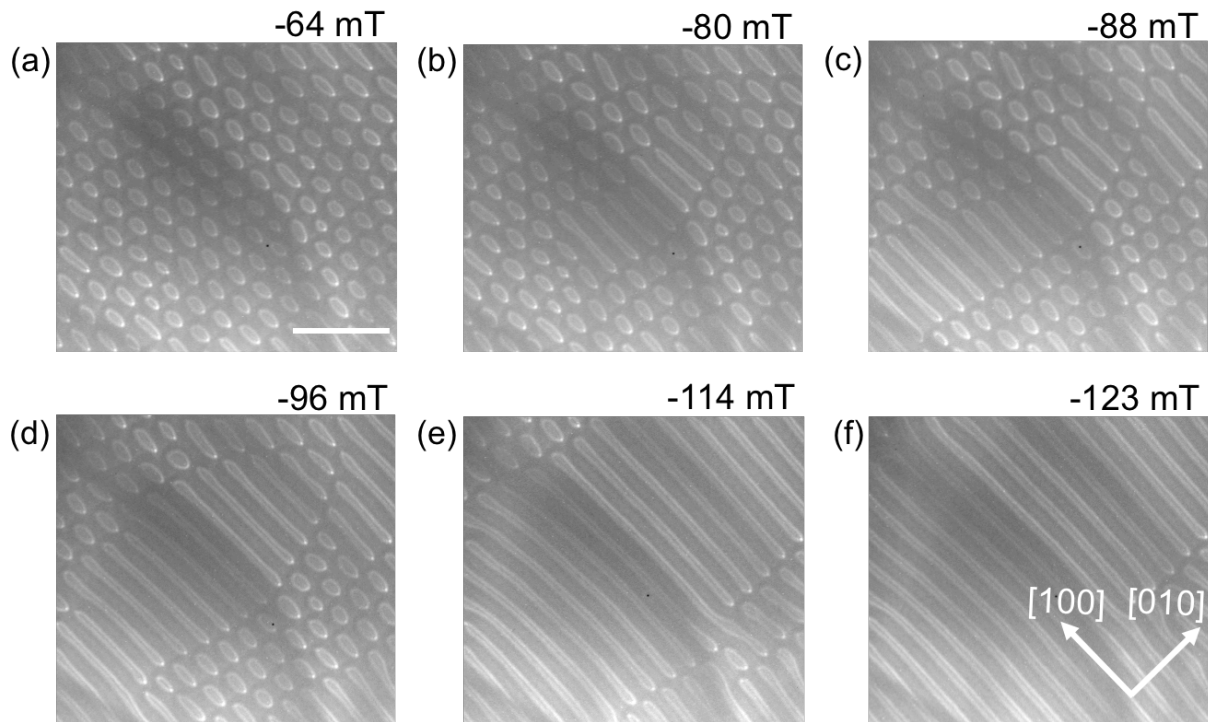


Figure 4 | Collapse dynamics of the elliptical Bloch skyrmions. In (a) lattices of elliptical skyrmions are found at -64 mT. (b) Elliptical skyrmions (in the middle) added with each other to make them elongated elliptical shape. (c-e) More short helices in elliptical shape are found on joining the elliptical skyrmions. (f) At -114 mT, only few elliptical skyrmions are left in the corner of the LTEM contrast and short helices are elongated more. The scale bar in (a) corresponds to 1 μm .

A similar kind of mechanism is found for elliptical Bloch skyrmions. However, due to the favored one kind of chirality here, the short elliptical helices are formed in one direction and later long helices by joining more elliptical skyrmions. In case of elliptical skyrmions, we

can observe lattice states even below zero field and negative biased fields at 100 K (Fig. 4a). Seven short helices are formed at -80 mT after joining two or three elliptical skyrmions, and further increase of the field to 8 mT, more short helices are formed (Fig. 4b-c). Increasing the field to -96 mT, the short helices are further elongated through the merging of neighboring elliptical skyrmions (Fig. 4d). At -114 mT, middle region short helices in Fig. 4d became much longer by joining with more elliptical skyrmions, and very few elliptical skyrmions are leftover in the LTEM contrast as shown in Fig. 4e. The short helices formed here have the elliptical shape precisely like the elliptical skyrmions. Therefore, it can be anticipated that they could bear the same topological charge of individual nano-objects of elliptical Bloch skyrmions. A similar analogy is applied for the rectangular shape of short helices that were formed from square antiskyrmions. In the case of elliptical skyrmions, due to the region is filled with one type of chiral object, the elongation of helices is more significant relative to the elongation process of antiskyrmions case. A full helical phase is observed at -123 mT (Fig. 4f), where helices touch the boundary region, so that the topological protection of elongated structure is destroyed. Such a case is not happening in the interior region of the collapsing process in the square antiskyrmion process even though near the boundary rectangular shape contrast destroys its topological protection.

This mechanism is in contrast to the dynamics of B20 compounds, where reduction of the applied field leads to a non-equilibrium phase separation composed of skyrmions and conical domains¹⁴¹. These conical domains of Q- vector parallel to the applied magnetic field evolve into a ground state helical phase (of Q- vector perpendicular to the applied magnetic field) near zero field. A strong uniaxial anisotropy and tubular non-twisted spin structure owing to the anisotropic DMI do not allow the conical spin arrangement in the D_{2d} system of $Mn_{1.4}Pt_{0.9}Pd_{0.1}Sn$. Though, similar to D_{2d} , the individual spin texture shape increases with decreasing magnetic fields keeping the distance between the cores of the structures nearly constant, such a prolonged length deformation of spin textures and their collapse dynamics (from a dense lattice state) are not observed so far for the cubic compound of B20 skyrmions. Moreover, as observed in Ch. 5, uniformly elongated spin textures on nano-strips of this compound have been found due to the constriction geometry, unlike here, the irregular elongation due to the large free space region of this extended lamella.

6.3.3 Fractional elliptical Bloch skyrmions and antiskyrmions

So far, we have covered the dynamics of phase transformation occurring in the interior of the lamella. In this section, we will discuss the remarkable dynamics of spin structures located near the lamella boundary. The boundaries are formed by the interface region of $\text{Mn}_{1.4}\text{Pt}_{0.9}\text{Pd}_{0.1}\text{Sn}$ and non-magnetic PtC_x (deposited by a focused ion beam). By this way, interface regions are formed in the lamella as shown in Fig. 5a. Here, we only focus on the

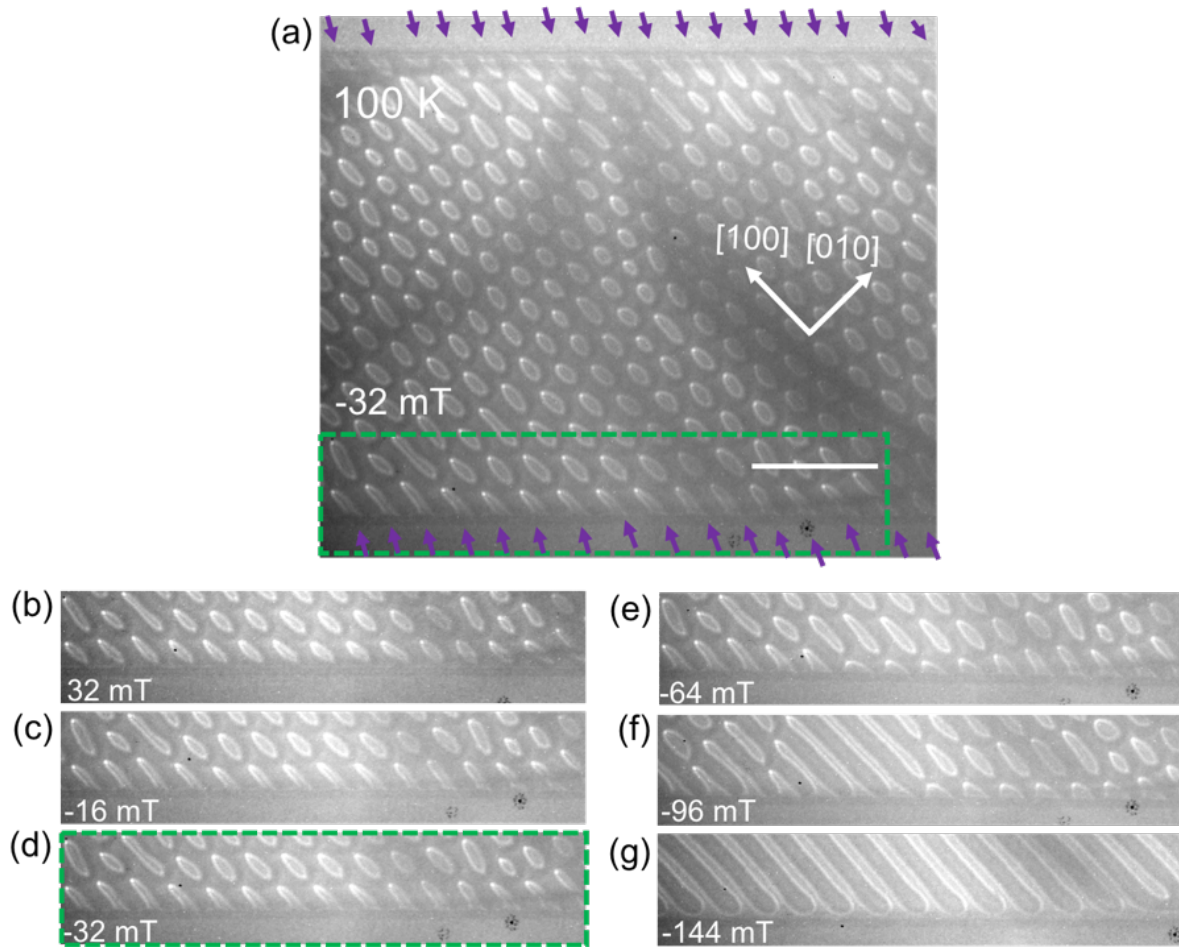


Figure 5 | Fractional elliptical Bloch skyrmions. (a) The LTEM contrast of the extended lamella at -32 mT and 100 K. The interior region is the lattice state. The nano-objects near to boundary are marked by the arrows. (b) At 32 mT and near the boundary, nano-objects are elliptical Bloch skyrmions. (c) Shows the fractional Bloch skyrmions at -16 mT. (d) Region marked by a green rectangle in (a) is shown separately here. (e, f) Fractional Bloch skyrmions exist up to -96 mT. (g) at -144 mT, they did not observe. The scale bar in (a) corresponds to $1\mu\text{m}$. The experiment is performed on a $\sim 280\text{ nm}$ thick specimen.

interface regions formed by $\text{Mn}_{1.4}\text{Pt}_{0.9}\text{Pd}_{0.1}\text{Sn}$ and PtC_x . The following discussion will be focused on the area marked with green rectangle in Fig. 5a. The field is decreased from the lattice stabilization of the elliptical skyrmion state. At 32 mT elliptical skyrmions are shown near the boundary (Fig. 5b). By reducing the field; fractional Bloch skyrmions are formed (Fig. 5c-d). The LTEM contrast in Fig. 5d is the same area marked in the green rectangle in Fig. 5a of the extended lamella at -32 mT and 100 K. The interior area is filled with the lattice state of elliptical Bloch skyrmions, whereas, in the boundary regions the nano-objects are not completely formed. Instead, they are incomplete form of the elliptical skyrmion, marked by arrows in Fig. 5a. Due to the incomplete form, their topological charge is non-integer. Since lamella has an edge, the moments in the texture are tilted according to the DMI^{76, 127, 142, 143}. Thus, they are termed as “fractional Bloch skyrmion” and are found to be only observed near the boundary of such materials. Further reducing the field to -64 mT (Fig. 5e), elliptical skyrmions start to elongate and fractional nano-objects shrink. At -96 mT (Fig. 5f) elliptical skyrmions and fractional skyrmions start to merge and elongated helix state starts to form. No fractional nano-objects are found at -144 mT (Fig. 5g). Note that, it is necessary to induce a full lattice stabilization before following this procedure to obtain fractional nano-objects.

From our experiments, we find that it is not possible to stabilize the fractional form of antiskyrmion on the boundaries at room temperature and above in the ~ 170 nm thick lamella. Similar to the low-temperature case, at high fields, integer topological charge number objects are formed. Moreover, upon lowering the applied field, these topological objects transform into elongated helices before reaching the boundary. Nevertheless, after stabilizing the square antiskyrmion lattice at high temperature, in a fixed value of field (200 mT), we cooled the specimen temperature down to 100 K as we did for stabilizing square antiskyrmions in section 6.2.2. Next, lowering the magnetic fields, antiskyrmions are moved towards the boundary (Fig. 6c, 6d). Fig. 6c-h shows the evolution of spin textures with the magnetic fields on the same area marked with the green rectangle of Fig. 6a. The two boundary regions show the formation of fractional antiskyrmions. Similar to the experiment, a micromagnetic simulation in Fig. 6b shows the appearance of fraction antiskyrmions at the boundaries. In Fig. 6e, the antiskyrmions get elongated and touch the edge so that they have formed the fractional antiskyrmions. Upon increasing the magnetic field in the negative directions, their size increases (Fig. 6f-h). At -160 mT (Fig. 6a and 6h), few of the fractional antiskyrmions appear as triangles on both edges of the lamella. Since the crystallographic [100] direction is nearly 45° to the edge, they appear as ‘cut in half’ from the square-shaped antiskyrmions at the edges. A detailed experiment will be carried out latter to understand the dynamics of the fractional nano-objects. Even though the

fractional Bloch skyrmions and antiskyrmions are exactly tied to the crystallographic directions of $[100]$ and $[010]$, their small portion near the edge region is not precisely along the high symmetry crystal directions. This may be related to the small contribution of the underlying DMI, which result in the edge twist and the fractional charges formation. There are several studies reported the edge twisting in skyrmions crystals both in theories^{76, 127, 142, 143} and experiments^{75, 136}. However, such type of fractional charges formation has not been reported experimentally yet. Recently, a theoretical study on antiskyrmion crystal shows the emergence of topological magnonic corner state due to the fractional antiskyrmion¹⁴⁴.

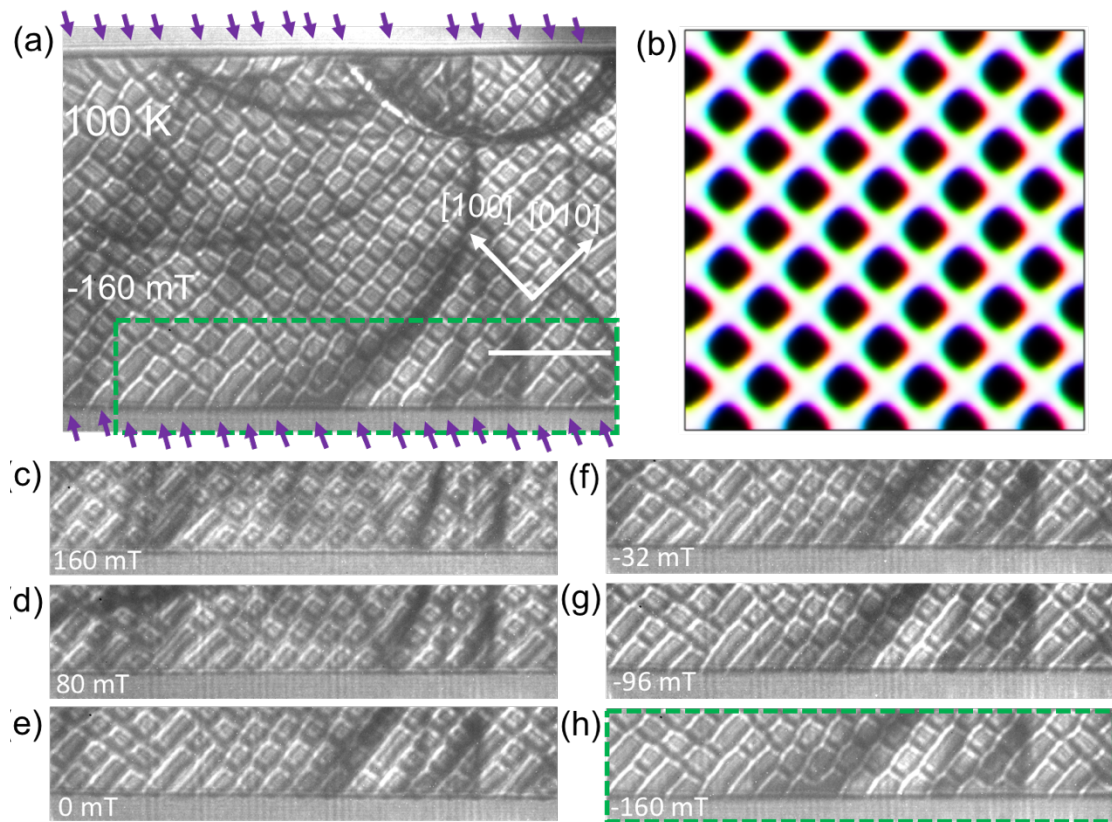


Figure 6 | Fractional antiskyrmions. (a) The formation of fractional antiskyrmions near the boundaries of the extended lamella are marked by arrows. After field cooled the specimen from the lattices state of square antiskyrmion at 350 K to 100 K on keeping the constant field value of 200 mT, the field is then reduced up to -160 mT and (c-h) LTEM contrasts are shown in a stepwise field value. Fractional antiskyrmions are observed (as shown in e-h). (b) The micromagnetic simulation shows the fractional antiskyrmions near the boundary at 0 mT. The simulation parameters used here are same as in Ch. 5. The scale bar in (a) corresponds to $1\mu\text{m}$.

6.3.4 In-plane field dependent metastability of spin textures

In section 6.2.2, there is a transition field upon which the condensed lattice structure of the skyrmions (or antiskyrmions) is transformed into the short helical structure. Here we show that this transition field depends significantly upon the density of the initial skyrmions (or antiskyrmions) phase.

It is possible to obtain weakly populated skyrmion states (or sparse states) by carefully engineering the initial field conditions. We first apply a combination of out-of-plane and in-plane field by tilting the specimen with respect to the normal. For this experiment, the temporary tilt angle is $\sim 40^\circ$. Subsequently, we apply three different fields of magnitudes 488 mT, 464 mT, 432 mT, and then reorient the specimen so that there is no longer an in-plane field. As shown in Fig. 7 (a, e, i) we obtain three sparse states with different elliptical skyrmion densities. After the sparse states are formed by temporary application of the in-plane field, we simply decrease the out-of-plane field (no color boundary). As discussed earlier, there is an intermediate field region, where short helices are formed. However, for sparse states cases, this intermediate region exists in the positive fields instead of the negative field as observed for the densely populated lattice state (Fig. 7b-d, 7f-h and 7j-l). The number of short helices forms in the positive state also depends on the initial density and more helices are formed for Fig. 7j-l (reducing field from Fig. 7i) when compared to Fig. 7f-h (from Fig. 7e), and more for Fig. 7f-h (from Fig. 7e) when compared to Fig. 4b-d (from Fig. 7a). It is due to the available space among the individual elliptical skyrmions that depend on the initial state formation via tilting. At zero magnetic field, the ratio of elliptical skyrmions to the helical objects increases as the density of the initial sparse state increases.

Similar experimental observations for antiskyrmion shows that on decreasing the out-of-plane field (without in-plane field component) from the sparse state, we do not get any antiskyrmion in the lower magnetic field (see Appendix C.2). Finally, we have also performed the same experiment starting with a field of 400 mT as shown in Fig. 8a. For this field, a lattice state of a much higher density is obtained and the transition field for the formation of helical objects is pushed beyond zero field. Since dipole-dipole interactions are always present in this tetragonal inverse Heusler alloy system, the size of these Bloch skyrmions (or antiskyrmions) increases as we decrease the field or vice versa¹³³. However, elliptical skyrmions in low fields have no regular size variation with the magnetic field. For example, as we show in LTEM images at 352 mT (Fig. 8b), 224 mT (Fig. 8c), 160 mT (Fig. 8d), 80 mT (Fig. 8e) and 0 mT (Fig. 8f), the sizes of individual elliptical skyrmions vary largely.

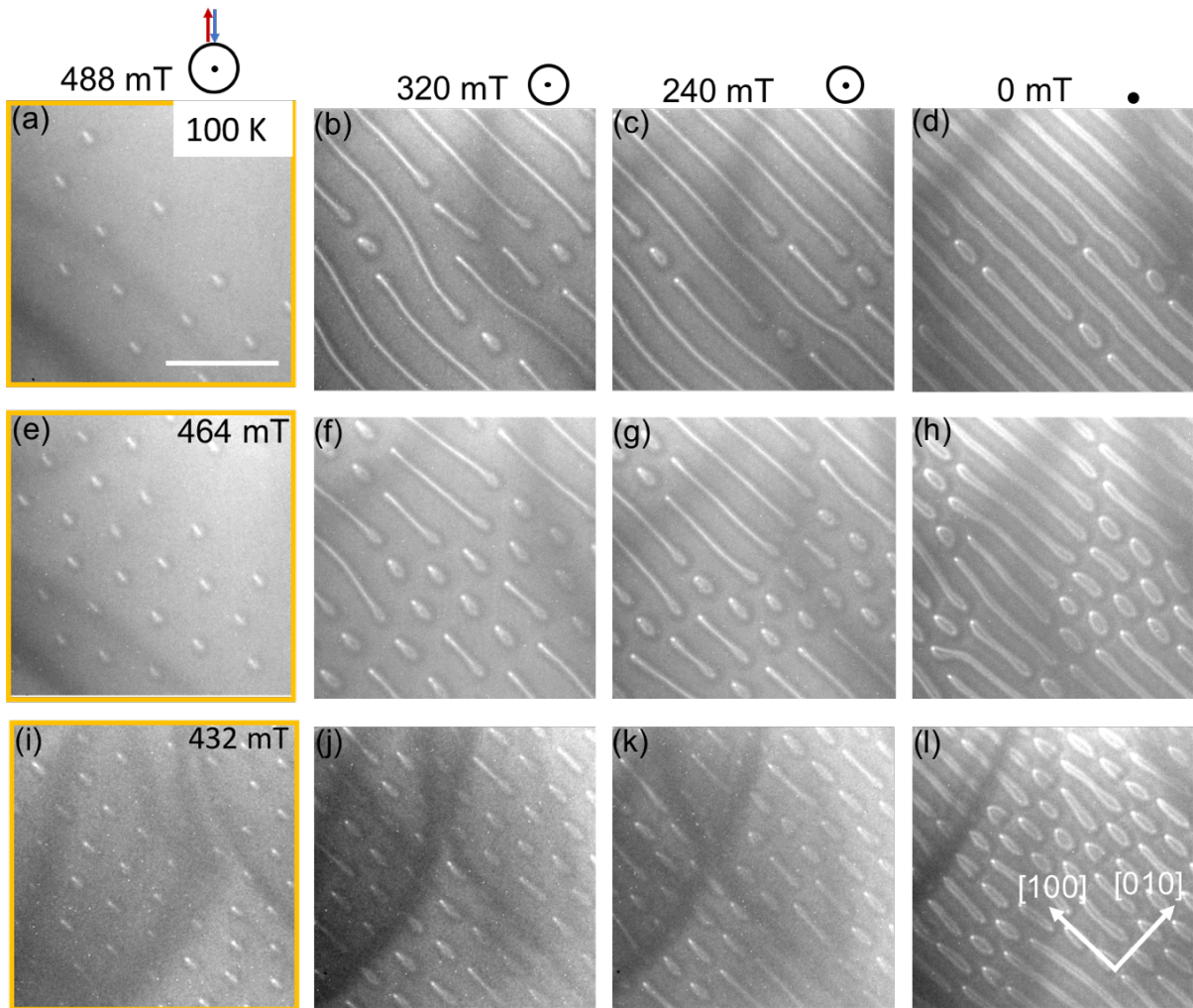


Figure 7 | *significance of In-plane field and its stability to nano-objects formation.* (a) LTEM image after the temporary application of in-plane field for an out-of-plane field of 488 mT (marked by an orange square). (b-d) In that row, the LTEM contrasts are imaged without the in-plane magnetic fields components. (e) and (i) are similar experiments for the 464 mT and 432 mT out-of-plane field after providing the temporary in-plane field components via tilting. (f-h) and (j-l) are LTEM contrasts without in-plane components from the state shown in (e) and (i). The density of elliptical Bloch Skyrmions at 432 mT is relatively higher than at 488 mT and 464 mT after the temporary application of magnetic field. The experiments for LTEM contrasts at each row are performed separately. The scale bar in (a) corresponds to 1 μm .

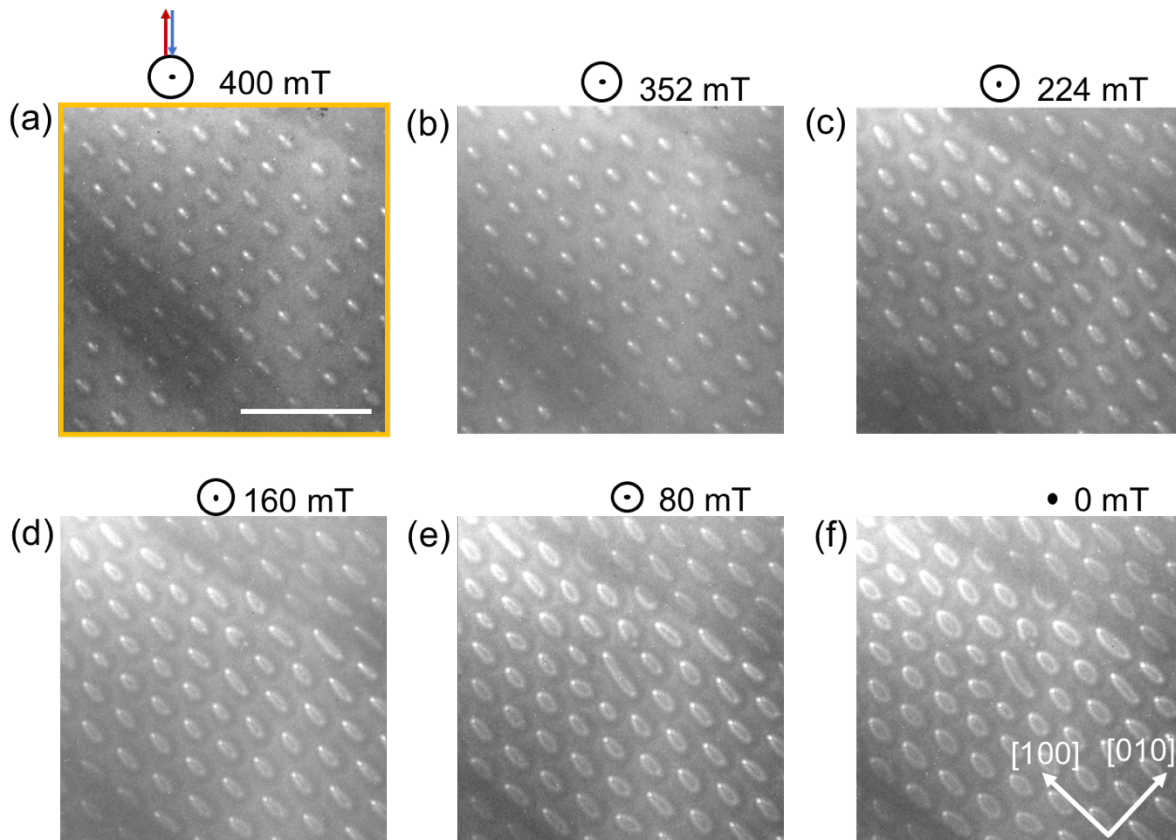


Figure 8 | *significance of In-plane field and its stability to lattice formation.* (a) Utilizing the temporary tilting angle ($\sim 40^\circ$) at an out-of-plane magnetic field of 400 mT, a dense lattice state is found. (b-f) These lattices states are existed as metastable state up to the lower magnetic field. The scale bar in (a) corresponds to 1 μm .

Overall, one can notice that various densities of those nano-objects can be formed in elevated field regions depending on the field stability protocols. When we decrease the out-of-plane field from sparse states (like in Fig. 7a, 7e, 7i), short helices easily appear in the relatively higher field. Whereas, for the dense lattice states, short helices form mostly after zero field in the negatively biased field direction as shown in Fig. 4. Also, the collapse dynamics among the individual nano-objects are mostly pronounced in lower fields, and produce short helices after dense lattice stabilization. On the other hand, short helices in sparse states are formed presumably due to the available space among the nano-objects.

6.3.5 Evaluation of spin textures from the helical state

So far, we have discussed the effect of reducing the applied field on the sparse states as well as lattice states, and observed a transition into the helical phase. We will next discuss the transitions with increased fields, starting from a helical ground state and use the same tilting procedure as before for the lattice stabilization. In this case, a narrower stability region is found for the topological spin textures. We have noticed that the field transition region from the helix plus non-trivial states to the fully condensed lattice state is smaller in comparison to the previously applied same protocol from the field polarized state to lattice state. It means that on decreasing mode of the field and using the lattice state stabilization of tilting protocol, a metastable state exists for a very large range of magnetic fields (see Ch. 4 also). For example, at 350 K, the ground state helical phase forms a helix plus antiskyrmion phase at 224 mT. An antiskyrmion lattice state forms at 240 mT i.e., only after the field of 16 mT more. As seen in Fig. 9a-d, around 80 mT of field region, antiskyrmions are found in increasing field mode. However, using the same tilting lattice stabilization protocol starting from the polarized phase, the metastable state persists for a much larger field region. It is probable to happen due to the field history, and there is no fixed sharp boundary between various states of transformation. It also indicates that the transformation to non-trivial topological phase from the trivial helical state requires higher energy than the trivial field polarized phase. Starting from the helical phase and in increasing field mode (using lattice stabilization via tilting), we experimented with several other temperatures in the ~ 170 nm thick specimen. The different magnetic phase evolution as a function of temperature and magnetic field, using the tilting protocol of lattice stabilization, is summarized in Fig. 10. Qualitatively, for the increasing field mode of helical state, the field stability is nearly four times less than the decreasing mode of the field. At 350 K, only square antiskyrmions in the lattice and sparse states are found (Fig. 9a-d). The same square-shaped antiskyrmion also finds for decreasing field mode using the same lattice stabilization method of tilting (see Fig. 3, Ch. 4). However, at room temperature, round antiskyrmions are only found in the increasing mode of field stability protocol (Fig. 9e-h), whereas in decreasing field mode, stability region has both round and square skyrmions (see Fig. 2 Ch. 4). At 268 K, we have also found the same co-existing result of skyrmion and antiskyrmions in the field increasing mode (Fig. 9i-l). At 250 K, 200 K, and 150 K, both lattices and sparse state of elliptical Bloch skyrmions are formed. Below the spin reorientation transition, only sparse states of elliptical skyrmions are observed similar to the decreasing mode of the field for the ~ 170 nm thicker film. Moreover, for ~ 280 nm thick lamella, we find the lattice state at 100 K (Appendix C.3).

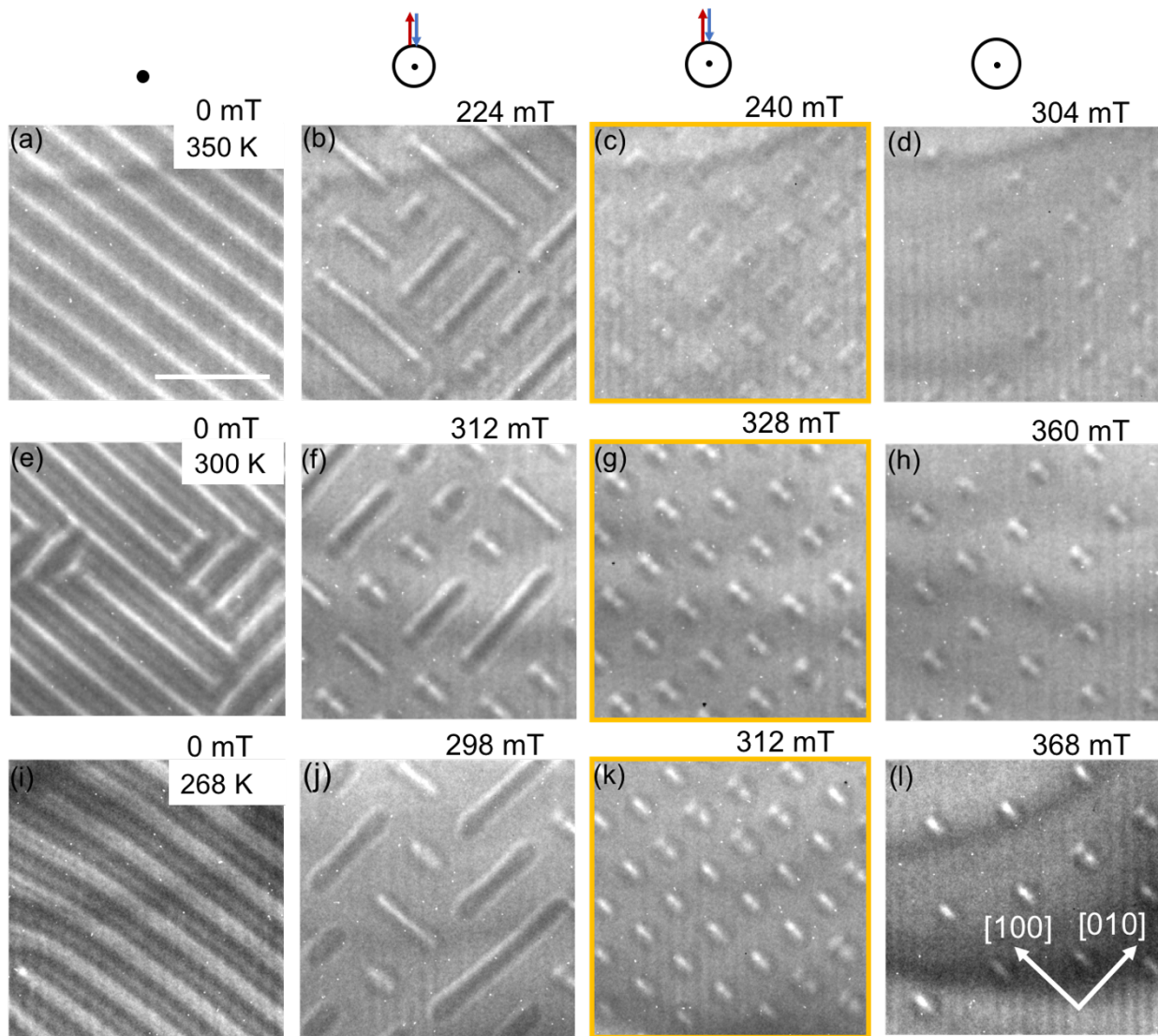


Figure 9 | Magnetic Phase diagram from the Helical state. The similar type lattice stabilization protocol used, as in Ch. 4, but this time, we started from the helical ground state in the increasing field mode. In (a-d), LTEM contrasts for the 350 K. The ground state is the helical state. A helical plus square antiskyrmion state is found at 224 mT. After that, we only decrease the out-of-plane field, and an isolated state is shown at 304 mT. (e-h) Similar experiment is performed at 300 K. Here, in increasing field mode, only round antiskyrmions are found. (i-l) LTEM measurement at 268 K. Four elliptical skyrmions with opposite chiralities (2 each) are found at 298 mT. At 312 mT and 368 mT; simultaneous observation of the elliptical Bloch skyrmions and antiskyrmions as the lattice and isolated state are formed. The scale bar in (a) corresponds to 500 nm.

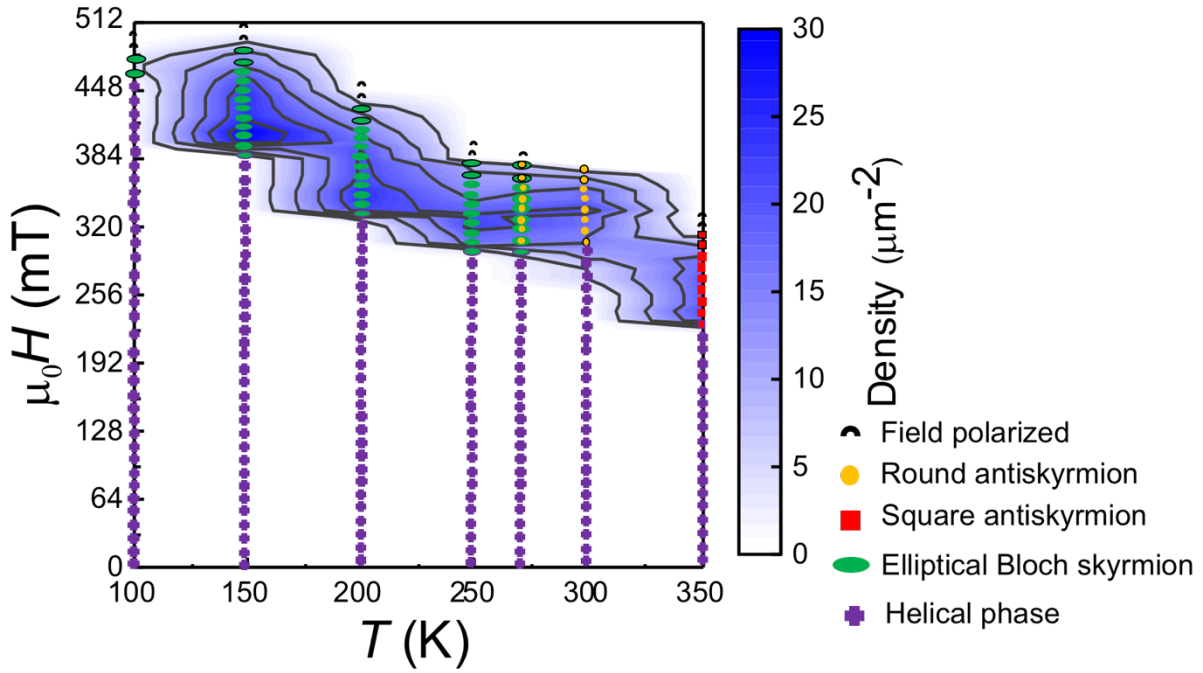


Figure 10 | Magnetic Phase diagram from the Helical state. Temperature vs. magnetic field phase diagram in the increasing mode of field. The magnetic phase diagram is constructed using the same lattice stabilization method as shown in Fig. 11 of Ch. 4, but this time, the LTEM measurement was performed from the helical phase and in the increasing mode of the magnetic field.

6.3.6 Stability of elliptical skyrmions against heating

In this section, we will present the experimental study of the elliptical Bloch skyrmions stability against heating at a constant magnetic field. We want to examine whether those Bloch elliptical skyrmions will survive up to the higher available temperature beyond the usual elliptical skyrmions stability region (below room temperature) or a transition to antiskyrmions will happen automatically without the application of in-plane field component.

First, the triangular lattice of elliptical skyrmions are stabilized at 100 K (in ~ 280 nm thick lamella) with the help of an in-plane field component. After that, we reduced the out-of-plane field to 180 mT (Fig. 11a). From there, we increase the temperature of the lamella using a heater controller up to 355 K. The schematic diagram of the heating experiment is shown in Fig. 11b. It is shown that the elliptical skyrmions are also found up to 260 K (Fig. 11c). At 297 K (Fig. 11d), distorted shape of elliptical skyrmions are found. The distorted shape nano-objects

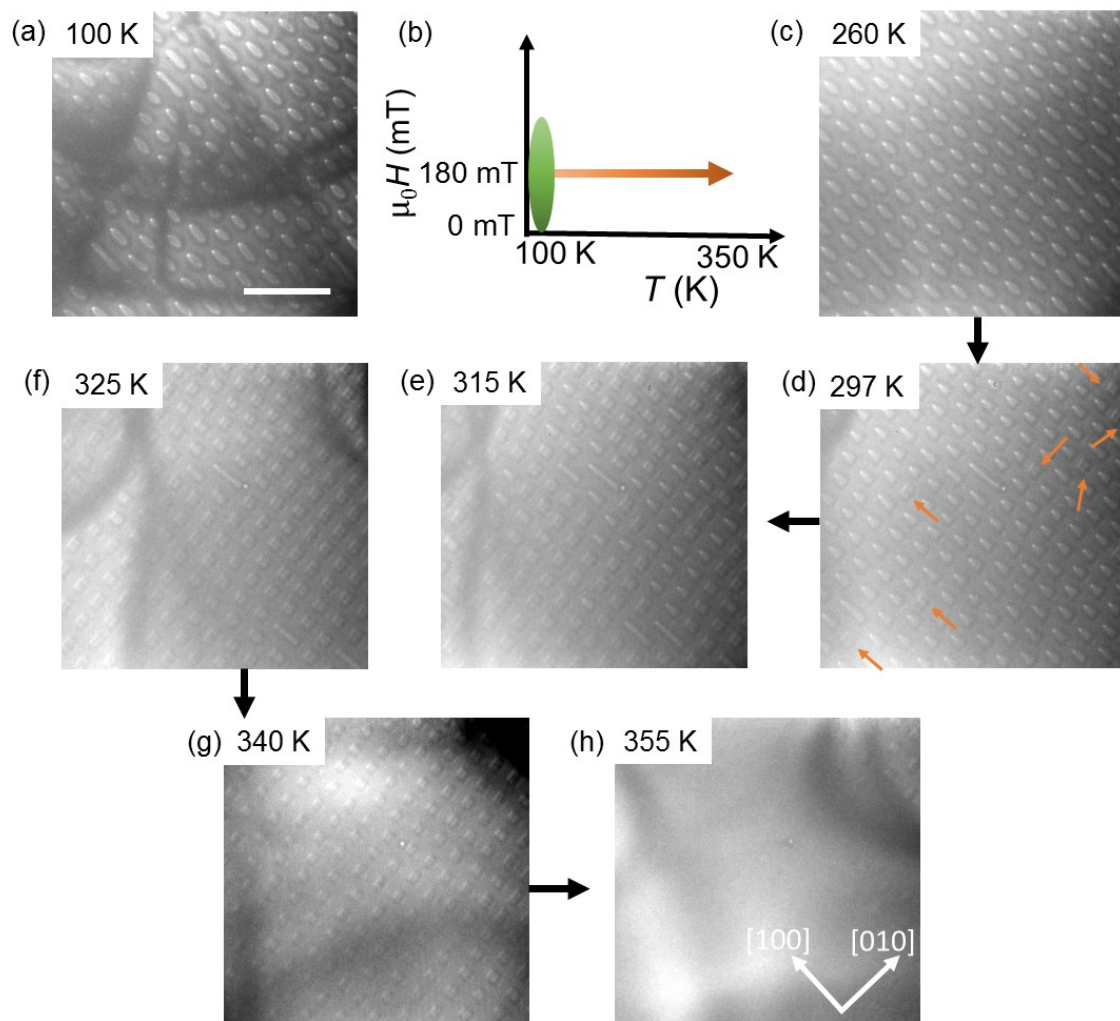


Figure 11 | Heating experiment from elliptical skyrmion lattice state. (a) Elliptical skyrmions triangular lattice state is formed at 100 K after the temporary in-plane field application in high magnetic field. The out-of-plane field is then reduced to 180 mT. (b) Schematic diagram of the heating experiment from the lattice state shown in (a). (c-h) Keeping the magnetic field constant, the temperature is increased up to 355 K. Different states are evolved as follows: (d, e) trivial bubble+ antiskyrmions, (f, g) antiskyrmions and (h) sparse state. Orange arrows in (d) points to antiskyrmions. The scale bar in (a) corresponds to 1 μm .

are similar to the structure of the trivial bubbles which are elongated along the [100] direction. Here, we have also observed the transformation to antiskyrmions of square-shaped as marked by the orange arrows. Further increase in temperature by 18 K (Fig. 11e), large number of antiskyrmions are observed and few trivial bubbles are found. Moreover, trivial bubbles are

transformed to antiskyrmions at 325 K (Fig. 11f). Few short helices are observed at 315 K which are existed up to 325 K. At 340 K, the lamella is filled with antiskyrmions only (Fig. 11g). On increasing the temperature, antiskyrmion starts to annihilate. Few antiskyrmions are left at 355 K and the region is mostly filled with polarized state as shown in Fig. 11h. This shows that elliptical skyrmions stability is more pronounced in low temperatures. The formation of square antiskyrmion by the heating experiment and the nucleation of them by in-plane field component (shown in Fig. 9b-d) lattice stabilization protocol at higher temperatures indicates that dipole-dipole interactions are less relevant due to the less saturation magnetization value, and DMI is the dominant interaction at higher temperature above 300 K on this tetragonal inverse Heusler compound.

6.4 Summary

In conclusion, we have inspected the different metastable state and their stability against the temperature and detail field history. The metastable square antiskyrmions have been formed in low temperatures using the field cooled protocol without the need of in-plane field components. The formation of short helices derives from elliptical Bloch skyrmions, antiskyrmions and their collapse dynamics are observed. Two new spin textures, namely fractional antiskyrmion and fractional elliptical Bloch skyrmion have been found for the first time and they are stabilized near the edge of the specimen. The stability of sparse and lattice states and their metastability against the in-field are demonstrated successfully in the experiment. Also, it is found that for similar protocol stability, the stability region of topological spin textures is nearly four times less for driving the magnetic field from the ground state helical phase than the polarized state. Finally, we have shown that in our experiment, at temperatures higher than that room temperature, the square antiskyrmions are almost the dominate spin textures and there is no elliptical skyrmions formation by various protocols; such as stabilization of lattice by in-plane field both in the increasing and decreasing field mode, and also by the heating experiment from an elliptical skyrmions lattice at the constant magnetic field from the 100 K to 350 K.

7 Observation of antiskyrmions and Bloch skyrmions in a low moment ferrimagnetic Heusler compound

7.1 Introduction

Ferrimagnet has more significant advantages over the ferromagnet due to the elimination of dipole fields derived from the moments of magnetic nano-objects, which holds the key for successful applications in spintronics devices¹⁴⁵⁻¹⁵⁰. Besides its significance importance in technological applications, very few attempts have been made to investigate skyrmionic spin textures in ferrimagnetic systems^{22, 151}. In this regard, low or even zero moment skyrmions or antiskyrmions hosting materials are very important. In the inverse tetragonal Heusler compounds such as Mn_2RhSn , the magnetic structure consists of two ferromagnetically aligned Mn sub-lattices that are antiferromagnetically coupled to each other¹⁵². This results in a low magnetic moment structure, and hence Mn_2RhSn is a ferrimagnetic Heusler compound.

Herein, we will explore the possibility of both antiskyrmions and Bloch skyrmions in a second ferrimagnetic inverse tetragonal Heusler compound $\text{Mn}_2\text{Rh}_{0.95}\text{Ir}_{0.05}\text{Sn}$. It has a significantly reduced magnetization compared to the only previous Heusler material ($\text{Mn}_{1.4}\text{Pt}_{0.9}\text{Pd}_{0.1}\text{Sn}$) in which topological spin textures were observed. Nevertheless, the small magnetization in this compound without significant Mn vacancies is enough to observe the spin textures using Lorentz transmission electron microscopy. Both individual and lattices of spin textures can be stabilized over a wide range of temperatures from near room temperature to 98 K. Helical spin textures are found in the low field region, which evolves into antiskyrmions or Bloch skyrmions structures in the presence of small magnetic fields. A weaker Dzyaloshinskii-

Moriya interaction is expected for the 4d element such as Rh compared to the 5d element like Pt, so that the observation of spin textures in $\text{Mn}_2\text{Rh}_{0.95}\text{Ir}_{0.05}\text{Sn}$ establishes the stability of them in these Heusler compounds. The finding of opposite topological charges in $\text{Mn}_2\text{Rh}_{0.95}\text{Ir}_{0.05}\text{Sn}$ opens up the path to the full exploitation of the considerable tunability of the D_{2d} Heusler compounds, via chemical tuning, for zero-moment antiferromagnetic skyrmion and antiskyrmions.

7.2 Experimental methods

7.2.1 Bulk polycrystalline synthesis

Polycrystalline ingots of $\text{Mn}_2\text{Rh}_{0.95}\text{Ir}_{0.05}\text{Sn}$ were prepared by the inductive melting method. The stoichiometric amounts of the elements Mn, Ir, Rh, and Sn of purity > 99.99% were taken in a dried alumina crucible. Because of the high melting points of Iridium and Rhodium, a pre-alloying step was carried out. The Rh and Ir powders were first pre-alloyed together with Sn. The alloy was then kept in the melted state for a minute (approximately) before cooling down. The above step was repeated three times in order to ensure good homogenization of the pre-alloy. In a second step, the Mn chips were added to the Rh/Ir-Sn ingot in order to prepare the desired Mn-Rh-Ir-Sn alloy followed by re-melting and turning the ingots several times for better homogeneity. After the last melting step, the ingot was finally cooled down by lowering the temperature slowly below the solidus temperature. Subsequently, the induction coil was switched off so that the ingot could cooled down naturally to room temperature. All alloying steps have been performed under inert gas conditions in a glove box. The procedure ensures a low loss of Mn due to evaporation, and indeed, the total mass loss was below 0.5 wt% for the final ingot. In this way, the composition of the ingot is close to the required stoichiometry. The as-prepared ingots were then packed in a closed tantalum crucible that was further encapsulated in an evacuated fused quartz glass ampoule. Subsequent heat treatment for one week at 900 °C was performed followed by quenching in an ice-water mixture resulting in the final polycrystalline bulk samples.

7.2.2 Powder XRD, EDXS, and EBSD

The crystal structure and phase purity were characterized by powder X-ray diffraction (PXRD) using an image-plate Guinier camera (Huber G670, Cu $K\alpha_1$, $\lambda = 1.54059 \text{ \AA}$). The peak searching, indexing, and calculation of the diffraction patterns were performed with the aid of

WinXPow package.¹⁵³ All the Bragg reflections can be indexed to a body-centered tetragonal unit cell with $a = 4.293 (3) \text{ \AA}$ and $c = 6.592 (4) \text{ \AA}$. So, the c/a ratio is 1.53. The Rietveld refinement was carried out using Jana2006 software¹⁵⁴. The crystal structure was resolved in analogy with Mn_2RhSn that crystallizes in $\bar{I}4m2$ (D_{2d} symmetry) space group¹⁵². Under the symmetry, Mn atoms occupy two different Wyckoff positions, namely MnI at $2b(0,0,1/2)$ and MnII at $2c(0,1/2,1/4)$; while Rh occupies $2d(0,1/2,3/4)$ and Sn in the $2a(0,0,0)$ position, respectively. In our refinement, Ir was assumed to occupy the Rh position and statistically distributed on the $2d$ site. Considering the cases in which Ir additionally occupies the Sn or Mn sites do not lead to an improvement of the refinement. Therefore, we discarded the latter possibility. The Rietveld refinement of the powdered XRD pattern is shown in Fig. 1. A schematic unit cell arrangement of different atoms in $\text{Mn}_2\text{Rh}_{0.95}\text{Ir}_{0.05}\text{Sn}$ is shown in the inset of Fig. 1.

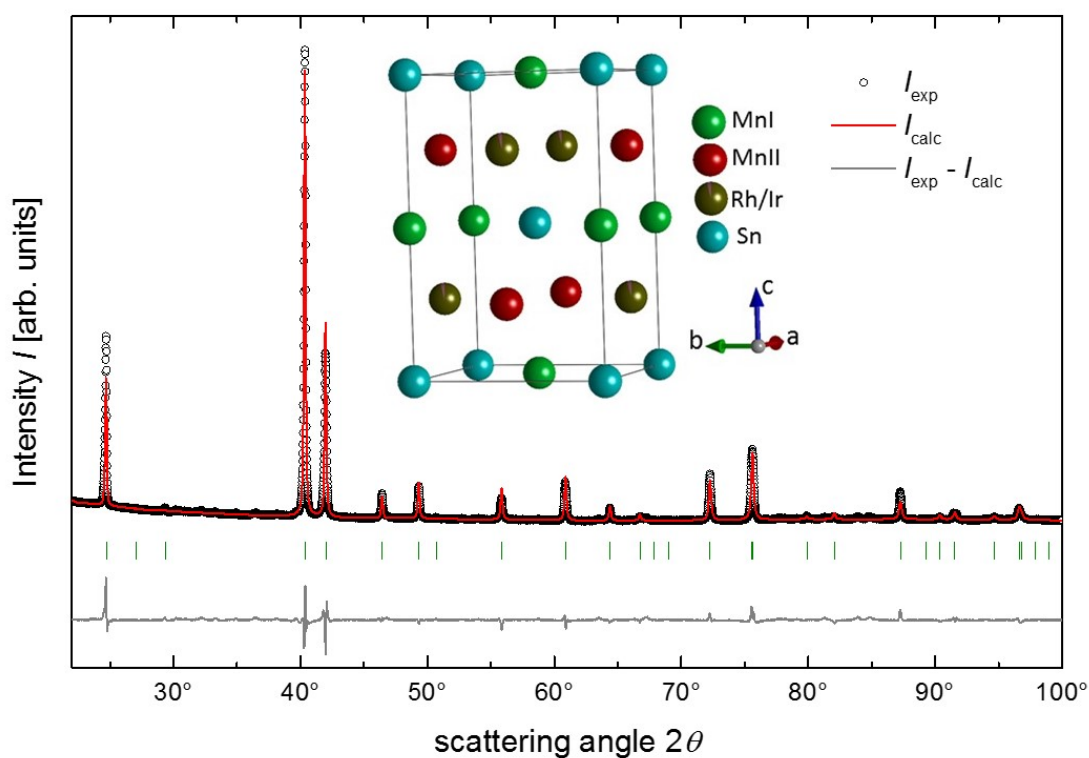


Figure 1 | XRD analysis. Rietveld refinement of powder X-ray diffraction (PXRD) pattern of $\text{Mn}_2\text{Rh}_{0.95}\text{Ir}_{0.05}\text{Sn}$.

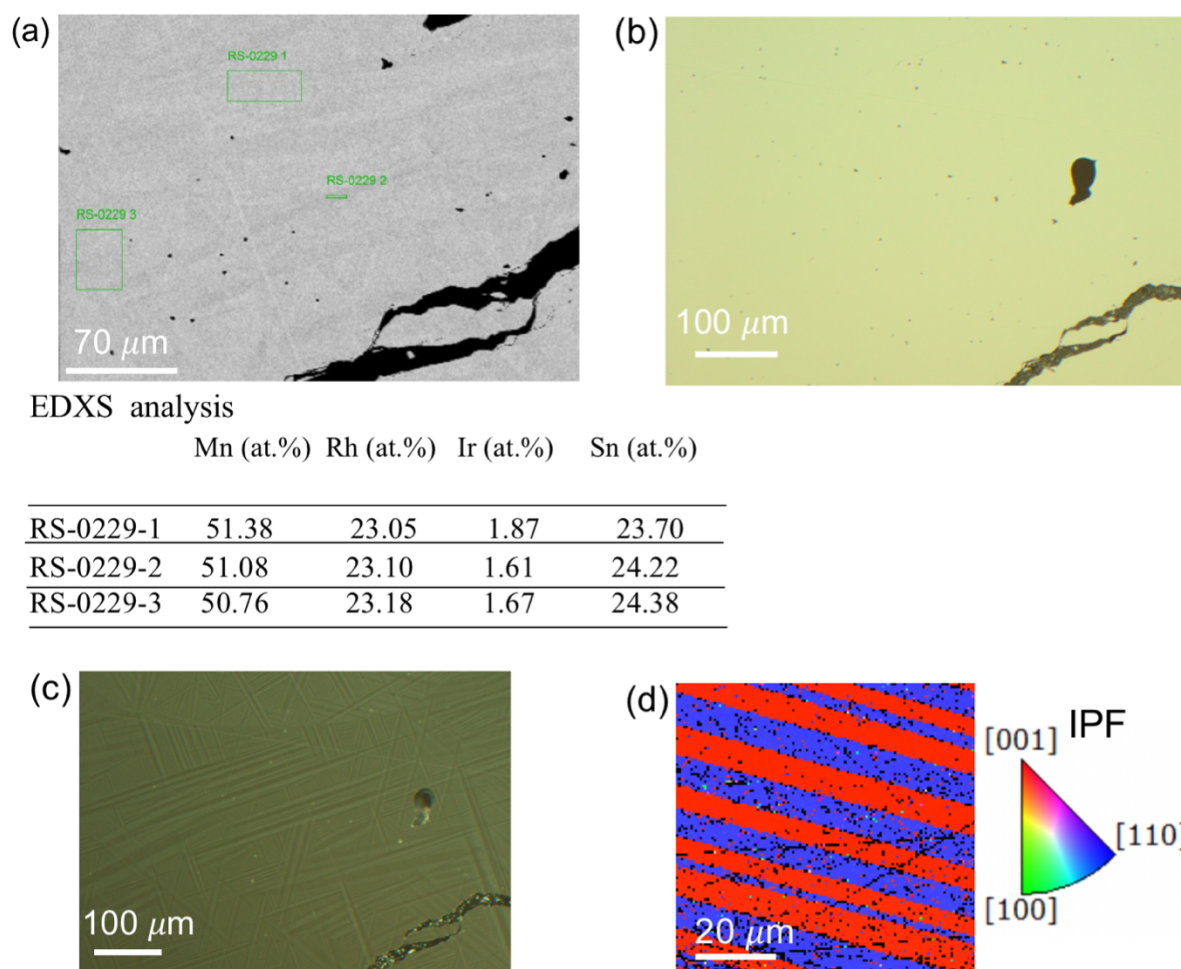


Figure 2 | Composition and grain analysis. (a) Scanning electron microscope (SEM) image of $\text{Mn}_2\text{Rh}_{0.95}\text{Ir}_{0.05}\text{Sn}$ sample. Black dots contrast is porous and the left side shows a small crack in the bulk sample. EDX is performed on the three different regions marked in green color. The analysis results in atomic % are given below the figure. (b) and (c) are bright and optical images overview. (d) EBSD measurement shows the IPFZ map and IPF the color key (right side) for the tetragonal compound $\text{Mn}_2\text{Rh}_{0.95}\text{Ir}_{0.05}\text{Sn}$.

The surface topography of the sample is analyzed using a scanning electron microscope (SEM). Fig. 2a shows the SEM image of a $\text{Mn}_2\text{Rh}_{0.95}\text{Ir}_{0.05}\text{Sn}$ bulk sample. The stoichiometry of the titled compound is found to be $\text{Mn}_{1.988}\text{Rh}_{0.949}\text{Ir}_{0.049}\text{Sn}_{1.015}$ (within an estimated standard deviation of 0.1-0.2 at%) from coupled plasma optical emission spectrometry (ICP-OES) analysis. Besides, the composition of the sample was also determined by Energy-dispersive X-

ray spectroscopy (EDXS). EDXS was carried out on the smooth surface of the sample that marked (in green color) as RS-0229 1, RS-0229 2, RS-0229 3 using a PhilipsXL30 system with an XFlash SDD detector. The EDXS analysis shown in Fig. 2a confirms that it is stoichiometric. In addition, a bright-field view confirms the single-phase nature of the bulk sample as shown in Fig. 2b. Polarized light image (Fig. 2c) and electron backscattering diffraction (EBSD) in Fig. 2d shows that grains are not big enough. The inverse pole figure (IPFZ) map of Fig. 2d indicates two different grains (red color [001] and blue color [110]) of varying sizes which are ranging from 10-15 microns. The IPF color key on the right side of Fig. 2d indicates the crystal axis orientations of this tetragonal system which perpendicular to the surface.

7.2.3 Magnetization measurements

The temperature (T) and field (H) dependent DC magnetization (M) measurements of the polycrystalline sample $\text{Mn}_2\text{Rh}_{0.95}\text{Ir}_{0.05}\text{Sn}$ were carried out in a SQUID [Quantum design, MPMS3]. The temperature dependent magnetization was performed in a field of 0.1 T for the temperature range from 2 to 390 K after both zero-field-cooling (ZFC) and field-cooling (FC) (Fig. 3a). In the ZFC mode, the temperature is lowered from the room temperature (paramagnetic state) to the lowest available temperature 2 K and magnetic moment with the increasing temperature being measured under the presence of 0.1 T. In the FC protocol, the same DC field of 0.1 T is subjected to decreasing temperature and after that magnetic moment is measured against increasing temperature. The sample undergoes a magnetic ordering transition from a paramagnetic to a ferrimagnetic state at $T_C \sim 270$ K and a second magnetic transition at $T_{\text{SRT}} \sim 80$ K as shown in Fig. 3a. Above 80 K up to the critical temperature, the sample is ferrimagnetically ordered. The latter transition (below ~ 80 K) has been attributed to a spin-reorientation transition that results from a competition between exchange interactions between Mn moments on neighboring and next-nearest planes¹⁵². The spin-canting transition is suppressed in a higher field at 1 T, as evident from the temperature-dependent magnetization data. Fig. 3b shows the $M(H)$ loops measured at different temperatures. The saturation magnetization of this material is found to be $\sim 2 \mu_B/\text{f.u}$ at 2 K from the measurement. The value reduces with the increase in temperature and it becomes $\sim 1 \mu_B/\text{f.u}$ at 250 K. The antiferromagnetically coupled Mn sub-lattices in $\text{Mn}_2\text{Rh}_{0.95}\text{Ir}_{0.05}\text{Sn}$ is forming the ferrimagnet. By contrast, in the case of Heusler compound such as $\text{Mn}_{1.4}\text{Pt}_{0.9}\text{Pd}_{0.1}\text{Sn}$, the Mn vacancies strongly affect the overall magnetization of the compound and it is much higher $\sim 4.5 \mu_B/\text{f.u}$ at 2 K^{51, 155}.

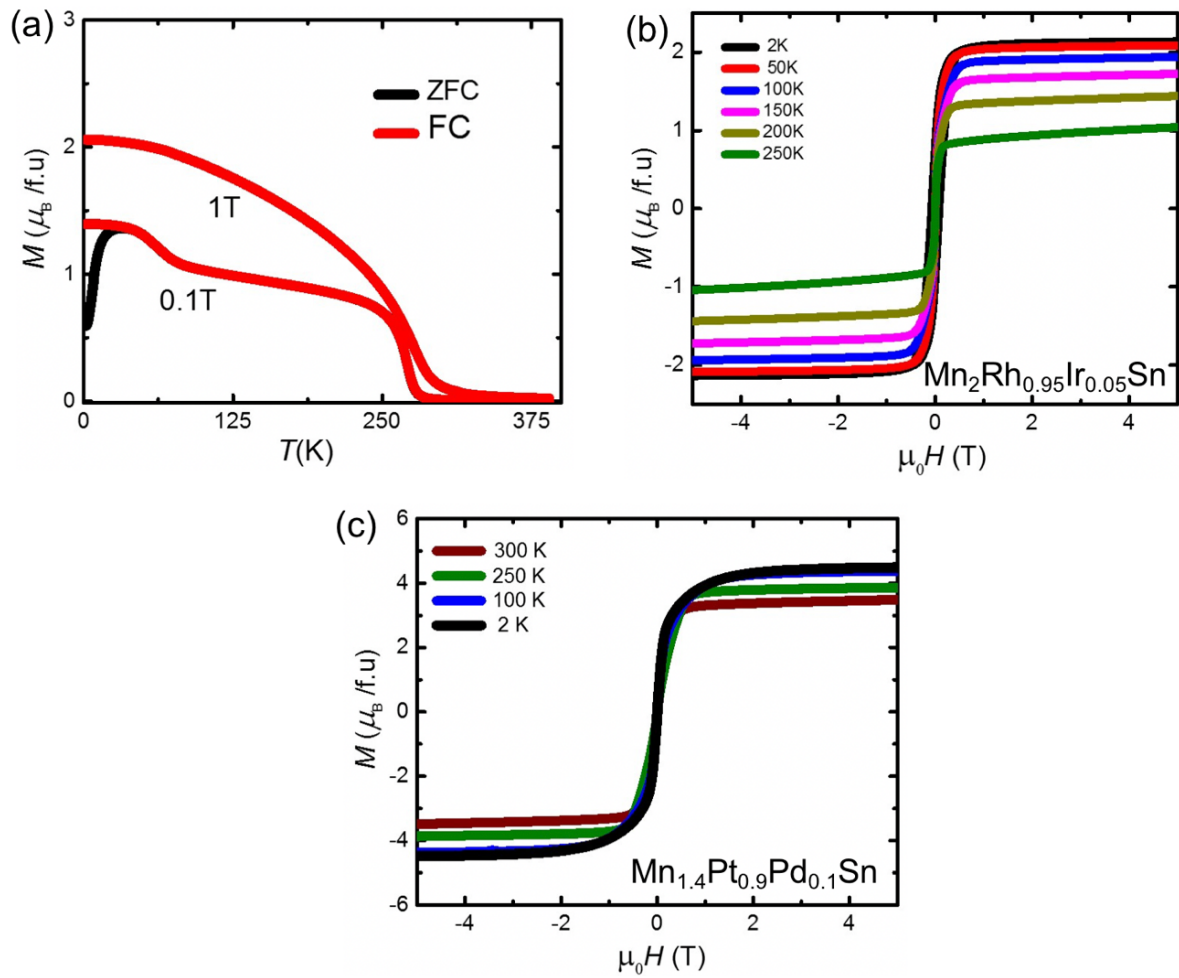


Figure 3 | Magnetization measurements. (a) and (b) are $M(T)$ and $M(H)$ measurements of the Heusler compound $\text{Mn}_2\text{Rh}_{0.95}\text{Ir}_{0.05}\text{Sn}$. (c) $M(H)$ for the Heusler compound $\text{Mn}_{1.4}\text{Pt}_{0.9}\text{Pd}_{0.1}\text{Sn}$.

The Mn vacancies reduce considerably the compensation of the moments between the two expected antiferromagnetically coupled Mn sub-lattices leading to a very high value of overall magnetization and the compound is almost a “ferromagnet”. Hence, it has been reported that both $\text{Mn}_{1.4}\text{Pt}_{0.9}\text{Pd}_{0.1}\text{Sn}$ and $\text{Mn}_{1.4}\text{PtSn}$ are effective ferromagnets¹⁵⁵⁻¹⁵⁷. The magnetization measurement for the $\text{Mn}_{1.4}\text{Pt}_{0.9}\text{Pd}_{0.1}\text{Sn}$ Heusler compound is shown in Fig. 3c. Importantly, the saturation magnetization of ferrimagnetic $\text{Mn}_2\text{Rh}_{0.95}\text{Ir}_{0.05}\text{Sn}$ is nearly two times smaller than that of the later material where the antiskyrmions were first observed ($\text{Mn}_{1.4}\text{Pt}_{0.9}\text{Pd}_{0.1}\text{Sn}$). It is apparent from the isothermal magnetization data that these compounds are magnetically soft.

7.2.4 Microscopy characterizations

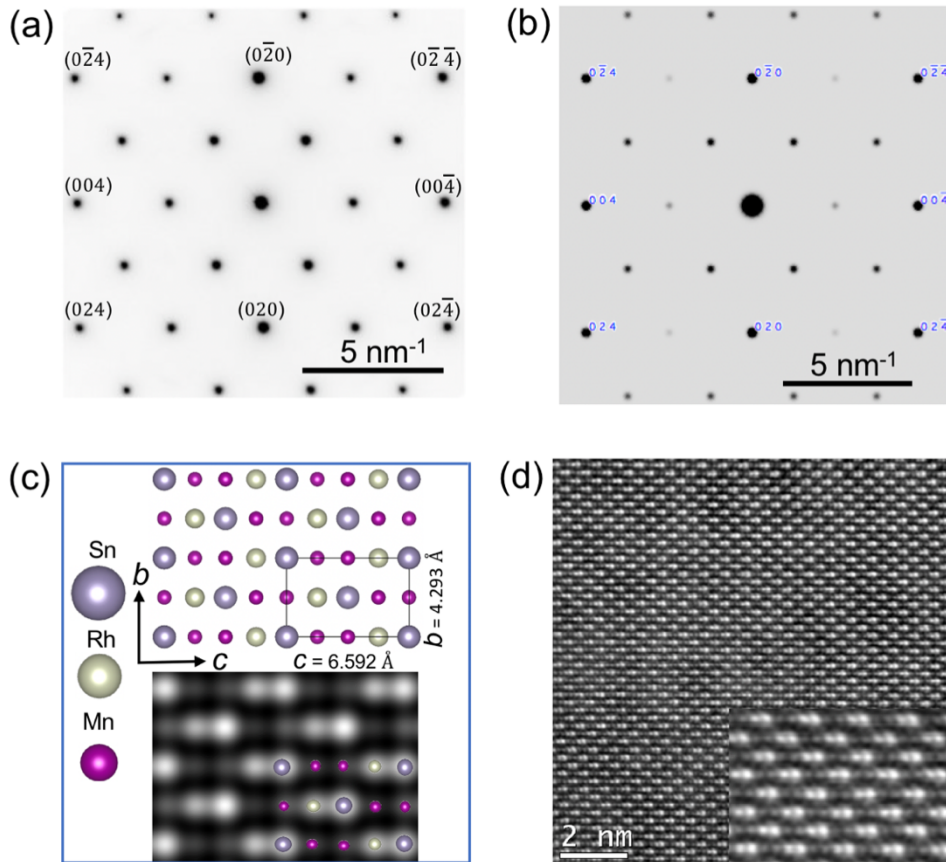


Figure 4 | Microscopic measurements. (a), (b) Experimental and simulated electron diffraction pattern for the [100] zone-axis lamella. (c) As a guide to the eye, the schematic atomic arrangements (upper panel) and the simulated STEM pattern (lower panel) for the [100] zone-axis is shown. The unit cell is drawn in the right corner of the upper panel. (d) The experimental STEM image. The inset shows the enlarged view.

In-situ transmission electron microscope (TEM) was used to investigate the diffraction pattern, HRTEM, STEM, and LTEM using thin lamellae. The single crystalline lamellae, oriented along different crystal directions, were lifted from the individual grains within the polycrystalline $\text{Mn}_2\text{Rh}_{0.95}\text{Ir}_{0.05}\text{Sn}$ bulk sample. In principle, a thin cross-section lamella from the red region in EBSD pattern of Fig. 2d will give rise to a [100] zone-axis oriented lamella and surface parallel prepared lamella as a [001] zone-axis, while the surface of both lamellae are placed perpendicular to the electron beam in TEM. However, the small grain size (~10–

15 μm) in a bulk sample meant that the as-prepared lamellae of particular orientation were non-trivial. A [100] oriented lamella of approximately 60 nm thick was prepared using the focused ion beam (FIB). The zone-axis orientation is confirmed by the exemplary selected area electron diffraction pattern (SAED) shown in Fig. 4a. The diffraction pattern matches exactly with the simulated diffraction pattern (using CrystalMaker software) shown in Fig. 4b. Fig. 4c represents a schematic atomic arrangement of the Sn, Rh, and Mn atomic columns along this zone-axis. The unit cell for this tetragonal structure is depicted in the upper panel of Fig. 4c, while in the lower panel, simulated scanning transmission electron microscopy (STEM) image using the aforementioned space group was shown¹¹⁷. These observations agree well with the experimental STEM image shown in Fig. 4d. The inset of Fig. 4d represents an enlarged portion of the image taken from the experimental STEM.

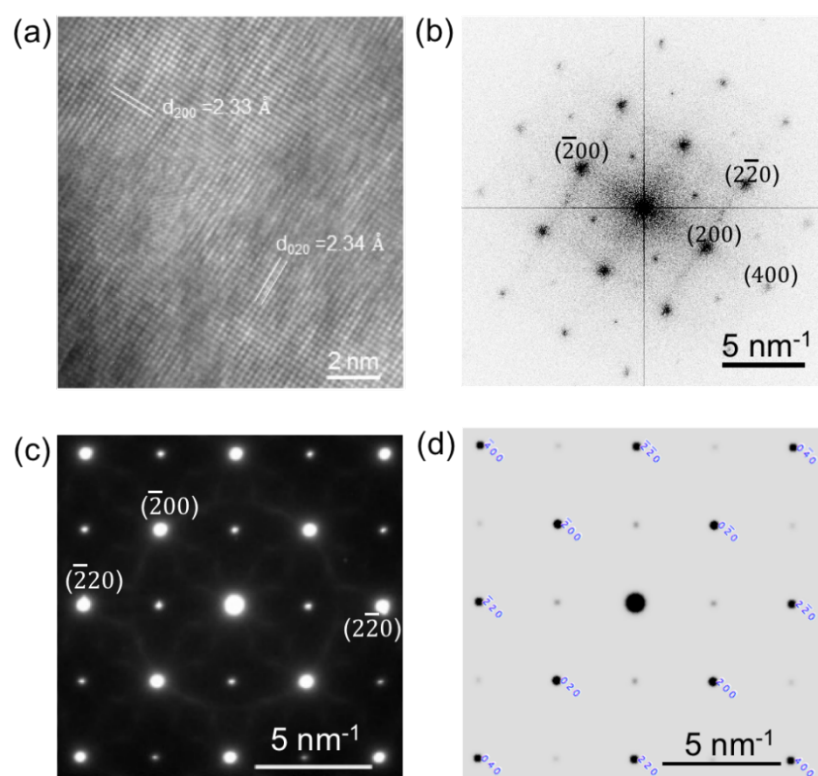


Figure 5 | Magnetic antiskyrmion in $\text{Mn}_2\text{Rh}_{0.95}\text{Ir}_{0.05}\text{Sn}$. (a) High-resolution transmission electron microscope (HRTEM) image for a [001] oriented lamella. (b) The corresponding fast Fourier transform is observed from the HRTEM. (c) Selected area electron diffraction (SAED) pattern of the [001] oriented lamella. (d) The simulated diffraction pattern of the [001] zone-axis that matches with (b) and (c).

A thin surface parallel lamella (thickness ~ 110 nm) is prepared from the red stripe region as shown in EBSD. High-resolution TEM (HRTEM) image of such a lamella showing (020) and (200) lattice planes are presented in Fig. 5a. A fast Fourier transform (FFT) is mapped out from HRTEM as shown in Fig. 5b. The selected area diffraction pattern (Fig. 5c) matches the simulation pattern (Fig. 5d) and it confirms that the lift out lamella is a [001] orientated zone-axis.

7.3 Results and discussion

7.3.1 Magnetic antiskyrmions in $Mn_2Rh_{0.95}Ir_{0.05}Sn$

Lorentz TEM (LTEM) imaging technique was carried out to explore magnetic textures within the lamella. A thickness of ~ 150 nm [001] zone-axis oriented lamella is used to image magnetic contrasts. Clear evidence of the presence of non-collinear spin texture in the lamella is found. In Fig. 6b shows a typical LTEM image of a single antiskyrmion at 150K, and 83 mT. The schematic of antiskyrmion spin structure is shown in Fig. 6a in which Bloch domain walls of opposite chirality are formed along [100] and [010] crystallographic directions, while Néel domain walls of opposite chirality are formed along [110] and $[\bar{1}10]$ directions. Néel domain does not have any LTEM contrast, whereas contrast profiles along the Bloch directions of [010] and [100], respectively are shown on the right side of Fig. 6b.

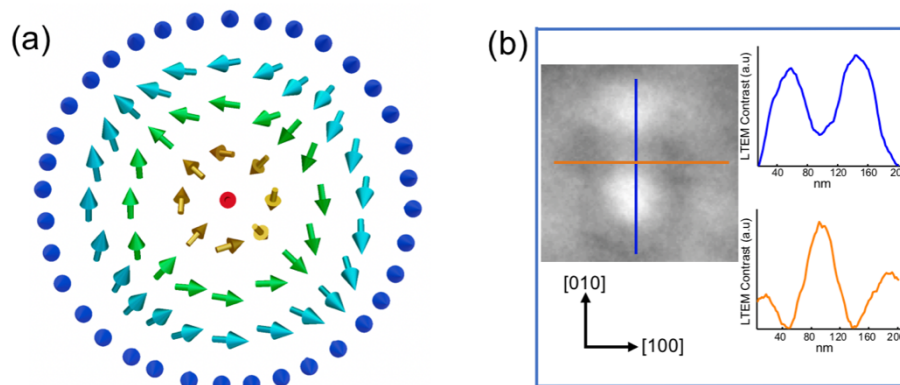


Figure 6 | Magnetic antiskyrmion in $Mn_2Rh_{0.95}Ir_{0.05}Sn$. (a) Schematic of an antiskyrmion spin texture. (b) LTEM image of single antiskyrmion at 150 K and a magnetic field of 83 mT. The right side shows the intensity profiles of the LTEM contrast along [010] (blue color) and [100] (orange color) directions.

7.3.2 Field driven formation of antiskyrmions

Here, we observe the magnetic field-driven evolution of spin textures at a constant temperature. The spin structure of the tetragonal basal plane lamella (plane perpendicular to [001] direction) is examined after cooling to 150 K in a zero magnetic field from the room temperature. After thermal stability at 150 K, the LTEM image is recorded in a zero field. The image pattern in the absence of a magnetic field is appeared in the form of alternating dark and light stripes as shown in Fig. 7a. These are the characteristic of a helical spin structure. The propagation direction of the helices is oriented nearly either along [010] or [100], in which the Bloch domain walls are formed. The magnetic dislocations are observed as the branching of helix marked by white arrows in Fig. 7a^{21, 158, 159}, whose movement and annihilation of these dislocations are observed upon the application of magnetic fields (Fig. 7b and 7c). The lamella is first tilted away from the zone-axis [001] by $\sim 25^\circ$ - 30° . The tilting direction is approximately along the [110] direction. A magnetic field is then applied along the microscope column (out-of-plane) by adjusting the current in the objective lens. The lamella is tilted back to the zone-axis of near zero-degree tilt to record the LTEM images. This process of tilting, which induces a small in-plane magnetic field on the lamella, is successively repeated to record at various other perpendicular (out-of-plane) magnetic fields. This tilting procedure is needed to overcome the energy barrier of the trivial helix state so that the antiskyrmion lattice can stabilize. Following the aforementioned protocol, antiskyrmions are found to emerge upon increasing the magnetic field from the helical spin texture at a field of ~ 75 mT. A co-existing state of antiskyrmion with the helical spin texture is found for fields up to ~ 83 mT (Fig. 7d, 7e). Further increment of the magnetic field (90 mT) leads to the formation of an antiskyrmion lattice, as shown in Fig. 7f, with a slightly distorted hexagonal array. We notice that a well-defined strong hexagonal lattice is not found. One of the possible reasons might be the low moment in $\text{Mn}_2\text{Rh}_{0.95}\text{Ir}_{0.05}\text{Sn}$, leading to weak magnetostatics interactions between themselves. With increasing the out-of-plane magnetic field up to a range of ~ 94 - 104 mT, the density of antiskyrmions decreases (Fig. 7g-h) before the transformation of the region to a fully field-polarized state at ~ 112 mT (Fig. 7i).

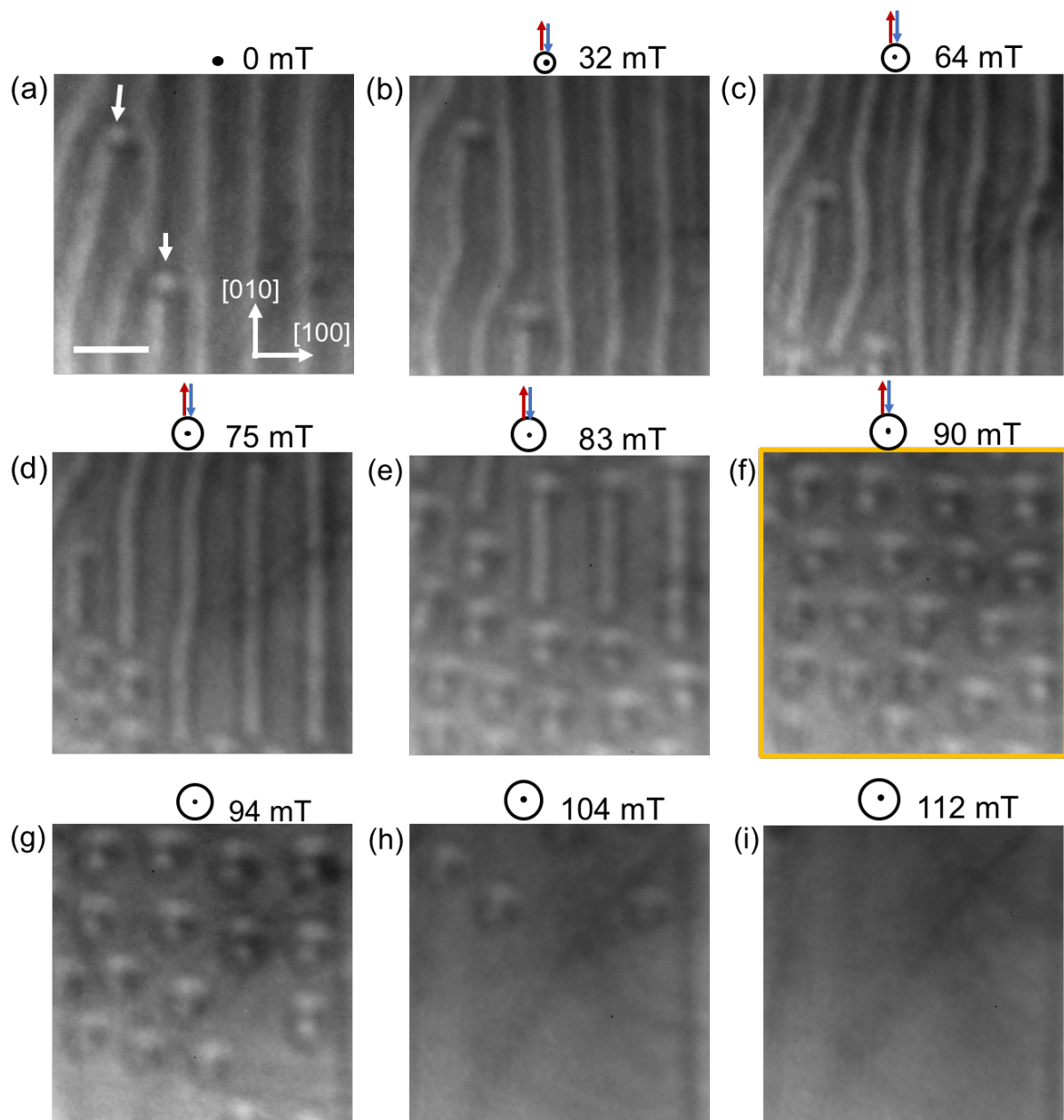


Figure 7 | Field dependent stability. Lorentz transmission electron microscopy (LTEM) images of magnetic spin-textures at (a) zero magnetic field and (b)–(i) various magnetic fields at 150 K. Red and blue arrows assigned to represent the temporary tilting of few degrees away from the [001] zone-axis followed by return back to the initial position of zero tilt. Then LTEM images are recorded. The application of temporary in-plane is continued up to a lattice state formed (marked by the yellow box) as shown in (f). After that, only the out-of-plane field is given without tilting the lamella. The scale bar in (a) corresponds to 300 nm.

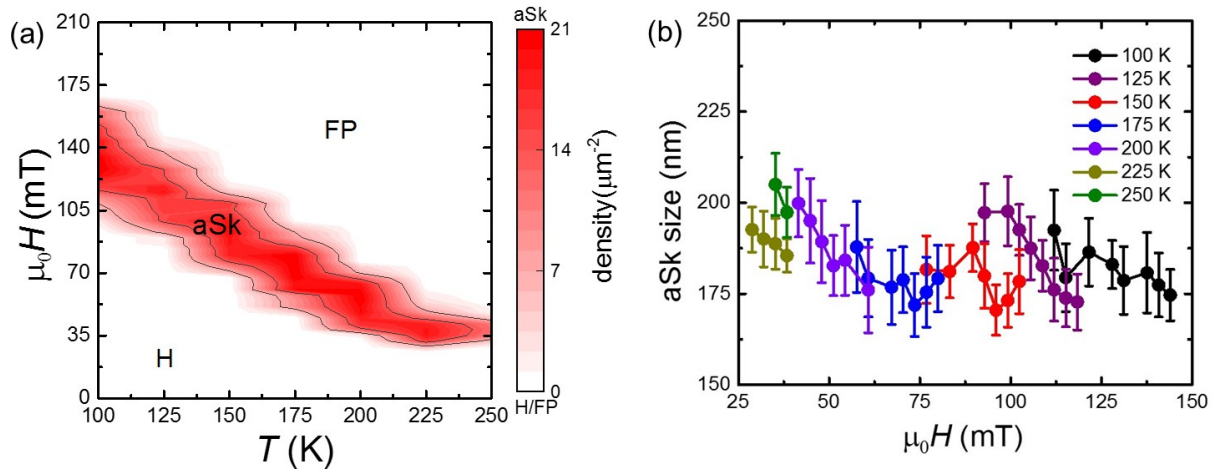


Figure 8 | Phase diagram for antiskyrmons. (a) Magnetic phase diagram of $\text{Mn}_2\text{Rh}_{0.95}\text{Ir}_{0.05}\text{Sn}$. The phase diagram is constructed on providing the temporary in-plane component of field along [110] direction (temporary tilting of the specimen) followed by returning to the initial zero tilt position. The temporary in-plane field component was provided until the antiskyrmion lattice state is formed (as in Fig. 7f) and then, only the out-of-plane field is increased up to the uniform magnetized state. (b) Antiskyrmion size as a function of the magnetic field (out-of-plane) at different temperatures. The error bars in (b) correspond to the standard deviation in the antiskyrmion size. Here aSk, H, FP correspond to antiskyrmion, helical and field polarized states, respectively.

The evolution of spin textures as a function of magnetic field is studied at several temperatures. First, the specimen is cooled down from 300 to 100 K in the absence of a magnetic field. After thermal stabilization, the nucleation of the antiskyrmion lattice from the helical phase is studied at 100 K using the protocol described in the previous paragraph. Subsequently, the temperature is increased successively in 25 K steps and LTEM studies are carried out at each temperature. These results are presented as a contour map of the antiskyrmion density (red color) in the temperature (T) - magnetic field (B) plane (Fig. 8a). It is clear from Fig. 8a that the nucleation of the antiskyrmion lattice from the helical phase requires relatively higher magnetic fields at a lower temperature or vice versa. In this Heusler compound, the antiskyrmion lattice is stabilized over a wide window of temperature, and in a relatively narrow magnetic field range. The effect on the antiskyrmion size as a function of magnetic fields at different temperatures is shown in Fig. 8b. From this figure, it is evident that there is a minute change in the size of antiskyrmion with the field at each temperature.

7.3.3 Helical periods of $\text{Mn}_2\text{Rh}_{0.95}\text{Ir}_{0.05}\text{Sn}$ and $\text{Mn}_{1.4}\text{Pt}_{0.9}\text{Pd}_{0.1}\text{Sn}$

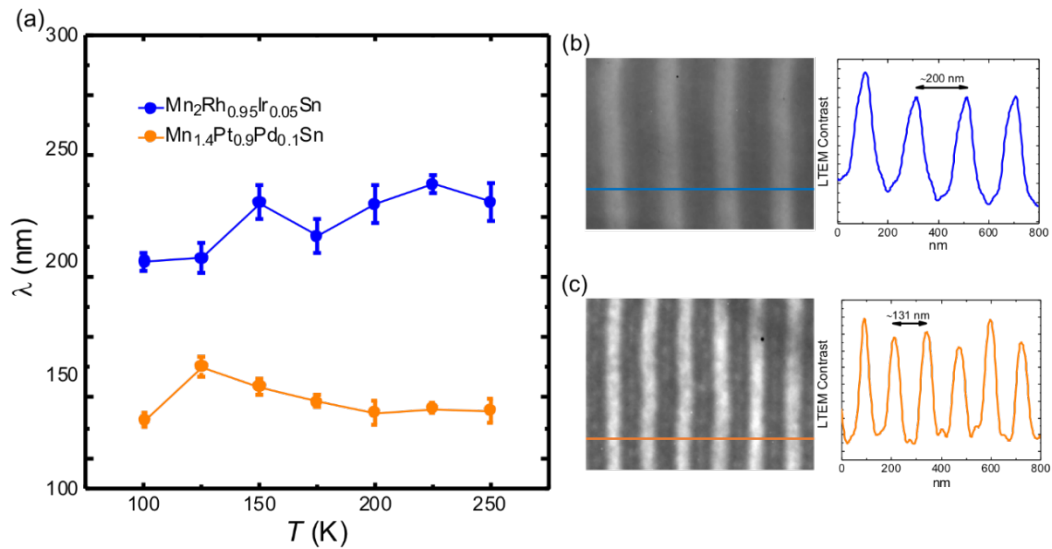


Figure 9 | Helical periods in the absence of magnetic field. (a) Comparison of the helix period (λ) for $\text{Mn}_2\text{Rh}_{0.95}\text{Ir}_{0.05}\text{Sn}$ (blue) and $\text{Mn}_{1.4}\text{Pt}_{0.9}\text{Pd}_{0.1}\text{Sn}$ (orange) as determined from LTEM, in zero magnetic field and various temperatures in lamellae of a comparable thickness of ~ 150 nm. The error bars correspond to one standard deviation. (b), (c) Typical LTEM images at 100 K and zero magnetic field and the corresponding line profiles for the two compounds: upper $\text{Mn}_2\text{Rh}_{0.95}\text{Ir}_{0.05}\text{Sn}$ (blue) and lower $\text{Mn}_{1.4}\text{Pt}_{0.9}\text{Pd}_{0.1}\text{Sn}$ (orange), respectively.

The ground state is the combinational helical phase in the absence of a magnetic field. The helical period (λ) is in the range of ~ 200 - 235 nm depending on the temperature as shown in Fig. 9a. The period is larger by $\sim 50\%$ than that of the reported Heusler compound $\text{Mn}_{1.4}\text{Pt}_{0.9}\text{Pd}_{0.1}\text{Sn}$ for the same thickness (~ 150 nm) of the LTEM lamella at zero magnetic field and different temperatures. A typical example of the helical periods obtained from the LTEM contrasts for both $\text{Mn}_2\text{Rh}_{0.95}\text{Ir}_{0.05}\text{Sn}$ and $\text{Mn}_{1.4}\text{Pt}_{0.9}\text{Pd}_{0.1}\text{Sn}$ lamellae at zero field and 100 K are shown in Figs. 9b and 9c, respectively. As λ is inversely proportional to DMI,^{160, 161} the larger helical period in $\text{Mn}_2\text{Rh}_{0.95}\text{Ir}_{0.05}\text{Sn}$ is consistent with a weaker value of the DMI⁵² expected for the 4d element Rh as compared to the 5d element Pt¹⁶²⁻¹⁶⁴. In addition, the smaller the DMI value and saturation magnetization⁵², the larger will be the helical period⁵².

7.3.4 Bloch skyrmions in $Mn_2Rh_{0.95}Ir_{0.05}Sn$

In the Heusler compound $Mn_{1.4}Pt_{0.9}Pd_{0.1}Sn$, other than antiskyrmions, Bloch skyrmions in elliptical shape were also found, and they are easily stabilized at low temperatures^{133, 134}. The long-range dipole-dipole interactions and the anisotropic DMI induce the stability of elliptical Bloch skyrmions in this compound. It was also found from the numerical calculation that dipolar energy scales nearly linear with the helical period (λ)⁵². We have already shown that for the same thickness ranges, λ is higher for the $Mn_2Rh_{0.95}Ir_{0.05}Sn$, and a higher dipole energy contribution may lead to the formation of Bloch skyrmions. Indeed, it is observed that Bloch skyrmions are observed from 98 K up to the near transition temperature. A typical example of LTEM contrast of a Bloch skyrmion of the circular shape is shown in Fig. 10a at 190 mT and 150 K. The central part is a bright contrast surrounded by the dark contrast. As dipole-dipole interactions induce opposite chirality, we similarly observe Bloch skyrmion with opposite chirality in this specimen, as shown in the LTEM image of dark contrast surrounded by the white contrast (Fig. 10b). Fig. 10c and 10d show the schematics of counter clock-wise and clock-wise chirality of Bloch skyrmions. Moreover, we also observe elliptically shaped Bloch skyrmions depending on the field strengths. This will discuss in the following sections.

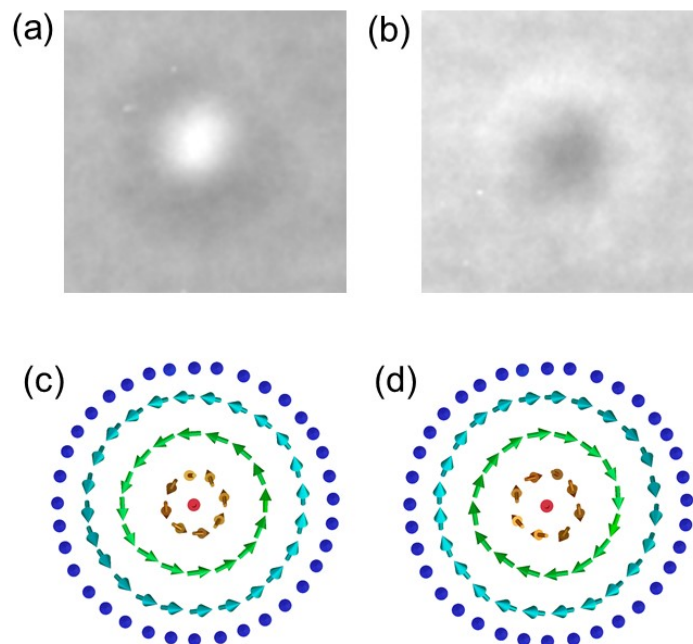


Figure 10 | *Bloch Skyrmions in $Mn_2Rh_{0.95}Ir_{0.05}Sn$.* (a), (b) Under-focused LTEM contrasts of Bloch skyrmions with opposite chiralities at 190 mT and 150 K. (c), (d) Schematics of the oppositely chiral Bloch skyrmions.

7.3.5 Field driven formation of Bloch skyrmions

The field-driven study of the spin textures nucleation is studied at 150 K (Fig. 11). The ground state consists of the combinational helical state (Fig. 11a). Here, we provide temporary in-plane field components by tilting the specimen along the $[100]$ direction. At 115 mT, following the same temporary tilting procedure as before, the spacing between the individual

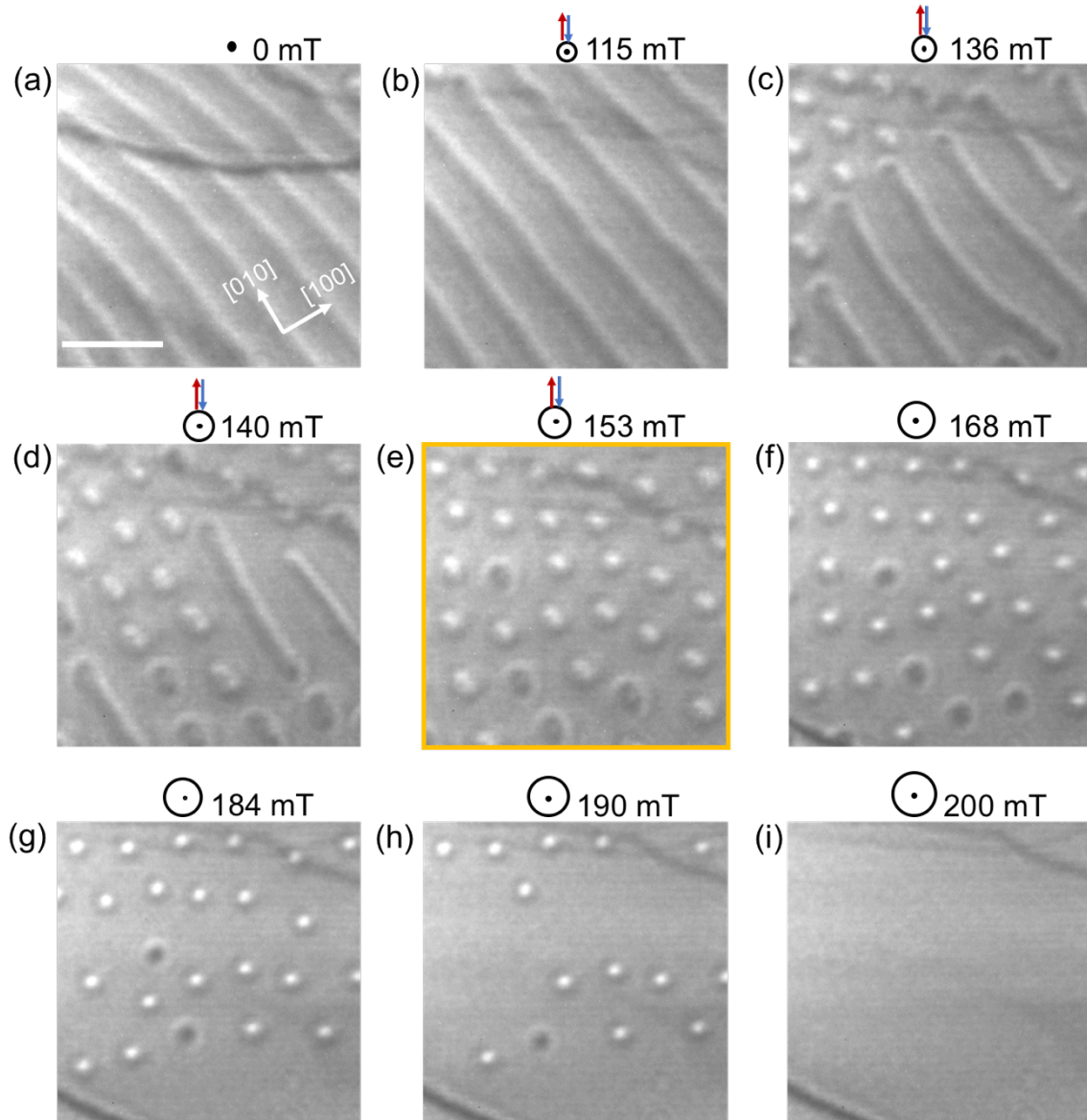


Figure 11 | Field dependent stability of Bloch Skyrmions. Lorentz transmission electron microscopy images of magnetic spin-textures at (a) zero magnetic field and (b)-(i) various magnetic fields at 150 K. The scale bar in (a) corresponds to 500 nm.

helix increases so that seven helices are found in the same area, which is two less in number than helices at zero-field (Fig. 11b). At 136 mT, LTEM contrast different from the antiskyrmion is found together with helices (Fig. 11c). These nano-objects are Bloch skyrmions with an elongated shape. Both the opposite chiralities of Bloch skyrmions owing to the favor of dipole-dipole interactions are observed clearly at 140 mT (Fig. 11d). Further increasing the field to 153 mT leads to the formation of a lattice state. However, the lattice state is not a strong hexagonal lattice, like the state found subsequently in antiskyrmions formation in this compound (see Fig. 7). Notably, the elongation of two type chiralities is nearly along the preferable [010] direction as shown in Fig. 11e. After 153 mT (Fig. 11f), we increase the out-of-plane field without temporary in-plane field components. The Bloch skyrmions are reduced in size and appeared as nearly circular in shape. Few sparse skyrmions are observed at 184 mT and 190 mT (Fig. 11g and 11h). At 200 mT (Fig. 11i), all the skyrmions are vanished making the region fully field polarized.

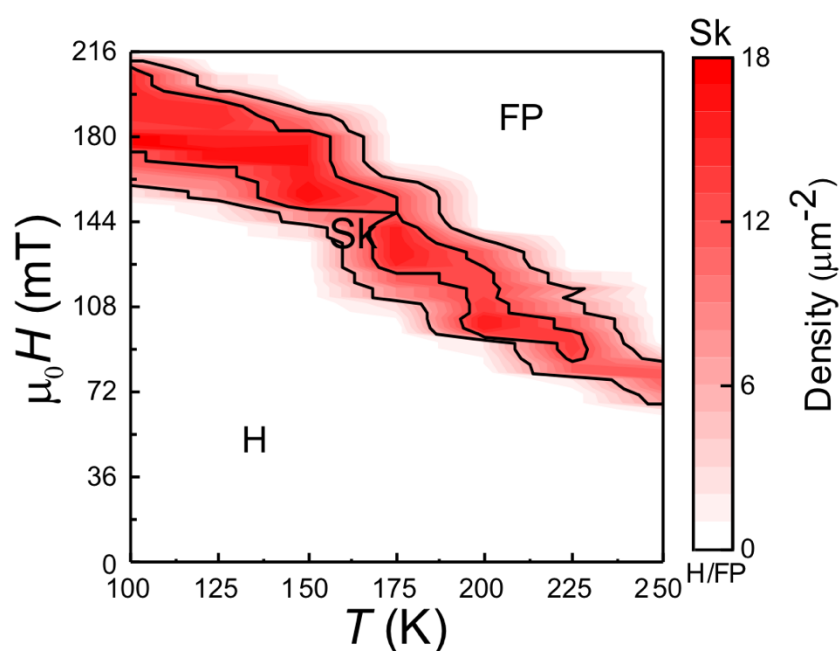


Figure 12 | Phase diagram for Bloch skyrmions. Magnetic phase diagram of $\text{Mn}_2\text{Rh}_{0.95}\text{Ir}_{0.05}\text{Sn}$. The phase diagram is constructed on providing the temporary in-plane field component nearly along [100] direction (temporary tilting of the specimen) followed by returning to the initial zero tilt position. The phase diagram has formed with those types of Bloch skyrmions: circular Bloch skyrmions of opposite chiralities and elliptical skyrmions of opposite chiralities whose long axis are elongated along the same direction i.e., [010].

The protocol is repeated in an interval of 50 K starting from 100 K to 250 K. In each temperature, the skyrmions of opposite chiralities are found, although one kind of chirality dominates over the other. A contour plot magnetic phase diagram is constructed as temperatures vs. magnetic fields as shown in Fig. 12. Similar to the magnetic phase diagram above for antiskyrmions, the helical state is dominated over others and Bloch skyrmions are found in a narrow field region. The Bloch skyrmion stability region becomes narrower with increasing temperature. The Bloch skyrmion stability region is shifted to a slightly higher field since the phase diagram is constructed in a different region of the lamella than the phase diagram created for antiskyrmions (Fig. 8a).

We will also perform the experiment starting from the field polarized state in the decreasing field mode (Fig. 13) as we did for $\text{Mn}_{1.4}\text{Pt}_{0.9}\text{Pd}_{0.1}\text{Sn}$ in Ch. 4. Two circular Bloch skyrmions of bright contrast are found at 192 mT (Fig. 13a). At 176 mT (Fig. 13b), both bright and dark contrasts of opposite chiralities of Bloch skyrmions are found. The number of circular objects increases at 160 mT (Fig. 13c) and the position of nano-objects is not fixed after the in-plane field application. The elongation of both kinds of Bloch skyrmions along one of the two crystallographic directions is observed similar to the increased field mode (Fig. 13d-e). Further decreasing field to 104 mT (Fig. 13f), the elongation process is extended further. At zero biased field, few Bloch skyrmions are left in the presence of helices (Fig. 13i). In the lower field values, short helices are found together with Bloch skyrmions as shown in Figs. 13f–i. Contrary to this, in the $\text{Mn}_{1.4}\text{Pt}_{0.9}\text{Pd}_{0.1}\text{Sn}$ Heusler compound, the Bloch skyrmions are always in an elongated shape. Moreover, two different kinds of contrasts for elliptical skyrmions similar to $\text{Mn}_2\text{Rh}_{0.95}\text{Ir}_{0.05}\text{Sn}$ is also found here. However, the major axis of the oppositely chiral objects in $\text{Mn}_{1.4}\text{Pt}_{0.9}\text{Pd}_{0.1}\text{Sn}$ is always perpendicular to each other and are tied to the [100] and [010] crystallographic directions. In a higher magnetic field of 272 mT (Fig. 14a), even though their size is small but the shape is elliptical. On decreasing the field value to 96 mT (Fig. 14b), their shape remains elliptical but the size is increased. Interestingly, those elliptical Bloch skyrmions with both kinds of chiralities exist in the absence of field (Fig. 14c) and even sustained along crystallographic directions in a negatively biased field of -32 mT (Fig. 14d) in this compound. At -64 mT (Fig. 14e), only a few Bloch skyrmions are left and the helix state is formed at -112 mT (Fig. 14f). It could be suspected that even a small strain in $\text{Mn}_2\text{Rh}_{0.95}\text{Ir}_{0.05}\text{Sn}$ will be enough to align the opposite contrast skyrmions along a particular direction out of two equally probable directions. Notably, in both increasing and decreasing field modes, the formation of circular shape nano-objects with opposite chiralities at higher magnetic fields points towards the

relatively large dipolar contribution in this compound compared to observe elliptical Bloch skyrmions in the D_{2d} compound, $Mn_{1.4}Pt_{0.9}Pd_{0.1}Sn$.

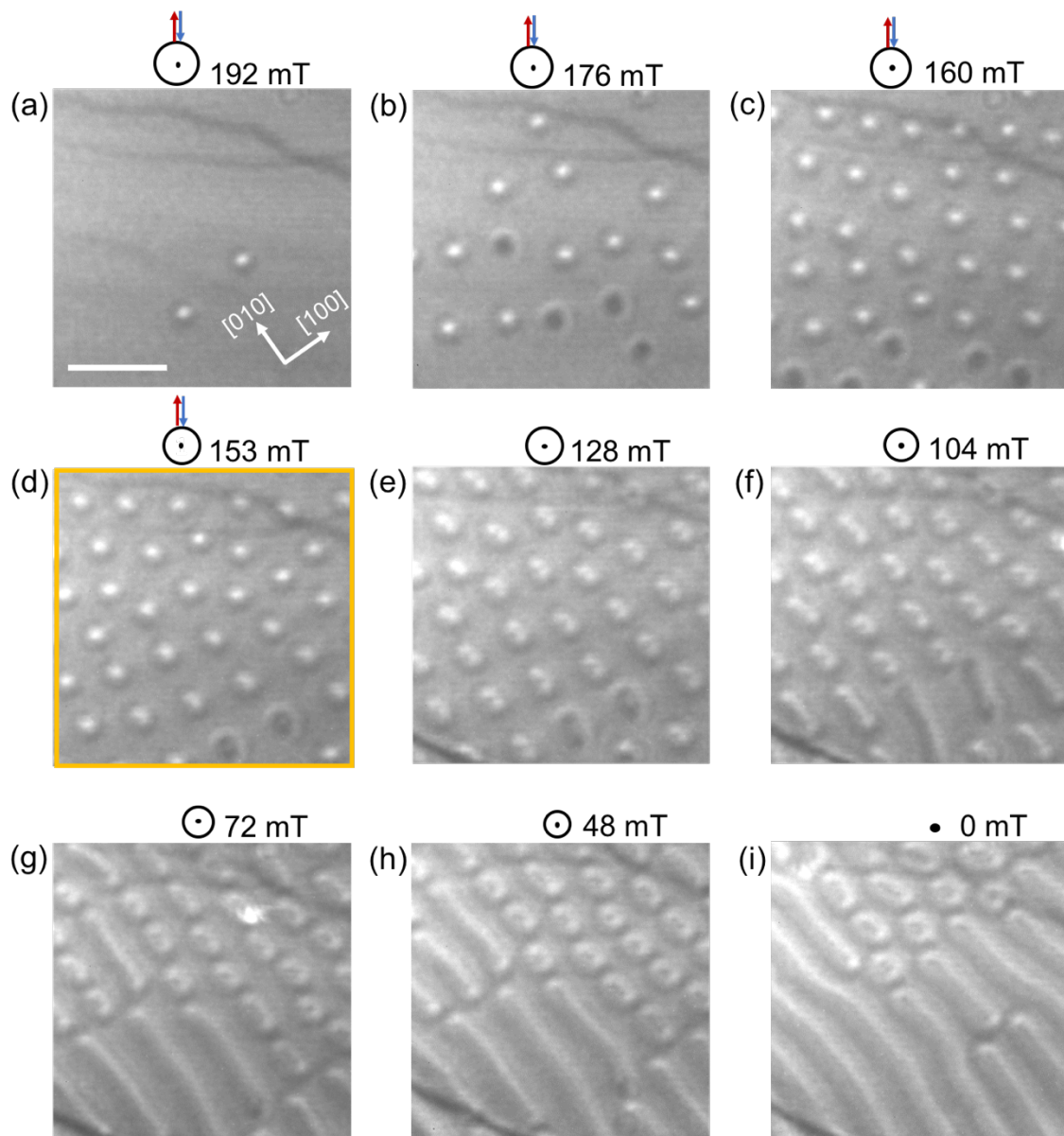


Figure 13 | Decreasing mode Field dependent stability of Bloch Skyrmions. LTEM images of magnetic spin-textures from field polarized state. Providing the temporal application of the in-plane component of field starting from the polarized state, isolated, and lattice states are formed. After the lattice stabilizing no further in-plane components of field is given. (a-i) are LTEM contrasts for $Mn_2Rh_{0.95}Ir_{0.05}Sn$. Circular Bloch skyrmions of opposite chiralities objects are found at higher field values (b) and (c). At lower fields, both types of chiral elliptical skyrmions are elongated along [010] direction. The scale bar in (a) is 500 nm.

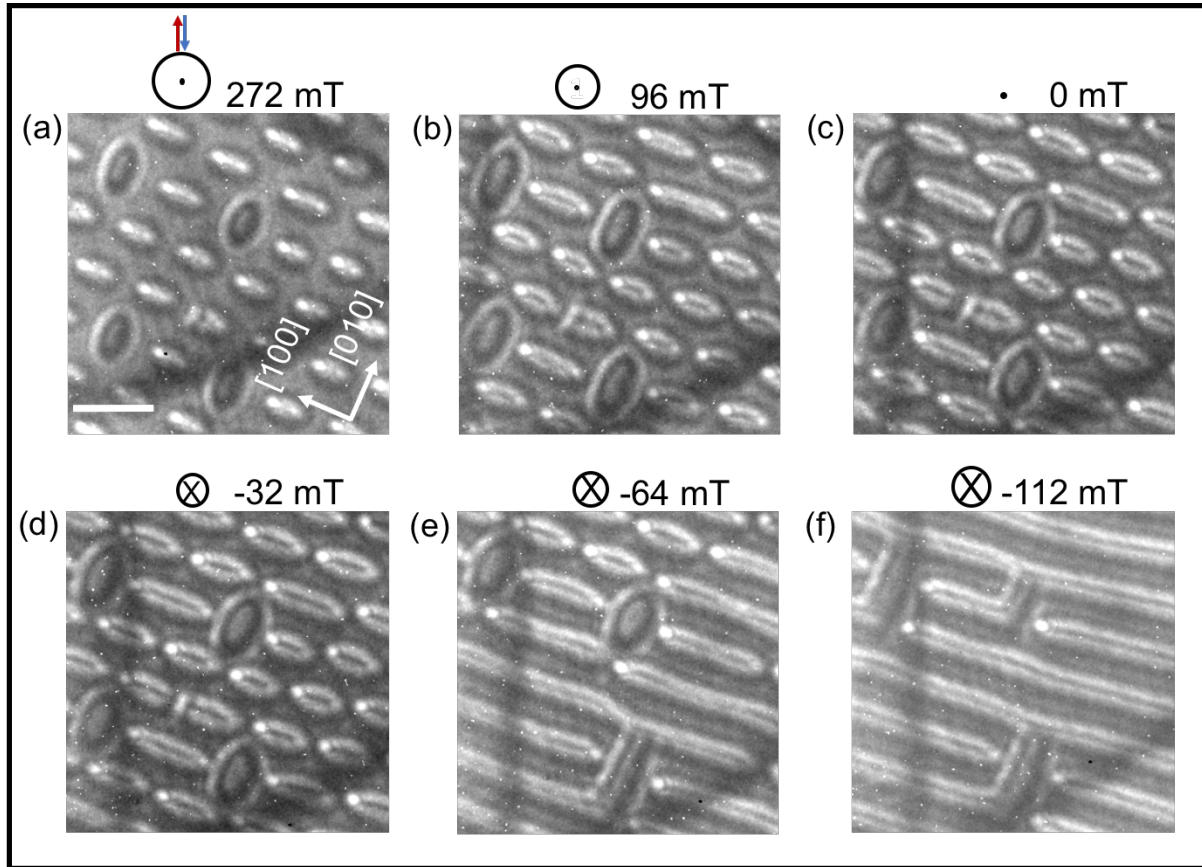


Figure 14 | Decreasing mode Field dependent stability of elliptical Bloch Skyrmions in $Mn_{1.4}Pt_{0.9}Pd_{0.1}Sn$. (a-f) LTEM contrasts for $Mn_{1.4}Pt_{0.9}Pd_{0.1}Sn$. Opposite chirality of elliptical skyrmions are tied to the crystallographic [010] and [100] directions. The scale bar in (a) corresponds to 300 nm.

A similar kind of LTEM contrast with opposite chirality of Bloch skyrmions was found without the presence of DMI in the hexaferrite centrosymmetric compound $Ba-Fe-Sc-Mg-O$ ^{39, 165}, where dipole-dipole interactions and anisotropy play an essential role in their formation. The shape of skyrmions in the centrosymmetric material is always circular, although their size variation (small or large) depends on the strength of the magnetic field. In the multilayer structure of Fe/Gd ¹⁶⁶, the circular Bloch skyrmions with opposite chiralities were formed due to the dominant dipole-dipole mechanism. Hence, in our D_{2d} system, the elongation of Bloch

skyrmions along the specific fixed crystallographic direction of Bloch wall propagations establishes the role of DM energy. Moreover, in both the non-centrosymmetric Heusler compounds studied in this thesis, DMI is always intrinsic subjected to the D_{2d} symmetry which eventually produces antiskyrmions and elliptical skyrmions. Nevertheless, non-centrosymmetric D_{2d} ferromagnet in $\text{Cr}_{11}\text{Ge}_{19}$ ¹⁶⁷, dipole-dipole interactions play a significant role such that neither antiskyrmions nor Bloch skyrmions were formed. Instead, closed-loop of oppositely pair spin vortices called bi-skyrmions were observed on applying magnetic field along [001] zone-axis. Here, in these D_{2d} compounds, on providing magnetic field along the [001] zone-axis, spin textures of opposite topological charges ∓ 1 are formed within the basal plane of the tetragonal systems. However, in the $\text{Mn}_{1.4}\text{Pt}_{0.9}\text{Pd}_{0.1}\text{Sn}$, the simultaneous observation of elliptical skyrmions and antiskyrmions have been found, and at high temperatures of 300 K-350 K mostly antiskyrmions are established. In the $\text{Mn}_2\text{Rh}_{0.95}\text{Ir}_{0.05}\text{Sn}$ compound, there is no such simultaneous observation of Bloch skyrmions and antiskyrmions, and their nucleation depends on the separately provided temporal tilting angles.

7.3.6 Stability of Bloch skyrmions against heating

A field heating experiment is performed to see the metastability of Bloch skyrmions against the rise in temperatures. Here a state of Bloch skyrmions and elongated short helices are formed at 80 mT and 98 K on repeating the same protocol as described above (Fig. 15a). The magnetic field of 80 mT is kept constant and the temperature of the specimen is increased as shown in the schematic Fig. 15b. At 125 K, 150 K, and 175 K, few short helices are transformed to Bloch skyrmions (Fig. 15c-e). At 175 K, only three short helices are left which are then transferred to Bloch skyrmions at 200 K (Fig. 15f). On the left side of Fig. 15f, a small portion of the region has no Bloch skyrmions and at 250 K (Fig. 15g), nearly half of the region has no spin textures, making the region field polarized with few Bloch skyrmions. Two Bloch skyrmions are left on the right-side corner of Fig. 15h at 261 K and upon further high temperature, these are vanished so that full lamella is in a polarized state. In $\text{Mn}_{1.4}\text{Pt}_{0.9}\text{Pd}_{0.1}\text{Sn}$, following the same heating experiment method, especially in the low moment and high temperature, antiskyrmions have been observed. However, in $\text{Mn}_2\text{Rh}_{0.95}\text{Ir}_{0.05}\text{Sn}$, once stabilize the Bloch skyrmions and perform the heating experiment, only Bloch skyrmions are found up to the transition temperature region.

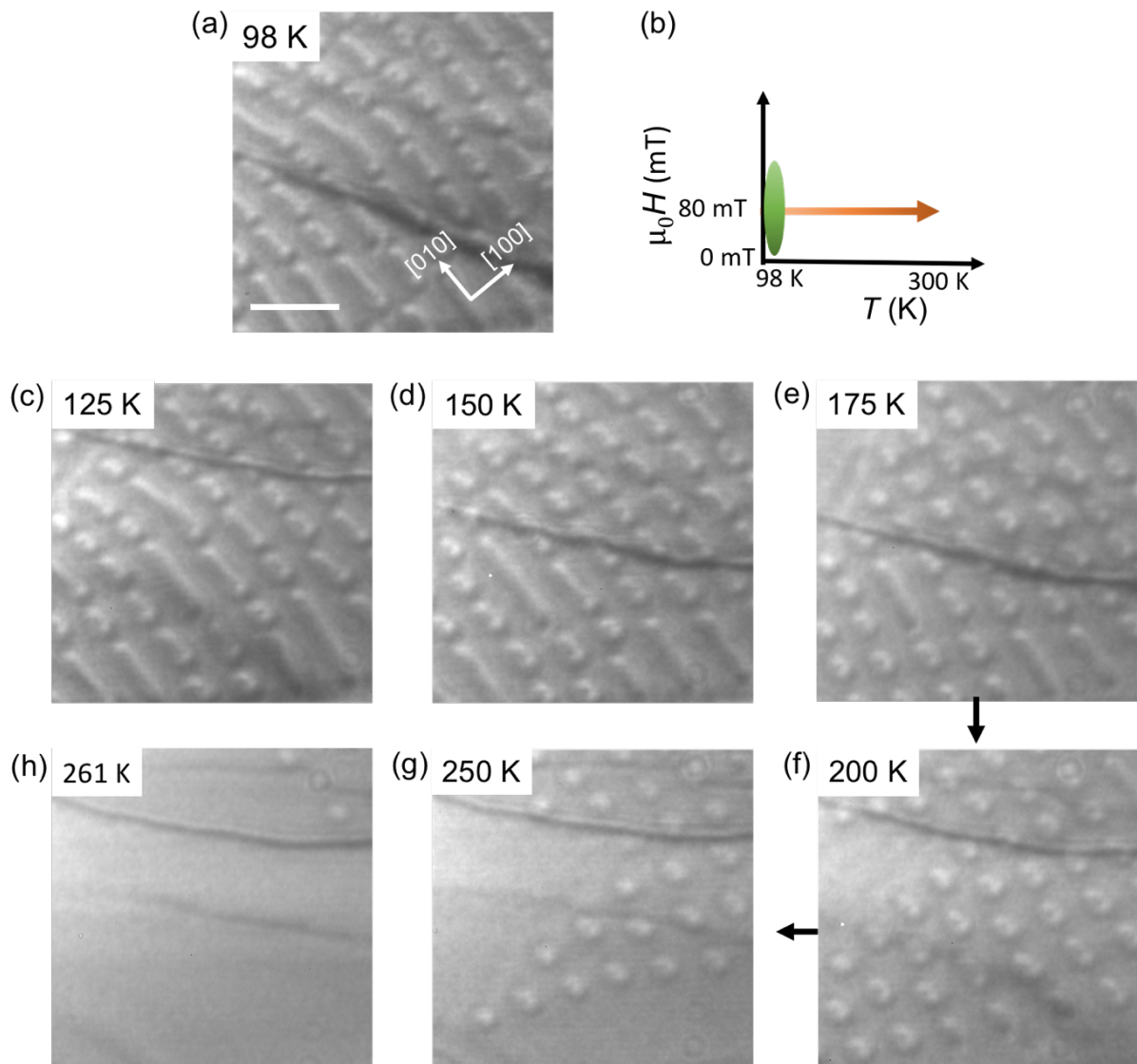


Figure 15 | Stability of Bloch Skyrmions against the heating. (a) After stabilizing the lattice state at a higher field and decreasing the out-of-plane field from there, Bloch skyrmions and short helices are found at 98 K and 80 mT. (c–h) Keeping the magnetic field constant (80 mT), the lamella is heated to higher temperatures and LTEM images are taken at 125 K, 150 K, 175 K, 200 K, 250 K, and 261 K respectively. A schematic of the heating experiment is shown in (b). The scale bar in (a) corresponds to 500 nm.

7.4 Summary

In conclusion, we have successfully identified the existence of magnetic antiskyrmions and Bloch skyrmions in a fully stoichiometric inverse ferrimagnetic Heusler compound, $\text{Mn}_2\text{Rh}_{0.95}\text{Ir}_{0.05}\text{Sn}$, without the Mn vacancies. Those spin textures are observed in a wide region of field and temperature for this compound. These results provide the intrinsic stability of a state composed of antiskyrmions and Bloch skyrmions in compounds with D_{2d} symmetry and, moreover, show that distinct spin textures can be found in materials with low saturation magnetization as well as smaller DMI. This work opens the path to the observation of chiral spin textures of Bloch skyrmions and antiskyrmions in a large number of D_{2d} symmetry materials. It also shows that by chemical substitution one can optimize the properties of the host compound, especially tuning the magnetization to low value, which would enable them to be highly useful for various technological applications.

8

Conclusion and outlook

8.1 Conclusion

Since the discovery of skyrmions in 2009, the investigation of topological spin textures has become an active research field in condensed matter physics, particularly in spintronics. In this dissertation, the focus has been on the examination of the static structures of various spin textures in D_{2d} inverse Heusler compounds and includes the following major findings:

- The structure of the antiskyrmion in a D_{2d} system is composed of Bloch walls, and Néel walls separated by intermediate walls. The antiskyrmion comes in two different forms, namely round and square-shaped antiskyrmions. These forms are extensively studied in the Heusler compound $\text{Mn}_{1.4}\text{Pt}_{0.9}\text{Pd}_{0.1}\text{Sn}$. A possible switching mechanism between these two forms is shown via the temporary application of an in-plane field component. Moreover, in the same compound, apart from antiskyrmions, for the first time, we reveal the unanticipated finding of a different topological nano-object, which is elliptical and forms with only Bloch walls. We name this spin texture an elliptical Bloch skyrmion. Dipole-dipole interactions play a significant role in the formation of such nano-objects. The elliptical Bloch skyrmions are found at low temperatures whereas antiskyrmions are observed at room temperature and higher. At the magnetic transition temperature of ~ 268 K, the co-existence of antiskyrmions and elliptical Bloch skyrmions is observed. Additionally, these nano-objects are found in zero field over a broad temperature window without any field cooling procedure.

- Within the tetragonal basal plane of the compound $\text{Mn}_{1.4}\text{Pt}_{0.9}\text{Pd}_{0.1}\text{Sn}$, nano-stripes are fabricated along different crystallographic directions that help to orient the antiskyrmions along different angles from the edges of the nano-stripes. Elongated antiskyrmions with terminated edges as $\frac{1}{2}$ topological charges are realized in several reliable ways in elevated fields. These elongated antiskyrmions transform into round shaped antiskyrmions under high magnetic fields. A single chain of antiskyrmions is formed in the middle of a nano-stripe which has a width slightly larger than the nano-object size. What is interesting in this finding that the antiskyrmions form in the absence of any in-plane field component and are not nucleated from the edge. A single chain of nano-objects formed from elliptical skyrmions and antiskyrmions, with a variable density in a nano-stripe, are obtained by varying the temporary tilting angle of the in-plane magnetic field. A crucial observation that can bring significant improvements in data storage technologies is the simultaneous observation of skyrmions and antiskyrmions in nano-stripes formed a uniform material of fixed thickness at room temperature. The room temperature observation of chiral nano-objects in racetracks that can be constructed from a D_{2d} material, without the need for a complicated multilayer structure, is highly relevant for turning a D_{2d} material into a spintronic device.

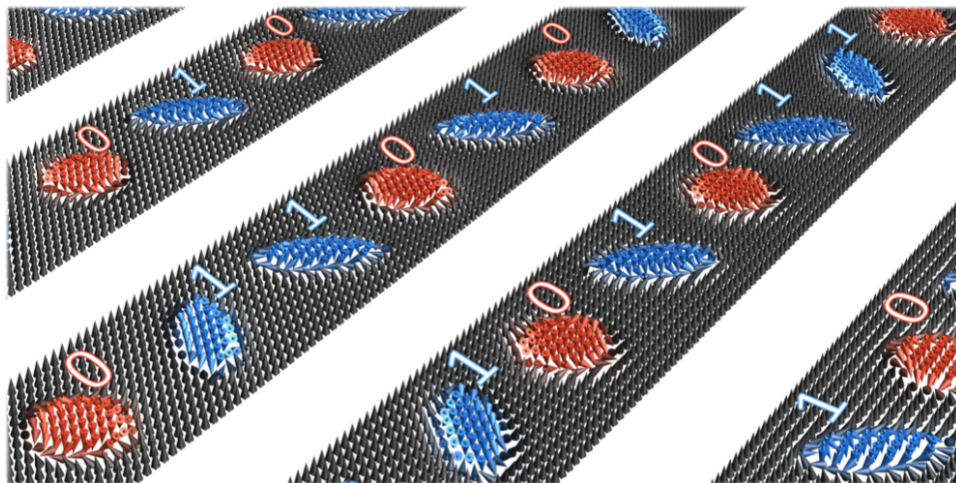


Figure 1 | Skyrmion-antiskyrmion racetrack. The figure is adopted from a press release based on our publication, Jena *et al.*, Nat. Commun., 11, 1115 (2020) [Press release, Magnetic whirls in future data storage devices, Martin-Luther-Universität Halle-Wittenberg, 4th of March 2020]. The elliptical skyrmions and antiskyrmions encode ‘1’ and ‘0’ bits, respectively.

- Furthermore, we discovered two additional nano-spin textures in the same tetragonal inverse Heusler compound $\text{Mn}_{1.4}\text{Pt}_{0.9}\text{Pd}_{0.1}\text{Sn}$, namely a 'fractional Bloch skyrmion' and a 'fractional antiskyrmion'. It is observed that they are formed at the specimen edge in low or negatively biased magnetic fields only after the stabilization of a dense lattice. In addition, in the interior of the lamella, short helices of different lengths of antiskyrmions and elliptical Bloch skyrmions are found. This is the case, when the out-of-plane field is decreased after the sparse state of topological objects is formed. Moreover, when the dense lattice state is stabilized, the nano-objects join together to build short helices whose central part is trivial (non-topological) but each end has a half topological number. For the constricted stripes the length of these short helices is same due to the confined geometry. However, for an extended lamella, the individual nano-objects of antiskyrmions join with each other to form rectangularly shaped short helices of different lengths, and similarly, elliptical Bloch skyrmions join together to form elliptically shaped short helices. Additionally, we observed that not only at room temperature and above but also at low temperatures (250 K-100 K), antiskyrmions are stabilized using a field cooling protocol. We also report a phase transition from elliptical Bloch skyrmions to antiskyrmions in field heating experiments.
- Finally, we investigated a second D_{2d} inverse tetragonal Heusler compound $\text{Mn}_2\text{Rh}_{0.95}\text{Ir}_{0.05}\text{Sn}$ with a very low magnetic moment compared to $\text{Mn}_{1.4}\text{Pt}_{0.9}\text{Pd}_{0.1}\text{Sn}$. The antiferromagnetically coupled moments of the Mn sub-lattices makes these compound ferrimagnetic. Both antiskyrmions and Bloch skyrmions are found separately after the temporal tilting of lamella along the [110] and [100] directions, in the TEM, respectively. Bloch skyrmions of opposite chiralities appear in two shapes; circular Bloch skyrmions (in higher magnetic field) and elliptical Bloch skyrmions (in relatively lower magnetic field). The larger helical period and the stability of Bloch skyrmions in $\text{Mn}_2\text{Rh}_{0.95}\text{Ir}_{0.05}\text{Sn}$ up to the transition temperature in subsequent heating studies is consistent with a lower value of the DMI in this compound. A lower DMI value may be expected from the 4d element Rh compared to the 5d element Pt in $\text{Mn}_{1.4}\text{Pt}_{0.9}\text{Pd}_{0.1}\text{Sn}$. The finding of opposite topological charges in a low moment ferrimagnet, $\text{Mn}_2\text{Rh}_{0.95}\text{Ir}_{0.05}\text{Sn}$, opens a path towards the realization of antiferromagnetic skyrmions and antiskyrmions in D_{2d} Heusler compounds.

8.2 Future perspectives

The findings in this thesis will stimulate a broad range of extensive future studies in both theory and experiment. These range from short-term objectives to long-term investigations as well as potential applications in future spintronic technologies.

- *Different experimental techniques for spin textures in the D_{2d} system:* The antiskyrmions, elliptical Bloch skyrmions, fractional antiskyrmions and fractional skyrmions have been observed experimentally using Lorentz TEM technique. MFM technique was used to study the out-of-plane component of the antiskyrmion spin texture⁵². A more detailed static and dynamical study of various spin textures in D_{2d} compounds can be examined using MFM, STM, XMCD, STXM, BLS, DPC, NV center, and neutron scattering. Again, a deep exploration into the 3D nature of various spin textures will be very interesting, beyond the description provided in the thesis.
- *Two special dynamics:* Due to the two-dimensional anisotropic DMI vector in D_{2d} , the twisting in the spin textures does not occur and mostly forms as tubular structure, unlike the B20 compounds⁵³. In Ch. 5 (Fig. 4), a special kind of shrinking and then expansion mechanism is found for the mixed type of helices arrangement. It indicates that under particular circumstances, there is a possible mechanism of shrinking and expansion occurring in the tubular structure of the D_{2d} compound. Also, the formation of short helices (Fig.3 and 4, Ch. 6) on collapsing the individual nano-objects of antiskyrmions or elliptical skyrmions is unusual. A better theoretical understanding of both the shrinking and expansion, and collapse dynamics of nano-objects will provide an interesting insight into the field of topological soliton.
- *Transport properties:* The various protocols described in this thesis will help to examine the transport properties of different nano-objects in a single compound. We can propose that the nano-objects of different topological charge number can be distinguished by their distinct topological Hall signatures or the anomalous Hall effect, which are expected to be different for the two objects.

- *Transition temperature region from the elliptical skyrmion to antiskyrmion:* The heating experiment (Fig. 11, Ch. 6) of elliptical skyrmions shows that antiskyrmions are found at higher temperatures for the $\text{Mn}_{1.4}\text{Pt}_{0.9}\text{Pd}_{0.1}\text{Sn}$ compound. A detailed experimental observation near the transition temperature region and the theoretical support (using the Monte-Carlo simulation) will provide a better understanding. The interplay of DMI, dipole-dipole interactions, and the dominance of one over others will provide deep insight into microscopy behavior.
- *Towards antiferromagnetic spin textures:* One of the interesting properties in the Heusler compound is the tuning of material properties by incorporating the chemical elements. In this way, the strength of spin-orbit coupling, magnetization, or electron occupation can be controlled. It is also possible to set the total magnetic moment to zero (compensated ferrimagnet) due to antiferromagnetically coupled magnetic sub-lattices. This will give rise to the antiferromagnetic antiskyrmions or skyrmions that are expected to move in a straight path irrespective of the applied current direction.
- *Topological superconductivity:* The hybrid system comprises of superconductor sandwich between antiskyrmion and D_{2d} Bloch skyrmions may realize Majorana zero modes and edge modes. The unique properties of different topological superconducting phases can be tune by changing the size of the different spin textures via applied external magnetic fields as reported in different theoretical studies¹⁶⁸⁻¹⁷⁰.
- *Magnonic quadrupole topological insulator:* Recent study proposed that the fractional antiskyrmions can produce robust magnetic corner state¹⁴⁴. The experimental discovery of the fractional antiskyrmions and fractional Bloch skyrmions in the present thesis may lead to the path for the experimental realization of the magnonic quadrupole topological insulator.
- *Technological applications:* The simultaneous observation of elliptical Bloch skyrmions and antiskyrmions in nano-strips having widths much larger than the size of the nano-objects themselves rules out the requirement of highly constrained geometries for use in memory and logic devices. Moreover, the electrical detection, movement, creation, annihilation and distinct readout mechanism of elliptical

skyrmions and antiskyrmions simultaneously present in a single device, which is less susceptible to diffusion and thermal drift, gives new directions towards technological applications.

Appendix A

Supplementary figure for elliptical Bloch skyrmions and antiskyrmions in a D_{2d} inverse Heusler compound

A.1 Elliptical Bloch skyrmions at 150 K and 250 K

The same temporary in-plane field components tilting procedure (of Ch.3) is applied to obtain the lattice state. At 150 K, after achieving the lattice state (400 mT), the field is decreased from there without tilting. The same protocol is also applied for the 250 K. The essential difference here is that at 250 K, the elliptical skyrmions transform to elongated short helices and/or helical state near around zero field. While the lattice state is found periodic at 150 K and 200 K. Since the net magnetization of the present Heusler compound decreases with increasing temperatures, the strength of the dipole-dipole interactions and hence the stabilization of skyrmionics spin textures is decreasing. At higher temperatures (300 K and 350 K), no elliptical skyrmions have been observed using the above protocol. It indicates that the DMI has a significantly important contribution than the dipole-dipole interactions at these higher temperatures. We also further confirm via a heating experiment (Ch. 6) that indeed antiskyrmions observe at a higher temperature. Hence, anisotropic DMI has a significant role due to low magnetization and dipole-dipole interactions.

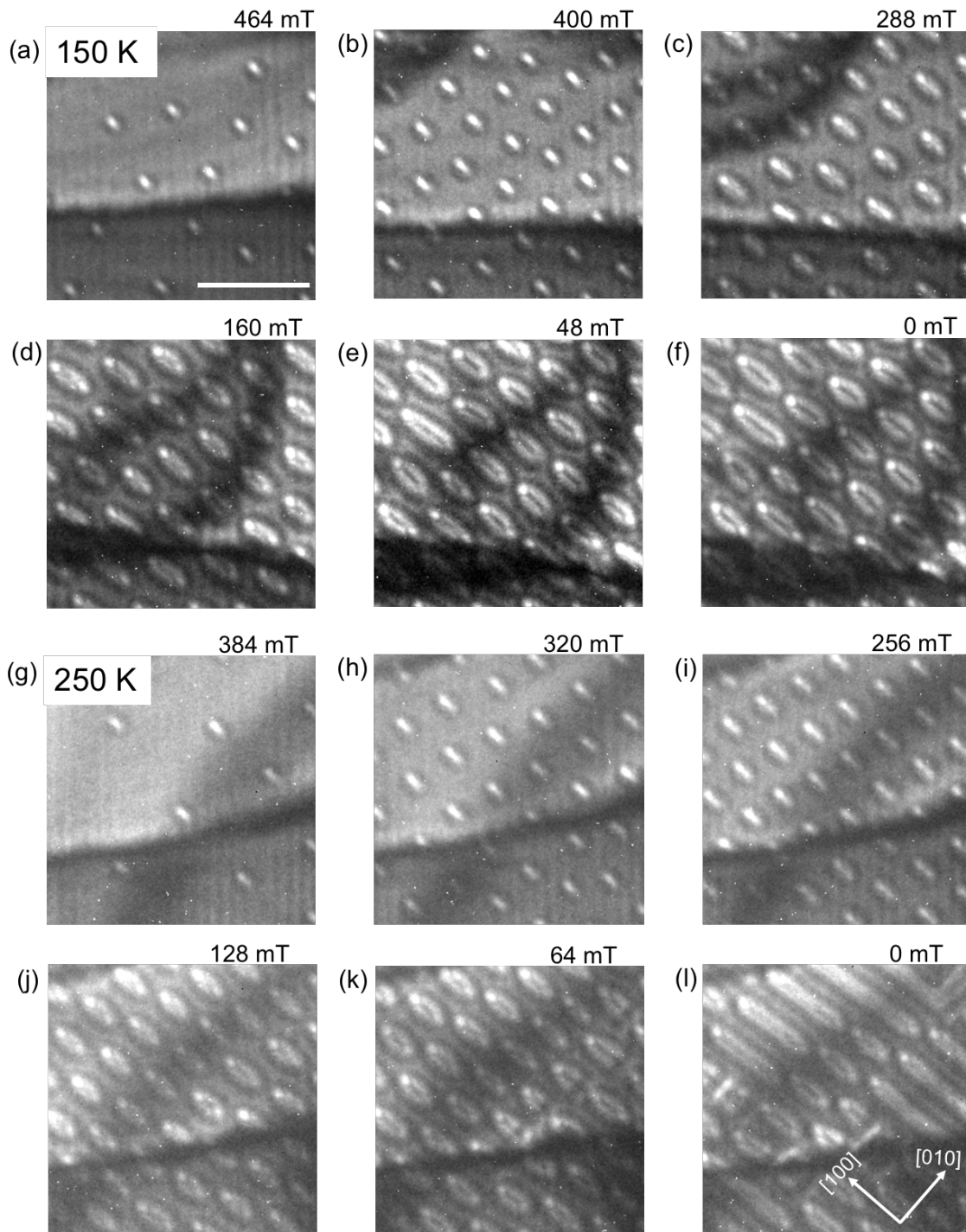


Figure A.1 | *Elliptical skyrmions at 150 K and 250 K.* (a-f) Field dependence of Lorentz TEM contrasts at 150 K. (g-l) Field dependence of Lorentz TEM contrasts at 250 K. The scale bar in (a) corresponds to 500 nm.

Appendix B

Supplementary figures for evolution and competition between chiral spin textures in nano-stripes

B.1 Effect of field on helix and magnetic domain

The [001] zone-axis consists of the helical phase, and the [100] zone-axis has large domains that are oriented perpendicular to the boundary of the stripe as shown in Fig. B.1a. We will examine the effect of the magnetic field on helices and magnetic domains (Fig. B.1b-h). The initial configuration in the [001] zone-axis oriented has a mixed helical phase. Since some region in [001] zone-axis has both horizontal (one) and vertical helix segments, a similar shrinking and expansion of them (Fig. B.1c-e) as shown in Fig. 4 of the Ch. 5, are happened upon increasing the magnetic field. On the other hand, for the [100] zone-axis, domains are present up to a much higher magnetic field. So, from here, we conclude two important observations. Firstly, the magnetic structures and the selected area diffraction from the left side region indicate that topological spin textures in the D_{2d} inverse Heusler compound form only within the basal plane of [001] zone-axis oriented specimen. Secondly, the shrinking and expansion mechanism of truncated helices happens in a nano-stripe only when both the horizontal and vertical helix segments present simultaneously in a region. We have experimented with the other different possible arrangements of helices shown in Fig. 5 (Ch. 5) and observed that such phenomena only found for the type of arrangement shown in Fig. 5a (Fig. B.1a) or in Fig. 4a (Ch. 5). For other types of helical arrangements, the helices or truncated helices simply transform to antiskyrmions as shown in Fig. 3a-f or in Fig. 3h-m (Ch. 5). Even

though in Fig. 5b-d (Ch. 5) have mixed segments of the helical phase, there is no simultaneous presence of mixed segments of helices like shown in Fig. B.1a, and hence no shrinking and expansion of the truncated helix segment will favour there.

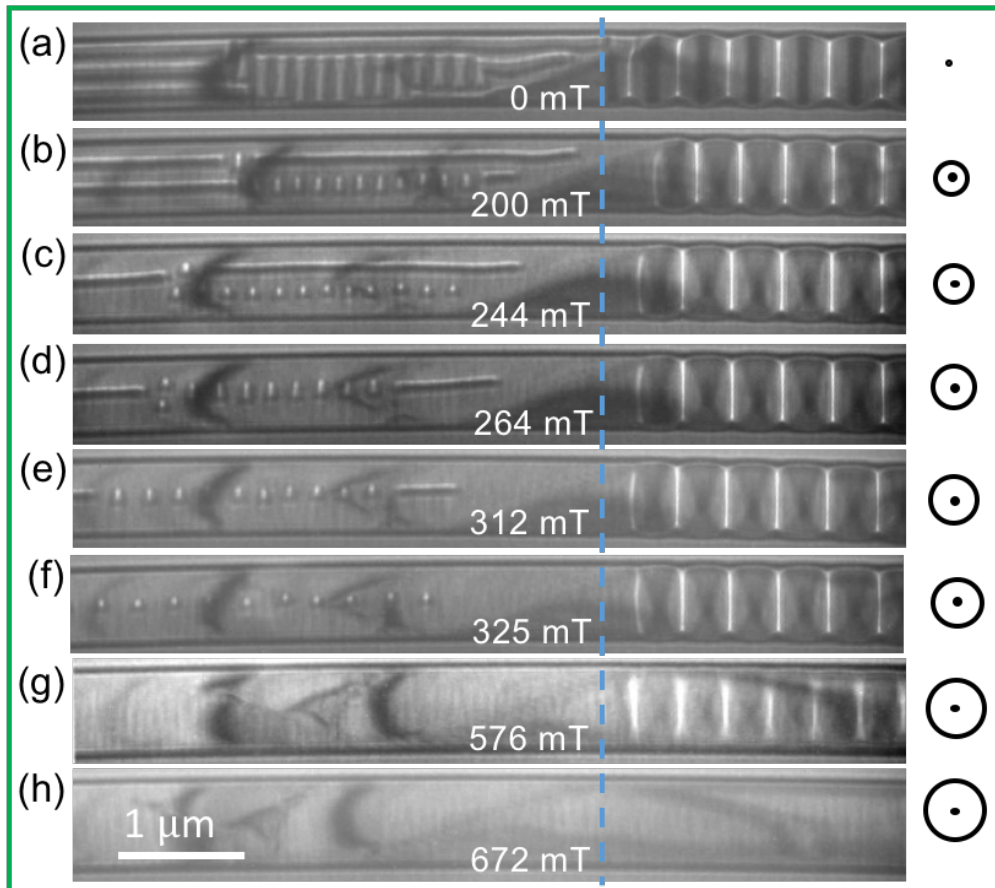


Figure B.1 | Effect of magnetic field on the helices and magnetic domains. (a) The Lorentz TEM image shown here is from the same nano-stripe NS 3 and the magnetic contrast arrangement of Fig. 5a of Ch. 5. The stripe has [001] zone-axis on the left side and [100] zone-axis orientations (conformed from SAED). (b-h) LTEM images at increasing strength of the perpendicular magnetic field. (b, c) The horizontal helix segment above the vertical segments moves towards the interior of the stripe region. (d) The horizontal longer helix segment vanishes at 264 mT; the vertical truncated helices segment expands. (e, f) Further increase in fields the nano-objects shrink. (g) There [001] zone-axis region become ferromagnetic/field polarized at 408 mT and magnetic domains in the [100] zone-oriented axis is existed up to 576 mT. (h) Further increase in fields, the domains are vanished and make the whole region of the nano-stripe to field polarized state.

B.2 Single, double and elongated antiskyrmions at 490 nm width stripe

In this Fig. B.2 below, we show the result for a nano-stripe of width ~ 490 nm. The stripe is also presented as NS 2 in Ch. 5, in which the orientation (ϕ) is $\sim 45^\circ$ instead of 0° or 28° . On increasing the out-of-plane field from the helical state, a single chain antiskyrmion form from the truncated helices. It does not form any further increase in the number of antiskyrmions. This is shown in Fig. 1i-j. Now, we start to experiment with a configuration of a polarized state having no magnetic contrast (Fig. B.2a). Moreover, providing in-plane field components, single-chain and double chains antiskyrmion form (Fig. B.2b-e). After that, we only decrease the out-of-plane field up to 0 mT (Fig. B.2f-l). The antiskyrmion starts to elongate (Fig. B.2f). That fits well our explanation that the antiskyrmions enlarge at decreasing fields (Fig. B.2f-j). In a wider stripe, however, there is enough space so that the antiskyrmions are not squeezed and the double row is preferred over a wider field range.

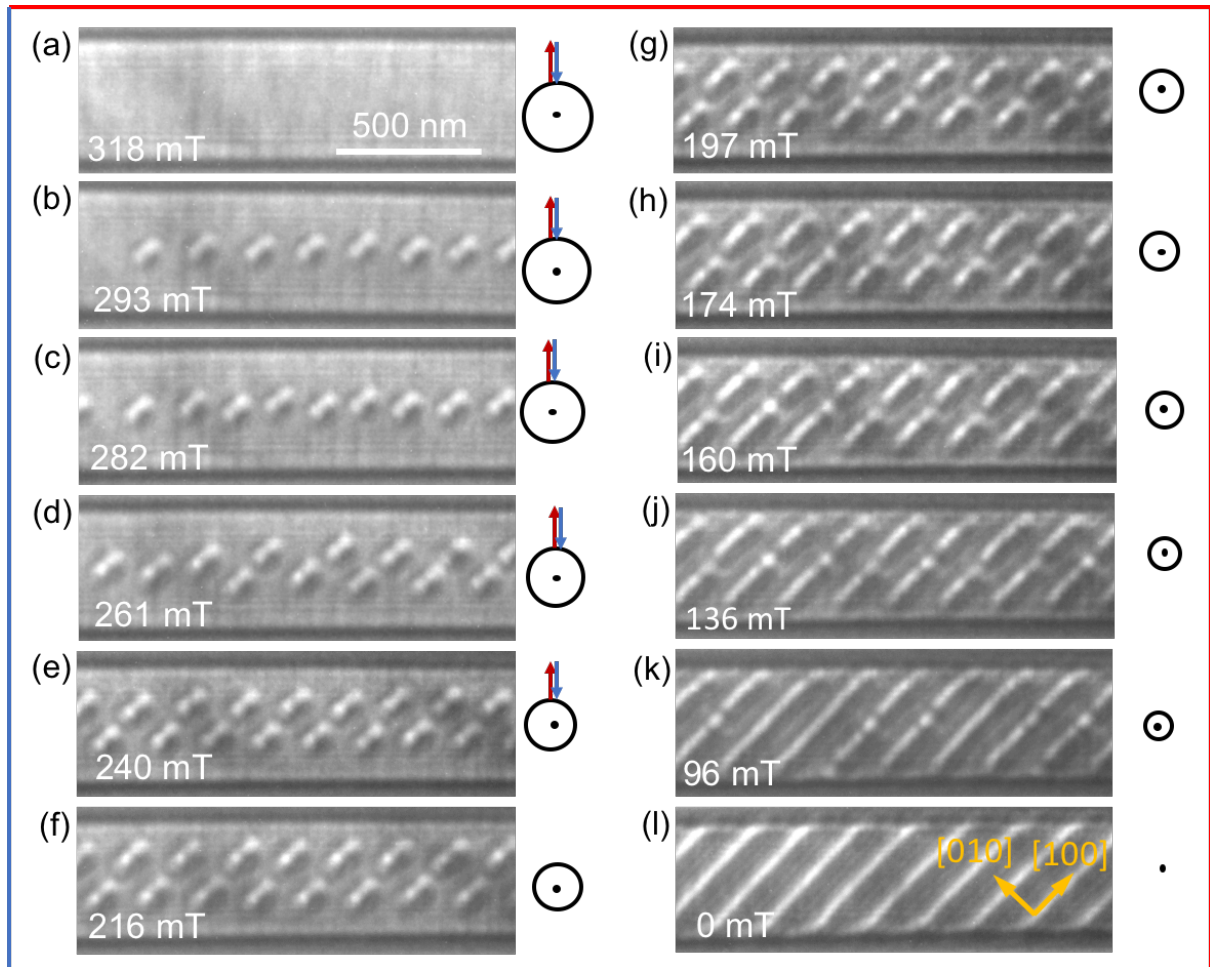


Figure B. 2 | Antiskyrmions in a 490 nm width nano-stripe. (a) At 318 mT, a field polarized state. (b) and (c) Single-chain of antiskyrmion. (d) Zig-zag form of antiskyrmion started to form at 261 mT. (e) At 240 mT, double chain antiskyrmion is formed. After (e) we do not provide any temporary in-plane field and slowly decrease the perpendicular field (out-of-plane field) to zero. (f-j) Antiskyrmion elongated on reducing the field strength. (k) Helices started to form at 96 mT and (l) at 0 mT; the helical state is restored.

Appendix C

Supplementary figures for stability, collapse dynamics and fractional form of antiskyrmions and elliptical Bloch skyrmions

C.1 Transition between the antiskyrmion and helices

Hereby the same field cooling measurement (of section 6.2.2), we observed the LTEM contrast in a different region. Fig. C.1a shows a square antiskyrmions lattice state at 350 K and 200 mT stabilized after using the temporary tilting lattice stabilizing protocol. Few trivial bubble objects are found near the boundary. The extended lamella at 200 K and 200 mT is shown in Fig. C.1b. At 200K, in the same region, few short helices are formed, and trivial bubbles are also observed near the boundary (Fig. C.1c). The interior region is mostly filled with antiskyrmion, whereas we mainly focus on the dashed marked region of $1800 \text{ nm} \times 1800 \text{ nm}$. On reducing the magnetic field, short and long helices are found at -16 mT (Fig. C.1e). On the edge, few long helices terminated at the boundary and destroyed their topological protection. Here a few of the [100] elongated corner helices transform along the [010] direction. From fig. C.1e, we recorded LTEM images in an increasing step of 16 mT out-of-plane field. At 160 mT (Fig. C.1f) the region is mostly filled with the topologically protected rectangular shape short helices and trivial long helices. On increasing the magnetic field, these are transforming to square shape antiskyrmions. The process of transformation to square-shaped

nano-objects is shown in Fig. C.1f-h. At 160 mT, the helices in the lower-left corner propagate along [010] direction. In Fig. C.1h, the short rectangular helices transform to nano-objects of antiskyrmions. This process shows the reversible transformation to square antiskyrmion from field cooled antiskyrmion to helices then to antiskyrmion. However, two helices in the left corner of Fig. C.1g transform to trivial nano-objects at 320 mT, insist on antiskyrmions.

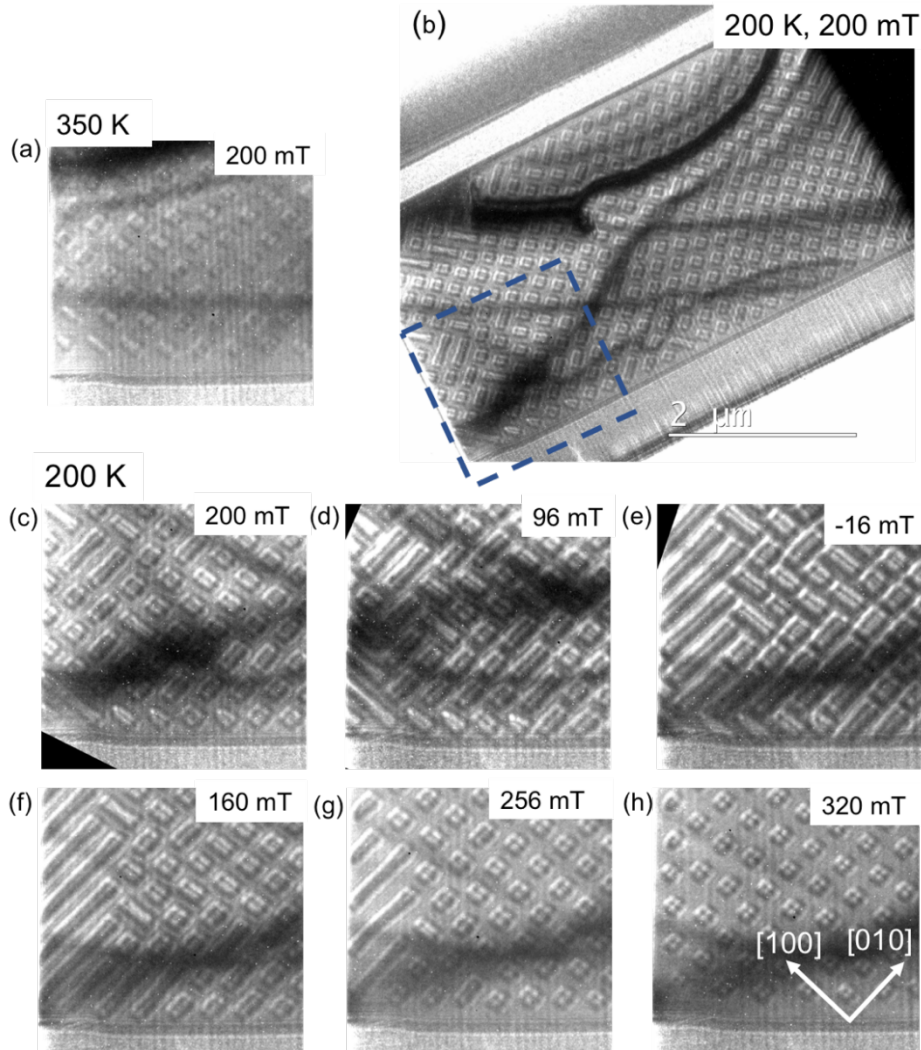


Figure C.1 | Transition between square antiskyrmions and short helices at 200 K. (a) Square antiskyrmion lattice at 350 K and 200 mT. Few trivial bubbles are found here also. (b) The lamella is cooled down to 200 K keeping the magnetic field constant. (a) and (c-h) are the LTEM contrasts from the region marked by the blue rectangle in (b). (c-e) LTEM contrasts on decreasing the magnetic field from 200 mT to -16 mT. From -16 mT, we increasing the magnetic field. (f-h) are LTEM contrasts from 0 mT up to the polarized state at 464 mT in an increasing mode of magnetic field.

C.2 Effect of in-plane field component on antiskyrmion

In the D_{2d} inverse tetragonal Heusler compound, in order to overcome the energy barrier between trivial and non-trivial states, the application of the in-plane field component is required. Their stability as a lattice state depends on the amount of the in-plane components, as discussed in section 6.2.4. Here, we gave an example of the same phenomena for the antiskyrmions. In Fig. C.2a, we stabilized a sparse state of antiskyrmion at 357 mT after the application of the in-plane field component via tilting the specimen (to $\sim 38^\circ$) followed by returning to the zero-tilt position (near [001] zone-axis). The resulting LTEM contrast is marked by the orange colour boundary mark. There, we decrease the out-of-plane field without giving in-plane field components. Here also, we show that the nano-objects are elongated (304 mT, Fig. C.2b) without forming the lattice state. Further reducing the field, the helical phase is formed (Fig. C.2b-f). Moreover, similar to the elliptical skyrmion cases, on stabilizing lattice state of antiskyrmions, the state remain exists up to below zero field (Ch. 4).

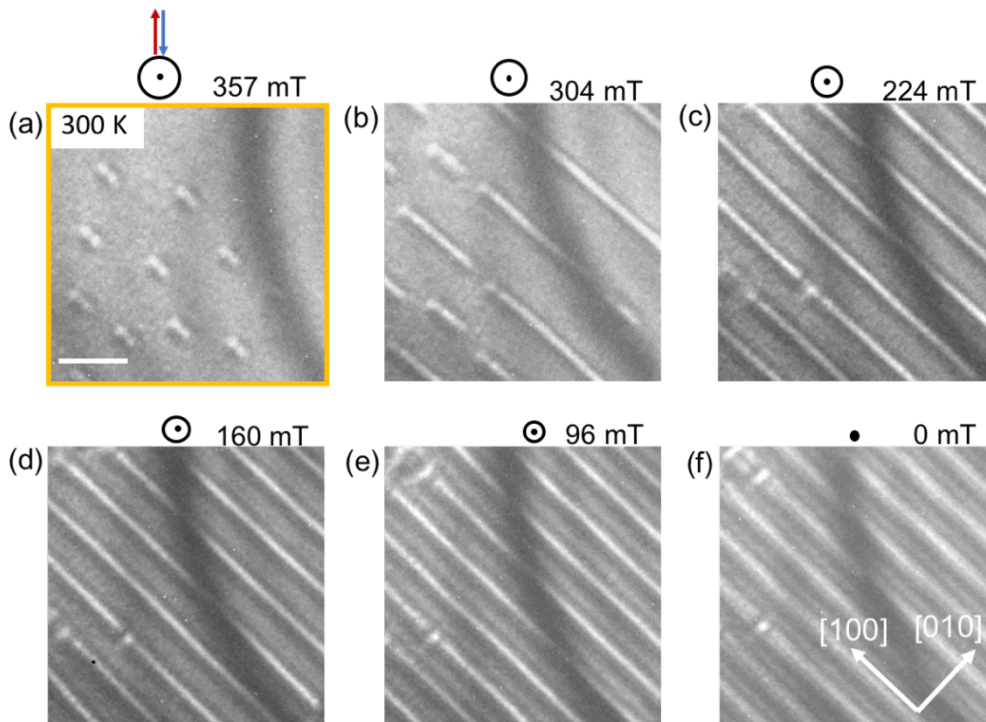


Figure C.2 | Effect of in-plane field component on antiskyrmion. (a) A sparse state of round antiskyrmion is formed at an out-of-plane field of 357 mT and room temperature after tilting the lamella nearly 38° degree away from the zone-axis followed by returning to the initial position. (b-f) Then, we do not provide any in-plane field component by tilting and the out-of-plane field is reduced to 0 mT. The scale bar in (a) corresponds to 300 nm.

C. 3 Elliptical Bloch skyrmion in the field increasing mode

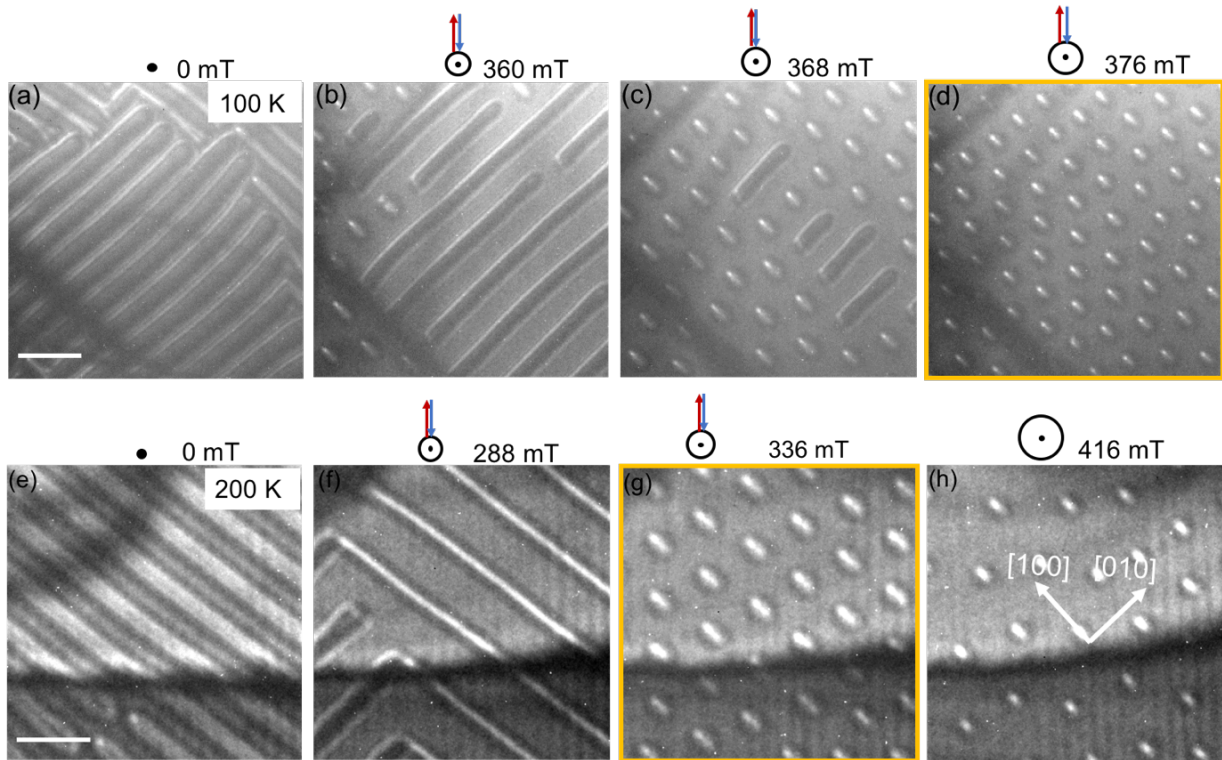


Figure C. 3 | Stability of elliptical skyrmions from helical phase. The evolution of topological spin textures at 100 K for a ~ 280 nm thick lamella starting from the helical phase. (a) The helical phases at 0 mT. (b) Elliptical Bloch skyrmions are nucleated at 360 mT. (c) 368 mT; most of the region filled with elliptical Bloch skyrmions only after increasing further 8 mT of the total magnetic field. (d) 376 mT; a dense lattice state is found. The scale bar in (a) corresponds to 500 nm. (e-h) The evolution of topological spin textures at 200 K for a ~ 170 nm thick lamella starting from the helical phase. Helical phase at 0 mT and 288 mT, respectively. Lattice state is found at 336 mT. At 416 mT; the density of the nano-objects decreases. The scale bar in (e) corresponds to 300 nm.

We have already discussed in Ch. 4 the dependence of spin textures formation with thickness. It is found that for the thin film of ~ 100 nm⁵¹ and ~ 170 nm, the lattice state of (elliptical skyrmions) spin textures is not possible to stabilize below the spin reorientation

transition (< 135 K) of the $\text{Mn}_{1.4}\text{Pt}_{0.9}\text{Pd}_{0.1}\text{Sn}$ compound. On the other hand, for a much thicker specimen of ~ 280 nm, the lattice state of elliptical skyrmions is found at 100 K, indicating the significance of thickness on dipole-dipole interactions. In Fig.6 of Ch.4, we found such a lattice state at 100 K upon using the usual lattice stabilization protocols starting from the field polarized state and lattices of elliptical Bloch skyrmion found up to wide-field range. Here, we conduct our experiment in a reverse order starting from the helical state (Fig. C.3a) in the field increasing mode using the same lattice stabilization protocol where, the helical phase is the dominant magnetic contrast. At 360 mT and 368 mT (Fig. C.3b-c), few elliptical skyrmions emerge. After applying more 8 mT, a lattice state is observed, as given in Fig. C. 3d. Similarly, for ~ 170 nm thick lamella, the helical phase is dominant in the increasing field mode and elliptical skyrmions are found for the 150, 200 and 250 K, using the lattice stabilization protocol. As an example, Fig. C.3e-h show the LTEM contrasts at 200 K.

References

- [1] Dzyaloshinsky, I. A thermodynamic theory of “weak” ferromagnetism of antiferromagnetics. *J. Phys. Chem. Solids* **4**, 241, 1958.
- [2] Moriya, T. Anisotropic superexchange interaction and weak ferromagnetism. *Phys. Rev.* **120**, 91, 1960.
- [3] Bogdanov, A. N.; Yablonskii, D. Thermodynamically stable “vortices” in magnetically ordered crystals. The mixed state of magnets. *Zh. Eksp. Teor. Fiz* **95**, 178, 1989.
- [4] Bogdanov, A.; Röbber, U.; Wolf, M.; Müller, K.-H. Magnetic structures and reorientation transitions in noncentrosymmetric uniaxial antiferromagnets. *Phys. Rev. B* **66**, 214410, 2002.
- [5] Parkin, S. S. P.; Hayashi, M.; Thomas, L. Magnetic domain-wall racetrack memory. *Science* **320**, 190-194, 2008.
- [6] Moore, G. E. Cramming more components onto integrated circuits. *Proc. IEEE* **86**, 82, 1998.
- [7] Fert, A.; Cros, V.; Sampaio, J. Skyrmions on the track. *Nat. Nanotechnol.* **8**, 152, 2013.
- [8] Hoffmann, M.; Zimmermann, B.; Müller, G. P.; Schürhoff, D.; Kiselev, N. S.; Melcher, C.; Blügel, S. Antiskyrmions stabilized at interfaces by anisotropic Dzyaloshinskii-Moriya interactions. *Nat. Commun.* **8**, 308, 2017.
- [9] Keffer, F. Spin waves. Springer, 1966.
- [10] Coey, J. Amorphous magnetic order. *J. Appl. Phys.* **49**, 1646-1652, 1978.
- [11] Knöpfle, K.; Sandratskii, L.; Kübler, J. Spin spiral ground state of γ -iron. *Phys. Rev. B* **62**, 5564, 2000.
- [12] Turek, I.; Kudrnovský, J.; Diviš, M.; Franek, P.; Bihlmayer, G.; Blügel, S. First-principles study of the electronic structure and exchange interactions in bcc europium. *Phys. Rev. B* **68**, 224431, 2003.
- [13] Di Napoli, S.; Llois, A.; Bihlmayer, G.; Blügel, S.; Alouani, M.; Dreysse, H. Magnetic structure and transport properties of noncollinear LaMn_2X_2 (X= Ge, Si) systems. *Phys. Rev. B* **70**, 174418, 2004.
- [14] Nagaosa, N.; Tokura, Y. Emergent electromagnetism in solids. *Phys. Scr.* **2012**, 014020, 2012.

- [15] Nagaosa, N.; Yu, X.; Tokura, Y. Gauge fields in real and momentum spaces in magnets: monopoles and skyrmions. *Philos. Trans. Royal Soc. A* **370**, 5806, 2012.
- [16] Jonietz, F.; Mühlbauer, S.; Pfleiderer, C.; Neubauer, A.; Münzer, W.; Bauer, A.; Adams, T.; Georgii, R.; Böni, P.; Duine, R. A.; Everschor, K.; Garst, M.; Rosch, A. Spin Transfer Torques in MnSi at Ultralow Current Densities. *Science* **330**, 1648, 2010.
- [17] Jiang, W.; Upadhyaya, P.; Zhang, W.; Yu, G.; Jungfleisch, M. B.; Fradin, F. Y.; Pearson, J. E.; Tserkovnyak, Y.; Wang, K. L.; Heinonen, O. Blowing magnetic skyrmion bubbles. *Science* **349**, 283, 2015.
- [18] Skyrme, T. H. R. A unified field theory of mesons and baryons. *Nucl. Phys.* **31**, 556, 1962.
- [19] Bogdanov, A.; Hubert, A. Thermodynamically stable magnetic vortex states in magnetic crystals. *J. Magn. Magn. Mater.* **138**, 255, 1994.
- [20] Mühlbauer, S.; Binz, B.; Jonietz, F.; Pfleiderer, C.; Rosch, A.; Neubauer, A.; Georgii, R.; Böni, P. Skyrmion lattice in a chiral magnet. *Science* **323**, 915, 2009.
- [21] Yu, X.; Onose, Y.; Kanazawa, N.; Park, J.; Han, J.; Matsui, Y.; Nagaosa, N.; Tokura, Y. Real-space observation of a two-dimensional skyrmion crystal. *Nature* **465**, 901, 2010.
- [22] Seki, S.; Yu, X.; Ishiwata, S.; Tokura, Y. Observation of skyrmions in a multiferroic material. *Science* **336**, 198, 2012.
- [23] Yu, X.; Kanazawa, N.; Onose, Y.; Kimoto, K.; Zhang, W.; Ishiwata, S.; Matsui, Y.; Tokura, Y. Near room-temperature formation of a skyrmion crystal in thin-films of the helimagnet FeGe. *Nat. Mater.* **10**, 106, 2011.
- [24] Tokunaga, Y.; Yu, X.; White, J.; Rønnow, H. M.; Morikawa, D.; Taguchi, Y.; Tokura, Y. A new class of chiral materials hosting magnetic skyrmions beyond room temperature. *Nat. Commun.* **6**, 7638, 2015.
- [25] Yu, X.; Kikkawa, A.; Morikawa, D.; Shibata, K.; Tokunaga, Y.; Taguchi, Y.; Tokura, Y. Variation of skyrmion forms and their stability in MnSi thin plates. *Phys. Rev. B* **91**, 054411, 2015.
- [26] Wild, J.; Meier, T. N.; Pöllath, S.; Kronseder, M.; Bauer, A.; Chacon, A.; Halder, M.; Schowalter, M.; Rosenauer, A.; Zweck, J.; Müller, J.; Rosch, A.; Pfleiderer, C.; Back, C. H. Entropy-limited topological protection of skyrmions. *Sci. Adv.* **3**, e1701704, 2017.
- [27] Bogdanov, A.; Rößler, U. Chiral symmetry breaking in magnetic thin films and multilayers. *Phys. Rev. Lett.* **87**, 037203, 2001.
- [28] Heinze, S.; Von Bergmann, K.; Menzel, M.; Brede, J.; Kubetzka, A.; Wiesendanger, R.; Bihlmayer, G.; Blügel, S. Spontaneous atomic-scale magnetic skyrmion lattice in two dimensions. *Nat. Phys.* **7**, 713, 2011.

- [29] Moreau-Luchaire, C.; Moutafis, C.; Reyren, N.; Sampaio, J.; Vaz, C.; Van Horne, N.; Bouzehouane, K.; Garcia, K.; Deranlot, C.; Warnicke, P.; Wohlhüter, P.; George, J.-M.; Weigand, M.; Raabe, J.; Cros, V.; Fert, A. Additive interfacial chiral interaction in multilayers for stabilization of small individual skyrmions at room temperature. *Nat. Nanotechnol.* **11**, 444, 2016.
- [30] Hrabec, A.; Porter, N.; Wells, A.; Benitez, M.; Burnell, G.; Mcvitie, S.; Mcgrouther, D.; Moore, T.; Marrows, C. Measuring and tailoring the Dzyaloshinskii-Moriya interaction in perpendicularly magnetized thin films. *Phys. Rev. B* **90**, 020402, 2014.
- [31] Belmeguenai, M.; Adam, J.-P.; Roussigné, Y.; Eimer, S.; Devolder, T.; Kim, J.-V.; Cherif, S. M.; Stashkevich, A.; Thiaville, A. Interfacial Dzyaloshinskii-Moriya interaction in perpendicularly magnetized Pt/Co/AlO_x ultrathin films measured by Brillouin light spectroscopy. *Phys. Rev. B* **91**, 180405, 2015.
- [32] Boulle, O.; Vogel, J.; Yang, H.; Pizzini, S.; De Souza Chaves, D.; Locatelli, A.; Mentes, T. O.; Sala, A.; Buda-Prejbeanu, L. D.; Klein, O. Room-temperature chiral magnetic skyrmions in ultrathin magnetic nanostructures. *Nat. Nanotechnol.* **11**, 449, 2016.
- [33] Kézsmárki, I.; Bordács, S.; Milde, P.; Neuber, E.; Eng, L.; White, J.; Rønnow, H. M.; Dewhurst, C.; Mochizuki, M.; Yanai, K. Néel-type skyrmion lattice with confined orientation in the polar magnetic semiconductor GaV₄S₈. *Nat. Mater.* **14**, 1116, 2015.
- [34] Kurumaji, T.; Nakajima, T.; Ukleev, V.; Feoktystov, A.; Arima, T.-H.; Kakurai, K.; Tokura, Y. Néel-type skyrmion lattice in the tetragonal polar magnet VOSe₂O₅. *Phys. Rev. Lett.* **119**, 237201, 2017.
- [35] Srivastava, A. K.; Devi, P.; Sharma, A. K.; Ma, T.; Deniz, H.; Meyerheim, H. L.; Felser, C.; Parkin, S. S. P. Observation of Robust Néel Skyrmions in Metallic PtMnGa. *Adv. Mater.* **32**, 1904327, 2020.
- [36] Park, T.-E.; Peng, L.; Zhang, X.; Kim, S. J.; Song, K. M.; Kim, K.; Weigand, M.; Schütz, G.; Finizio, S.; Raabe, J. Observation of magnetic skyrmion crystals in a van der Waals ferromagnet Fe₃GeTe₂. *preprint arXiv:1907.01425*, 2019.
- [37] Lin, Y.; Grundy, P.; Giess, E. Bubble domains in magnetostatically coupled garnet films. *Appl. Phys. Lett.* **23**, 485, 1973.
- [38] Takao, S. A study of magnetization distribution of submicron bubbles in sputtered Ho-Co thin films. *J. Magn. Magn. Mater.* **31**, 1009, 1983.
- [39] Yu, X.; Mostovoy, M.; Tokunaga, Y.; Zhang, W.; Kimoto, K.; Matsui, Y.; Kaneko, Y.; Nagaosa, N.; Tokura, Y. Magnetic stripes and skyrmions with helicity reversals. *Proc. Natl. Acad. Sci.* **109**, 8856, 2012.

- [40] Hirschberger, M.; Nakajima, T.; Gao, S.; Peng, L.; Kikkawa, A.; Kurumaji, T.; Kriener, M.; Yamasaki, Y.; Sagayama, H.; Nakao, H. Skyrmion phase and competing magnetic orders on a breathing kagome lattice. *Nat. Commun.* **10**, 5831, 2019.
- [41] Khanh, N. D.; Nakajima, T.; Yu, X.; Gao, S.; Shibata, K.; Hirschberger, M.; Yamasaki, Y.; Sagayama, H.; Nakao, H.; Peng, L.; Nakajima, K.; Takagi, R.; Arima, T.-H.; Tokura, Y.; Seki, S. Nanometric square skyrmion lattice in a centrosymmetric tetragonal magnet. *Nat. Nanotechnol.*, 444, 2020.
- [42] Peng, L.; Zhang, Y.; Wang, W.; He, M.; Li, L.; Ding, B.; Li, J.; Sun, Y.; Zhang, X.-G.; Cai, J.; Wang, S.; Wu, G.; Shen, B. Real-space observation of nonvolatile zero-field biskyrmion lattice generation in MnNiGa magnet. *Nano Lett.* **17**, 7075, 2017.
- [43] Loudon, J. C.; Twitchett-Harrison, A. C.; Cortés-Ortuño, D.; Birch, M. T.; Turnbull, L. A.; Štefančič, A.; Ogrin, F. Y.; Burgos-Parra, E. O.; Bukin, N.; Laurensen, A. Do Images of Biskyrmions Show Type-II Bubbles? *Adv. Mater.* **31**, 1806598, 2019.
- [44] Göbel, B.; Mook, A.; Henk, J.; Mertig, I.; Tretiakov, O. A. Magnetic bimerons as skyrmion analogues in in-plane magnets. *Phys. Rev. B* **99**, 060407, 2019.
- [45] Kim, S. K. Dynamics of bimeron skyrmions in easy-plane magnets induced by a spin supercurrent. *Phys. Rev. B* **99**, 224406, 2019.
- [46] Bogdanov, A.; Hubert, A. The stability of vortex-like structures in uniaxial ferromagnets. *J. Magn. Magn. Mater.* **195**, 182, 1999.
- [47] Zhang, S.; Kronast, F.; Van Der Laan, G.; Hesjedal, T. Real-space observation of skyrmionium in a ferromagnet-magnetic topological insulator heterostructure. *Nano Lett.* **18**, 1057, 2018.
- [48] Finazzi, M.; Savoini, M.; Khorsand, A.; Tsukamoto, A.; Itoh, A.; Duo, L.; Kirilyuk, A.; Rasing, T.; Ezawa, M. Laser-induced magnetic nanostructures with tunable topological properties. *Phys. Rev. Lett.* **110**, 177205, 2013.
- [49] Hietarinta, J.; Salo, P. Faddeev-Hopf knots: Dynamics of linked un-knots. *Phys. Lett. B* **451**, 60, 1999.
- [50] Liu, Y.; Hou, W.; Han, X.; Zang, J. Three-dimensional dynamics of magnetic hopfion driven by spin transfer torque. *preprint arXiv:2001.00417*, 2020.
- [51] Nayak, A. K.; Kumar, V.; Ma, T.; Werner, P.; Pippel, E.; Sahoo, R.; Damay, F.; Rößler, U. K.; Felser, C.; Parkin, S. S. P. Magnetic antiskyrmions above room temperature in tetragonal Heusler materials. *Nature* **548**, 561, 2017.

- [52] Ma, T.; Sharma, A. K.; Saha, R.; Srivastava, A. K.; Werner, P.; Vir, P.; Kumar, V.; Felser, C.; Parkin, S. S. P. Tunable Magnetic Antiskyrmion Size and Helical Period from Nanometers to Micrometers in a D_{2d} Heusler Compound. *Adv. Mater.*, 20202043, 2020.
- [53] Saha, R.; Srivastava, A. K.; Ma, T.; Jena, J.; Werner, P.; Kumar, V.; Felser, C.; Parkin, S. S. P. Intrinsic stability of magnetic anti-skyrmions in the tetragonal inverse Heusler compound $Mn_{1.4}Pt_{0.9}Pd_{0.1}Sn$. *Nat. Commun.* **10**, 5305, 2019.
- [54] Zheng, F.; Rybakov, F. N.; Borisov, A. B.; Song, D.; Wang, S.; Li, Z.-A.; Du, H.; Kiselev, N. S.; Caron, J.; Kovács, A.; Tian, M.; Zhang, Y.; Blügel, S.; Dunin-Borkowski, R. E. Experimental observation of chiral magnetic bobbars in B20-type FeGe. *Nat. Nanotechnol.* **13**, 451, 2018.
- [55] Braun, H.-B. Topological effects in nanomagnetism: from superparamagnetism to chiral quantum solitons. *Adv. Phys.* **61**, 1, 2012.
- [56] Nagaosa, N.; Tokura, Y. Topological properties and dynamics of magnetic skyrmions. *Nat. Nanotechnol.* **8**, 899, 2013.
- [57] Rózsa, L.; Palotás, K.; Deák, A.; Simon, E.; Yanes, R.; Udvardi, L.; Szunyogh, L.; Nowak, U. Formation and stability of metastable skyrmionic spin structures with various topologies in an ultrathin film. *Phys. Rev. B* **95**, 094423, 2017.
- [58] Bak, P.; Jensen, M. H. Theory of helical magnetic structures and phase transitions in MnSi and FeGe. *J. Phys. C: Solid State* **13**, L881, 1980.
- [59] Lebech, B.; Bernhard, J.; Freltoft, T. Magnetic structures of cubic FeGe studied by small-angle neutron scattering. *J. Phys.: Condens. Matter* **1**, 6105, 1989.
- [60] Leonov, A. O.; Bogdanov, A. N. Crossover of skyrmion and helical modulations in noncentrosymmetric ferromagnets. *New J. Phys.* **20**, 043017, 2018.
- [61] Thiaville, A.; Rohart, S.; Jué, É.; Cros, V.; Fert, A. Dynamics of Dzyaloshinskii domain walls in ultrathin magnetic films. *EPL (Europhysics Letters)* **100**, 57002, 2012.
- [62] Xia, J.; Zhang, X.; Ezawa, M.; Shao, Q.; Liu, X.; Zhou, Y. Dynamics of an elliptical ferromagnetic skyrmion driven by the spin-orbit torque. *Appl. Phys. Lett.* **116**, 022407, 2020.
- [63] Li, S.; Kang, W.; Huang, Y.; Zhang, X.; Zhou, Y.; Zhao, W. Magnetic skyrmion-based artificial neuron device. *Nanotechnology* **28**, 31LT01, 2017.
- [64] Zhang, X.; Zhou, Y.; Ezawa, M.; Zhao, G.; Zhao, W. Magnetic skyrmion transistor: skyrmion motion in a voltage-gated nanotrack. *Sci. Rep.* **5**, 11369, 2015.
- [65] Zhang, X.; Ezawa, M.; Zhou, Y. Magnetic skyrmion logic gates: conversion, duplication and merging of skyrmions. *Sci. Rep.* **5**, 9400, 2015.

- [66] Zhang, X.; Ezawa, M.; Xiao, D.; Zhao, G.; Liu, Y.; Zhou, Y. All-magnetic control of skyrmions in nanowires by a spin wave. *Nanotechnology* **26**, 225701, 2015.
- [67] Wang, W.; Beg, M.; Zhang, B.; Kuch, W.; Fangohr, H. Driving magnetic skyrmions with microwave fields. *Phys. Rev. B* **92**, 020403, 2015.
- [68] Romming, N.; Hanneken, C.; Menzel, M.; Bickel, J. E.; Wolter, B.; Von Bergmann, K.; Kubetzka, A.; Wiesendanger, R. Writing and deleting single magnetic skyrmions. *Science* **341**, 636, 2013.
- [69] Flovik, V.; Qaiumzadeh, A.; Nandy, A. K.; Heo, C.; Rasing, T. Generation of single skyrmions by picosecond magnetic field pulses. *Phys. Rev. B* **96**, 140411, 2017.
- [70] Zhang, S.; Zhang, J.; Zhang, Q.; Barton, C.; Neu, V.; Zhao, Y.; Hou, Z.; Wen, Y.; Gong, C.; Kazakova, O. Direct writing of room temperature and zero field skyrmion lattices by a scanning local magnetic field. *Appl. Phys. Lett.* **112**, 132405, 2018.
- [71] Hsu, P.-J.; Kubetzka, A.; Finco, A.; Romming, N.; Von Bergmann, K.; Wiesendanger, R. Electric-field-driven switching of individual magnetic skyrmions. *Nat. Nanotechnol.* **12**, 123, 2017.
- [72] White, J.; Živković, I.; Kruchkov, A.; Bartkowiak, M.; Magrez, A.; Rønnow, H. Electric-Field-Driven Topological Phase Switching and Skyrmion-Lattice Metastability in Magnetoelectric Cu_2OSeO_3 . *Phys. Rev. Appl.* **10**, 014021, 2018.
- [73] Sampaio, J.; Cros, V.; Rohart, S.; Thiaville, A.; Fert, A. Nucleation, stability and current-induced motion of isolated magnetic skyrmions in nanostructures. *Nat. Nanotechnol.* **8**, 839, 2013.
- [74] Schäffer, A. F.; Dürr, H. A.; Berakdar, J. Ultrafast imprinting of topologically protected magnetic textures via pulsed electrons. *Appl. Phys. Lett.* **111**, 032403, 2017.
- [75] Du, H.; Che, R.; Kong, L.; Zhao, X.; Jin, C.; Wang, C.; Yang, J.; Ning, W.; Li, R.; Jin, C. Edge-mediated skyrmion chain and its collective dynamics in a confined geometry. *Nat. Commun.* **6**, 8504, 2015.
- [76] Lin, S.-Z. Edge instability in a chiral stripe domain under an electric current and skyrmion generation. *Phys. Rev. B* **94**, 020402, 2016.
- [77] Maccariello, D.; Legrand, W.; Reyren, N.; Garcia, K.; Bouzehouane, K.; Collin, S.; Cros, V.; Fert, A. Electrical detection of single magnetic skyrmions in metallic multilayers at room temperature. *Nat. Nanotechnol.* **13**, 233, 2018.
- [78] Milde, P.; Köhler, D.; Seidel, J.; Eng, L.; Bauer, A.; Chacon, A.; Kindervater, J.; Mühlbauer, S.; Pfleiderer, C.; Buhrandt, S. Unwinding of a skyrmion lattice by magnetic monopoles. *Science* **340**, 1076, 2013.

- [79] Neubauer, A.; Pfleiderer, C.; Binz, B.; Rosch, A.; Ritz, R.; Niklowitz, P.; Böni, P. Topological Hall effect in the A phase of MnSi. *Phys. Rev. Lett.* **102**, 186602, 2009.
- [80] Jiang, W.; Zhang, X.; Yu, G.; Zhang, W.; Wang, X.; Jungfleisch, M. B.; Pearson, J. E.; Cheng, X.; Heinonen, O.; Wang, K. L.; Zhou, Y.; Hoffmann, A.; Velthuis, G. E. Direct observation of the skyrmion Hall effect. *Nat. Phys.* **13**, 162, 2017.
- [81] Barker, J.; Tretiakov, O. A. Static and dynamical properties of antiferromagnetic skyrmions in the presence of applied current and temperature. *Phys. Rev. Lett.* **116**, 147203, 2016.
- [82] Legrand, W.; Maccariello, D.; Ajejas, F.; Collin, S.; Vecchiola, A.; Bouzehouane, K.; Reyren, N.; Cros, V.; Fert, A. Room-temperature stabilization of antiferromagnetic skyrmions in synthetic antiferromagnets. *Nat. Mater.* **19**, 34, 2020.
- [83] Dohi, T.; Duttagupta, S.; Fukami, S.; Ohno, H. Formation and current-induced motion of synthetic antiferromagnetic skyrmion bubbles. *Nat. Commun.* **10**, 5153, 2019.
- [84] Huang, S.; Zhou, C.; Chen, G.; Shen, H.; Schmid, A. K.; Liu, K.; Wu, Y. Stabilization and current-induced motion of antiskyrmion in the presence of anisotropic Dzyaloshinskii-Moriya interaction. *Phys. Rev. B* **96**, 144412, 2017.
- [85] Shibata, K.; Iwasaki, J.; Kanazawa, N.; Aizawa, S.; Tanigaki, T.; Shirai, M.; Nakajima, T.; Kubota, M.; Kawasaki, M.; Park, H. S.; Shindo, D.; Nagaosa, N.; Tokura, Y. Large anisotropic deformation of skyrmions in strained crystal. *Nat. Nanotechnol.* **10**, 589, 2015.
- [86] Matsumoto, T.; So, Y.-G.; Kohno, Y.; Sawada, H.; Ikuhara, Y.; Shibata, N. Direct observation of $\Sigma 7$ domain boundary core structure in magnetic skyrmion lattice. *Sci. Adv.* **2**, e1501280, 2016.
- [87] Yu, X.; Koshibae, W.; Tokunaga, Y.; Shibata, K.; Taguchi, Y.; Nagaosa, N.; Tokura, Y. Transformation between meron and skyrmion topological spin textures in a chiral magnet. *Nature* **564**, 95, 2018.
- [88] Nagase, T.; So, Y.; Yasui, H.; Ishida, T.; Yoshida, H.; Tanaka, Y.; Saitoh, K.; Ikarashi, N.; Kawaguchi, Y.; Kuwahara, M. Observation of domain wall skyrmions in chiral magnets. *preprint arXiv:2004.06976*, 2020.
- [89] Rybakov, F. N.; Borisov, A. B.; Blügel, S.; Kiselev, N. S. New type of stable particlelike states in chiral magnets. *Phys. Rev. Lett.* **115**, 117201, 2015.
- [90] Okubo, T.; Chung, S.; Kawamura, H. Multiple-q states and the skyrmion lattice of the triangular-lattice Heisenberg antiferromagnet under magnetic fields. *Phys. Rev. Lett.* **108**, 017206, 2012.

- [91] Zhang, X.; Xia, J.; Zhou, Y.; Liu, X.; Zhang, H.; Ezawa, M. Skyrmion dynamics in a frustrated ferromagnetic film and current-induced helicity locking-unlocking transition. *Nat. Commun.* **8**, 1717, 2017.
- [92] Kurumaji, T.; Nakajima, T.; Hirschberger, M.; Kikkawa, A.; Yamasaki, Y.; Sagayama, H.; Nakao, H.; Taguchi, Y.; Arima, T.-H.; Tokura, Y. Skyrmion lattice with a giant topological Hall effect in a frustrated triangular-lattice magnet. *Science* **365**, 914, 2019.
- [93] Camosi, L.; Rohart, S.; Fruchart, O.; Pizzini, S.; Belmeguenai, M.; Roussigné, Y.; Stashkevich, A.; Cherif, S. M.; Ranno, L.; De Santis, M. Anisotropic dzyaloshinskii-moriya interaction in ultrathin epitaxial Au/Co/W(110). *Phys. Rev. B* **95**, 214422, 2017.
- [94] Von Ardenne, M. Das elektronen-rastermikroskop. Praktische ausführung. *Zeitschrift für technische Physik* **19**, 407, 1938.
- [95] Goldstein, J. I.; Newbury, D. E.; Michael, J. R.; Ritchie, N. W.; Scott, J. H. J.; Joy, D. C., *Scanning electron microscopy and X-ray microanalysis*. Springer: 2017.
- [96] Smith, K.; Oatley, C. The scanning electron microscope and its fields of application. *Br. J. Appl. Phys.* **6**, 391, 1955.
- [97] Maitland, T.; Sitzman, S., *Electron backscatter diffraction (EBSD) technique and materials characterization examples*. Springer Berlin: 2007; Vol. 14.
- [98] Wilkinson, A. J.; Britton, T. B. Strains, planes, and EBSD in materials science. *Mater. Today* **15**, 366, 2012.
- [99] Dingley, D. Progressive steps in the development of electron backscatter diffraction and orientation imaging microscopy. *J. Microsc.* **213**, 214, 2004.
- [100] Schwartz, A. J.; Kumar, M.; Adams, B. L.; Field, D. P., *Electron backscatter diffraction in materials science*. Springer: 2009; Vol. 2.
- [101] Bragg, W. H.; Bragg, W. L. The reflection of X-rays by crystals. *Proceedings of the Royal Society of London. Series A, Containing Papers of a Mathematical and Physical Character* **88**, 428, 1913.
- [102] Williams, D. B.; Carter, C. B., *Transmission Electron Microscopy: A Textbook for Materials Science*. Springer Science & Business Media: 1996; Vol. 1.
- [103] Saruwatari, K.; Akai, J.; Fukumori, Y.; Ozaki, N.; Nagasawa, H.; Kogure, T. Crystal orientation analyses of biominerals using Kikuchi patterns in TEM. *J. Miner. Petrol. Sci.* **103**, 16, 2007.
- [104] Britton, T.; Jiang, J.; Guo, Y.; Vilalta-Clemente, A.; Wallis, D.; Hansen, L. N.; Winkelmann, A.; Wilkinson, A. Tutorial: Crystal orientations and EBSD—Or which way is up? *Mater. Charact.* **117**, 113, 2016.

- [105] Randle, V. Electron backscatter diffraction: Strategies for reliable data acquisition and processing. *Mater. Charact.* **60**, 913, 2009.
- [106] Hall, C. E., *Introduction to electron microscopy*. LWW: 1954; Vol. 77.
- [107] Egerton, R. F., *Physical principles of electron microscopy*. Springer: 2005; Vol. 56.
- [108] Orloff, J. Charged Particle Optics. *Encyclopedia of Imaging Science and Technology*, 2002.
- [109] Crewe, A. V.; Isaacson, M.; Johnson, D. A simple scanning electron microscope. *Rev. Sci. Instrum.* **40**, 241, 1969.
- [110] Rose, H. H. Optics of high-performance electron microscopes. *Sci. Technol. Adv. Mater.* **9**, 014107, 2008.
- [111] Reimer, L. Electron diffraction methods in TEM, STEM and SEM. *Scanning* **2**, 3, 1979.
- [112] Cowley, J. Diffraction Physics North Holland. *Publ. Co., Amsterdam*, 1975.
- [113] CrystalMaker Software, <http://www.crystallmaker.com/>.
- [114] Hopster, H.; Oepen, H. P., *Magnetic microscopy of nanostructures*. Springer Science & Business Media: 2006.
- [115] Shibata, N.; Findlay, S. D.; Kohno, Y.; Sawada, H.; Kondo, Y.; Ikuhara, Y. Differential phase-contrast microscopy at atomic resolution. *Nat. Phys.* **8**, 611, 2012.
- [116] Petford-Long, A.; De Graef, M. Lorentz microscopy. *Characterization of materials*, 1, 2002.
- [117] Ishizuka, K. A practical approach for STEM image simulation based on the FFT multislice method. *Ultramicroscopy* **90**, 71, 2002.
- [118] Malozemoff, A. P.; Slonczewski, J. C., *Magnetic Domain Walls in Bubble Materials*. Academic press: New York, 1979; Vol. 1.
- [119] Rybakov, F. N.; Borisov, A. B.; Blügel, S.; Kiselev, N. S. New spiral state and skyrmion lattice in 3D model of chiral magnets. *New J. Phys.* **18**, 045002, 2016.
- [120] Morikawa, D.; Yu, X.; Karube, K.; Tokunaga, Y.; Taguchi, Y.; Arima, T.-H.; Tokura, Y. Deformation of topologically-protected supercooled skyrmions in a thin plate of chiral magnet $\text{Co}_8\text{Zn}_8\text{Mn}_4$. *Nano Lett.* **17**, 1637, 2017.
- [121] Li, Z.-A.; Zheng, F.; Tavabi, A. H.; Caron, J.; Jin, C.; Du, H.; Kovács, A. S.; Tian, M.; Farle, M.; Dunin-Borkowski, R. E. Magnetic skyrmion formation at lattice defects and grain boundaries studied by quantitative off-axis electron holography. *Nano Lett.* **17**, 1395, 2017.
- [122] Jin, C.; Li, Z.-A.; Kovács, A.; Caron, J.; Zheng, F.; Rybakov, F. N.; Kiselev, N. S.; Du, H.; Blügel, S.; Tian, M.; Zhang, Y.; Farle, M.; Dunin-Borkowski, R. E. Control of

- morphology and formation of highly geometrically confined magnetic skyrmions. *Nat. Commun.* **8**, 15569, 2017.
- [123] Camosi, L.; Rougemaille, N.; Fruchart, O.; Vogel, J.; Rohart, S. Micromagnetics of antiskyrmions in ultrathin films. *Phys. Rev. B* **97**, 134404, 2018.
- [124] Jena, J.; Stinshoff, R.; Saha, R.; Srivastava, A. K.; Ma, T.; Deniz, H.; Werner, P.; Felser, C.; Parkin, S. S. P. Observation of Magnetic Antiskyrmions in the Low Magnetization Ferrimagnet $\text{Mn}_2\text{Rh}_{0.95}\text{Ir}_{0.05}\text{Sn}$. *Nano Lett.* **20**, 59, 2020.
- [125] Tomasello, R.; Martinez, E.; Zivieri, R.; Torres, L.; Carpentieri, M.; Finocchio, G. A strategy for the design of skyrmion racetrack memories. *Sci. Rep.* **4**, 6784, 2014.
- [126] Iwasaki, J.; Mochizuki, M.; Nagaosa, N. Current-induced skyrmion dynamics in constricted geometries. *Nat. Nanotechnol.* **8**, 742, 2013.
- [127] Leonov, A.; Mostovoy, M. Edge states and skyrmion dynamics in nanostripes of frustrated magnets. *Nat. Commun.* **8**, 14394, 2017.
- [128] Woo, S.; Litzius, K.; Krüger, B.; Im, M.-Y.; Caretta, L.; Richter, K.; Mann, M.; Krone, A.; Reeve, R. M.; Weigand, M. Observation of room-temperature magnetic skyrmions and their current-driven dynamics in ultrathin metallic ferromagnets. *Nat. Mater.* **15**, 501, 2016.
- [129] Litzius, K.; Lemesh, I.; Krüger, B.; Bassirian, P.; Caretta, L.; Richter, K.; Büttner, F.; Sato, K.; Tretiakov, O. A.; Förster, J. Skyrmion Hall effect revealed by direct time-resolved X-ray microscopy. *Nat. Phys.* **13**, 170, 2017.
- [130] Iwasaki, J.; Mochizuki, M.; Nagaosa, N. Universal current-velocity relation of skyrmion motion in chiral magnets. *Nat. Commun.* **4**, 1463, 2013.
- [131] Chen, G. Spin-orbitronics: Skyrmion Hall effect. *Nat. Phys.* **13**, 112, 2017.
- [132] Koshibae, W.; Nagaosa, N. Theory of antiskyrmions in magnets. *Nat. Commun.* **7**, 10542, 2016.
- [133] Jena, J.; Göbel, B.; Ma, T.; Kumar, V.; Saha, R.; Mertig, I.; Felser, C.; Parkin, S. S. P. Elliptical Bloch skyrmion chiral twins in an antiskyrmion system. *Nat. Commun.* **11**, 1115, 2020.
- [134] Peng, L.; Takagi, R.; Koshibae, W.; Shibata, K.; Nakajima, K.; Arima, T.-H.; Nagaosa, N.; Seki, S.; Yu, X.; Tokura, Y. Controlled transformation of skyrmions and antiskyrmions in a non-centrosymmetric magnet. *Nat. Nanotechnol.* **15**, 181, 2020.
- [135] Suess, D.; Vogler, C.; Bruckner, F.; Heistracher, P.; Slanovc, F.; Abert, C. Spin torque efficiency and analytic error rate estimates of skyrmion racetrack memory. *Sci. Rep.* **9**, 4827, 2019.
-

- [136] Song, D.; Li, Z.-A.; Caron, J.; Kovács, A.; Tian, H.; Jin, C.; Du, H.; Tian, M.; Li, J.; Zhu, J.; Dunin-Borkowski, R. E. Quantification of Magnetic Surface and Edge States in an FeGe Nanostripe by Off-Axis Electron Holography. *Phys. Rev. Lett.* **120**, 167204, 2018.
- [137] Lee, S.; Zhu, F.; Chien, C.; Marković, N. Effect of geometry on magnetic domain structure in Ni wires with perpendicular anisotropy: a magnetic force microscopy study. *Phys. Rev. B* **77**, 132408, 2008.
- [138] Zuo, S.; Zhang, B.; Qiao, K.; Peng, L.; Li, R.; Xiong, J.; Zhang, Y.; Zhao, X.; Liu, D.; Zhao, T. Direct observation of the magnetic domain evolution stimulated by temperature and magnetic field in PrMnGeSi alloy. *AIP Adv.* **8**, 056801, 2018.
- [139] Phatak, C.; Petford-Long, A.; Zheng, H.; Mitchell, J.; Rosenkranz, S.; Norman, M. Ferromagnetic domain behavior and phase transition in bilayer manganites investigated at the nanoscale. *Phys. Rev. B* **92**, 224418, 2015.
- [140] Nakajima, H.; Kotani, A.; Harada, K.; Ishii, Y.; Mori, S. Foucault imaging and small-angle electron diffraction in controlled external magnetic fields. *Microscopy* **65**, 473, 2016.
- [141] Yu, X.; Morikawa, D.; Yokouchi, T.; Shibata, K.; Kanazawa, N.; Kagawa, F.; Arima, T.-H.; Tokura, Y. Aggregation and collapse dynamics of skyrmions in a non-equilibrium state. *Nat. Phys.* **14**, 832, 2018.
- [142] Meynell, S.; Wilson, M.; Fritzsche, H.; Bogdanov, A.; Monchesky, T. Surface twist instabilities and skyrmion states in chiral ferromagnets. *Phys. Rev. B* **90**, 014406, 2014.
- [143] Müller, J.; Rosch, A.; Garst, M. Edge instabilities and skyrmion creation in magnetic layers. *New J. Phys.* **18**, 065006, 2016.
- [144] Hirose, T.; Diaz, S. A.; Klinovaja, J.; Loss, D. Magnonic Quadrupole Topological Insulator in Antiskyrmion Crystals. *preprint arXiv:2005.05884*, 2020.
- [145] Jungwirth, T.; Marti, X.; Wadley, P.; Wunderlich, J. Antiferromagnetic spintronics. *Nat. Nanotechnol.* **11**, 231, 2016.
- [146] Baltz, V.; Manchon, A.; Tsoi, M.; Moriyama, T.; Ono, T.; Tserkovnyak, Y. Antiferromagnetic spintronics. *Rev. Mod. Phys.* **90**, 015005, 2018.
- [147] Duine, R.; Lee, K.-J.; Parkin, S. S. P.; Stiles, M. D. Synthetic antiferromagnetic spintronics. *Nat. Phys.* **14**, 217, 2018.
- [148] Gomonay, O.; Baltz, V.; Brataas, A.; Tserkovnyak, Y. Antiferromagnetic spin textures and dynamics. *Nat. Phys.* **14**, 213, 2018.
- [149] Zhang, X.; Zhou, Y.; Ezawa, M. Antiferromagnetic skyrmion: stability, creation and manipulation. *Sci. Rep.* **6**, 24795, 2016.

- [150] Yang, S.-H.; Ryu, K.-S.; Parkin, S. S. P. Domain-wall velocities of up to 750 m s^{-1} driven by exchange-coupling torque in synthetic antiferromagnets. *Nat. Nanotechnol.* **10**, 221, 2015.
- [151] Hirata, Y.; Kim, D.-H.; Kim, S. K.; Lee, D.-K.; Oh, S.-H.; Kim, D.-Y.; Nishimura, T.; Okuno, T.; Futakawa, Y.; Yoshikawa, H. Vanishing skyrmion Hall effect at the angular momentum compensation temperature of a ferrimagnet. *Nat. Nanotechnol.* **14**, 232, 2019.
- [152] Meshcheriakova, O.; Chadov, S.; Nayak, A.; Rößler, U.; Kübler, J.; André, G.; Tsirlin, A.; Kiss, J.; Hausdorf, S.; Kalache, A.; Schnelle, W.; Nicklas, M.; Felser, C. Large noncollinearity and spin reorientation in the novel Mn_2RhSn Heusler magnet. *Phys. Rev. Lett.* **113**, 087203, 2014.
- [153] Winxpow, S. Stoe & Cie GmbH. *Darmstadt, Germany* **298**, 2011.
- [154] Petricek, V.; Dusek, M.; Palatinus, L. Jana2006. Structure determination software programs. *Prague (Czech Republic): Institute of Physics, University of Prague*, 2006.
- [155] Vir, P.; Kumar, N.; Borrmann, H.; Jamijansuren, B.; Kreiner, G.; Shekhar, C.; Felser, C. Tetragonal superstructure of the antiskyrmion hosting Heusler compound $\text{Mn}_{1.4}\text{PtSn}$. *Chem. Mater.* **31**, 5876, 2019.
- [156] Vir, P.; Gayles, J.; Sukhanov, A.; Kumar, N.; Damay, F.; Sun, Y.; Kübler, J.; Shekhar, C.; Felser, C. Anisotropic topological Hall effect with real and momentum space Berry curvature in the antiskyrmion-hosting Heusler compound $\text{Mn}_{1.4}\text{PtSn}$. *Phys. Rev. B* **99**, 140406, 2019.
- [157] Kumar, V.; Kumar, N.; Reehuis, M.; Gayles, J.; Sukhanov, A.; Hoser, A.; Damay, F.; Shekhar, C.; Adler, P.; Felser, C. Detection of antiskyrmions by topological Hall effect in Heusler compounds. *Phys. Rev. B* **101**, 014424, 2020.
- [158] Uchida, M.; Onose, Y.; Matsui, Y.; Tokura, Y. Real-space observation of helical spin order. *Science* **311**, 359, 2006.
- [159] Dussaux, A.; Schoenherr, P.; Koumpouras, K.; Chico, J.; Chang, K.; Lorenzelli, L.; Kanazawa, N.; Tokura, Y.; Garst, M.; Bergman, A.; Degen, C. L.; Meier, D. Local dynamics of topological magnetic defects in the itinerant helimagnet FeGe . *Nat. Commun.* **7**, 12430, 2016.
- [160] Kanazawa, N.; Seki, S.; Tokura, Y. Noncentrosymmetric magnets hosting magnetic skyrmions. *Adv. Mater.* **29**, 1603227, 2017.
- [161] Tokunaga, Y.; Yu, X.; White, J.; Rønnow, H. M.; Morikawa, D.; Taguchi, Y.; Tokura, Y. A new class of chiral materials hosting magnetic skyrmions beyond room temperature. *Nat. Commun.* **6**, 7638, 2015.

- [162] Jia, H.; Zimmermann, B.; Blügel, S. First-principles investigation of chiral magnetic properties in multilayers: Rh/Co/Pt and Pd/Co/Pt. *Phys. Rev. B* **98**, 144427, 2018.
- [163] Hellman, F.; Hoffmann, A.; Tserkovnyak, Y.; Beach, G. S.; Fullerton, E. E.; Leighton, C.; Macdonald, A. H.; Ralph, D. C.; Arena, D. A.; Dürr, H. A. Interface-induced phenomena in magnetism. *Rev. Mod. Phys.* **89**, 025006, 2017.
- [164] Ryu, K.-S.; Yang, S.-H.; Thomas, L.; Parkin, S. S. P. Chiral spin torque arising from proximity-induced magnetization. *Nat. Commun.* **5**, 3910, 2014.
- [165] Yu, X.; Shibata, K.; Koshibae, W.; Tokunaga, Y.; Kaneko, Y.; Nagai, T.; Kimoto, K.; Taguchi, Y.; Nagaosa, N.; Tokura, Y. Thermally activated helicity reversals of skyrmions. *Phys. Rev. B* **93**, 134417, 2016.
- [166] Montoya, S.; Couture, S.; Chess, J.; Lee, J.; Kent, N.; Henze, D.; Sinha, S.; Im, M.-Y.; Kevan, S.; Fischer, P. Tailoring magnetic energies to form dipole skyrmions and skyrmion lattices. *Phys. Rev. B* **95**, 024415, 2017.
- [167] Takagi, R.; Yu, X.; White, J.; Shibata, K.; Kaneko, Y.; Tatara, G.; Rønnow, H.; Tokura, Y.; Seki, S. Low-field bi-skyrmion formation in a noncentrosymmetric chimney ladder ferromagnet. *Phys. Rev. Lett.* **120**, 037203, 2018.
- [168] Mascot, E.; Bedow, J.; Graham, M.; Rachel, S.; Morr, D. K. Topological Superconductivity in Skyrmion Lattices. *preprint arXiv:2005.00027*, 2020.
- [169] Garnier, M.; Mesaros, A.; Simon, P. Topological superconductivity with deformable magnetic skyrmions. *Commun. Phys.* **2**, 126, 2019.
- [170] Güngördü, U.; Sandhoefner, S.; Kovalev, A. A. Stabilization and control of Majorana bound states with elongated skyrmions. *Phys. Rev. B* **97**, 115136, 2018.

Author contributions

Jagannath Jena conceived the idea of the work discussed in chapter 4. Vivek Kumar prepared the Bulk polycrystalline sample under the supervision of Claudia Felser. Electron back scattering diffraction experiment is done by **Jagannath Jena**. **Jagannath Jena** prepared the different thickness of lamellae for TEM investigation. The spin textures stability optimization and magnetic contrast imaging using Lorentz TEM experiments are carried out by **Jagannath Jena**. **Jagannath Jena** analyzed the experimental data. Börge Göbel carried out the micromagnetic simulation with input from Ingrid Mertig. Stuart S. P. Parkin supervised the project. This work is published in *Nature Communication*, 11, 1115 (2020).

Jagannath Jena conceived the idea for studying the nano-object magnetic textures in nano-tracks that discussed in chapter 5. Fabrication of nano-tracks is optimized by **Jagannath Jena**. **Jagannath Jena** performed the Lorentz TEM experiment and analyzed the data. Börge Göbel carried out the micromagnetic simulation with input from Ingrid Mertig. Stuart S. P. Parkin supervised the project. The manuscript is published in *Science Advances*, 6, eabc0723 (2020).

Jagannath Jena conceived the idea of the work studied in chapter 6. Various protocols used for studying different topological spin textures are optimized by **Jagannath Jena**. **Jagannath Jena** performed the Lorentz TEM experiment and analyzed the data. Stuart S. P. Parkin supervised the project. Some important experiments are still going on and we hope that a fruitful analysis will give a clear picture of this project in recent future.

Jagannath Jena conceived the idea of the work discussed in chapter 7. The FIB lamellae are prepared by **Jagannath Jena** and Abhay K. Srivastava. Lorentz TEM imaging and their analysis are carried out by **Jagannath Jena**. Bulk sample is prepared by Rolf Stinshoff under the supervision of Claudia Felser. **Jagannath Jena**, Rana Saha and Rolf Stinshoff carried out magnetization measurement. **Jagannath Jena** and Hakan Deniz performed the TEM experiments. Electron back scattering diffraction experiment is done by **Jagannath Jena**. Tianping Ma and Peter Werner contributed to the analysis. Stuart S. P. Parkin supervised the project. Part of the work is published in *Nano Letter*, 20, 59 (2019) and the remaining part is published in *Advanced Materials*, 2101323 (2021).

Acknowledgements

First and foremost, I would like to express gratitude to my supervisor, Stuart S. P. Parkin, for the opportunity to carry out my doctoral project in his group at the Max Planck Institute of Microstructure Physics in Halle. I am so grateful that he supervised my thesis and gave me ample freedom to work on a new, meaningful and challenging research field. The scientific discussions with him are always a great opportunity for me to learn how to approach topics, brainstorm ideas, give critical comments, and learn editing manuscripts. He supported me constantly on a scientific, creative, financial and personal level. I really enjoy working with him.

Apart from Stuart, I would like to thank Claudia Felser (MPI CPfS, Dresden) and her team members Vivek Kumar and Rolf Stinshoff, for providing the bulk samples. I want to thank Ingrid Mertig (MLU, Halle) and Børge Göbel for carrying out simulations. I appreciate the continuous help and support of many colleagues Rana Saha, Abhay Kant Srivastava, Ankit Sharma, Hakan Deniz, Tianping Ma, Peter Werner, Holger Meyerheim, Ajaya Nayak, See-Hun Yang, and Jakob Gauert.

Teachers play an essential role throughout my educational path and added a great value to my life. I am thankful to R.C. Budhani for giving me the chance to work on a project in his group and strengthening my confidence to work in the condensed matter field during my coursework at IIT Kanpur. I also would like to thank S. C Nayak for his guidance during my Bachelor studies. I owe my sincere gratitude to my junior college principal, Late Rabinarayan Sathpaty, for acknowledging my interest in science and for his helping hand to my change from the Arts section to science. His faith, encouragement and financial help during my studies mean a lot to me. I will always be grateful to him. Besides, I would like to acknowledge my primary and high school teachers Santi Apa, Bikash Bhai, Srikant Bhai, Sanjay Bhai, Rajendu Sir, Bidyadhar Sir, Babi Sir and Rabindra Sir.

It is necessary to have a good and joyful atmosphere to accomplish goals in professional life. I must mention here, Tamadur, Banabir, Binoy, Mazhar, Samiran, Malli, Pranava, Anastasios, Ajesh, Arpit, Avanindra, Chirag, Hao, Prajwal, Amilcar, Bharat, Chuanshou, Souvik, Pedram, Kajol, Anirban for lightening the atmosphere during tense moments.

My friends, back in India, are always supporting to me. Let me acknowledge here Sudhir, Deepak, Nitya, Purna, Subhajyoti, Siba, Shashi, Manas, Sukant, Sorna, Jogesh, Sanjukta, Partha, Chandan, Asit, Jagdish, Jaya, Balia, Nasib, and Deba.

Also, I duly acknowledge the support from our technical and administrative staff. Special thanks to Simone and Antje for providing support with various administrative matters which allowed me to better focus on my work. Simone really care about our time as a doctoral candidate here at the institute.

Thank you, to my sisters Anju, Kati, Tiki, Nili, brother Dillip and my cousin Manoranjan who encourage me since my early childhood. I would like to express my sweetest love to my parents for always believing in me. They have been and will always be a pillar of support and source of inspiration in my life. Last but not least, a special thanks to my loving sister Kati for everything. I am always grateful to her for care and unconditional love for me. My thesis is dedicated to the memory of her.

Curriculum vitae

Jagannath Jena

Personal information

Date of birth 30th April 1991

Place of birth Odisha, India

Nationality Indian

Education

11/2016 - 05/2021 Ph.D. student at Max-Planck-Institute of Microstructure
Physics, Halle, Germany

Supervisor: Prof. Stuart S. P. Parkin

08/2015 - 10/2016 Ph.D. student at Indian Institute of Technology
(IIT) Kanpur, Uttar Pradesh, India

07/2011 - 07/2013 M.Sc. in Physics
Utkal University, Vanivihar, Odisha, India

07/2008 - 06/2011 B.Sc. in Physics, Chemistry, Mathematics
Fakir Mohan (Auto) College, Odisha, India

List of publications

Thesis related publications

J. Jena, B. Göbel, T. Ma, V. Kumar, R. Saha, I. Mertig, C. Felser, S. S. P. Parkin, "Elliptical Bloch skyrmion chiral twins in an antiskyrmion system". Nature Communication, 11, 1115, (2020).

J. Jena, B. Göbel, V. Kumar, I. Mertig, C. Felser, S. S. P. Parkin, "Evolution and competition between chiral spin textures in nano-stripes with D_{2d} symmetry". Science Advances 6, eabc0723, (2020).

J. Jena, R. Stinshoff, R. Saha, A. K. Srivastava, T. Ma, H. Deniz, P. Werner, C. Felser, S. S. P. Parkin, "Observation of magnetic antiskyrmions in the low magnetization ferrimagnet $Mn_2Rh_{0.95}Ir_{0.05}Sn$ ". Nano Letter, 20, 59, (2020).

A. K. Sharma*, **J. Jena***, Kumari G. Rana, A. Markou, H. Meyerheim, K. Mohseni, A. K. Srivastava, I. Kostanoskiy, C. Felser, S. S. P. Parkin, "Nanoscale noncollinear spin textures in thin films of a D_{2d} Heusler compounds". Advanced Materials, 2101323 (2021).

J. Jena, S. S. P. Parkin, "Protocol dependent stability of various magnetic spin textures in a non-centrosymmetric magnet". [Manuscript in preparations].

*These authors contributed equally.

Other publications during Ph.D. period

R. Saha, A. K. Srivastava, T. Ma, **J. Jena**, V. Kumar, C. Felser, S. S. P. Parkin, "Intrinsic stability of magnetic antiskyrmion in the tetragonal inverse Heusler compound $Mn_{1.4}Pt_{0.9}Pd_{0.1}Sn$ ". Nature Communication, 10, 5305, (2019).

P. K. Sivakumar, B. Göbel, E. Lense, A. Markou, J. Gidugu, J. M. Taylor, H. Deniz, **J. Jena**, C. Felser, I. Mertig, S. S. P. Parkin, “Topological Hall signatures of two chiral spin textures hosted in a single tetragonal inverse Heusler thin film”. *ACS Nano*, 14, 13463, (2020).

A. Bedoya-Pinto, A. K. Pandeya, D. Liu, H. Deniz, K. Chang, H. Tan, H. Han, **J. Jena**, I. Kostanovskiy, S. S. P. Parkin, “Realization of epitaxial NbP and TaP Weyl semimetal thin films”. *ACS Nano*, 14, 4405, (2020).

G. Li, Q. Yang, K. Manna, C. Fu, H. Deniz, **J. Jena**, F. Li, S. S. P. Parkin, G. Auffermann, Y. Sun, C. Felser, “Optimization of catalytic active sites in non-collinear anti-ferromagnetic Mn_3Pt bulk single-crystal”. *Materials Today Physics* 10, 1000137, (2019).

W. Shi, B. J. Wieder, H. Meyerheim, Y. Sun, Y. Zhang, Y. Li, L. Shen, Y. Qi, L. Yang, **J. Jena**, P. Werner, K. Koepernik, S. S. P. Parkin, Y. Chen, C. Felser, B. A. Bernevig, Z. Wang, “A charge-density-wave Weyl semimetal”. *Nature Physics* 17, 381, (2021).

Patents

J. Jena, S. S. P. Parkin, “Antiskyrmions and elliptical skyrmions in nano-stripes”. [Submitted].

Eidesstattliche Erklärung

Hiermit erkläre ich, Jagannath Jena, die vorliegende Arbeit “ **Discovery of Co-existing Non-collinear Spin Textures in D_{2d} Heusler Compounds**” selbständig und ohne fremde Hilfe verfasst zu haben. Es wurden keine anderen als die von mir angegebenen Quellen und Hilfsmittel benutzt. Die den benutzen Werken wörtlich oder inhaltlich entnommenen Stellen sind als solche kenntlich gemacht worden. Ich erkläre, die Angaben wahrheitsgemäß gemacht, keine vergeblichen Promotionsversuche unternommen und keine Dissertation an einer anderen wissenschaftlichen Einrichtung zur Erlangung eines akademischen Grades eingereicht zu haben. Ich bin weder vorbestraft noch sind gegen mich Ermittlungsverfahren anhängig.

Halle (Saale), den 02.11.2020
Jagannath Jena